Development of New Off-Axis Near Detector Samples for the T2K Oscillation Analysis

Tristan Alexander Doyle

This thesis is submitted for the degree of
Doctor of Philosophy

Physics Department
Lancaster University
United Kingdom
June 6, 2022

Abstract

The Tokai-to-Kamioka (T2K) experiment is a long-baseline (anti)neutrino experiment designed to make world-leading measurements of several of the parameters that describe neutrino oscillations: θ_{13}, θ_{23}, Δm^2_{23} and δ_{CP}. The experiment uses a beam of muon (anti)neutrinos produced at the Japan Proton Accelerator Research Complex (J-PARC) which is categorised by a suite of near detectors before oscillation samples are selected at the far detector, Super-Kamiokande.

Charged Current (CC) ν_μ interactions in the near detector ND280 are categorised based on reconstructed final state particles. The resulting samples are fitted to near detector data to provide constraints on flux and cross section systematic uncertainties in the oscillation analysis.

In this thesis, a new selection of CC ν_μ interactions in the ND280 detector that produce final state photons is developed. The new photon sample has an efficiency of 43.0±0.1% (43.9±0.1%) and a purity of 53.9±0.2% (54.2±0.2%) in FGD1 (FGD2). Detector systematic uncertainties associated with the new selections are also evaluated.

The new photon sample, along with a new proton tag, are used in a new categorisation of CC ν_μ interactions at the near detector in the oscillation analysis. One of the fitting methods used to fit the near detector data is described in this thesis. The new near detector samples are used to constrain uncertainties in the flux and cross section models used in the analysis, reducing the uncertainties on the far detector event rates.

Declaration

No part of this thesis has previously been submitted for the award of a higher degree and the work presented within has been performed by the author.

This work has been made possible through the support of T2K collaborators and the use of software developed by the T2K collaboration. Work that has not been performed by the author has been clearly referenced.

The main contributions of the author to the T2K collaboration are through analysis of near detector data, the development of the new CC-Photon sample, updating the near detector fitting code to incorporate the new classification of ND280 events, and performing one of the near detector data fits for the oscillation analysis.

A selection of events with final state photons, described in Chapter 3, has been developed within the T2K Selection Development group. Detector systematic uncertainties associated with the new selection, described in Chapter 4, have been evaluated in co-ordination with the T2K Selections and Systematics group. The fit to near detector data for the oscillation analysis, described in Chapter 5, has been performed within the T2K Near Detector Fitting and T2K Oscillation Analysis groups.

In addition to analysis work, the author has worked as an on-call data acquisition expert, assisting with the operation and maintenance of the ND280 detector, and training other collaborators to take monitoring shifts during beam time.

Tristan Doyle

Acknowledgements

Although the work presented in this thesis is my own, it would not have been possible without the help, support and guidance given to me by a great number of people. Here I wish to express my gratitude to those people.

Firstly, I'd like to thank my supervisor, Prof. Helen O'Keeffe. Her constant support throughout my PhD has been invaluable. I've enjoyed our many discussions about photons, DAQ and Bake Off. I also give special thanks to you for being one of the few people that will ever read this thesis in its entirety, and for doing that more than once!

I'd also like to thank the rest of the T2K Lancaster group: Laura Kormos, Alex Finch, Matt Lawe, Tom Dealtry, Joe Walsh, Yongheng Xu, Menai Lamers-James and Adam Speers. It has been a pleasure working with all of you. In particular I'd like to thank Matt for giving me so much of his time during the early stages of this analysis. Thanks also go to the many other people I met at Lancaster that made the time I spent on campus so enjoyable. Special thanks go to Katherine Rybacki, Neza Ribaric and Ryan Cross who started this journey with me.

Within the wider T2K collaboration there are many more people I should thank than I have space for here. I'd like to thank Helen O'Keeffe, Ciro Riccio, Alexander Izmaylov, Sophie King, Mark Scott and Clarence Wret, who have overseen each stage of the analysis presented in this thesis, providing consistently good advice throughout. In particular I'd like to thank Ciro who, during the pressures of the oscillation analysis, has been available at all times of the day across several timezones. I'd also like to thank the rest of my fellow near detector fit analysers: Kamil Skwarczynski, Alex Carter, Joe Walsh, Laura Munteanu and Soichiro Kuribayashi. Thanks also to Kendall Mahn, Sara Bolognesi and Christophe Bronner for their leadership in the T2K analysis.

From my time in Tokai, I'd like to thank the ND280 DAQ experts: Helen O'Keeffe, Alfons Weber, Giles Barr, Lukas Koch, Federico Nova, Laurence Cook and Dan Barrow. Together we were able to keep the detector running, even in less than ideal circumstances! My time in Tokai would have been much less fun had it not been for the other students there with me: Jordan McElwee, Sam Jenkins, Gabriel Penn and Charlie Ruggles. Thank you all!

Unfortunately, my work on supernova burst monitoring for Hyper-Kamiokande didn't make it into this thesis. In any case, I'm very grateful to the other members of the HK DAQ group: Helen O'Keeffe, Ben Richards, Tom Dealtry, Federico Nova, Jost Migenda, Alex Finch and Lukas Koch. We'll all be keeping our fingers crossed in hope that there are no galactic supernovae before the detector comes online! In particular I'd like to thank Tom for the much needed support in using the HK software.

Thanks also go to my friends outside the field of physics, who are the most effective at pulling me away from my laptop. Amelia, Arjun, Charlotte, Eilidh, Emily, Kate, Lewis, Matthew, Neal, Sam and Shannon: I hope our friendships remain strong as our lives continue to diverge. I'd also like to thank the secondary school teachers I now call friends: David Jones, Keith Finlinson and Steve Davidson. Each of whom was so inspiring during those formative years.

Finally, I want to thank the most important people in my life: my family. Thank you Mam and Dad, for always surrounding me with love and support, and always encouraging me to chase after my dreams. Thank you Teresa, for always being there and always being able to make me smile. Thank you Nana, for always putting others first and always being able to make people laugh. Thank you Andrea, for supporting us all and for sharing my enthusiasm for cooking. I hope I've made you all proud.

Contents

List of Figures

List of Tables

Chapter 1

Introduction

The neutrino was first postulated by Pauli in 1930 [1], but more than two decades passed before it was first detected [2]. Development of the theoretical framework describing neutrino oscillations, a phenomenon in which neutrinos change from one flavour to another without interacting with any other particle, started soon after [3–5]. It was four decades before such oscillations were observed [6].

This chapter provides a brief overview of the field of neutrino physics, starting with a historical overview of the neutrino from postulation to discovery in Section 1.1. The Standard Model picture of neutrinos is described in Section 1.2. Section 1.3 describes neutrino interactions and Section 1.4 details the mathematical description of neutrino oscillations. Neutrino oscillation experiments from the past, present and future are described in Section 1.5. Finally, a summary of the current knowledge of neutrino oscillations is given in Section 1.6.

1.1 History of Neutrino Physics

In 1914, the energy spectrum of electrons produced in β decays was measured by James Chadwick [7]. At that time, the electron and proton were the only known fundamental particles, and it was thought that β decay would occur via a two-body decay:

$$^{A}_{Z}X \rightarrow ^{A}_{Z+1} Y + e^{-} \tag{1.1}$$

where an atom X decays to atom Y with the emission of an electron. In this picture, the energy of the emitted electrons can be calculated exactly using energy and momentum conservation as:

$$E_e = \frac{m_X^2 - m_Y^2 + m_e^2}{2m_X} \tag{1.2}$$

where m_X, m_Y and m_e are the masses of atom X, atom Y and the electron respectively. Therefore, Chadwick expected that all the electrons produced by the β decay of a given isotope would have exactly the same energy. However a broad, continuous energy spectrum with an end point at the energy given by Eq. (1.2) was observed [7].

This finding presented two problems to physicists, since the decay appeared to violate both energy and angular momentum conservation. In an open letter in 1930, Wolfgang Pauli presented an elegant solution to both problems: the existence of a third, neutral particle in the decay which had a very low (or zero) mass and had spin-1/2 [1]. Pauli referred to this particle as a “neutron”, and thought that its mass would make it impossible to detect. Chadwick later discovered the more massive neutral nucleon, now known as the neutron [8], and Enrico Fermi developed a theoretical description of β decay including the particle postulated by Pauli, which he named the “neutrino” [9]. The process of β decay was redefined as a three-body process including the (electron anti)neutrino:

$$^A_ZX \rightarrow ^A_{Z+1} Y + e^- + \bar{\nu}_e. \tag{1.3}$$

Fermi’s theory of β decay allowed for the inverse of the process in Eq. (1.3):

$$\bar{\nu}_e + p \rightarrow e^+ + n, \tag{1.4}$$

referred to as Inverse Beta Decay (IBD), which provided a possible route for detection of the neutrino. Clyde Cowan and Frederick Reines were the first to observe this process in 1956, corresponding to the discovery of the (electron anti)neutrino [2]. To make this discovery, two water tanks loaded with cadmium chloride ($CdCl_2$) were placed between three liquid scintillator detectors. They searched for two coincident signals to identify IBD interactions. First, the positron annihilated with an electron, and produced two photons with a combined energy greater than 1.02 MeV, which corresponds to the rest mass of an electron-positron pair. Second, the neutron produced via IBD was captured on a cadmium nucleus, forming an excited state. De-excitation photons were emitted approximately $5\,\mu$s after the electron-positron annihilation. Observation of both signals in coincidence amounted to confirmation of the IBD process, and hence the discovery of the first neutrino flavour. Since then, the muon neutrino was discovered in 1962 at an experiment at the Brookhaven National Laboratory [10], and the tau neutrino was discovered by the DONUT experiment in 2000 [11].

1.2 Neutrinos in the Standard Model

The Standard Model (SM) describes the interactions of the fundamental particles through three forces: the electromagnetic, strong and weak. The three forces are mediated by spin-1 bosons; the electromagnetic force by photons, the strong force by gluons, and the weak force by $W^{\pm}$ and Z^0 bosons. The fundamental particles that interact via these forces are known as fermions, which have spin of 1/2 and are separated into quarks and leptons. An additional spin-0 boson, the Higgs boson, is responsible for the mechanism that gives many of the bosons and fermions mass.

Neutrinos are electrically neutral and have no colour charge, meaning they only interact via the weak interaction. The number of neutrino flavours that couple to the weak interaction can be calculated using the shape of the Z^0 resonance. The total width of the resonance, Γ_Z, can be expressed as a sum of the partial widths to different decay products:

$$\Gamma_Z = \Gamma_{Z\to l^+l^-} + \Gamma_{Z\to hadrons} + N_\nu \Gamma_{Z\to\nu\bar{\nu}} \tag{1.5}$$

where $\Gamma_{Z\to l^+l^-}$, $\Gamma_{Z\to hadrons}$ and $\Gamma_{Z\to\nu\bar{\nu}}$ are the partial widths for decays to charged lepton pairs, hadrons and neutrino/antineutrino pairs respectively, and N_ν is the number of neutrino flavours that couple to the weak interaction. The total width of the resonance, and the partial widths $\Gamma_{Z\to l^+l^-}$ and $\Gamma_{Z\to hadrons}$, can be measured by experiment, while $\Gamma_{Z\to\nu\bar{\nu}}$ is calculated using the SM prediction. Then, N_ν can be calculated as the only remaining unknown in Eq. (1.5). Four experiments at the Large Electron-Positron collider (LEP) at CERN produced a joint measurement of

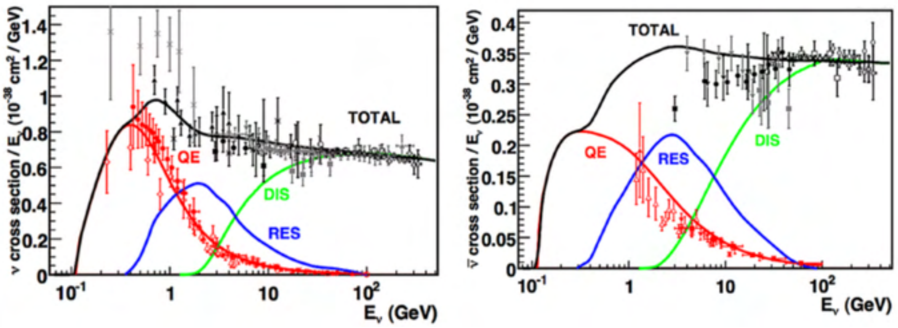

Figure 1.1: Muon neutrino (left) and antineutrino (right) per nucleon interaction cross section as a function of neutrino energy. The cross section contributions from quasi-elastic (QE), resonant (RES) and deep inelastic scattering (DIS) interactions are shown. Figure adapted from [14].

N_ν, and reported a value of 2.9840 ± 0.0082 [12]. This result suggests the three neutrino flavours discovered thus far, ν_e, ν_μ and ν_τ, are the only light neutrinos that couple to the weak interaction.

The helicity of neutrinos was measured by Goldhaber *et al* in 1958 [13]. The experiment found that neutrinos are always left-handed particles with a helicity of -1, while antineutrinos are always right-handed particles with a helicity of $+1$. This property does not extend to the charged leptons, which can have either helicity.

1.3 Neutrino Interactions

Neutrino interactions via the weak force are categorised as Charged Current (CC) interactions if mediated by a $W^\pm$ boson, and as Neutral Current (NC) interactions if mediated by a Z^0 boson. The interactions of interest for the analysis presented in this thesis are charged current interactions. The total charged current cross section and breakdowns by interaction type are shown in Fig. 1.1.

At neutrino energies below 1 GeV, the dominant contribution to the CC cross section is from quasi-elastic (QE) interactions. The interaction leads to the production of a charged lepton and a nucleon:

$$\begin{aligned} \nu_l + n &\rightarrow l^- + p \\ \bar{\nu}_l + p &\rightarrow l^+ + n \end{aligned} \tag{1.6}$$

where l represents one of the three lepton flavours. At energies in the range 1-

5 GeV, resonant (RES) interactions contribute significantly to the cross section. In a resonant process, a nucleon is excited to a resonant state which then decays to a nucleon through the emission of a pion. Above 5 GeV, Deep Inelastic Scattering (DIS) processes become the dominant contribution to the cross section. In these interactions, the neutrino interacts with an individual quark inside a nucleon, breaking the nucleon apart and producing several hadronic states.

1.3.1 Interactions with Nuclei

Interactions between a neutrino and a free nucleon are relatively easy to understand. In an experiment, neutrinos interact with nucleons inside a larger nucleus, and the effect the rest of the nucleus has on the interaction and the particles produced must also be considered.

Nucleons within a nucleus are not at rest; they have some motion even in the ground state. This is known as Fermi motion [15]. The motion of an individual nucleon is unknown in any given interaction. In the nuclear ground state, the energy levels are full up to the Fermi momentum [16] of the nucleus. Therefore a neutrino must be able to excite a nucleon to a state above this momentum in order for an interaction to occur. This is known as Pauli blocking [15], and the result is a reduced cross section compared to predictions based on free nucleons.

The particles produced in a neutrino interaction must leave the nucleus in order to be detected. On the path out of the nucleus, these particles can undergo additional interactions, changing their kinematics or producing additional particles. Such processes are known as Final State Interactions (FSI) [15].

1.4 Neutrino Oscillations

Neutrinos are commonly referred to by their flavour eigenstates ν_e, ν_μ and ν_τ, corresponding to the three charged leptons that are produced in charged current neutrino interactions. These flavour eigenstates can be expressed as a linear combination of three mass eigenstates ν_1, ν_2 and ν_3, related by a unitary transformation U:

$$\begin{pmatrix} \nu_e \\ \nu_\mu \\ \nu_\tau \end{pmatrix} = \begin{pmatrix} U_{e1} & U_{e2} & U_{e3} \\ U_{\mu 1} & U_{\mu 2} & U_{\mu 3} \\ U_{\tau 1} & U_{\tau 2} & U_{\tau 3} \end{pmatrix} \begin{pmatrix} \nu_1 \\ \nu_2 \\ \nu_3 \end{pmatrix} \tag{1.7}$$

where U_{lm} represents the proportion of each mass eigenstate present in a flavour eigenstate. Neutrinos propagate in these linear combinations until collapsing into a flavour eigenstate during a charged current interaction, producing the corresponding charged lepton. It is not possible to determine the neutrino flavour in a neutral current interaction, since no charged lepton is produced. There is no theoretical requirement that the masses of ν_1, ν_2 and ν_3 should be equal, so the coupling terms U_{lm} cause phase differences between parts of the wavefunction, allowing neutrino oscillations to occur.

The unitary matrix, U, is referred to as the Pontecorvo-Maki-Nakagawa-Sakata (PMNS) matrix [17], and can be written as:

$$U = \begin{pmatrix} c_{12}c_{13} & s_{12}c_{13} & s_{13}e^{-i\delta_{CP}} \\ -s_{12}c_{23} - c_{12}s_{23}s_{13}e^{i\delta_{CP}} & c_{12}c_{23} - s_{12}s_{23}s_{13}e^{i\delta_{CP}} & s_{23}c_{13} \\ s_{12}s_{23} - c_{12}c_{23}s_{13}e^{i\delta_{CP}} & -c_{12}s_{23} - s_{12}c_{23}s_{13}e^{i\delta_{CP}} & c_{23}c_{13} \end{pmatrix} \tag{1.8}$$

where s_{ij} and c_{ij} correspond to the sine and cosine respectively of θ_{ij}, the so-called mixing angles, and δ_{CP} is a CP-violating phase.

1.4.1 Two Flavour Oscillations

The PMNS matrix can be used to derive neutrino oscillation probabilities. This is demonstrated more clearly by considering only two flavour states, ν_α and ν_β, and two mass states ν_1 and ν_2. These are related by a two dimensional rotation of angle θ, given by:

$$\begin{pmatrix} \nu_\alpha \\ \nu_\beta \end{pmatrix} = \begin{pmatrix} \cos\theta & \sin\theta \\ -\sin\theta & \cos\theta \end{pmatrix} \begin{pmatrix} \nu_1 \\ \nu_2 \end{pmatrix}. \tag{1.9}$$

This allows each flavour state to be written as a linear superposition of the mass states. As the neutrino propagates through time, each mass state gains a complex phase, and the wavefunctions of the mass states can be written:

$$|\nu_{1,2}(t)\rangle = e^{iE_{1,2}t} |\nu_{1,2}\rangle . \tag{1.10}$$

Combining Eq. (1.9) and Eq. (1.10) allows the flavour state wavefunctions to be written as:

$$|\nu_\alpha(t)\rangle = \left(\cos\theta |\nu_1\rangle + \sin\theta |\nu_2\rangle e^{i(E_2-E_1)t}\right) e^{iE_1t} \tag{1.11}$$

and

$$|\nu_\beta(t)\rangle = \left(-\sin\theta |\nu_1\rangle + \cos\theta |\nu_2\rangle e^{i(E_2-E_1)t}\right) e^{iE_1t}. \tag{1.12}$$

The energy of the neutrino can be written in terms of its mass, m, and momentum, p, using the standard expression:

$$E^2 = p^2 + m^2, \tag{1.13}$$

which trivially rearranges to:

$$E = p\sqrt{1 + \frac{m^2}{p^2}}. \tag{1.14}$$

The small but finite neutrino masses allow them to be considered as highly relativistic particles, meaning $E \approx p$. Performing a Taylor expansion of Eq. (1.14) to the first order gives:

$$E \approx p\left(1 + \frac{m^2}{2p^2}\right) \approx p\left(1 + \frac{m^2}{2E^2}\right). \tag{1.15}$$

Since momentum is conserved, p is the same for the two mass states, meaning the energy difference between the two states can be written as:

$$E_2 - E_1 \approx \frac{m_2^2}{2E} - \frac{m_1^2}{2E} \approx \frac{\Delta m^2}{2E}, \tag{1.16}$$

where $\Delta m^2 = m_2^2 - m_1^2$. Inserting Eq. (1.16) into Eqs. (1.11) and (1.12) gives:

$$|\nu_\alpha(t)\rangle = \left(\cos\theta |\nu_1\rangle + \sin\theta |\nu_2\rangle e^{\frac{i\Delta m^2 t}{2E}}\right) e^{iE_1t} \tag{1.17}$$

and

$$|\nu_\beta(t)\rangle = \left(-\sin\theta\,|\nu_1\rangle + \cos\theta\,|\nu_2\rangle\, e^{\frac{i\Delta m^2 t}{2E}}\right) e^{iE_1 t}. \tag{1.18}$$

The probability of an initial state i being observed in another state j at a time t can be calculated as:

$$P(\nu_i \to \nu_j) = |\,\langle\nu_j|\nu_i(t)\rangle\,|^2. \tag{1.19}$$

So the probability of observing a ν_α some time after it is produced, known as the survival probability, is:

$$P(\nu_\alpha \to \nu_\alpha) = |\,\langle\nu_\alpha|\nu_\alpha(t)\rangle\,|^2 \tag{1.20}$$

$$P(\nu_\alpha \to \nu_\alpha) = \left|(\cos\theta\,\langle\nu_1| + \sin\theta\,\langle\nu_2|) \times \left(\left(\cos\theta\,|\nu_1\rangle + \sin\theta\,|\nu_2\rangle\, e^{\frac{i\Delta m^2 t}{2E}}\right) e^{iE_1 t}\right)\right|^2. \tag{1.21}$$

Since the mass states are orthogonal, $\langle\nu_i|\nu_j\rangle = \delta_{ij}$ where $i, j = 1, 2$. Using this and the standard expression $|e^{iE_1 t}|^2 = 1$, the survival probability can be simplified to give:

$$\begin{aligned} P(\nu_\alpha \to \nu_\alpha) &= \left|\cos^2\theta + \sin^2\theta e^{\frac{i\Delta m^2 t}{2E}}\right|^2 \\ &= \cos^4\theta + \cos^2\theta\sin^2\theta\left(e^{\frac{i\Delta m^2 t}{2E}} + e^{\frac{-i\Delta m^2 t}{2E}}\right) + \sin^4\theta \\ &= \cos^4\theta + \sin^4\theta + 2\cos^2\theta\sin^2\theta\cos\left(\frac{\Delta m^2 t}{2E}\right) \end{aligned} \tag{1.22}$$

where the final step uses the identity $\cos\theta = \frac{1}{2}\left(e^{+i\theta} + e^{-i\theta}\right)$. This can be further simplified using the identity $\cos^2\theta + \sin^2\theta = 1$ to give:

$$\begin{aligned} P(\nu_\alpha \to \nu_\alpha) &= (\cos^2\theta + \sin^2\theta)^2 - 2\cos^2\theta\sin^2\theta + 2\cos^2\theta\sin^2\theta\cos\left(\frac{\Delta m^2 t}{2E}\right) \\ &= 1 - 2\cos^2\theta\sin^2\theta\left(1 - \cos\left(\frac{\Delta m^2 t}{2E}\right)\right). \end{aligned} \tag{1.23}$$

Finally, using the identities $2\cos\theta\sin\theta = \sin 2\theta$ and $1 - \cos\theta = 2\sin^2(\frac{\theta}{2})$, the survival probability as a function of time can be written as:

$$P(\nu_\alpha \rightarrow \nu_\alpha) = 1 - \sin^2 2\theta \sin^2 \left(\frac{\Delta m^2 t}{4E} \right). \tag{1.24}$$

Since neutrinos have very little mass, they travel at almost the speed of light, so converting the probability given in Eq. (1.24) from a time-dependent expression to a distance-dependent expression is possible. Doing this, and converting variables into more intuitive units, gives:

$$P(\nu_\alpha \rightarrow \nu_\alpha) = 1 - \sin^2 2\theta \sin^2 \left(\frac{1.27 \Delta m^2 L}{E} \right), \tag{1.25}$$

where L is the distance from the point at which the neutrino was produced to where it was detected in km, Δm^2 is given in eV^2, and E is given in GeV.

The probability of a ν_α oscillating to a ν_β can be derived in the same way as the survival probability shown above. For the two flavour case this can be obtained trivially:

$$\begin{aligned} P(\nu_\alpha \rightarrow \nu_\beta) &= 1 - P(\nu_\alpha \rightarrow \nu_\alpha) \\ &= \sin^2 2\theta \sin^2 \left(\frac{1.27 \Delta m^2 L}{E} \right). \end{aligned} \tag{1.26}$$

1.4.2 Three Flavour Oscillations and Matter Effects

Calculation of the three flavour oscillation probabilities can be approached in the same manner as the two flavour case. The probability for a ν_μ to ν_e oscillation in the three flavour picture can be expressed as [18]:

$$\begin{aligned} P(\nu_\mu \rightarrow \nu_e) = {} & 4c_{13}^2 s_{13}^2 s_{23}^2 \sin^2 \Phi_{31} \\ & + 8c_{13}^2 s_{12} s_{13} s_{23} (c_{12} c_{23} \cos \delta_{CP} - s_{12} s_{13} s_{23}) \cos \Phi_{32} \sin \Phi_{31} \sin \Phi_{21} \\ & - 8c_{13}^2 c_{12} c_{23} s_{12} s_{13} s_{23} \sin \delta_{CP} \sin \Phi_{32} \sin \Phi_{31} \sin \Phi_{21} \\ & + 4s_{12} c_{13} (c_{12} c_{23} + s_{12} s_{23} s_{13} - 2c_{12} c_{23} s_{12} s_{23} s_{13} \cos \delta_{CP}) \sin^2 \Phi_{21} \end{aligned} \tag{1.27}$$

where s_{ij} and c_{ij} correspond to the sine and cosine respectively of the mixing angle θ_{ij}, and $\Phi_{ij} = \frac{\Delta m_{ij}^2 L}{4E}$. This oscillation probability, along with those derived in Section 1.4.1, assume that the neutrinos in question are travelling in a vacuum. In

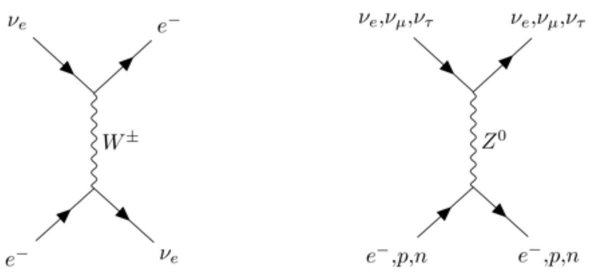

Figure 1.2: Feynman diagrams of the charged current (left) and neutral current (right) elastic scattering processes in matter.

reality, neutrinos travel through matter, and this must be taken into account when computing these probabilities.

As neutrinos travel through matter, all three flavours can interact through neutral current interactions, while electron neutrinos are also able to interact through charged current interactions due to the presence of electrons. The Feynman diagrams for these processes are shown in Fig. 1.2. The possibility of charged current interactions for electron neutrinos introduces an additional potential in the interaction Hamiltonian that only electron neutrinos experience. This additional potential is:

$$V_{CC} = \sqrt{2} G_F n_e \tag{1.28}$$

where G_F is the Fermi constant and n_e is the average density of electrons in the medium. Including a correction for matter effects was first proposed by Wolfenstein [19] and extended by Mikheyev and Smirnov [20], and is now known as the Mikheyev-Smirnov-Wolfenstein (MSW) effect.

To include the MSW effect in Eq. (1.27), assuming constant density of the medium in which neutrinos are travelling, the following terms should be added:

$$\begin{aligned} &- 8\frac{aL}{4E} c_{13}^2 s_{13}^2 s_{23}^2 (1 - 2s_{13}^2) \cos\Phi_{32} \sin\Phi_{31} \\ &+ 8\frac{a}{\Delta m_{31}^2} c_{13}^2 s_{13}^2 s_{23}^2 (1 - 2s_{13}^2) \sin\Phi_{31}, \end{aligned} \tag{1.29}$$

where a in eV^2 is equal to $7.56 \times 10^{-5} \times \rho \times E_\nu$, ρ is the matter density in g cm^{-3}, and E_ν is the neutrino energy in GeV.

This more complete picture of neutrino oscillations shows the dependence of the oscillation probabilities on the PMNS parameters. All three mixing angles, θ_{12}, θ_{13}

and θ_{23}, and the CP-violating phase δ_{CP} appear in these probabilities, along with the squared mass differences of the mass eigenstates, and the ratio of L/E.

The dependence of the oscillation probabilities on the squared mass differences highlights an outstanding question in neutrino physics, known as the neutrino mass ordering problem. There are two independent squared mass differences, Δm^2_{32} and Δm^2_{21}, and while solar and reactor experiments [21, 22] have confirmed Δm^2_{21} is positive, the sign of Δm^2_{32} is still unknown. This means there are two possible mass orderings: normal ordering where $m_3 > m_2 > m_1$ and inverted ordering where $m_2 > m_1 > m_3$. This problem, and other open questions in the field, are discussed in Section 1.6.1.

1.5 Neutrino Oscillation Experiments

Since the development of the theory of neutrino oscillations, many experiments have been devised to study this unique phenomenon and make precision measurements of the PMNS matrix parameters. These experiments can be separated into categories based on how the neutrinos are produced: solar, atmospheric, reactor and accelerator neutrino experiments. Notable experiments and results from each category are outlined in Sections 1.5.1 to 1.5.4.

1.5.1 Solar Neutrino Experiments

Nuclear fusion within the Sun's core generates a significant number of neutrinos. Since neutrinos only interact weakly with matter, most are able to pass through the solar matter without interacting. This means there is a significant neutrino flux on Earth coming from the Sun. The flux was predicted by the Solar Standard Model (SSM) developed by John Bahcall in 1963 [23].

The first measurements of the solar neutrino flux were made in 1968 at an experiment in the Homestake mine in South Dakota led by Raymond Davis [24]. The neutrinos could be identified when they underwent inverse beta decay on chlorine atoms producing argon, which could be collected from the detector. The threshold of this interaction is 0.814 MeV [17], so the experiment was sensitive to all neutrinos with energies above this threshold. Davis found that the neutrino flux observed at the Homestake mine was a factor of two to three smaller than Bahcall's prediction. In the 1990's the GALLEX [25], SAGE [26], and Kamiokande [27] experiments performed model-dependent measurements of the neutrino spectrum, confirming Davis' results. Helioseismological observations also confirmed Bahcall's predictions, and this discrepancy between experiment and theory became known as the solar neutrino problem.

The Sudbury Neutrino Observatory (SNO) experiment [21], which used a spherical heavy water Cherenkov detector, was the first experiment to measure both the electron neutrino flux, through charged current interactions, confirming Davis' results, and the total neutrino flux from the Sun through neutral current interactions. The neutral current process was equally sensitive to all flavours of neutrino and the measured flux was consistent with Bahcall's SSM prediction. For solving the solar neutrino problem, this result was awarded the Nobel Prize in Physics in 2015 alongside the Super-Kamiokande result discussed in Section 1.5.2.

The first measurements of θ_{12} and Δm^2_{21} were made using solar neutrino analyses, so these parameters are often referred to as the solar parameters, though reactor experiments also have sensitivity to these parameters. Two dimensional contours for these parameters from solar measurements and from the KamLAND reactor antineutrino experiment [22] are shown in Fig. 1.3. Since KamLAND provides a strong constraint on Δm^2_{21}, and the solar measurements have a stronger constraint on θ_{12}, the strongest constraints in both dimensions are achieved by combining the results.

1.5.2 Atmospheric Neutrino Experiments

Cosmic rays consist mostly of protons. When cosmic rays enter the upper layers of the Earth's atmosphere, they interact with nuclei producing showers of particles. Many of these particles are charged pions that decay to muons and muon neutrinos:

$$\begin{aligned} \pi^+ &\rightarrow \mu^+ + \nu_\mu \\ \pi^- &\rightarrow \mu^- + \bar{\nu}_\mu . \end{aligned} \tag{1.30}$$

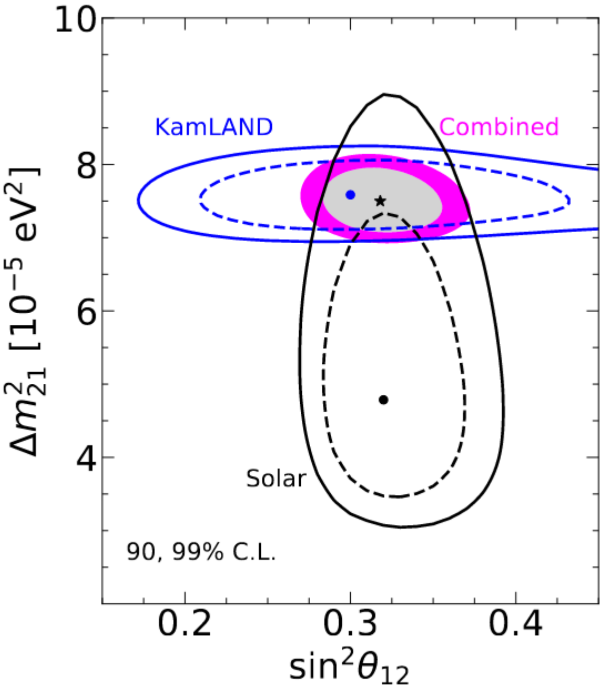

Figure 1.3: Confidence regions of θ_{12} and Δm^2_{21} from combined solar measurements and from KamLAND [28]. The strongest constraints are achieved by combining the solar measurements with the KamLAND result.

The muons produced in these processes also decay via:

$$\begin{aligned} \mu^+ &\to e^+ + \nu_e + \bar{\nu}_\mu \\ \mu^- &\to e^- + \bar{\nu}_e + \nu_\mu . \end{aligned} \tag{1.31}$$

Neutrinos produced in this way are referred to as atmospheric neutrinos. From Eqs. (1.30) and (1.31), the ratio of muon (anti)neutrinos to electron (anti)neutrinos can be estimated to be two. However, the IMB [29], Kamiokande [30,31] and Super-Kamiokande [32] experiments observed a 1:1 ratio of atmospheric muon and electron neutrino interactions.

Super-Kamiokande uses the zenith angle with respect to the detector as a proxy for the distance travelled by atmospheric neutrinos. The number of electron-like and muon-like events can then be plotted as a function of L/E. The observed data show excellent agreement with the predicted distribution assuming neutrino oscillations take place. This result provided the first evidence of neutrino oscillations, and was awarded the Nobel Prize in Physics in 2015 alongside the SNO result discussed in Section 1.5.1.

The first measurements of θ_{23} and Δm^2_{32} were made using atmospheric neutrino

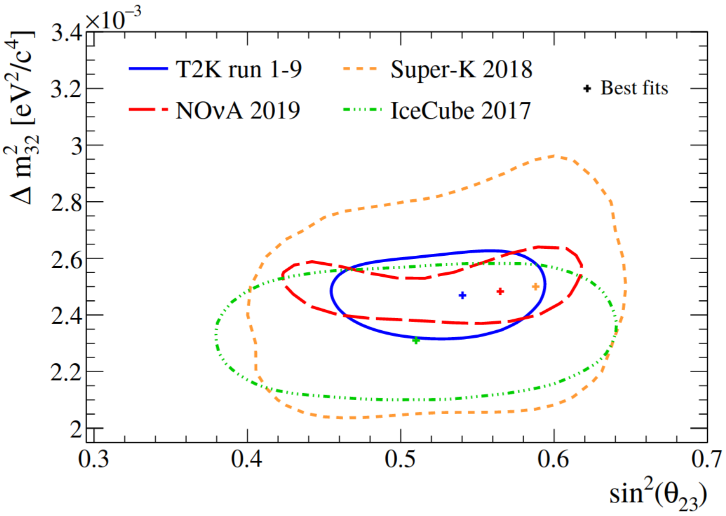

Figure 1.4: The 90% confidence regions of $\sin^2\theta_{23}$ and Δ^2_{32} from T2K, Super-Kamiokande, NOνA and IceCube [35].

analyses, so these parameters are often referred to as the atmospheric parameters, though accelerator neutrino experiments now also contribute. Two-dimensional contours for these parameters produced by the Super-Kamiokande [33], IceCube [34], T2K [35] and NOνA [36] experiments are shown in Fig. 1.4. Good agreement is observed between the atmospheric and accelerator neutrino experiments.

1.5.3 Reactor Neutrino Experiments

The KamLAND experiment, discussed in Section 1.5.1, measured the electron antineutrino flux from 55 Japanese nuclear power plants, with an average baseline of 180 km [22]. The flux was measured using the IBD interaction of electron antineutrinos, and an energy-dependent disappearance of these electrons, consistent with the theory of neutrino oscillations, was observed.

More recent reactor experiments such as Double CHOOZ [37], Daya Bay [38] and RENO [39] have baselines shorter than 2 km, and have focused on precision measurements of the third PMNS matrix mixing angle, θ_{13}, using the same IBD interaction channel of electron antineutrinos as used by KamLAND. The best constraint on this parameter is presented together with the constraint on the final neutrino oscillation parameter, δ_{CP}, in Section 1.5.4.

1.5.4 Accelerator Neutrino Experiments

While reactors produce a neutrino flux covering the whole range of solid angles, accelerator neutrino experiments are able to produce beams of neutrinos by selecting charged parent particles before they decay. Typically, the neutrino beam is categorised by a near detector before oscillations take place, and then again at a far detector after oscillation. These experiments are able to measure the final PMNS matrix parameter, δ_{CP}, as well as providing measurements of the atmospheric parameters, θ_{23} and Δm^2_{32}, and the parameter most significantly constrained by reactor experiments, θ_{13}.

The first long-baseline experiment was the KEK to Kamioka (K2K) [40] experiment based in Japan. The K2K experiment used the Super-Kamiokande detector as its far detector and a 1 ktonne water Cherenkov detector as its near detector. The experiment measured muon neutrino disappearance at a significance of 4.3σ [40]. Other long-baseline experiments that have stopped collecting data include MINOS [41] and OPERA [42]. MINOS measured both muon neutrino disappearance and electron neutrino appearance, reporting measurements for θ_{23} and Δm^2_{32}, while OPERA measured tau neutrino appearance at a significance of 5σ.

The current long-baseline oscillation experiments, T2K [43] and NOνA [44], use the same beam production facilities as K2K and MINOS respectively. Both experiments measure muon neutrino disappearance and electron neutrino appearance. The T2K experiment is described in detail in Chapter 2, and is the main focus of this thesis. It was the first experiment to exclude the CP-conserving values 0 and π of δ_{CP} at the 95% confidence level [45], and has made significant measurements of θ_{23}, Δm^2_{32} and θ_{13}. The T2K two-dimensional contours for δ_{CP} and θ_{13} with and without the reactor constraint on θ_{13} are shown in Fig. 1.5.

NOνA has also produced measurements of θ_{23}, Δm^2_{32} and δ_{CP}, and the two-dimensional contours for θ_{23} and δ_{CP} are shown in Fig. 1.6, alongside equivalent contours from T2K and Super-Kamiokande.

The next generation of long-baseline neutrino experiments is well into development, with the Hyper-Kamiokande [47] and DUNE [48] experiments expected to start taking data during this decade. These experiments, through muon neutrino disappearance and electron neutrino appearance measurements, have the potential

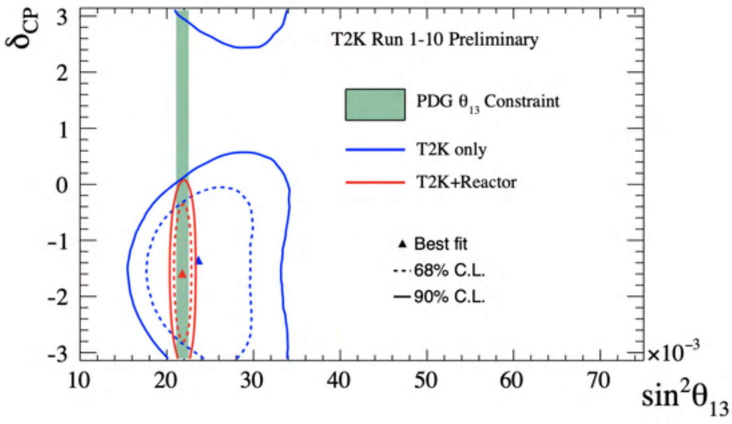

Figure 1.5: The T2K 68% and 90% credible intervals with and without the reactor constraint, which is also shown [46].

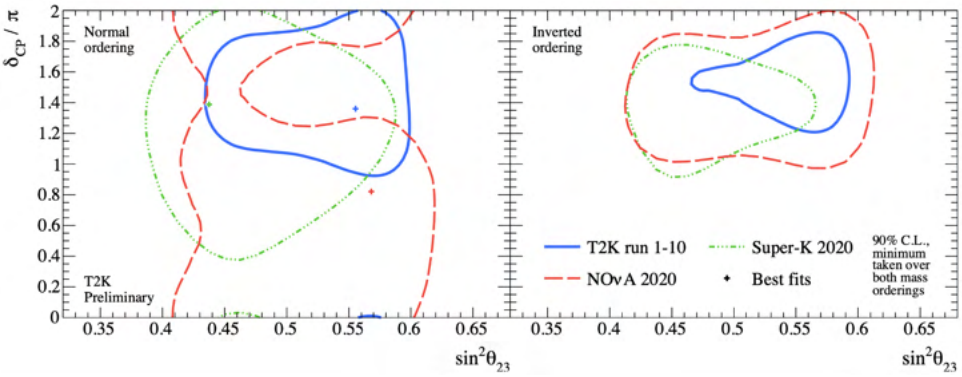

Figure 1.6: The 90% confidence regions of $\sin^2\theta_{23}$ and δ_{CP} for T2K, NOνA and Super-Kamiokande [46]. All three experiments show a slight preference for the normal mass ordering, with the best fit points sitting in the left pane.

Parameter	Best Fit $\pm 1\sigma$	3σ Range
Δm^2_{21} $[10^{-5}\text{eV}^2]$	$7.50^{+0.22}_{-0.20}$	$6.94 - 8.14$
$\lvert\Delta m^2_{31}\rvert$ $[10^{-3}\text{eV}^2]$ (NO)	$2.55^{+0.02}_{-0.03}$	$2.47 - 2.63$
$\lvert\Delta m^2_{31}\rvert$ $[10^{-3}\text{eV}^2]$ (IO)	$2.45^{+0.02}_{-0.03}$	$2.37 - 2.53$
$\sin^2\theta_{12}/10^{-1}$	3.18 ± 0.16	$2.71 - 3.69$
$\sin^2\theta_{23}/10^{-1}$ (NO)	5.74 ± 0.14	$4.34 - 6.10$
$\sin^2\theta_{23}/10^{-1}$ (IO)	$5.78^{+0.10}_{-0.17}$	$4.33 - 6.08$
$\sin^2\theta_{13}/10^{-2}$ (NO)	$2.200^{+0.069}_{-0.062}$	$2.000 - 2.405$
$\sin^2\theta_{13}/10^{-2}$ (IO)	$2.225^{+0.064}_{-0.070}$	$2.018 - 2.424$
δ_{CP}/π (NO)	$1.08^{+0.13}_{-0.12}$	$0.71 - 1.99$
δ_{CP}/π (IO)	$1.58^{+0.15}_{-0.16}$	$1.11 - 1.96$

Table 1.1: The global best fit values and 3σ confidence ranges of the PMNS parameters. Separate values are found for the normal ordering (NO) and inverted ordering (IO) scenarios for many parameters. The inverted ordering values refer to the local minimum for this mass ordering. Table adapted from [28].

to achieve 5σ measurements of δ_{CP} for a wide range of δ_{CP} values. It is hoped that current generation experiments will be able to determine the neutrino mass ordering, either through the T2K-NOνA joint fit [49] or the IceCube experiment [50]. However if the neutrino mass ordering remains unknown when the next generation experiments come online, they are expected to be able to make the determination.

1.6 Current Knowledge of Neutrino Oscillations

Since the discovery of neutrino oscillations, all of the neutrino oscillation parameters discussed in Sections 1.5.1 to 1.5.4 have been measured to various levels of accuracy. A summary of the global best fit values for all of the parameters, along with the associated 3σ confidence ranges, is presented in Table 1.1.

The solar and reactor parameters are determined to relatively good precision, and global constraints on these parameters are typically used by long-baseline neutrino oscillation experiments to provide constraints on the other oscillation parameters. The T2K experiment was the first experiment to provide hints of CP violation in the lepton sector by excluding values of 0 and π at the 95% confidence level [45], however the CP-violating phase, δ_{CP}, still has the largest uncertainty.

1.6.1 Unanswered Questions in Neutrino Physics

While the oscillation parameters have been measured to varying degrees of accuracy, there are still several open questions in the field of neutrino physics. A statistically significant (5σ) measurement of a non-conserving value of δ_{CP} would be the first observation of CP violation in the lepton sector. If the value of δ_{CP} is close to maximal ($\delta_{CP} \sim 1.5\pi$), this could provide an explanation for the matter dominance in the universe. In the Standard Model, matter is always created with an equal amount of antimatter. In this picture, the two would have annihilated in the early universe, preventing the formation of the universe observed today. CP violation has been observed in the quark sector [51–53], but not in a way significant enough to explain the matter-antimatter imbalance of the universe today.

As mentioned in Section 1.4.2, current measurements of neutrino oscillations allow for two possible neutrino mass orderings. In the normal ordering, $m_3 > m_2 > m_1$, while in the inverted ordering, $m_2 > m_1 > m_3$. The mass ordering can be determined by oscillation experiments, but the absolute mass scale of neutrinos can not, since oscillation probabilities depend only on the difference in the masses. Other experiments are required to determine the mass scale of neutrinos, such as KATRIN [54] which uses the β decay spectrum of tritium to set bounds on the neutrino masses.

The neutrino mass ordering has implications for experiments looking to answer another question about the nature of neutrinos: whether they are Dirac or Majorana fermions. Dirac fermions have separate particles and antiparticles, while Majorana fermions are their own antiparticles. Neutrinoless double beta decay experiments are trying to make this determination, and the theoretical rate of neutrinoless double beta decay is dependent on the neutrino mass ordering.

Measurements of θ_{23} have shown that it may not be at the maximal value of $45°$, however whether it lies in the upper octant ($\theta_{23} > 45°$) or the lower octant ($\theta_{23} < 45°$) remains unknown. Since the oscillation probabilities depend on θ_{23}, which octant θ_{23} belongs to affects the number of events observed in neutrino and antineutrino oscillation measurements. Data is currently consistent with both octants, so more data for both neutrinos and antineutrinos will be needed to determine the octant of θ_{23}.

Another topic of active research is the search for sterile neutrinos. These are additional neutrinos that do not couple weakly, as the ν_e, ν_μ and ν_τ do, but could provide additional terms in the oscillation probabilities. The first potential signal was observed as an excess of low energy ν_e events in the LSND experiment [55]. The MiniBooNE experiment also observed a low energy excess (4.8σ) of ν_e events [56]. However other experiments, such as MINOS+ [57], have not observed such an excess. Experiments such as MicroBooNE [58], the successor of MiniBooNE, are actively searching for the low energy excess observed in these experiments. Recent results from MicroBooNE [59–62] reject two hypotheses that attempted to explain the excess, neutrino-induced NC Δ radiative decay and CC ν_e interactions, at a confidence level greater than 90%.

Answering the questions outlined in this section are of great importance to the field of neutrino physics, and doing so will require continued effort from current experiments, such as T2K, as well as the technological advancements that will be introduced in the next generation of experiments.

Chapter 2

The Tokai-to-Kamioka Experiment

The Tokai-to-Kamioka (T2K) experiment is a long-baseline neutrino oscillation experiment based in Japan [43]. A beam of predominantly muon (anti)neutrinos is produced on the east coast at the Japan Proton Accelerator Research Complex (J-PARC), which is then categorised by a suite of near detectors 280 m downstream of the beam target. The far detector, Super-Kamiokande, sits 295 km from the beam target, at an angle of 2.5° off-axis with respect to the beam's axis. This 50 ktonne water Cherenkov detector measures muon (anti)neutrino disappearance and electron (anti)neutrino appearance. A schematic overview of the experiment is shown in Fig. 2.1.

The main aims of the T2K experiment are to perform precision measurements of the neutrino oscillation parameters θ_{13}, θ_{23} and Δm^2_{23}, and to constrain the allowed values of the CP-violating phase δ_{CP}. As well as world-leading measurements of neutrino oscillation parameters, T2K also performs an extensive program of cross section measurements and searches for exotic phenomena.

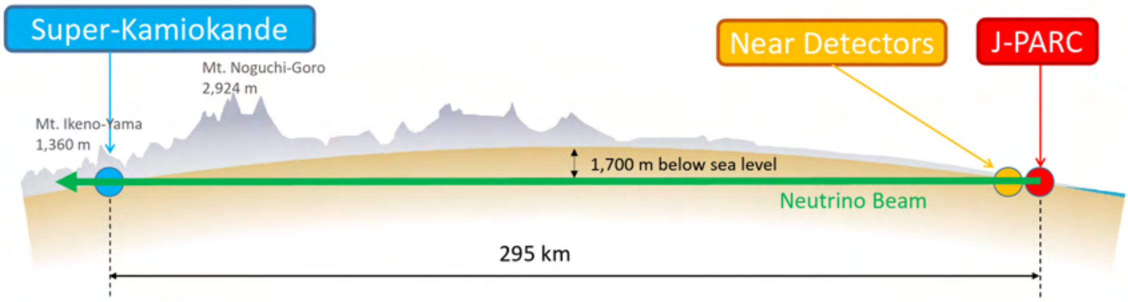

Figure 2.1: A schematic overview of the T2K experiment showing the path of the (anti)neutrino beam from J-PARC to Super-Kamiokande [43].

The rest of this chapter discusses the experimental setup in detail: Section 2.1 describes the production of the (anti)neutrino beam, Section 2.2 describes the on-axis near detector INGRID, Section 2.3 describes the off-axis near detector ND280, Section 2.4 briefly discusses the other T2K near detectors which are not used in this analysis, and Section 2.5 describes the far detector Super-Kamiokande.

2.1 The T2K Beam

The (anti)neutrino beam used by the T2K experiment is produced at the Japan Proton Accelerator Research Complex (J-PARC). There are three on-site accelerators used in series to achieve this: a LINear ACcelerator (LINAC), a Rapid Cycling Synchrotron (RCS), and the Main Ring synchrotron (MR) [43].

To produce the proton beam, H^- ions are accelerated to 180 MeV in the LINAC and then converted to H^+ ions (protons) by charge-stripping foils at the injection point of the RCS. In the RCS, protons are accelerated up to 3 GeV and separated into bunches. The RCS contains two bunches per cycle, with a cycle rate of 25 Hz. Bunches injected into the MR are accelerated further up to an energy of 30 GeV. The MR can hold up to eight bunches at a time and allows for fast extraction to the neutrino beamline.

This fast extraction deflects all eight bunches into the neutrino beamline in a single turn using five kicker magnets. Each bunch has a temporal width of 58 ns and bunches are separated from each other by 581 ns [63]. This timing information is passed to the near detectors via a direct fibre link and to the far detector via GPS, allowing precise triggering of beam neutrino events.

The neutrino beamline is formed of six parts: preparation section, arc section, final focusing section, target station, decay volume, and beam dump. The former three constitute the primary beamline which directs the beam towards Kamioka, while the latter three form the secondary beamline where the protons interact and the neutrino beam is produced. A schematic of the neutrino beamline is shown in Fig. 2.2.

In the preparation section the beam intensity, position and profile are monitored to ensure it is ready for the arc section. Here, the beam is bent by 80.7° to align

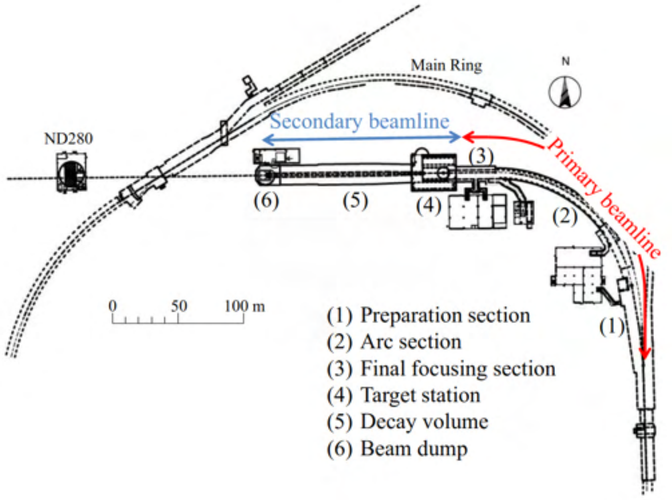

Figure 2.2: Schematic of the T2K neutrino beamline [43]. The major components that make up the primary beamline, which directs the beam to Kamioka, and the secondary beamline, where protons interact and neutrinos are produced, are labelled.

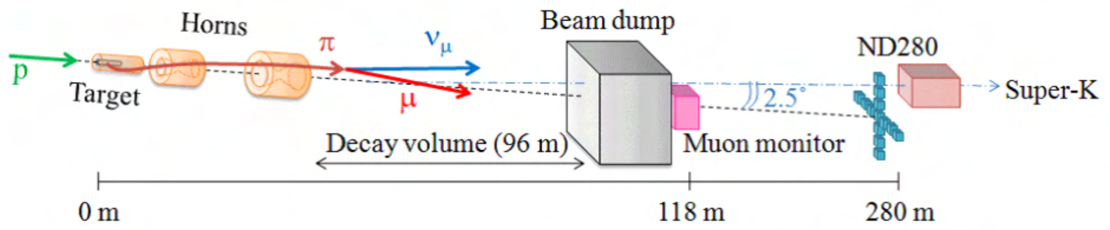

Figure 2.3: Schematic of the secondary beamline. Three horns and the muon monitor are aligned with the beam axis. Tracks illustrate a pion decay to muon and muon neutrino [63].

the beam horizontally with respect to the far detector. In the final focusing section magnets focus the beam onto the target and align it vertically. At this point the beam is pointing at the desired 2.5° away from the Super-Kamiokande detector and enters the secondary beamline. A schematic of the secondary beamline is shown in Fig. 2.3.

In the target station the beam position and direction immediately before hitting the target is measured precisely using the Optical Transition Radiation Monitor (OTR). The OTR can measure the beam position within 1 mm and the direction within 0.5 mrad [64]. The target is a 91.4 cm (1.9 interaction lengths) long, 2.6 cm diameter graphite rod. It is surrounded by a tube of graphite that is 2 mm thick and a 0.3 mm thick titanium case. Helium gas flows between the target layers to provide the cooling necessary to prevent rapid deterioration.

As the protons in the beam collide with the target, they interact with the carbon nuclei producing many secondary mesons. Pions are the most abundantly produced secondary mesons, followed by kaons which are the second most abundant. The graphite target sits in the inner conductor of the first in a series of three magnetic horns. This first magnetic horn collects the secondary mesons, while the second and third focus them into a narrow beam in the same direction as the incoming proton beam. The horns are designed such that most of the particles they collect are pions.

As the secondary mesons travel through the helium-filled decay volume, muon neutrinos are produced predominantly via the following processes:

$$\begin{aligned} \pi^+ &\rightarrow \mu^+ + \nu_\mu, \\ K^+ &\rightarrow \mu^+ + \nu_\mu, \\ K^+ &\rightarrow \pi^0 + \mu^+ + \nu_\mu. \end{aligned}$$

Kaon and muon decays can also produce other flavours of neutrinos, with the most common processes being:

$$\begin{aligned} K^+ &\rightarrow \pi^0 + e^+ + \nu_e, \\ \mu^+ &\rightarrow e^+ + \nu_e + \bar{\nu}_\mu. \end{aligned}$$

By reversing the polarity of the magnetic horns, negatively charged mesons can be selected which decay to predominately antineutrinos. In this way, T2K can run in two modes: Forward Horn Current (FHC) mode where a predominantly muon neutrino beam is produced, and Reverse Horn Current (RHC) mode where a predominantly muon antineutrino beam is produced.

At the end of the decay volume there is a 75 tonne, water-cooled graphite block, and 15 iron plates that have a combined depth of 2.4 m. This constitutes the beam dump, which is designed to cause muons to interact before they can decay to wrong-sign ($\bar{\nu}_\mu$ in FHC, ν_μ in RHC) neutrino background. Only muons with momentum greater than 5 GeV are able to pass through to the muon monitor (MUMON [63]) behind, which measures the direction and intensity of the beam.

Aiming the beam 2.5° away from Super-Kamiokande has the effect of narrowing the energy spectrum so L/E is well defined and can be selected such that it aligns with a peak in the oscillation probability. This energy spectrum and oscillation

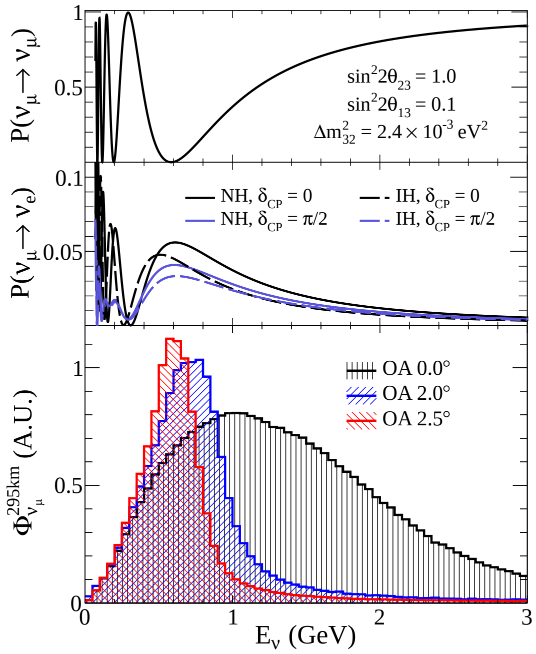

Figure 2.4: Muon neutrino survival probability (top) and electron neutrino appearance probability (middle) at 295 km, and the neutrino flux as a function of energy for on- and off-axis scenarios (bottom) [46]. At larger off-axis angles a narrower energy spectrum is seen, and at 2.5° off-axis the spectrum peak at 600 MeV is aligned with the maximum disappearance probability for the 295 km baseline.

probability at 295 km is shown in Fig. 2.4. It is clear that the peak energy observed at 2.5° off-axis, 600 MeV, aligns with a minimum in the muon survival probability and a maximum in the oscillation probability to electron neutrinos. By using the off-axis technique, the narrow energy spectrum also minimises high energy backgrounds, providing a higher purity oscillation sample.

The total number of neutrinos produced by the T2K beam cannot be measured. However it is possible to measure the number of protons that hit the beam target, referred to as Protons On Target (POT). Since the number of neutrinos produced is directly proportional to the number of protons that hit the target, the total integrated POT can be used as a proxy for the total integrated neutrino flux. The accumulated POT over time is shown in Fig. 2.5 along with the beam power used in each T2K run.

The simulated neutrino flux at ND280 for runs 1 to 10 are shown in Fig. 2.6, broken down by neutrino flavour. The FHC beam has a purity exceeding 90%, while the RHC beam has a purity of around 60%. The wrong-sign background is larger in RHC mode, particularly at higher energies, which is due to the higher production

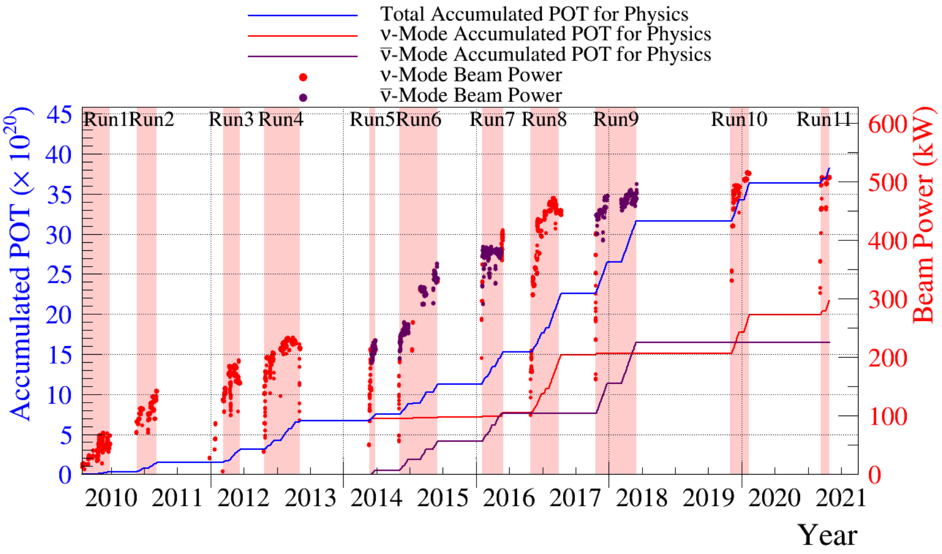

Figure 2.5: Accumulated protons on target (POT) and beam power at T2K for runs 1-11 [46].

multiplicities of positive parent particles. In both FHC and RHC, the ν_e and $\bar{\nu}_e$ components account for less than 1% at the flux peak.

2.2 INGRID

The Interactive Neutrino GRID (INGRID) [66] is the on-axis near detector used to profile the beam and its direction. The detector is composed of 14 identical modules, arranged in two rows of seven modules. One row is vertical and one is horizontal, with the horizontal row sitting immediately downstream of the vertical. The configuration of the INGRID modules is shown in Fig. 2.7.

Each INGRID module is made of nine iron target plates and eleven tracking scintillator planes. Each scintillator plane comprises two layers of plastic scintillator bars which are optically separated and perpendicular to each other. Each component scintillator bar has a wavelength shifting (WLS) fibre through its centre which is mirrored at one end and read out at the other by a Multi-Pixel Photon Counter (MPPC). The modules have scintillator veto planes on all sides to reject charged particles entering from outside the module. An exploded view of an INGRID module is shown in Fig. 2.8.

Each module contains 7.1 tonnes of iron, meaning there are enough interactions in each module to allow daily monitoring of the neutrino event rate. The observed event

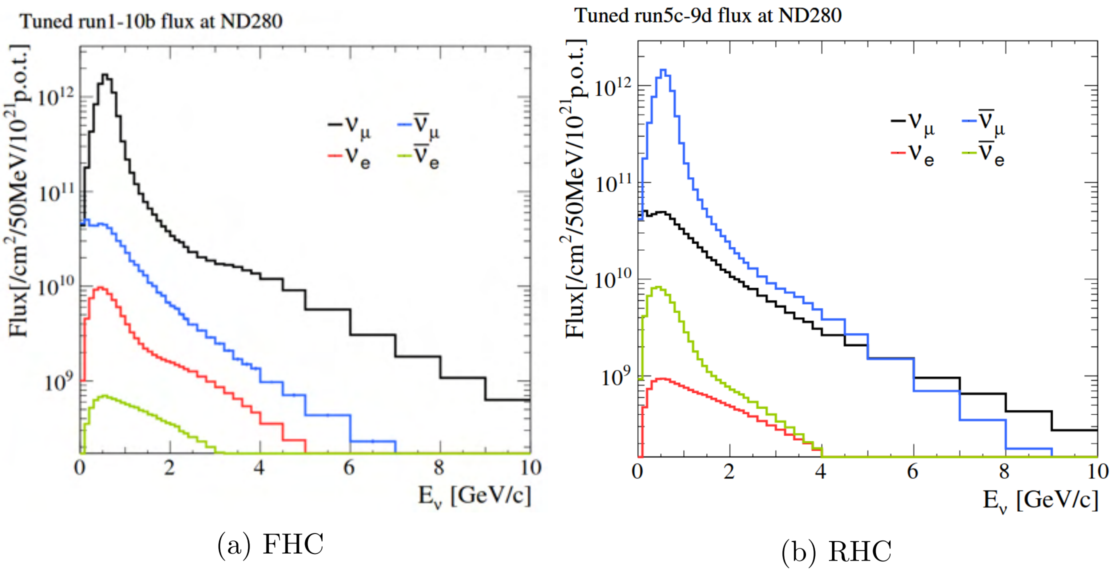

(a) FHC (b) RHC

Figure 2.6: Simulated neutrino flux at ND280 in FHC (a) and RHC (b) modes [65].

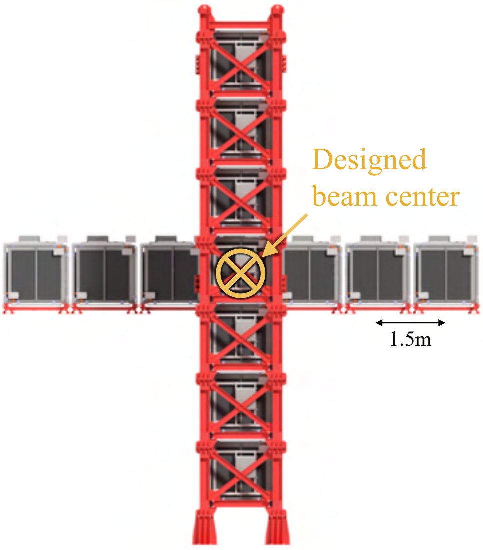

Figure 2.7: The on-axis near detector INGRID [46]. The 14 modules are arranged in a horizontal row and a vertical column, forming a cross-shaped detector.

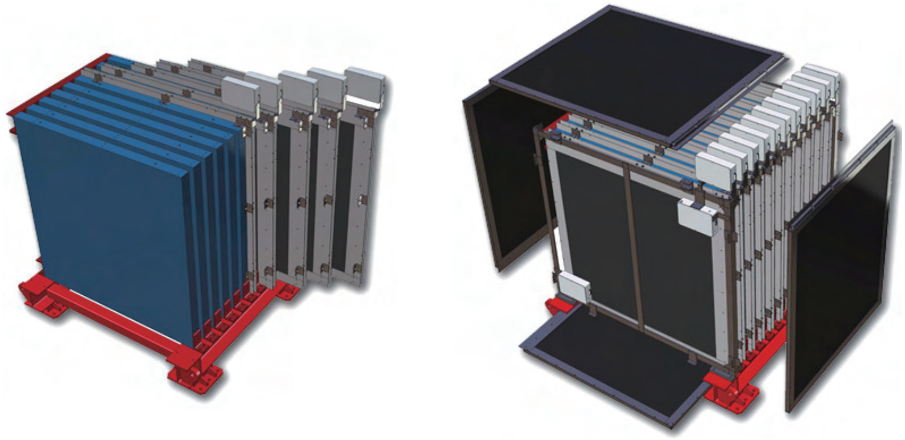

Figure 2.8: Exploded view of an INGRID module [43]. On the left, iron plates are shown in blue which are separated by tracking scintillator planes shown in grey. On the right, scintillator veto planes are also shown in black.

rates have consistently remained within the expected statistical fluctuation of 1.7% [67]. The beam direction is monitored using the neutrino events accumulated over one month. The beam direction is measured with an accuracy better than 0.4 mrad, and has remained consistent with the expected beam direction when statistical and systematic uncertainties are considered [67]. A deviation of 1 mrad in the beam direction would shift the peak neutrino energy by 2%, so this stability in beam direction is essential for the off-axis technique used by the T2K experiment.

2.3 ND280

The Near Detector at 280 m (ND280) is immediately downstream of INGRID and sits at the same 2.5° off-axis angle as the far detector. The detector is used to categorise the beam before oscillations occur, measuring the beam flux, energy spectrum and ν_e contamination, as well as making measurements of neutrino interaction cross sections.

This detector is composed of several sub-detectors enclosed in a magnet yoke, as shown in Fig. 2.9. Each sub-detector has a unique design purpose, and each makes use of different technology to achieve this. These are discussed in detail below.

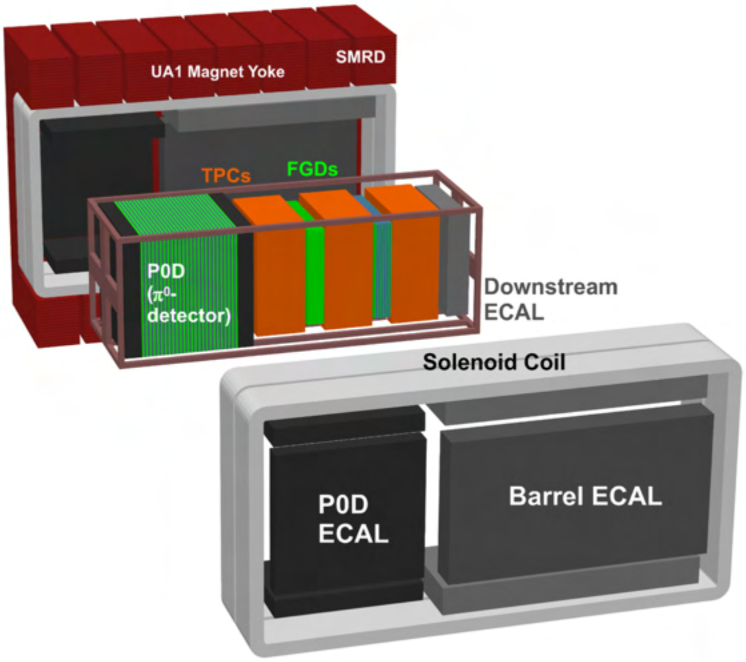

Figure 2.9: Exploded view of the off-axis near detector ND280 [43]. The detector is comprised of several sub-detectors: the π^0 detector (PØD), time projection chambers (TPCs), fine-grained detectors (FGDs), electromagnetic calorimeters (ECals) and the side muon range detector (SMRD). The sub-detectors are contained within a magnet yoke.

2.3.1 The π^0 Detector

The π^0 detector (PØD) [68] is the most upstream sub-detector and was designed to measure the cross section of neutral current neutrino interactions on water with one π^0 in the final state. This channel is of particular importance for T2K as it is a background to the far detector ν_e appearance search. Measuring the cross section of the neutral current process at the near detector allows constraint of the far detector ν_e appearance uncertainty.

The target mass of the detector is separated into an upstream water target and a central water target, and consists of alternating scintillator planes, water bags and brass sheets. The target mass is bookended with the upstream and central electromagnetic calorimeters (ECals), composed of alternating scintillator planes and lead sheets. A schematic of the PØD is shown in Fig. 2.10.

Each scintillator plane is composed of two perpendicular layers of triangular scintillator bars. There are 134 vertical bars and 126 horizontal bars per plane. Each bar has a WLS fibre through its centre which is read out at one end by an

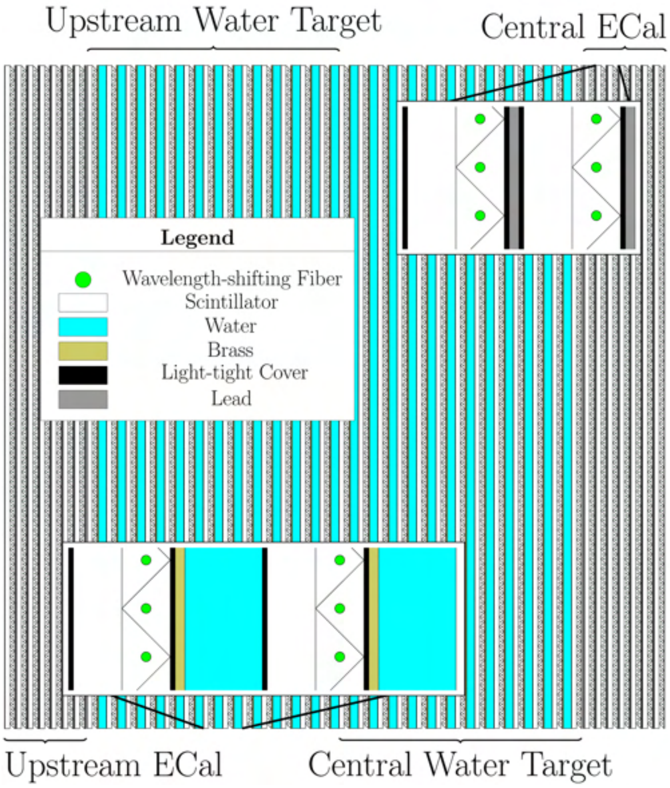

Figure 2.10: Schematic of the π^0 detector (PØD) [43]. The water, scintillator, brass and lead layers are shown, and the orientation of the triangular scintillator bars is illustrated.

MPPC. The upstream and central ECals have seven scintillator planes each, while the upstream and central water targets both have 13.

The water bags can be filled and emptied relatively easily, and measurements are made in both configurations. The difference in neutral current π^0 production in the two cases can be used to constrain uncertainties at the far detector associated with this process.

The ECals at either end of the target mass improve the containment of electromagnetic showers within the PØD, as well as providing a veto for interactions occurring in other ND280 sub-detectors.

2.3.2 The Fine-Grained Detectors

Downstream of the PØD is the tracking region, comprising two Fine-Grained Detectors (FGDs) sandwiched between three Time Projection Chambers (TPCs). The FGDs [69] are the target mass of the tracking region, and each is 2300 mm wide, 2400 mm high, and 365 mm deep. The most upstream FGD is referred to as FGD1 and is composed entirely of scintillator. The other, FGD2, has alternate layers of scintillator and water target. Both FGDs have target masses of 1.1 tonnes.

FGD1 contains 30 layers of rectangular scintillator bars which alternate between vertical and horizontal orientations to enable 3D reconstruction. Each layer contains 192 scintillator bars and, as in the PØD, each bar has a WLS fibre through its centre which is read out at one end.

FGD2 contains 14 layers of scintillator bars arranged in seven perpendicular pairs that are separated by six 2.5 cm deep water layers. The water target mass allows measurement of various neutrino interaction cross sections on water, which in turn are used to constrain the predicted far detector event rate. Such constraints are discussed in detail in Chapter 5.

As well as providing the target mass for neutrino interactions, the FGDs also have reconstruction and particle identification (PID) capabilities. Tracks with hits in the TPCs are matched to FGD tracks to determine the position of the interaction vertex, and low momentum particles that are contained within the FGD are also reconstructed. Particle identification in the FGD is used to distinguish protons from pions and muons, and is considered only for the contained particles.

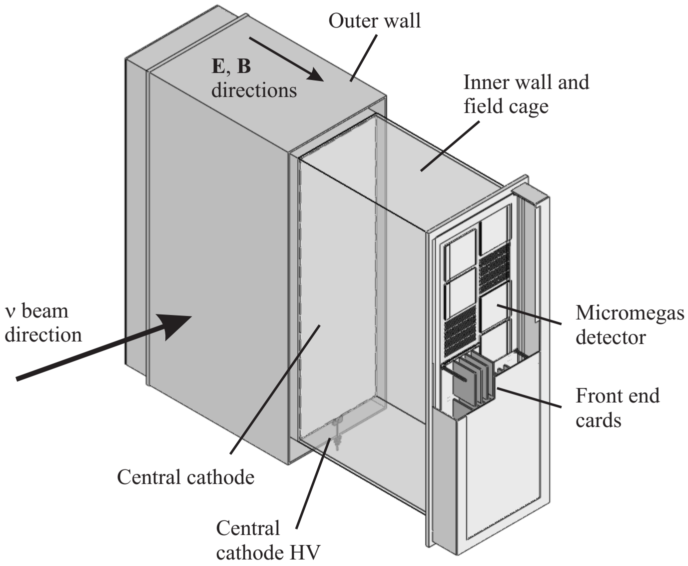

Figure 2.11: Simplified diagram of a TPC showing the main components of the design [70].

2.3.3 The Time Projection Chambers

The three Time Projection Chambers (TPCs) [70] in the tracking region are referred to as TPC1, TPC2 and TPC3 moving in the downstream direction. The TPCs, together with the magnetic field, allow effective track reconstruction, charge identification, momentum measurement, and particle identification.

Each TPC comprises an inner box filled with an argon-based drift gas, $Ar:CF_4:iC_4H_{10}$ (95:3:2), inside an outer box filled with CO_2 which acts as an insulator. Together, a strip pattern machined onto the copper inner box walls and a central cathode that splits the inner volume in half produce a uniform electric field in each TPC that is aligned with the detector's magnetic field. A simplified diagram of a TPC is shown in Fig. 2.11.

As a charged particle passes through the TPC it ionises the drift gas and the ionisation electrons drift away from the central cathode towards micromegas in the readout planes. The micromegas amplify and measure these electrons. There are 12 micromegas per readout plane and each of the micromegas are segmented into 1728 rectangular anode pads. This allows measurements of horizontal and vertical positions, which is combined with the known ionisation drift velocity to allow precise 3D tracking in the TPCs. The curvature of a track in the magnetic field allows

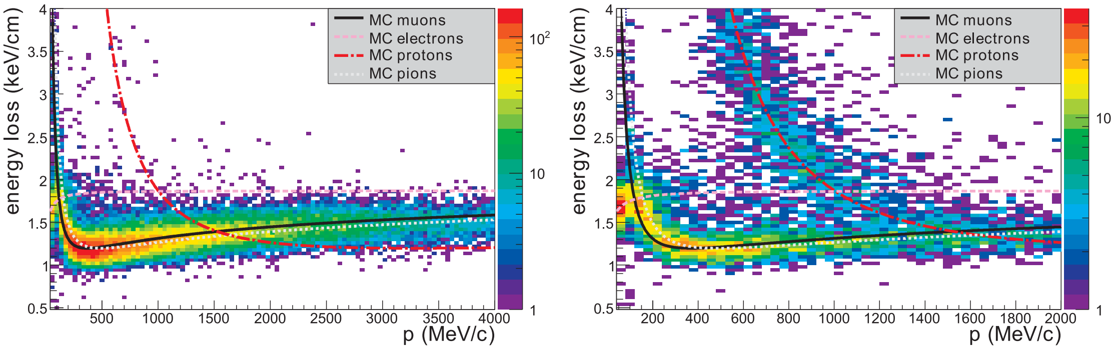

(a) Negative particles

(b) Positive particles

Figure 2.12: Energy loss per unit length as a function of momentum for (a) negative and (b) positive particles in the ND280 TPCs [70]. Lines show Monte Carlo predictions for each particle hypothesis and points are real data collected during the first T2K physics run.

determination of its momentum and charge.

Particle identification in the TPCs relies on the measured energy loss per unit length of the particle, $\mathrm{d}E/\mathrm{d}x$. Distributions of $\mathrm{d}E/\mathrm{d}x$ for the most common charged particles produced in ND280 are shown in Fig. 2.12. The resolution of the energy deposit measurement is $7.8\pm0.2\%$ for minimum ionising particles, meaning the probability of incorrectly identifying a muon as an electron is only 0.2% for muons with momentum below 1 GeV/c [70]. Proton tracks of less than 0.8 GeV/c momentum can also be identified correctly with a high accuracy.

2.3.4 The Electromagnetic Calorimeters

The Electromagnetic Calorimeters (ECals) [71] in ND280 are separated into three sections: the PØD ECal surrounds the four faces of the PØD that are parallel with the beam axis, the barrel ECal surrounds the four faces of the tracking region that are parallel with the beam axis, and the downstream ECal covers the most downstream face of TPC3. This configuration can be seen in Fig. 2.9.

The barrel and PØD ECals both consist of six modules, two vertical and four horizontal, while the downstream ECal is a single module. All modules are scintillator and lead sampling calorimeters which complement the central detectors in full event reconstruction. The rectangular scintillator bars are read out using WLS fibres and MPPCs much like the other scintillator-based detectors described in this chapter.

The PØD ECal is primarily used to tag particles exiting the PØD, distinguishing between electromagnetic showers ($e^{\pm}/\gamma$) and tracks ($\mu^{\pm}$). Full reconstruction is not required so the PØD ECal has the fewest layers, with just six scintillator planes separated by 4 mm thick lead sheets. All of the scintillator bars in each plane are parallel to the beam axis. Despite having only six layers of scintillator, the thickness of the lead sheets mean that the PØD ECal comprises approximately 4.3 electron radiation lengths (X_0) worth of material, which is enough to achieve the tagging function it is designed for.

The barrel and downstream ECals are designed for full track and shower reconstruction and particle identification. Therefore, they consist of more layers than the PØD ECal: 31 in the barrel ECal and 34 in the downstream ECal. Each scintillator layer is separated by 1.75 mm thick lead sheets, meaning the barrel and downstream ECals correspond to $9.7X_0$ and $10.6X_0$ respectively. The bars in each scintillator layer are perpendicular to the adjacent layers to allow 3D reconstruction. In the downstream ECal the bars are read out from both ends, while in the barrel ECal the bars parallel to the beam are read out from both ends and those perpendicular to the beam are read out at one end only.

2.3.5 Magnet

The ND280 sub-detectors described above are housed in the refurbished UA1/NOMAD dipole magnet. At a current of 2.7 kA, the magnet produces a uniform magnetic field of 0.2 T. This allows high resolution measurements of momentum (6% at 600 MeV [70]) and charge identification for charged particles in the tracking region. Each half of the magnet is segmented into eight C-shaped sections. Each section comprises 16 low-carbon steel plates which are 48 mm thick and separated by 17 mm air gaps [72]. The magnet has a mass of 850 tonne meaning it contributes most of the detector mass. Therefore, most neutrino interactions in the detector occur in the magnet structure.

2.3.6 The Side Muon Range Detector

The Side Muon Range Detector (SMRD) [72] is a collection of 440 scintillator paddles placed in the air gaps of the magnet. Its main purposes are to tag high angle muons

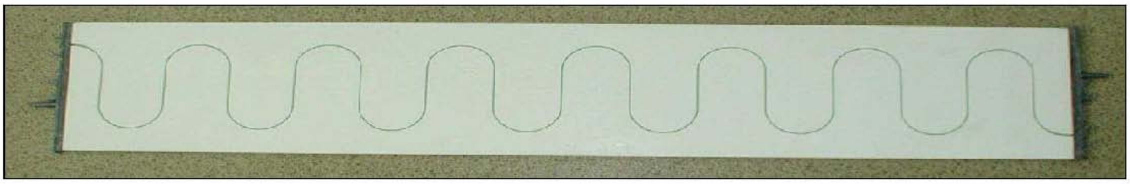

Figure 2.13: SMRD scintillator paddle showing a WLS fibre in the characteristic S-shape [72].

coming from interactions within the detector and to detect particles coming from interactions outside of the detector such as cosmic ray muons.

The top and bottom parts of each C-shaped section of the magnet have the three innermost layers instrumented with scintillator paddles. The number of layers instrumented on the sides varies going from the most upstream section to the most downstream. The first five sections have paddles in the three innermost layers, section six has paddles in the four innermost layers, and the final two sections have paddles in the six innermost layers. More layers are instrumented at the downstream end of the detector to improve reconstruction for tracks in the forward direction. The scintillator paddles are much wider than the bars used in other sub-detectors so the WLS fibres follow a repeating S-shaped groove in the paddle, as shown in Fig. 2.13. The WLS fibres in the paddles are read out at only one end.

2.3.7 Electronics and Data Acquisition

The ND280 ECals, SMRD and PØD, and the INGRID modules are read out using Multi-Pixel Photon Counters (MPPCs) and Trip-T electronics boards [73]. Each MPPC contains an array of 667 photodiodes, and up to 16 MPPCs can be read out by a single Trip-T chip. Up to four Trip-T chips can be read out by a Trip-T Frontend Board (TFB). Data from up to 48 TFBs is collected by a Readout Merger Module (RMM), and up to two of these RMMs are read out by a Frontend Processing Node (FPN). The TPCs and FGDs do not make use of the Trip-T electronics, instead collecting their data through Data Concentrator Cards (DCCs).

A Main Clock Module (MCM) receives triggers from various sources and issues these to Secondary Clock Modules (SCMs) associated with each sub-detector. These SCMs control the triggering of the corresponding RMMs and DCCs. Beam triggers are issued when a signal is received from the beamline indicating that a beam spill has been sent. The Cosmic Trigger Module (CTM) is a separate board used to trigger cosmic ray events. A cosmic trigger is issued if TFBs on two different sides of the ND280 detector see coincident activity. There are also other trigger types are used for calibration. Beam triggers take priority over all other triggers, with the other trigger types occurring in sequence between beam triggers.

2.4 Other Near Detectors

The near detector target nuclei in the FGDs are carbon (in the scintillator) and oxygen (in the water), whilst the far detector target nuclei are simply oxygen. This difference in target nuclei requires a non-trivial extrapolation of neutrino-nucleus interaction models. Differences between the nuclei, such as binding energy, mean that this extrapolation is a leading cause of uncertainty in the oscillation analysis. For this reason the WAter-Grid-And-SCIntillator detector (WAGASCI) [74] and a Magnetised Iron Neutrino Detector (Baby MIND) [75] have recently been added to the T2K near detector suite. Although these detectors are not used in the analysis presented in this thesis, they are briefly described below.

The WAGASCI target volume consists of two water modules and one hydrocarbon module which have muon range detectors (wall MRDs) on two sides, parallel to the beam direction. The target water modules contain a 3D grid structure made of thin scintillator bars, with the cells between the bars being filled with water. This maximises the amount of target material in these modules while providing the ability to track particles with sufficient resolution. The hydrocarbon module is the "proton module" that was previously part of INGRID [66]. The proton module consists of scintillator planes which, much like the INGRID modules, are surrounded by veto planes. The scintillator bars used in this module are thinner than the INGRID modules to improve track reconstruction. The wall MRDs are composed of alternating iron and scintillator layers and allow muons to be identified and their momenta to be measured.

Baby MIND is located immediately downstream of WAGASCI and aims to make precise momentum measurements and charge identification of muons exiting the WAGASCI target volume using a 1.5 T magnetic field. The detector consists of

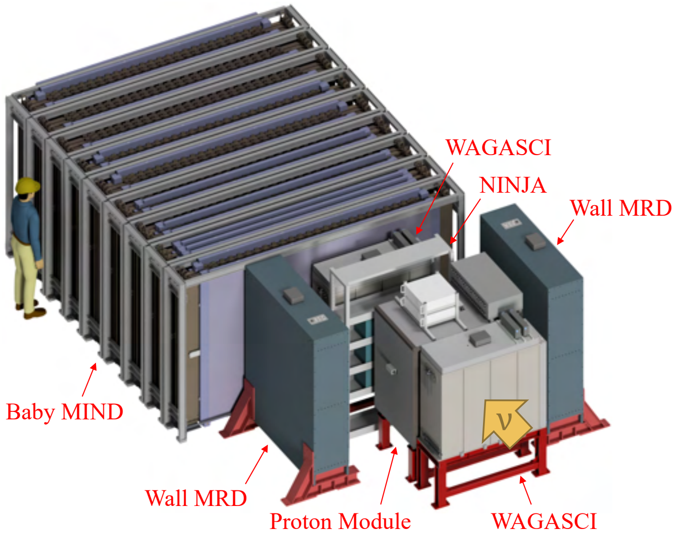

Figure 2.14: The layout of the WAGASCI and Baby MIND detectors [77]. The emulsion detector used by the NINJA experiment is also shown.

33 magnetised 30 mm thick iron plates and 18 scintillator planes, the configuration of which was optimised through simulation. This allows muon momentum to be measured precisely in the range 0.3-5.0 GeV/c, giving good coverage across the peak flux region.

The layout of the WAGASCI and Baby MIND detectors is shown in Fig. 2.14. The NINJA experiment [76] is not part of T2K, however it also houses its emulsion detector here and this is labelled in Fig. 2.14.

2.5 Super-Kamiokande

The Super-Kamiokande (SK) detector [78] is used as the T2K far detector, and is located in a cavern 1 km below Mt. Ikenoyama, 295 km west of J-PARC. This distance and the peak beam energy at 2.5° degrees off-axis puts SK at an oscillation maximum, as shown in Fig. 2.4. The detector is a 41.2 m high, 38.8 m diameter cylinder that contains 50 ktonnes (22.5 ktonnes fiducial volume) of ultra-pure water. SK is instrumented with over 13,000 photomultiplier tubes (PMTs) that detect Cherenkov light produced by charged particles that result from neutrino interactions. A sketch of the detector is shown in Fig. 2.15.

The detector is composed of two volumes, an inner detector (ID) and an outer detector (OD) which are optically separated by a 50 cm thick stainless steel cylinder

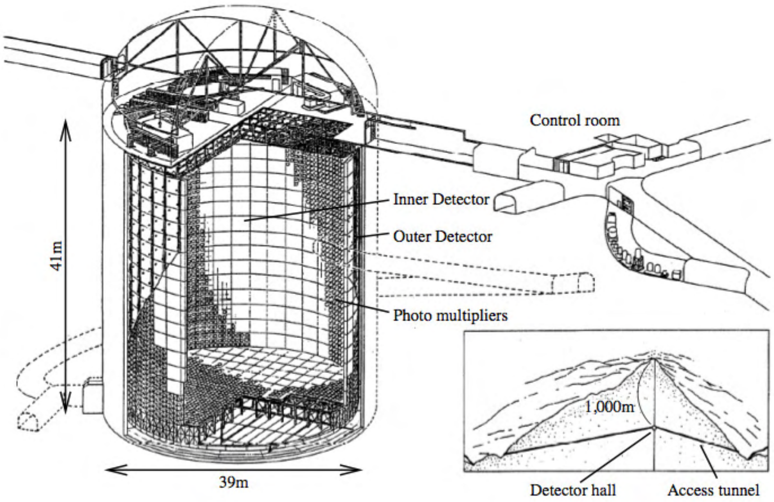

Figure 2.15: Sketch of the Super-Kamiokande detector and its position under Mt. Ikenoyama [43].

covered in black plastic sheets. The ID is 36.2 m high and has a diameter of 33.8 m; the OD extends 2 m beyond the ID walls. The walls of the ID hold 11,129 inward-facing 50 cm diameter PMTs which provide photo-coverage across 40% of the inner surface. The inner walls of the OD hold 1,885 outward-facing 20 cm diameter PMTs. Although this gives the OD much lower photo-coverage than the ID, 7%, it is enough to perform the primary goal of the OD in vetoing cosmic ray muons entering the detector with almost 100% efficiency [43].

If a charged particle travels through a medium faster than the local speed of light (light travels at approximately $0.75c$ in water), it will produce a cone of Cherenkov light. In a charged-current quasi-elastic (CCQE) neutrino interaction, a proton and either an electron or muon are produced. Both electrons and muons produced in this way are commonly above their Cherenkov thresholds in SK, and the Cherenkov light they produce can be used to perform particle identification.

As the charged leptons travel through the detector, they polarise the surrounding water molecules. After the lepton passes, the molecules return to an unpolarised state through the emission of photons. If the lepton is travelling faster than the speed of light in water, constructive interference occurs and Cherenkov radiation is emitted as a coherent wavefront at a fixed angle to the trajectory of the particle. This effect produces the characteristic cone shape of Cherenkov radiation, which is observed as a ring on the detector walls. As the lepton travels through water it will collide with molecules causing deviations around its initial trajectory. Since the electron mass is around 200 times smaller than the muon mass, electrons undergo multiple scattering processes whereas muons do not. This causes a “shower” effect for electrons, leading to a “fuzzy” Cherenkov ring compared to that of a muon.

Since the neutrino oscillation probabilities measured by T2K are dependent on the number of interactions for each neutrino flavour it is important to be able to distinguish electrons and muons in this way. Although many of the muon neutrinos produced at J-PARC will oscillate to tau neutrinos, the large mass of the tau lepton prevents it being produced at the peak T2K beam energy. Even if a tau lepton was produced by a particularly high energy neutrino interaction, the Cherenkov threshold for these particles is 2.7 GeV, which would be unachievable given T2K energies, so they would not be detected. However there are other particles that can lead to signals similar to muons and electrons in the detector.

When a neutrino interacts via a neutral current (NC) exchange, no charged lepton is produced and it is not possible to determine the neutrino flavour. Such an interaction can however produce a π^0, e.g. through a resonant process, which will decay to two photons. An individual photon can produce a fuzzy ring much like an electron, so two rings in coincidence are rejected. However if one of the photons is not energetic enough, or if the photons have a small enough angle between them, the resulting signal can appear electron-like. This makes NC π^0 production a background in the electron neutrino appearance search.

Although neutrons are not electrically charged, and therefore cannot produce Cherenkov radiation, they can still be detected in SK. Historically this has been done via neutron capture on hydrogen nuclei, however SK recently began doping its ultra-pure water with gadolinium sulphate, $\mathrm{Gd_2(SO_4)_3}$. Once doping is complete gadolinium sulphate will account for 0.2% of the fiducial mass, leading to 90% of neutrons capturing on gadolinium nuclei [79]. As well as an increased capture efficiency, the tagging efficiency will also be improved due to the higher energy released in capture on gadolinium (8 MeV cascade vs. single 2.2 MeV photon) and the shorter time for the energy to be released ($\sim$20 μs vs. $\sim$180 μs) [79]. An improved neutron tagging efficiency will help distinguish ν_μ and $\bar{\nu}_\mu$ interactions, which is not currently possible since the detector is not magnetised.

When making measurements of the oscillation parameters, the T2K experiment uses the near detector ND280 to constrain the flux and cross section uncertainties at Super-Kamiokande. The constraint from ND280 in the oscillation analysis is the main topic of this thesis. As a first step towards making the constraint, the ND280 data must be categorised into samples corresponding to different interaction modes. This is the subject of Chapter 3.

Chapter 3

Selecting CC ν_μ Events with Final State Photons in ND280

As discussed in Section 2.3, interactions in the near detector can be used to constrain the flux and cross section uncertainties in the T2K oscillation analysis. This is achieved by classifying selected events according to their final state particles and performing a simultaneous fit to data for all samples. The fitting method is described in Chapter 5.

Previously, selected charged current (CC) events were categorised according to the pion content of their final state [45, 80]. The charged current events were separated into three categories: CC0π, CC1$\pi^{\pm}$ and CC-Other. The CC0π sample contains zero pions in the final state, the CC1$\pi^{\pm}$ contains one positive (negative) pion in the final state in FHC (RHC), and the CC-Other sample contains events with any other combination of final state mesons, including events containing neutral pions.

Two changes have been made to the FHC near detector samples since the previous oscillation analysis: the CC0π sample has been split based on the absence or presence of protons in the final state into the CC0π0p and CC0πNp samples [81]; and a photon tag, targeting π^0s and other photon-producing particles (see Section 3.5), has been introduced that splits the old CC-Other sample into the CC-Photon and CC-Other samples, as well as improving the purity of the CC0π and CC1π^+ samples. The work presented in this thesis focuses on the development of the photon tag and its effect in the T2K oscillation analysis.

T2K Run	**Data POT/10^{20}**	**MC POT/10^{20}**	**MC Sand POT/10^{20}**
Run 2 Air	0.360	16.802	10.730
Run 2 Water	0.434	12.038	10.730
Run 3 Air	1.593	30.780	10.730
Run 4 Air	1.789	36.122	10.730
Run 4 Water	1.695	36.122	10.730
Run 8 Air	4.150	44.532	10.730
Run 8 Water	1.581	27.168	10.730
Total	11.602	203.563	N/A

Table 3.1: Protons on target (POT) for each T2K data-taking period used in this analysis for data and MC.

3.1 Data and Monte Carlo Samples

The development of the photon selection was performed using data and Monte Carlo (MC) corresponding to T2K runs 2, 3, 4 and 8. These are the runs in which the beam has been operated in FHC mode. While run 1 was also an FHC run period, the barrel ECals had not been installed in ND280 at that point, so it is excluded from the analysis. Runs 2, 4 and 8 are each separated into two samples based on whether or not the PØD water bags were filled. The PØD water bags were empty for the entirety of run 3. The total number of protons on target for each data run and the corresponding MC samples are shown in Table 3.1.

Interactions occurring inside the ND280 sub-detectors, the magnet and the rock of the cavern in which ND280 is located (referred to as “sand”) have been simulated using version `5.4.0` of the NEUT Monte Carlo generator [82]. For CCQE interactions, the nuclear model uses a Benhar Spectral Function (SF) [16] with an axial mass of $M_A^{QE} = 1.21\,\mathrm{GeV}/c^2$ to simulate the initial nucleon momentum distribution in the target mass. For all non-CCQE interactions the initial nucleon momentum distribution is simulated using a Relativistic Fermi Gas (RFG) [83]. The two-particle-two-hole (2p2h) model from Nieves *et al.* [84] is used to simulate interactions with nucleon pairs. Resonant pion production (RES) interactions are modelled using the Rein-Sehgal model [85] with an invariant hadronic mass $W \leq 2.0\,\mathrm{GeV}$, which are then tuned to form factor corrections from the model of Graczyk and Sobczyk [86]. Coherent pion production uses the Berger-Seghal model [87]. Deep Inelastic Scattering (DIS) is implemented using a custom hadronisation model:

for invariant hadronic masses $1.3 < W < 2.0\,\mathrm{GeV}$, interactions are modelled with NEUT's multiple-pion (multi-pi) mode and Bodek-Yang [88] corrections are applied; for $W > 2.0\,\mathrm{GeV}$, PYTHIA 5.7 [89] is used to model interactions. Single pion production through DIS is suppressed for $W \leq 2.0\,\mathrm{GeV}$, since this region of phase space is already covered by the RES interactions. Final State Interactions (FSI) are simulated using NEUT intranuclear cascades.

The particles simulated with NEUT are then propagated through the detector using GEANT4 [90]. The ND280 electronics are simulated using a custom package ElecSim [43], developed by the T2K collaboration.

Event selections at ND280 are developed using the Highland2 (HIGH Level Analysis at the Near Detector 2) framework. The framework provides an easy interface for users to interact with the data and Monte Carlo, accessing variables and implementing cuts to select events of interest. A set of tools for plotting analysis variables, selection efficiencies and purities, and detector systematic uncertainties is also provided in the framework. Mature selections are implemented in the Psyche (Propagation of SYstematics and CHaracterisation of Events) framework developed by the T2K collaboration. This framework includes only variables that are necessary for the implemented selections and systematics, as well as the code for the cuts in those selections and propagation of the relevant systematics. As a result, systematic propagation is efficient and the output files that are passed on to the near detector fitters have smaller file sizes.

3.2 Charged Current Muon Selection

The first stage of the charged current selections is to identify the muon candidate produced when a ν_μ interacts in one of the near detector FGDs. With additional cuts, the resultant inclusive CC sample can be separated using pion, proton and photon tags. This inclusive CC sample is obtained using the following cuts, applied sequentially:

Event quality: As described in Section 2.1, the neutrino beam is produced by eight proton bunches of 15 ns width impinging on a graphite target. Only events that are compatible with one of these bunches are selected, with an event required to be within 4σ of the mean of one of the bunches. To account for changes in beam power and accelerator conditions, the mean of the bunches is calculated on a run-by-run basis. An eight-peak Gaussian fit is used to find the mean of each bunch and the width is taken to be $\sigma = 15\,\mathrm{ns}$. Using a fixed Gaussian width leads to the tails of some bunches being cut, however this is a sub-percent level effect over the whole data set and is covered by systematic uncertainties [80].

Total multiplicity: An event must contain at least one reconstructed negative track crossing TPC2 or TPC3. A negative track is required since the muon produced in a CC ν_μ interaction is negatively charged. The tracks are required to cross a TPC because these sub-detectors are needed for momentum measurements and particle identification in subsequent cuts.

Track quality and fiducial: The highest momentum negative track is selected as the muon candidate and the starting position of the track is used to define the interaction vertex position. The starting position of the track is generally defined as the point at which the reconstructed muon track intersects the most upstream XY plane that has hits associated with the track. The reconstructed vertex of an event must be inside the FGD1 or FGD2 fiducial volume (FV). The FV is defined to minimise acceptance of events where the true vertex is outside the FGD but is reconstructed as being inside. For this reason, the vertex must be at least five scintillator bars away from the edge of the FGD in the x and y directions. In the z direction the most upstream XY module is excluded in FGD1, while in FGD2 only the first scintillator layer is removed. In the TPC, tracks must consist of more than 18 clusters (sets of adjoining pads in a row or column). This rejects shorter tracks for which the likelihood cuts described below are less efficient.

Upstream background veto: A muon produced in an interaction in the PØD that undergoes a large scattering in FGD1 can be reconstructed as two tracks instead of one. To avoid such reconstruction failures, events are rejected if the second highest momentum track starts within 150 mm in the upstream direction of the muon candidate. In the FGD2 selection events are also vetoed if a secondary track starts in the FGD1 FV.

Broken track: This cut is applied to reject events with mis-reconstructed tracks, where instead of one muon candidate track originating in FGD FV, the reconstruction breaks this track into two components: one fully contained FGD track (isoFGD track) followed by a second track which starts in the last layers of the FGD and passes into the TPC. In such events, the second track is considered as the muon candidate. Therefore if the muon candidate starts in the last two layers of the FGD and there is also an isoFGD track present in the FGD, then the event is rejected.

Muon particle identification: For events which satisfy all of the criteria described above, a TPC particle identification (PID) procedure is applied to select muon candidates. In general, the energy deposit measured in the TPC is compared with the expected energy deposit under several charged-particle hypotheses: muon, electron, pion and proton. Based on these comparisons, pulls are calculated and then used to form likelihood variables. A pull for a given hypothesis i is defined as:

$$\text{Pull}_i = \frac{dE/dx_{\text{measured}} - dE/dx_{\text{expected},i}}{\sigma_{dE/dx_{\text{measured}} - dE/dx_{\text{expected},i}}}, \tag{3.1}$$

where $\sigma_{dE/dx_{\text{measured}} - dE/dx_{\text{expected},i}}$ is the uncertainty on the difference between measured and expected values of dE/dx. The pull is used to define the likelihood:

$$\mathscr{L}_i = \frac{e^{-\text{Pull}_i^2}}{\sum_l e^{-\text{Pull}_l^2}}. \tag{3.2}$$

Electrons are rejected by requiring:

$$\mathscr{L}_{\text{MIP}} = \frac{\mathscr{L}_\mu + \mathscr{L}_\pi}{1 - \mathscr{L}_p} > 0.8 \quad \text{if} \quad p < 500\,\text{MeV}/c, \tag{3.3}$$

where MIP stands for minimally ionising particle (such as a true muon) and p represents the momentum of the muon candidate. Protons and pions are removed by requiring:

$$\mathscr{L}_\mu > 0.05. \tag{3.4}$$

Cut name	**Cut description**
Event Quality	The event must occur in a defined bunch window.
Total Multiplicity	At least one track must cross TPC2(3).
Track Quality & Fiducial	The highest momentum negative track in the event must have its origin in the FGD1(2) FV and >18 TPC clusters.
Upstream Background Veto	Veto backwards events and those coming from outside the FV.
Broken Track	Reject external background from the last two layers of FGD1(2).
TPC PID	μ^- selection using TPC PID: $\mathscr{L}_{\text{MIP}} > 0.8$ if $p < 500$ MeV/c, and $\mathscr{L}_\mu > 0.05$.

Table 3.2: Summary table of the muon selection criteria.

The cuts used to select ν_μ CC interactions are summarised in Table 3.2. The reconstructed momentum, p_μ, and cosine of the reconstructed angle with the beam axis, $\cos\theta_\mu$, of the selected muon candidates are shown in Fig. 3.1.

3.3 Pion Tagging

To target specific interaction modes, the inclusive muon selection described in Section 3.2 is separated into sub-samples based on the other reconstructed particles in the final state. The signal at the far detector consists of CCQE interactions, while resonant pion production interactions are considered background. In order to constrain these processes at the near detector a pion tag is used in event categorisation. Several methods are used to tag pions in the tracking region, which select tracks other than the muon candidate, and then apply TPC or FGD PID information to distinguish them.

The tracks considered are required to be in the same time bunch as the muon candidate, and they must start in the same FGD FV as the muon candidate. If

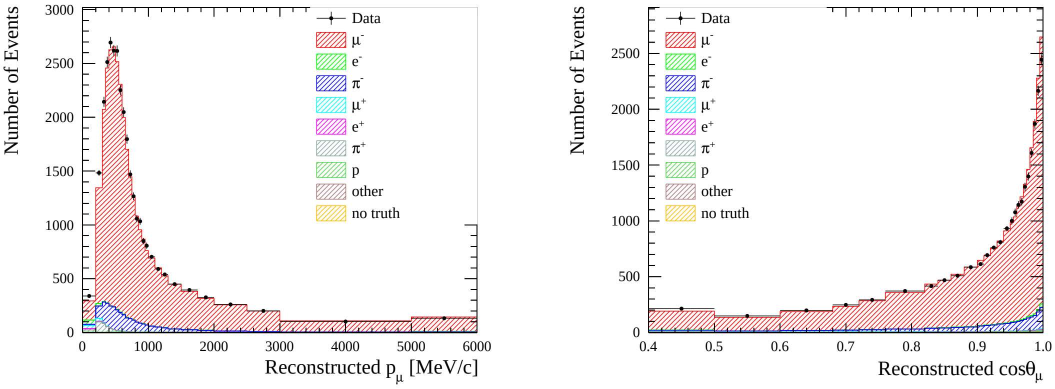

(a) FGD1

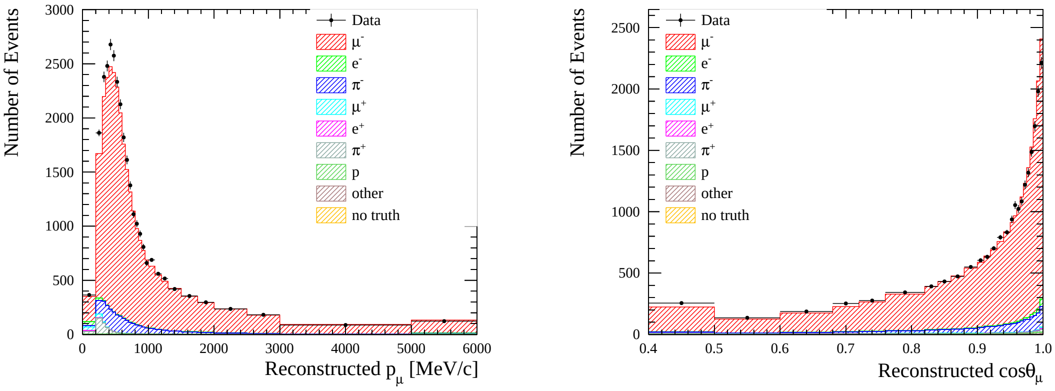

(b) FGD2

Figure 3.1: Reconstructed momentum (left) and $\cos\theta$ (right) of the selected FGD1 (a) and FGD2 (b) muon candidates broken down by true particle type.

they enter one of the downstream TPCs they are also required to satisfy the TPC quality cut. Tracks that pass those criteria are subjected to TPC PID cuts. In the case of positive tracks, three particle hypotheses are considered: pion, positron and proton. For negative tracks only the pion and electron hypotheses are considered. To identify pions in the TPC, pulls assuming these different particle hypotheses are calculated, and the following cuts on the likelihoods are applied:

$$\mathscr{L}_{\mathrm{MIP}} = \frac{\mathscr{L}_\mu + \mathscr{L}_\pi}{1 - \mathscr{L}_p} > 0.8 \quad \text{if} \quad p < 500\,\mathrm{MeV}/c \tag{3.5}$$

$$\mathscr{L}_\pi > 0.3 \tag{3.6}$$

Neutral pions can only be identified in the TPCs if one or both of their decay photons pair-produces. The presence of positrons and electrons from this process, identified by requiring that the likelihood given in Eq. (3.2) is largest for positrons and electrons, is used to infer the presence of a neutral pion. Further details on TPC PID for pion identification can be found in [91].

If a particle does not enter a TPC, information from the FGD can be used to determine whether the track is a pion. It is important to stress that this is possible only for charged pions, since electrons and positrons are not distinguished in the FGDs, preventing the identification of neutral pions. Here two methods of pion identification are considered depending on the momentum of the pion. A pion whose momentum is too low to be reconstructed as an FGD track can be identified using Michel electron tagging. Michel electrons are those produced as the result of two sequential decay processes: charged pions first decay to muons, and these subsequently decay to electrons. As the time difference between the pion and the electron is dominated by the muon lifetime, these Michel electrons can be identified via signals in the FGD that occur outside the beam time window. Such signals must have at least 7 hits in FGD1 or 6 hits in FGD2. If a Michel electron is tagged, it is more likely generated by a positively charged pion since negatively charged pions are more likely to be absorbed. For higher momentum pions, a pion pull is defined in order to identify charged pions based on the energy deposited by the particle as a function of track length. This method provides a discrimination between protons,

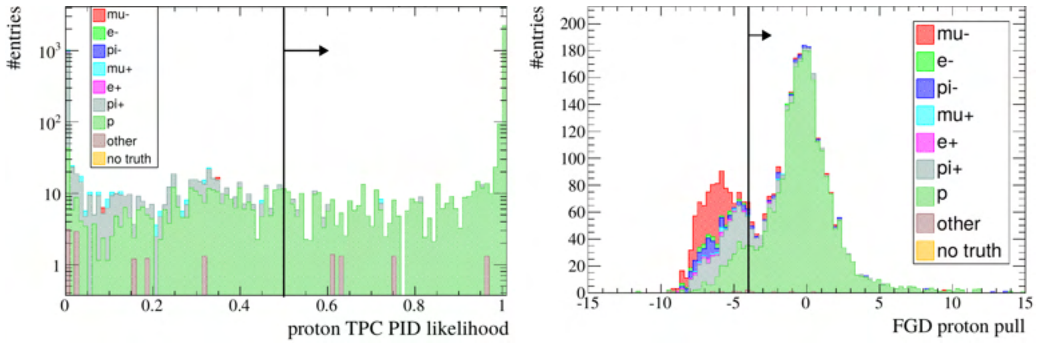

Figure 3.2: Proton likelihood for TPC-matched tracks (left) and proton pull for isoFGD tracks (right) for a selection of tracks in the development of the proton selection [92]. Arrows at the cut values show which tracks would be selected.

muons and pions for tracks which start and stop inside an FGD and are in the same time bunch as the muon candidate. In this case, to be tagged as a pion, its pull must be $-2 < \text{Pull}_\pi^{\text{FGD}} < 2.5$.

3.4 Proton Tagging

Proton candidates are selected from tracks which originate in the same FGD as the muon candidate and haven't been categorised as muons or pions by the cuts described in Sections 3.2 and 3.3. Proton candidates with a TPC component must have $\mathscr{L}_p > 0.5$, where $\mathscr{L}_p$ is given in Eq. (3.2). Tracks contained within the FGD (isoFGD tracks) with $Pull_p^{FGD} > -4$ are assigned as protons, where:

$$\text{Pull}_i^{\text{FGD}} = \frac{E_{\text{measured}} - E_i(L_{\text{measured}})}{\sigma_{E_i(L_{\text{measured}})}}. \tag{3.7}$$

Distributions of $\text{Pull}_p^{\text{FGD}}$ and $\mathscr{L}_p^{\text{TPC}}$ are shown in Fig. 3.2. The cut values used in the selection stated here are based on previous cross section studies which used proton based selections [92]. The overall purity of the selected proton candidates is greater than 90%.

Events in the CC0π sample that have no reconstructed proton candidate are categorised as CC0π0p events, while those with at least one TPC- or isoFGD-matched protons are categorised as CC0πNp events. Most of the CC0π events have no reconstructed protons, meaning more events are assigned to CC0π0p than CC0πNp.

Signal Channel	**Proportion**
$\pi^0 \rightarrow \gamma + \gamma$	84.07%
$\eta \rightarrow \gamma + \gamma$	5.09%
$\eta \rightarrow \pi^0 + X \rightarrow \gamma + \gamma + X$	8.62%
$K \rightarrow \pi^0 + X \rightarrow \gamma + \gamma + X$	1.91%
$\Lambda \rightarrow \pi^0 + X \rightarrow \gamma + \gamma + X$	0.31%

Table 3.3: The proportion of true signal photons that convert in the ECal from each of the five signal channels.

3.5 Photon Selection

Neutral pions almost always decay to two photons (the branching fraction of this decay is $\sim 99\%$ [93]) and in ND280 these photons can either pair produce and be detected in the TPC, or could convert in the ECals. The selection of neutral pions by identifying electrons and positrons from pair production is discussed in Section 3.3. For the oscillation analysis presented in this thesis, a selection of photons converting in the ECal is introduced, which is combined with the TPC π^0 tag to produce a new CC-Photon sample. Though most photons converting in the ECal come from neutral pion decays, other signal channels are also considered. The following five decays are considered signal channels for the CC-Photon sample:

- $\pi^0 \rightarrow \gamma + \gamma$
- $\eta \rightarrow \gamma + \gamma$
- $\eta \rightarrow \pi^0 + X \rightarrow \gamma + \gamma + X$
- $K \rightarrow \pi^0 + X \rightarrow \gamma + \gamma + X$
- $\Lambda \rightarrow \pi^0 + X \rightarrow \gamma + \gamma + X$

where X can be a variety of particles depending on the specific decay. The proportion of photons converting in the ECal in CC events that are produced by each channel is given in Table 3.3. In terms of the underlying interaction modes, about 68% of true CC-Photon events come from DIS interactions, while the other 32% come from resonant interactions. An example of a signal event is shown in Fig. 3.3.

To select photons, isolated objects in the ECal, i.e. those not associated with TPC or FGD tracks, are considered. These objects must meet two criteria to be

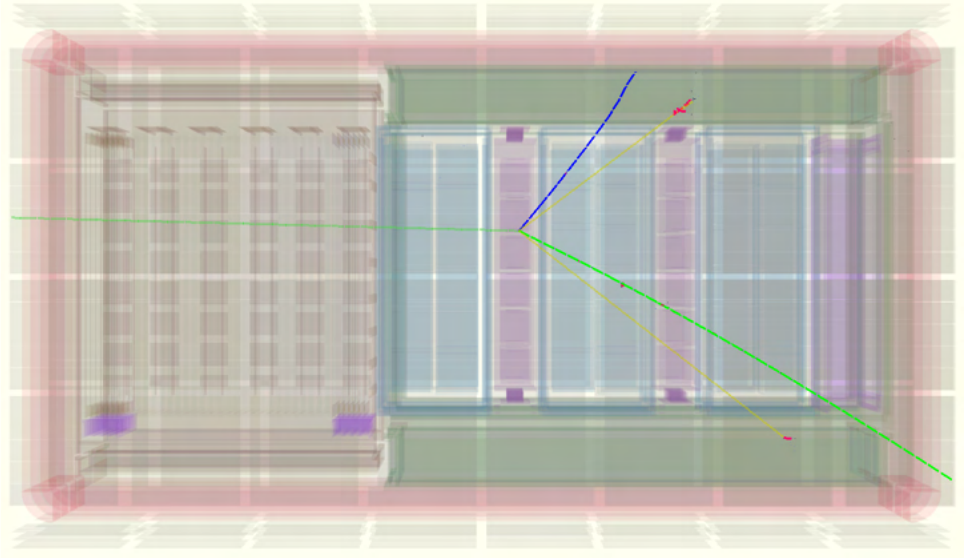

Figure 3.3: A signal event in the photon selection. The solid lime green line represents a muon, the solid blue line represents a proton, and the two dashed yellow lines represent photons produced in a π^0 decay close to the vertex in FGD1. Both photons shower in the barrel ECal - the red tracks are e^+/e^- in the shower. The incoming ν_μ is shown as a dashed dark green line.

tagged as photons, which are described in detail below.

3.5.1 ECal Particle Identification (PID)

Firstly, ECal PID is used to determine whether an isolated ECal object is electromagnetic-like, using a variable known as PIDEmHip. This variable is designed to discriminate $e^\pm/\gamma$ from highly ionising particles such as protons. For each isolated ECal object, several low level variables are computed and used as inputs to the ECal PID. The inputs to the algorithm used in this analysis were:

Circularity gives a measure of how round a cluster is. This separates short-and-wide electromagnetic-shower-like clusters from long-and-narrow track-like clusters.

QRMS is the standard deviation of the hit charges in the cluster. This is divided by the mean of the hit charges to produce a dimensionless quantity that is independent of the overall charge scale. EM showers tend to have larger QRMS values when compared with minimally ionising particles (MIP) such as muons.

Truncated Max Ratio is the ratio of the charge deposited in the ECal layers with the highest and lowest total charge. Before the charge per layer is computed, the highest and lowest charge hits are removed to reduce sensitivity to noise and saturated channels.

Front Back Ratio is a measure of the dE/dx along a track. It is defined as the total charge in the back quarter divided by the total charge in the front quarter. The front and back quarters are defined as the 25% of hits closest to and furthest from the start-point of the object. This ratio is sensitive to the dE/dx profile of stopping tracks, but also discriminates electrons from muons as showers tend to deposit most of their charge at the front end of a cluster.

Single particle MC simulations are used to generate probability density functions (PDFs) for each particle type and variable, and a combined likelihood is formed from the product of the PDFs. The variable PIDEmHip is defined as the log-likelihood ratio of the proton and electron hypotheses. More detail on ECal PID algorithms at ND280 can be found in [94].

Distributions of PIDEmHip for the barrel and downstream ECals can be found in Fig. 3.4. Electromagnetic showers typically produce values of PIDEmHip < 0, so a cut is placed here in the selection of photons. A difference in the number of isolated ECal objects is observed between data and MC; it is expected that this is caused by pile-up interactions occurring in the ECal. A discussion of ECal pile-up can be found in Section 4.2.4 in relation to systematics, where it is found that there is indeed more pile-up in the ECal in data than in MC. Since the majority of neutrino interactions at ND280 are CCQE interactions, which produce only muons (and protons), the data-MC difference is larger for positive values of PIDEmHip.

3.5.2 Pile-Up in the ECal

Although the interactions of interest for this analysis occur in the FGD, neutrinos can interact in any of the ND280 subdetectors. When these interactions occur in the ECal, in coincidence with an FGD interaction, they can produce objects that are considered to be a background in this analysis. The second criterion an isolated ECal object must meet to be tagged as a photon is on the variable MostUpStreamLayerHit, which aims to reject these pile-up interactions. This variable represents the ECal layer closest to the tracking region with charge deposit from the isolated

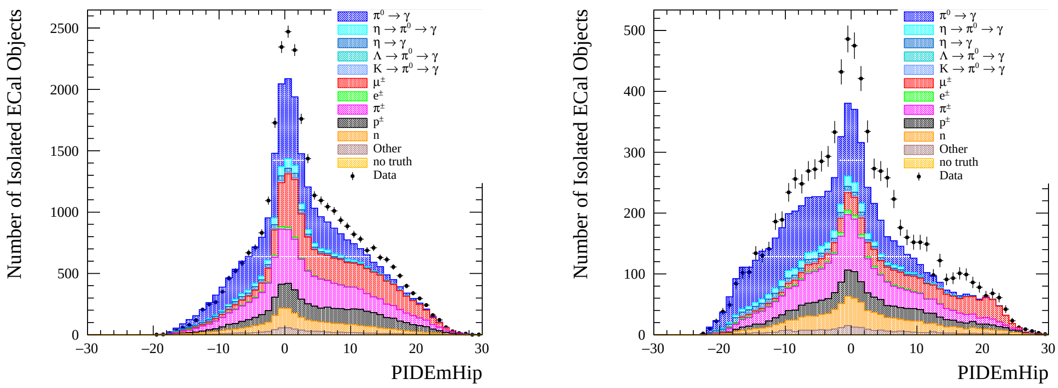

(a) Barrel ECal (b) Downstream ECal

Figure 3.4: Distributions of PIDEmHip in the barrel (a) and downstream (b) ECals. Objects produced by photon signal channels are shown in shades of blue. A cut of PIDEmHip < 0 is applied to select these objects.

object. As described in Section 2.3.4, the ND280 ECal modules are made of alternating lead and plastic scintillator layers. Each of the lead layers in the barrel and downstream ECal modules is one radiation length thick, meaning photons coming from the tracking region are most likely to shower in the first layers of the ECals. Objects in the outer layers are more likely to be from pile-up, where a second neutrino interaction occurs in the ECal. This pile-up becomes more likely with increasing beam power.

Distributions of MostUpStreamLayerHit for the barrel and downstream ECals can be found in Fig. 3.5. To reject objects from pile-up interactions in the outer layers, it is required that the isolated ECal object has MostUpStreamLayerHit < 6.

3.5.3 Photon Selection Results

Events with an ECal-tagged photon and/or a TPC-tagged π^0 (see Section 3.3) are categorised as CC-Photon events. The topology breakdown of the resulting sample is shown in Fig. 3.6. These true topologies are defined by the meson content of the final state: CC0π events contain no mesons in the final state, CC1π^+ contain a single positive pion and no other mesons in the final state, CC-Photon events contain at least one of the meson decays listed above, and the CC-Other category encompasses all other selected CC events. The FGD1 CC-Photon sample has an efficiency of 43.0±0.1% and a purity of 53.9±0.2%. The FGD2 sample has an

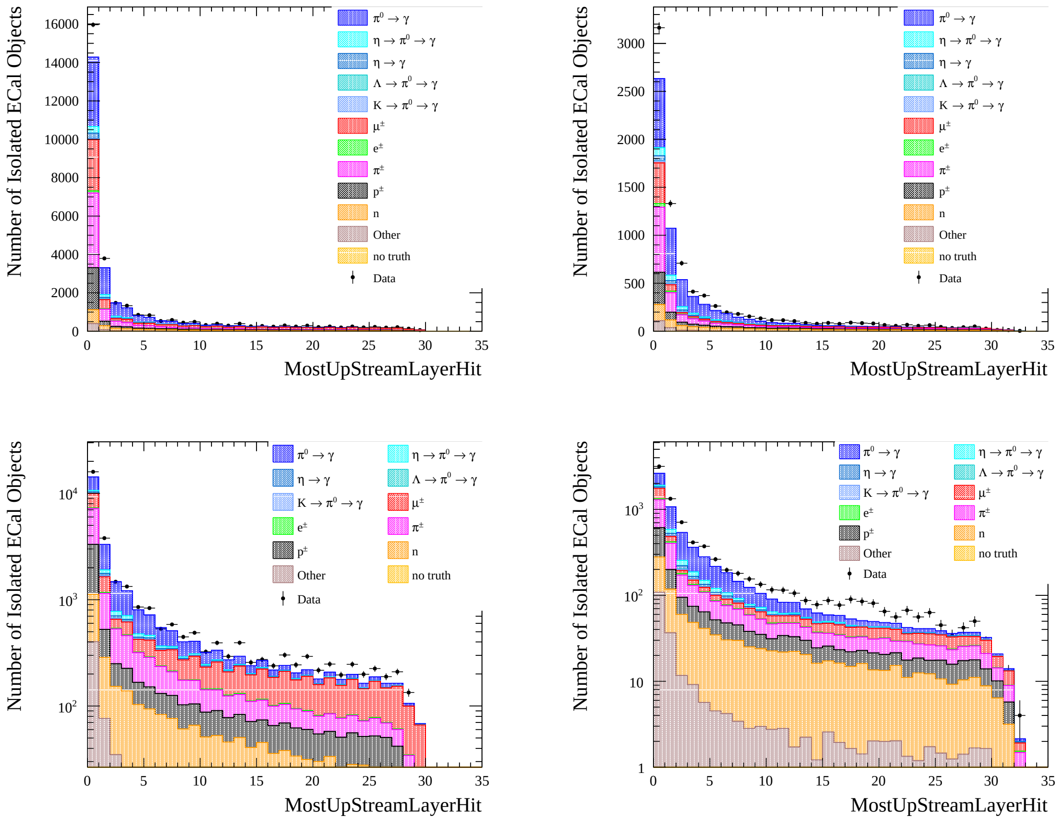

(a) Barrel ECal

(b) Downstream ECal

Figure 3.5: Distributions of MostUpStreamLayerHit in the barrel (a) and downstream (b) ECals shown on linear (top) and logarithmic (bottom) axes. Objects produced by photon signal channels are shown in shades of blue. A cut of MostUpStreamLayerHit < 6 is applied to select these objects.

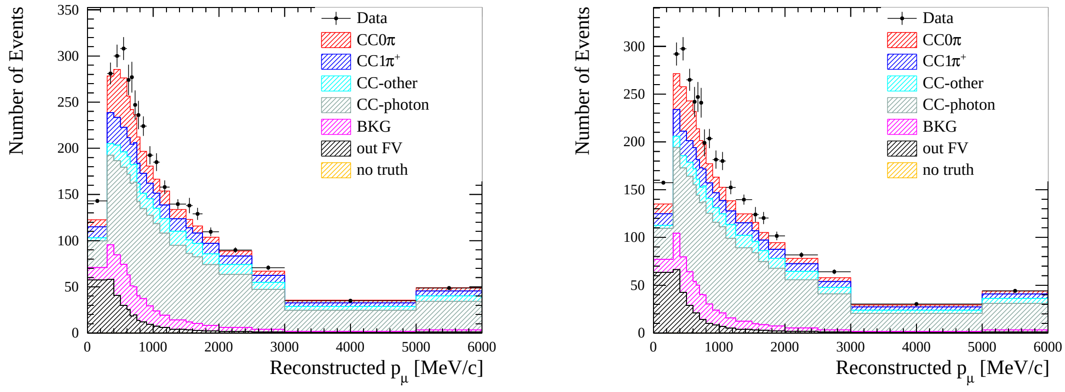

(a) FGD1

(b) FGD2

Figure 3.6: Reconstructed momentum of muon candidates in the CC-Photon sample for the FGD1 (a) and FGD2 (b) selections, showing the true topology breakdown of the MC.

Sample	**Efficiency**	**Efficiency Change**	**Purity**	**Purity Change**
FGD1 CC0π	46.86%	-1.14%	76.3%	+5.04%
FGD2 CC0π	47.47%	-0.53%	72.8%	+4.62%
FGD1 CC1π^+	27.06%	-1.94%	60.2%	+7.75%
FGD2 CC1π^+	23.03%	-0.97%	58.5%	+7.25%

Table 3.4: CC0π and CC1π^+ efficiencies and purities with photon rejection, and differences with respect to the previous analysis [45, 80].

efficiency of 43.9±0.1% and a purity of 54.2±0.2%.

The photon tag is applied before events are categorised into the CC0π and CC1π^+ samples, therefore removing photon-containing events and increasing the purities of those samples. For example, the event shown in Fig. 3.3 would have previously been in the CC0π sample. Table 3.4 shows the efficiencies and purities for these new samples and the previous selection described in [45, 80]. The photon tag increases the purity of the CC0π and CC1π^+ samples by ~5-7% at a minimal cost to efficiency.

3.6 Categorising Near Detector Events

The above selections of pions, protons and photons are combined with the inclusive muon selection to produce five samples each for FGD1 and FGD2:

CC0π0p: Events containing no reconstructed protons, pions or photons.

CC0πNp: Events containing no reconstructed pions or photons and one or more reconstructed protons.

CC1π^+: Events containing only one reconstructed pion which is positively charged, and no reconstructed photons.

CC-Photon: Events containing one or more reconstructed photons or neutral pions.

CC-Other: Events containing no reconstructed photons or neutral pions, with more than one postively charged pion and/or any number of negatively charged pions.

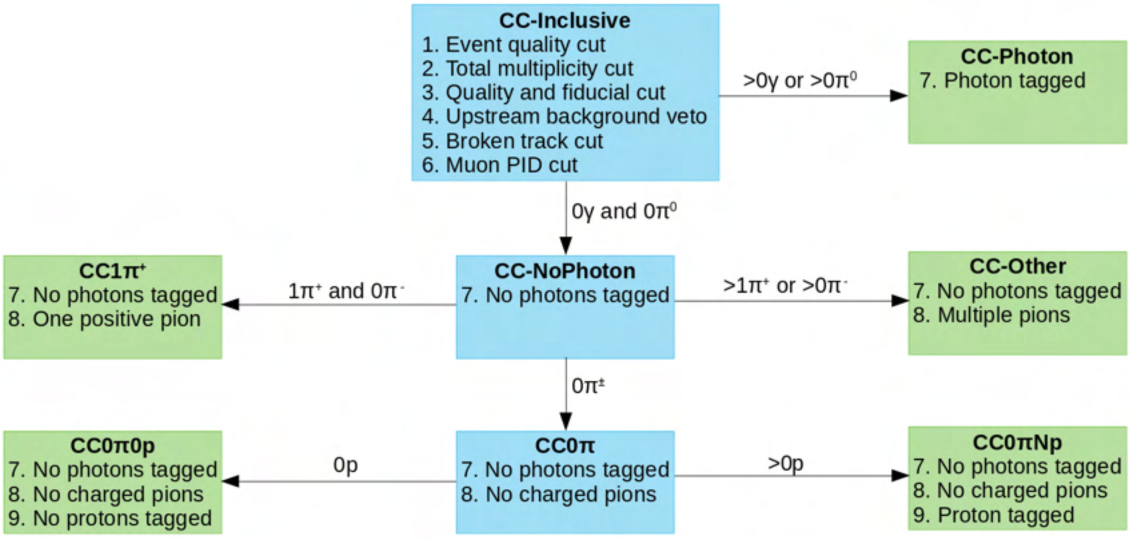

Figure 3.7: Selection flow diagram. First a CC-Inclusive sample is selected, and then is split into five samples: CC0π0p, CC0πNp, CC1π^+, CC-Photon and CC-Other. The selection is applied in both FGD1 and FGD2, giving a total of 10 samples in FHC. The corresponding selection cuts are shown in each box, with green boxes representing the final samples and blue boxes showing intermediate stages in the selection.

A flow diagram of the cuts applied to each sample is shown in Fig. 3.7. In this section, the results of these selections are discussed. Data and MC distributions of the reconstructed muon momentum and cosine of the scattering angle ($\cos\theta_\mu$), defined as the angle between the outgoing muon and the beam direction, are compared. The reconstructed muon momentum and $\cos\theta_\mu$ are presented using the same binning as used in the near detector fit, which is discussed in Chapter 5.

In Figs. 3.8 and 3.9 the MC in each FGD1 sample is broken down by true topology: CC0π, CC1π^+, CC-Photon and CC-Other. Equivalent plots for the FGD2 samples are presented in Figs. 3.10 and 3.11. CC0π events contain no mesons in the final state, CC1π^+ contain a single positive pion and no other mesons in the final state, CC-Photon events contain at least one of the meson decays listed in Section 3.5, and the CC-Other category encompasses all other selected CC events. The BKG category indicates background coming from NC, $\bar{\nu}_\mu$ CC or ν_e CC interactions, and OOFV labels events with true neutrino interaction vertices outside of the FGD1 (FGD2) FV. Table 3.5 shows the true topology content of each sample.

The contribution of different types of interactions to each FGD1 sample according to NEUT is shown in Figs. 3.12 and 3.13. Equivalent plots for the FGD2 samples are shown in Figs. 3.14 and 3.15. More details of the composition in terms of true

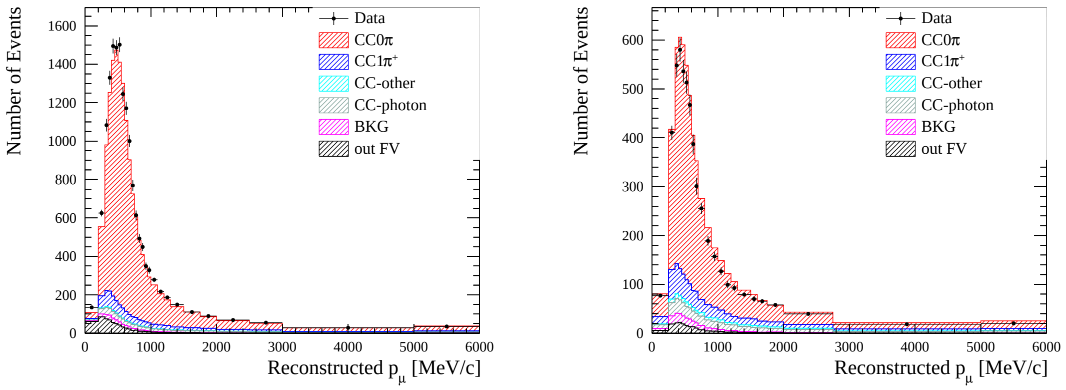

(a) CC0π0p (b) CC0πNp

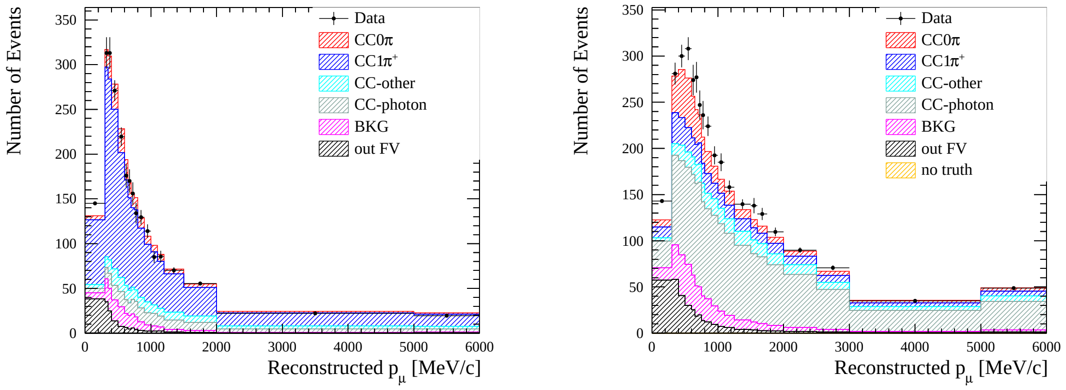

(c) CC1π^+ (d) CC-Photon

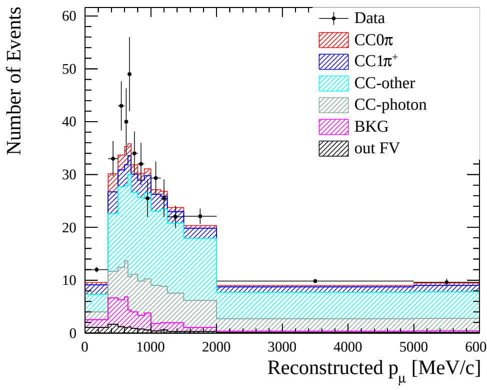

(e) CC-Other

Figure 3.8: Reconstructed muon momentum distributions for ν_μ CC0π0p (a), CC0πNp (b), CC1π^+ (c), CC-Photon (d) and CC-Other (e) samples in FGD1. Colours show contributions from different true topologies based on true MC information. The last bin in momentum includes all events with p_μ greater than 5000 MeV/c.

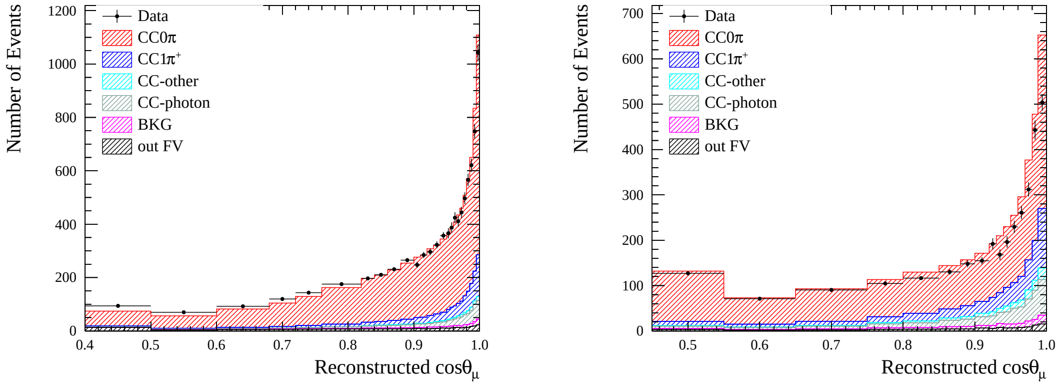

(a) CC0π0p (b) CC0πNp

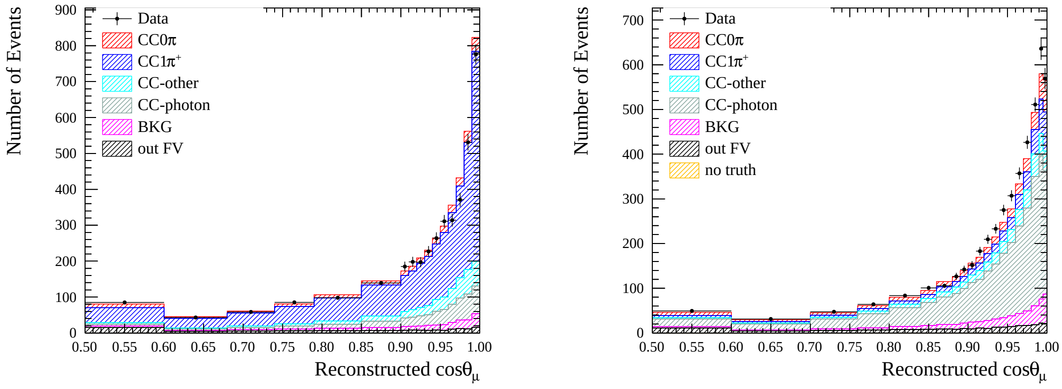

(c) CC1π^+ (d) CC-Photon

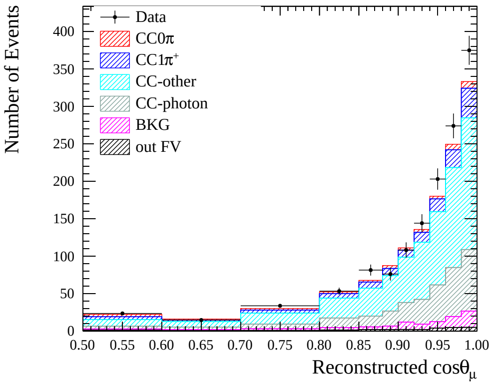

(e) CC-Other

Figure 3.9: Reconstructed muon $\cos\theta$ distributions for ν_μ CC0π0p (a), CC0πNp (b), CC1π^+ (c), CC-Photon (d) and CC-Other (e) samples in FGD1. Colours show contributions from different true topologies based on true MC information. The first bin in $\cos\theta_\mu$ includes all events with $\cos\theta_\mu$ below 0.6.

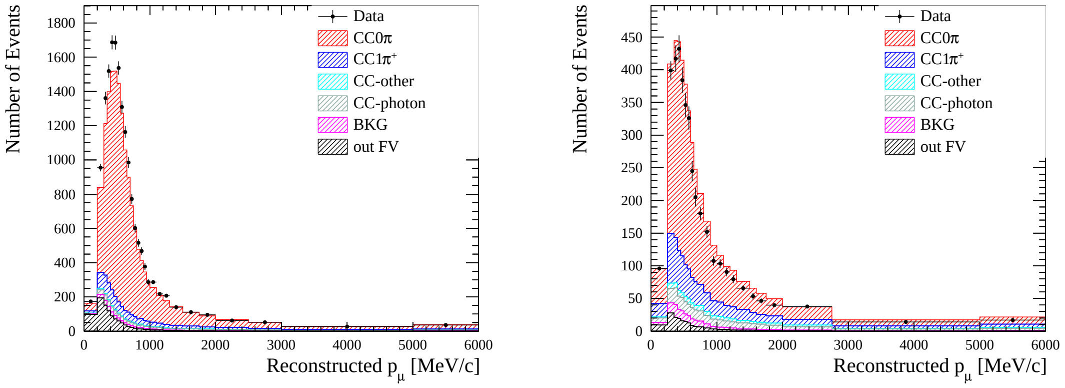

(a) CC0π0p (b) CC0πNp

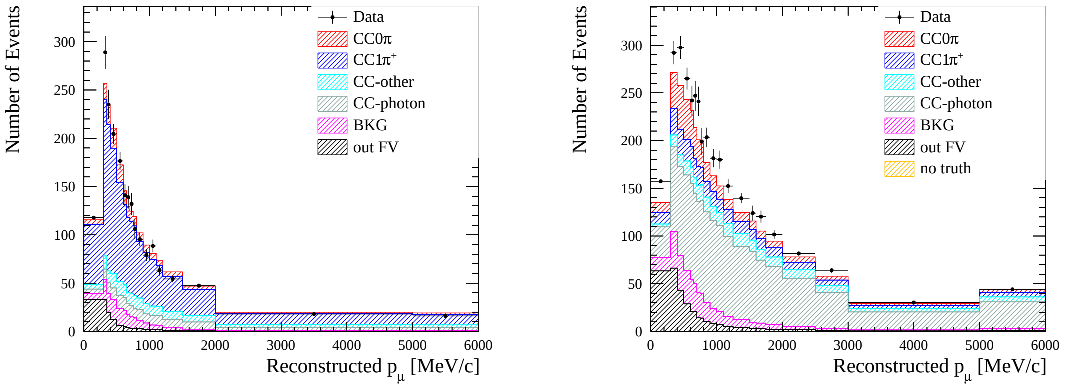

(c) CC1π^+ (d) CC-Photon

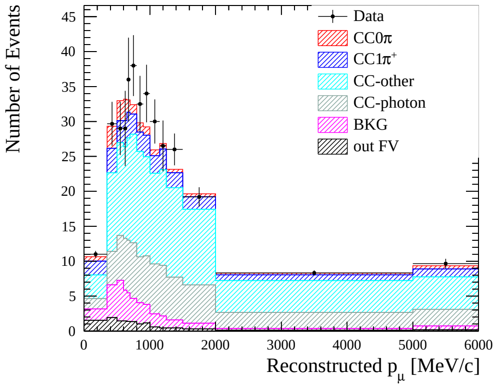

(e) CC-Other

Figure 3.10: Reconstructed muon momentum distributions for ν_μ CC0π0p (a), CC0πNp (b), CC1π^+ (c), CC-Photon (d) and CC-Other (e) samples in FGD2. Colours show contributions from different true topologies based on true MC information. The last bin in momentum includes all events with p_μ greater than 5000 MeV/c.

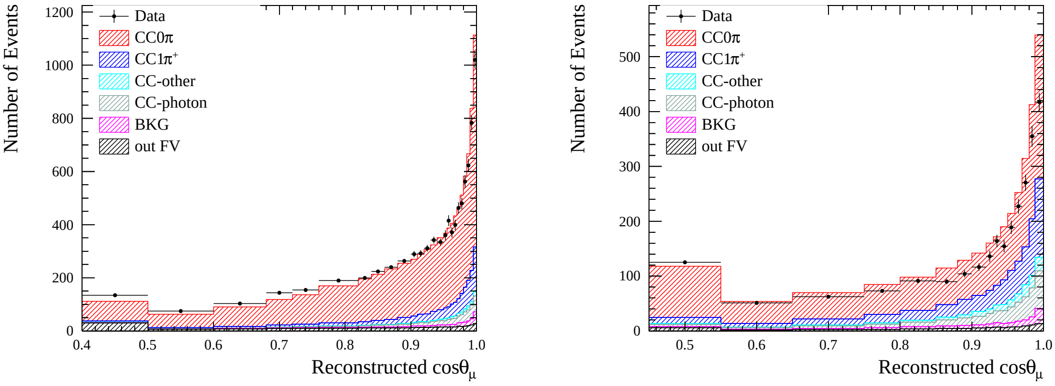

(a) CC0π0p (b) CC0πNp

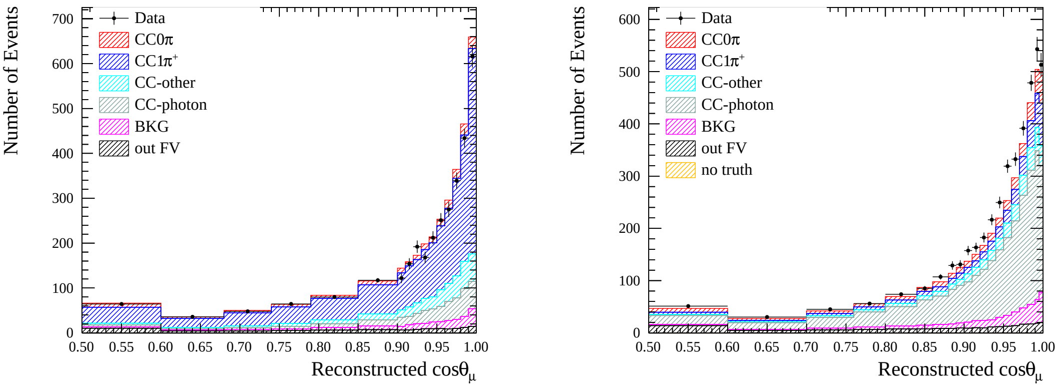

(c) CC1π^+ (d) CC-Photon

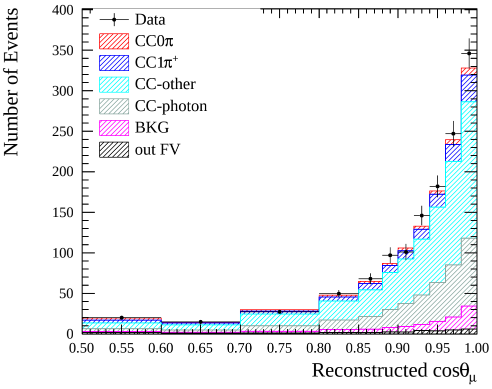

(e) CC-Other

Figure 3.11: Reconstructed muon $\cos\theta$ distributions for ν_μ CC0π0p (a), CC0πNp (b), CC1π^+ (c), CC-Photon (d) and CC-Other (e) samples in FGD2. Colours show contributions from different true topologies based on true MC information. The first bin in $\cos\theta_\mu$ includes all events with $\cos\theta_\mu$ below 0.6.

Sample	**Topology**	**True Composition (%)**	
		FGD1	FGD2
CC0π0p	CC0π	79.65	76.92
	CC1π^+	8.16	8.85
	CC-Photon	4.44	3.55
	CC-Other	1.04	1.15
	BKG	1.58	1.87
	OOFV	4.85	7.53
	Sand μ	0.28	0.14
CC0πNp	CC0π	69.60	62.03
	CC1π^+	13.22	18.31
	CC-Photon	8.58	8.81
	CC-Other	3.01	3.74
	BKG	2.79	3.45
	OOFV	2.75	3.61
	Sand μ	0.05	0.05
CC1π^+	CC0π	7.29	7.33
	CC1π^+	60.24	58.46
	CC-Photon	11.07	10.79
	CC-Other	9.51	10.79
	BKG	5.45	6.22
	OOFV	6.10	6.34
	Sand μ	0.34	0.08
CC-Photon	CC0π	9.33	9.13
	CC1π^+	10.36	9.97
	CC-Photon	53.88	54.21
	CC-Other	9.52	9.00
	BKG	8.56	8.24
	OOFV	8.27	9.39
	Sand μ	0.08	0.06
CC-Other	CC0π	4.23	4.09
	CC1π^+	11.19	10.50
	CC-Photon	23.82	25.07
	CC-Other	52.15	50.28
	BKG	6.25	7.11
	OOFV	2.27	2.93
	Sand μ	0.09	0.02

Table 3.5: True composition (in %) in terms of topology for each sample in the FGD1 and FGD2 selections.

interaction for each of the samples are shown in Table 3.6. Only events from ν_μ interactions are broken down by channel; events from $\bar{\nu}_\mu$ and $\nu_e, \bar{\nu}_e$ interactions are grouped. As expected, the CC0π samples are dominated by CCQE scattering, with a contribution from two-particle two-hole (2p2h) interactions. The background in this selection is rich in resonant pion production (RES) events where the pion has either not exited the nucleus or has not been reconstructed in the detector. The CC1π^+ sample is abundant in RES interactions, with DIS being the largest background. The CC-Photon sample is dominated by DIS interactions, with significant contribution from resonant π^0 production also. There is some CCQE background in this sample, arising mostly from pile-up in the ECal and broken tracks. The CC-Other sample is also dominated by DIS interactions.

The FGD1 MC samples are broken down by true particle type of the muon candidate in Figs. 3.16 and 3.17. Equivalent plots are shown in Figs. 3.18 and 3.19 for the FGD2 samples. Table 3.7 shows the true identities of the selected muon candidates in the five samples. The majority of misidentified negatively charged muons are negatively charged pions. This is due to PID variables being based on the energy loss observed in the TPCs, which is similar for muons and pions. Therefore when a negative pion is produced with more momentum than the muon in a ν_μ interaction, it is often incorrectly selected as the muon candidate.

The efficiency and purity for each FGD1 sample as a function of the true muon momentum and $\cos\theta_\mu$ is shown in Figs. 3.20 and 3.21. Equivalent plots for the FGD2 samples are shown in Figs. 3.22 and 3.23. The efficiency is defined as the number of selected true events in a given topology divided by the total number of generated events in the FGD fiducial volume that correspond to the same topology. The purity is defined as the number of selected true events in a given topology divided by the total number of selected events. Mathematically, this is:

$$\begin{aligned} \text{efficiency} &= \frac{\text{number of selected signal events}}{\text{number of generated signal events}}, \\ \text{purity} &= \frac{\text{number of selected signal events}}{\text{number of selected events}}. \end{aligned} \tag{3.8}$$

Table 3.8 reports the integrated efficiency and purity of each sample in both FGD1 and FGD2.

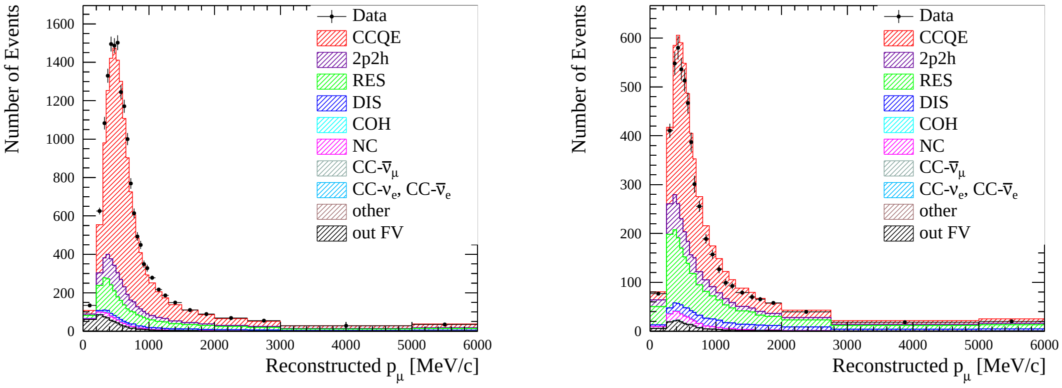

(a) CC0π0p (b) CC0πNp

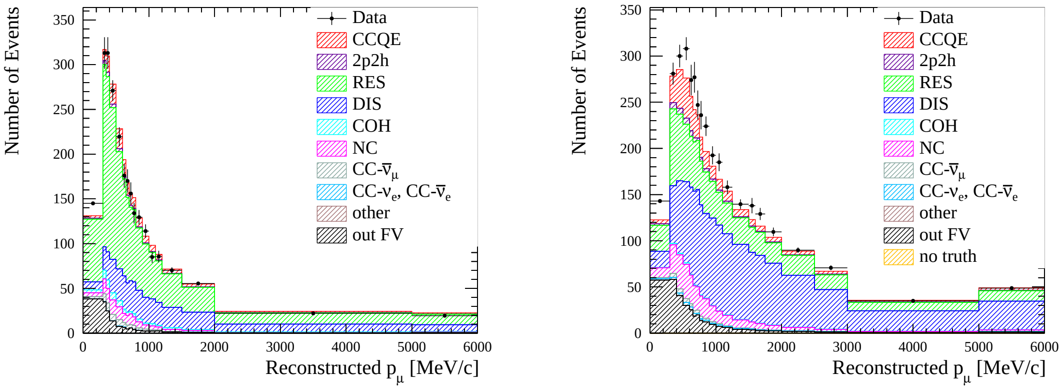

(c) CC1π^+ (d) CC-Photon

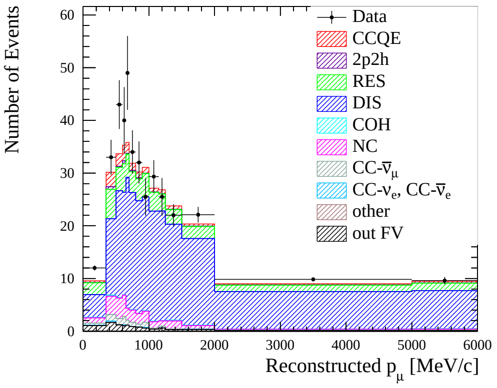

(e) CC-Other

Figure 3.12: Reconstructed muon momentum distributions for ν_μ CC0π0p (a), CC0πNp (b), CC1π^+ (c), CC-Photon (d) and CC-Other (e) samples in FGD1. Colours show contributions from different true interaction modes based on true MC information. The last bin in momentum includes all events with p_μ greater than 5000 MeV/c.

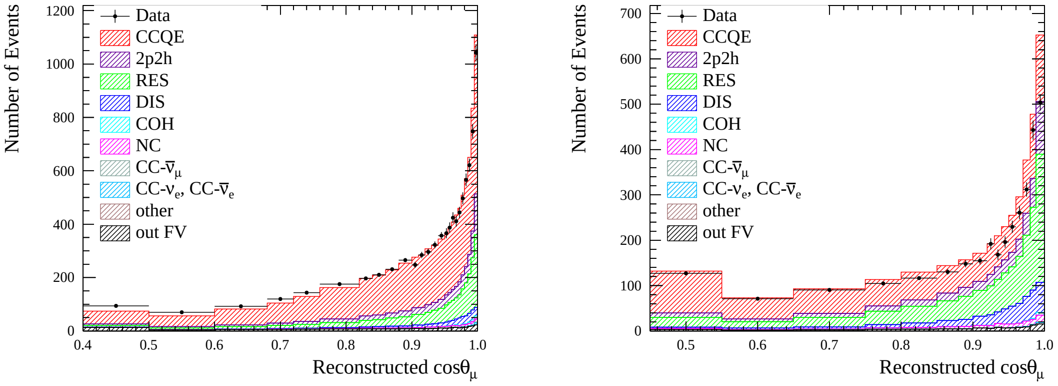

(a) CC0π0p (b) CC0πNp

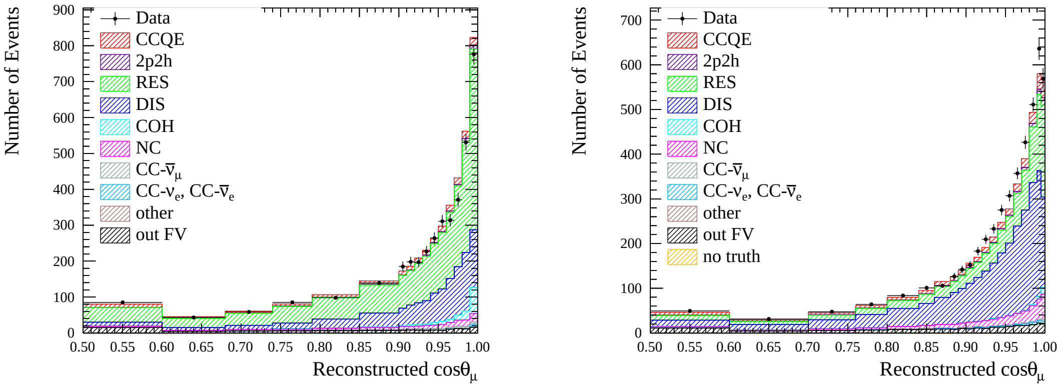

(c) CC1π^+ (d) CC-Photon

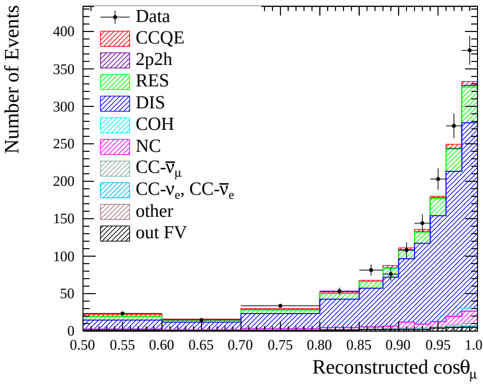

(e) CC-Other

Figure 3.13: Reconstructed muon $\cos\theta$ distributions for ν_μ CC0π0p (a), CC0πNp (b), CC1π^+ (c), CC-Photon (d) and CC-Other (e) samples in FGD1. Colours show contributions from different true interaction modes based on true MC information. The first bin in $\cos\theta_\mu$ includes all events with $\cos\theta_\mu$ below 0.6.

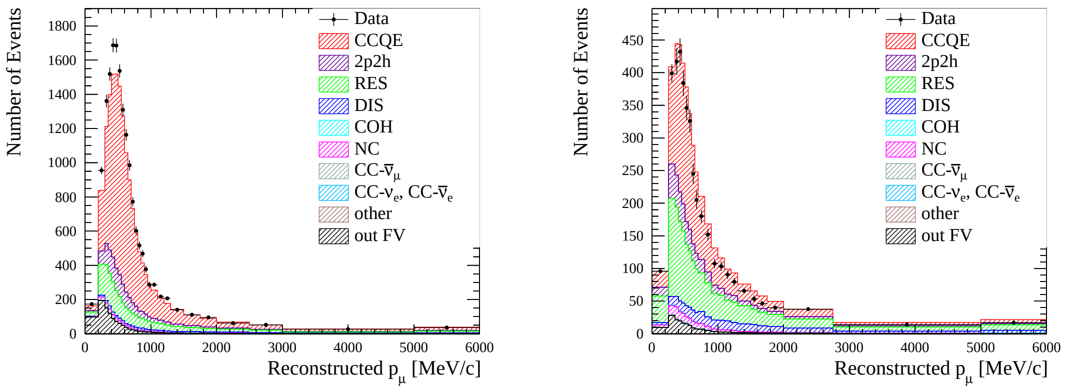

(a) CC0π0p (b) CC0πNp

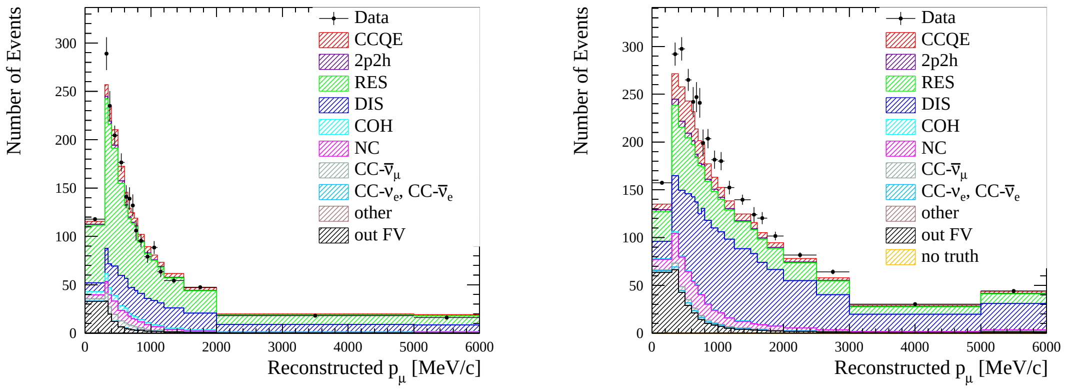

(c) CC1π^+ (d) CC-Photon

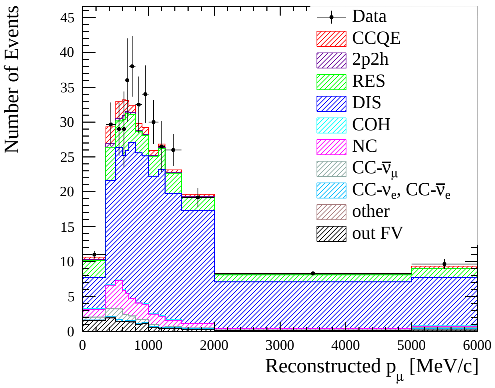

(e) CC-Other

Figure 3.14: Reconstructed muon momentum distributions for ν_μ CC0π0p (a), CC0πNp (b), CC1π^+ (c), CC-Photon (d) and CC-Other (e) samples in FGD2. Colours show contributions from different true interaction modes based on true MC information. The last bin in momentum includes all events with p_μ greater than 5000 MeV/c.

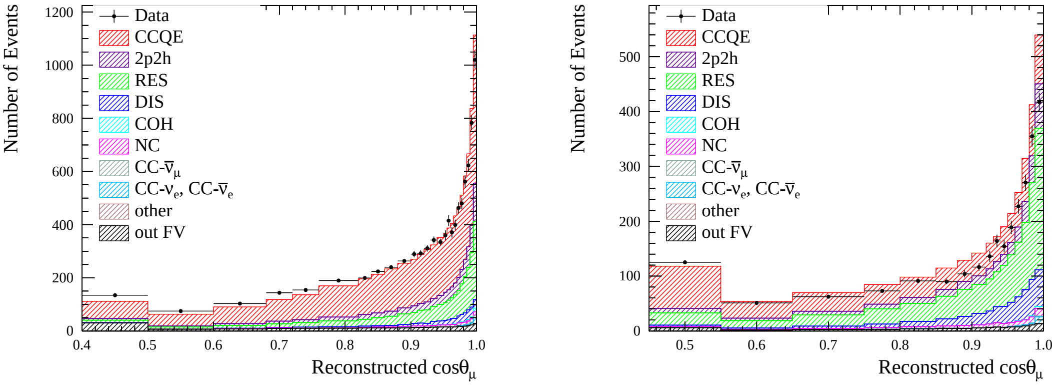

(a) CC0π0p

(b) CC0πNp

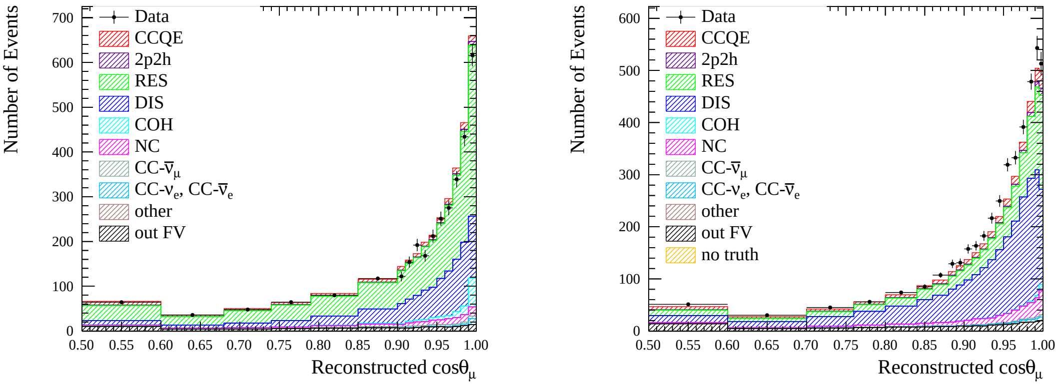

(c) CC1π^+

(d) CC-Photon

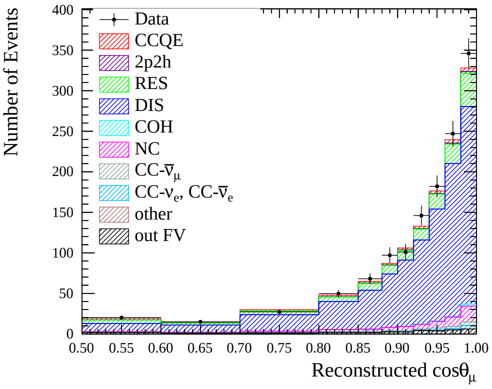

(e) CC-Other

Figure 3.15: Reconstructed muon $\cos\theta$ distributions for ν_μ CC0π0p (a), CC0πNp (b), CC1π^+ (c), CC-Photon (d) and CC-Other (e) samples in FGD2. Colours show contributions from different true interaction modes based on true MC information. The first bin in $\cos\theta_\mu$ includes all events with $\cos\theta_\mu$ below 0.6.

Sample	**Interaction Mode**	**True Composition(%)**	
		FGD1	FGD2
CC0π0p	CCQE	66.42	62.88
	2p2h	9.20	9.00
	RES	14.70	15.62
	DIS	2.74	2.74
	COH	0.23	0.23
	NC	1.31	1.41
	$\bar{\nu}_\mu$	0.15	0.19
	$\nu_e, \bar{\nu}_e$	0.11	0.27
	OOFV	4.85	7.53
	Sand μ	0.28	0.14
CC0πNp	CCQE	46.76	39.55
	2p2h	11.26	10.28
	RES	28.24	33.11
	DIS	7.97	9.75
	COH	0.18	0.18
	NC	2.53	2.81
	$\bar{\nu}_\mu$	0.14	0.20
	$\nu_e, \bar{\nu}_e$	0.13	0.44
	OOFV	2.75	3.61
	Sand μ	0.05	0.05
CC1π^+	CCQE	5.97	5.72
	2p2h	1.02	0.94
	RES	54.75	52.43
	DIS	23.85	25.61
	COH	2.52	2.64
	NC	3.66	4.02
	$\bar{\nu}_\mu$	1.51	1.65
	$\nu_e, \bar{\nu}_e$	0.28	0.55
	OOFV	6.10	6.34
	Sand μ	0.34	0.08
CC-Photon	CCQE	6.98	6.73
	2p2h	1.36	1.32
	RES	23.38	23.86
	DIS	50.94	50.05
	COH	0.42	0.34
	NC	7.04	6.68
	$\bar{\nu}_\mu$	0.70	0.67
	$\nu_e, \bar{\nu}_e$	0.82	0.89
	OOFV	8.27	9.39
	Sand μ	0.08	0.06
CC-Other	CCQE	3.33	3.04
	2p2h	0.55	0.61
	RES	13.87	12.59
	DIS	73.29	73.39
	COH	0.34	0.29
	NC	4.67	5.13
	$\bar{\nu}_\mu$	1.29	1.35
	$\nu_e, \bar{\nu}_e$	0.29	0.63
	OOFV	2.27	2.93
	Sand μ	0.09	0.02

Table 3.6: True composition (in %) in terms of interaction mode for each sample in the FGD1 and FGD2 selections.

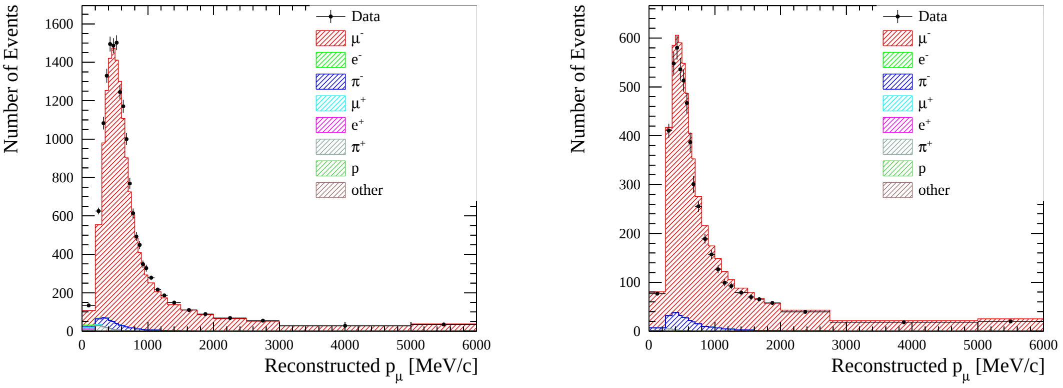

(a) CC0π0p (b) CC0πNp

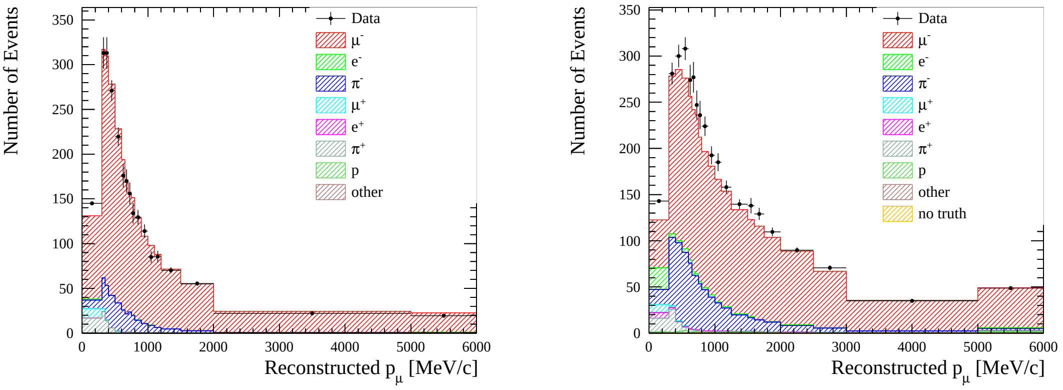

(c) CC1π^+ (d) CC-Photon

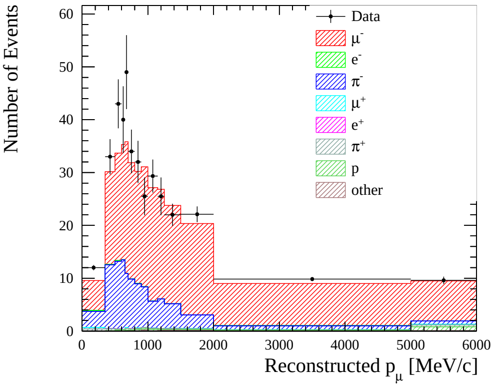

(e) CC-Other

Figure 3.16: Reconstructed muon momentum distributions for ν_μ CC0π0p (a), CC0πNp (b), CC1π^+ (c), CC-Photon (d) and CC-Other (e) samples in FGD1. Colours show contributions from different true particle types of the selected muon candidate based on true MC information. The last bin in momentum includes all events with p_μ greater than 5000 MeV/c.

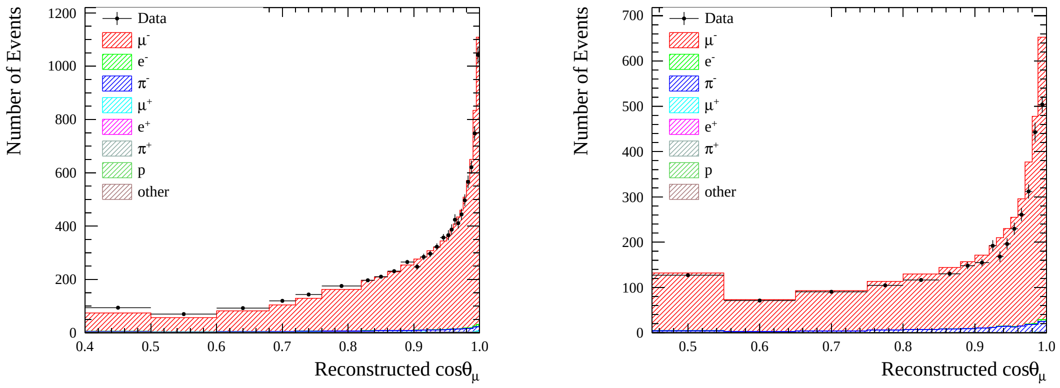

(a) CC0π0p (b) CC0πNp

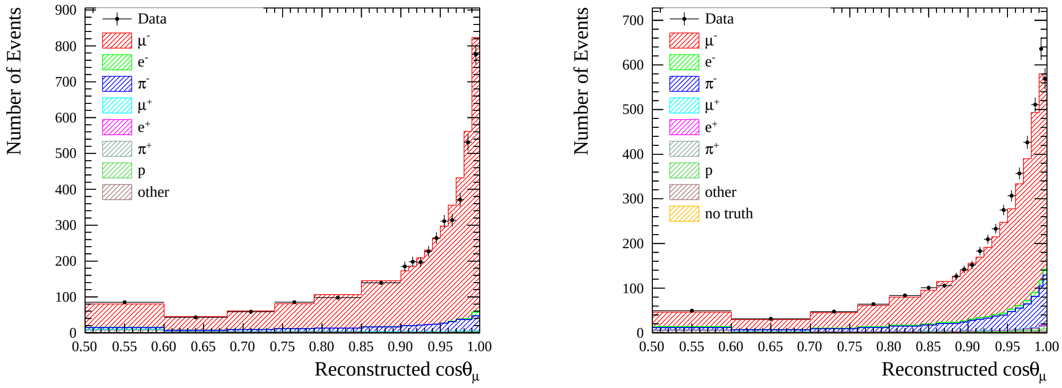

(c) CC1π^+ (d) CC-Photon

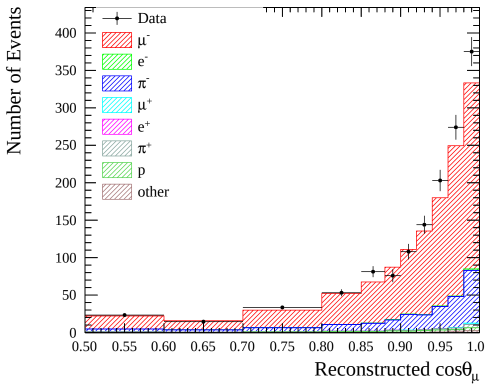

(e) CC-Other

Figure 3.17: Reconstructed muon $\cos\theta$ distributions for ν_μ CC0π0p (a), CC0πNp (b), CC1π^+ (c), CC-Photon (d) and CC-Other (e) samples in FGD1. Colours show contributions from different true particle types of the selected muon candidate based on true MC information. The first bin in $\cos\theta_\mu$ includes all events with $\cos\theta_\mu$ below 0.6.

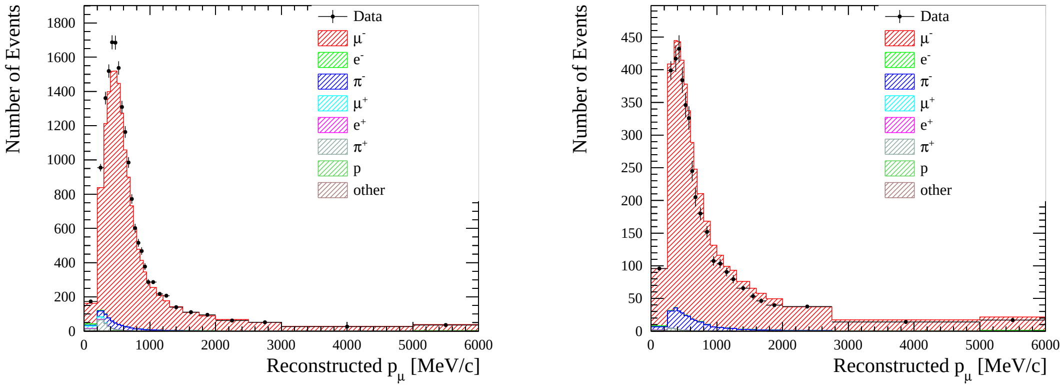

(a) CC0π0p (b) CC0πNp

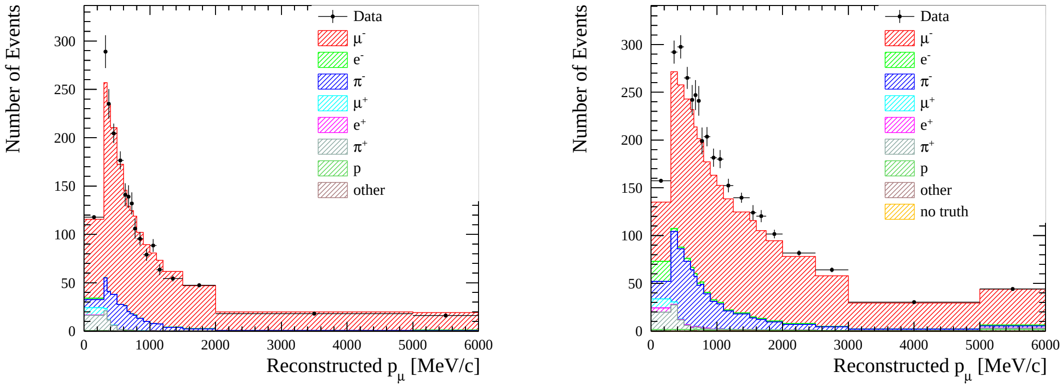

(c) CC1π^+ (d) CC-Photon

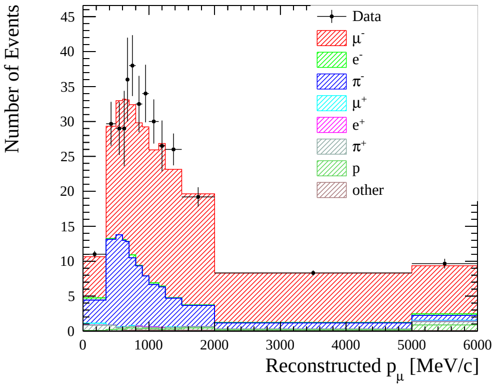

(e) CC-Other

Figure 3.18: Reconstructed muon momentum distributions for ν_μ CC0π0p (a), CC0πNp (b), CC1π^+ (c), CC-Photon (d) and CC-Other (e) samples in FGD2. Colours show contributions from different true particle types of the selected muon candidate based on true MC information. The last bin in momentum includes all events with p_μ greater than 5000 MeV/c.

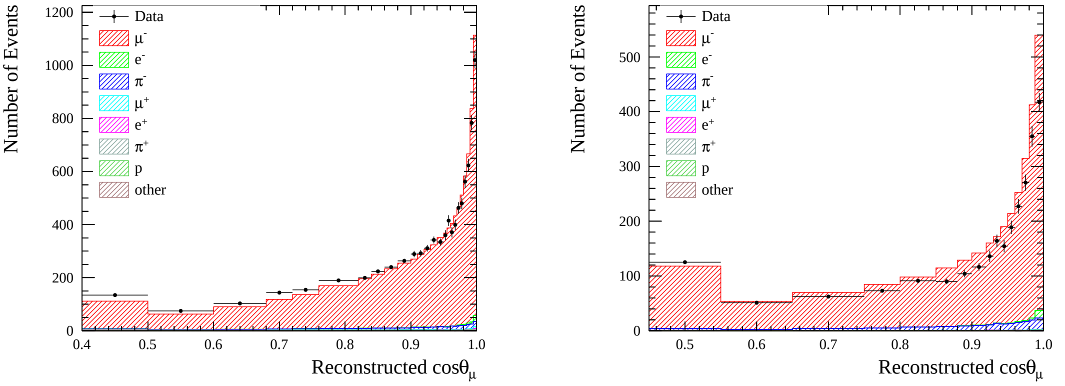

(a) CC0π0p (b) CC0πNp

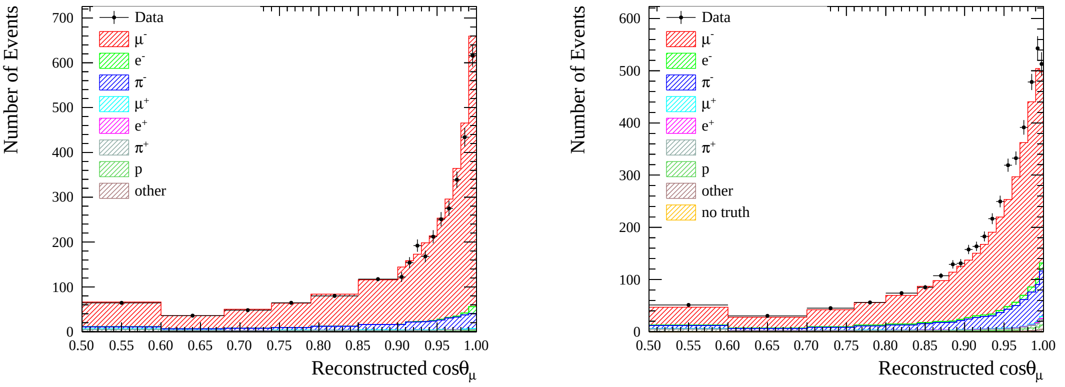

(c) CC1π^+ (d) CC-Photon

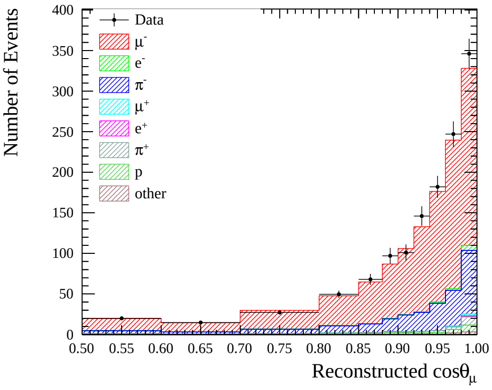

(e) CC-Other

Figure 3.19: Reconstructed muon $\cos\theta$ distributions for ν_μ CC0π0p (a), CC0πNp (b), CC1π^+ (c), CC-Photon (d) and CC-Other (e) samples in FGD2. Colours show contributions from different true particle types of the selected muon candidate based on true MC information. The first bin in $\cos\theta_\mu$ includes all events with $\cos\theta_\mu$ below 0.6.

Sample	**Particle Type**	**True Composition(%)**	
		FGD1	FGD2
CC0π0p	μ^-	95.77	94.87
	e^-	0.37	0.45
	π^-	2.42	2.45
	μ^+	0.32	0.55
	e^+	0.11	0.10
	π^+	0.76	1.32
	p	0.25	0.25
	other	0.00	0.01
	Sand μ	0.00	0.00
CC0πNp	μ^-	95.12	94.11
	e^-	0.18	0.54
	π^-	4.32	4.81
	μ^+	0.03	0.06
	e^+	0.01	0.03
	π^+	0.24	0.32
	p	0.08	0.11
	other	0.01	0.02
	Sand μ	0.00	0.00
CC1π^+	μ^-	88.48	87.13
	e^-	0.36	0.66
	π^-	7.50	8.28
	μ^+	1.13	0.95
	e^+	0.02	0.03
	π^+	2.31	2.66
	p	0.15	0.23
	other	0.04	0.04
	Sand μ	0.00	0.00
CC-Photon	μ^-	78.84	78.63
	e^-	2.29	2.36
	π^-	14.57	14.00
	μ^+	0.62	0.77
	e^+	0.64	0.51
	π^+	2.06	2.57
	p	0.70	0.90
	other	0.27	0.27
	Sand μ	0.00	0.00
CC-Other	μ^-	78.34	74.93
	e^-	0.35	0.85
	π^-	17.58	19.24
	μ^+	0.36	0.41
	e^+	0.05	0.13
	π^+	1.18	1.85
	p	1.73	2.15
	other	0.39	0.45
	Sand μ	0.00	0.00

Table 3.7: True composition (in %) in terms of the particle type of the muon candidate for each sample in the FGD1 and FGD2 selections.

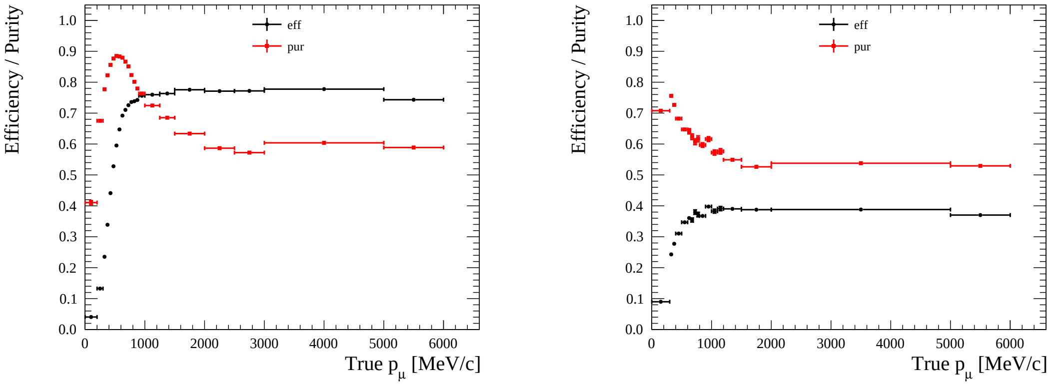

(a) CC0π (b) CC1π^+

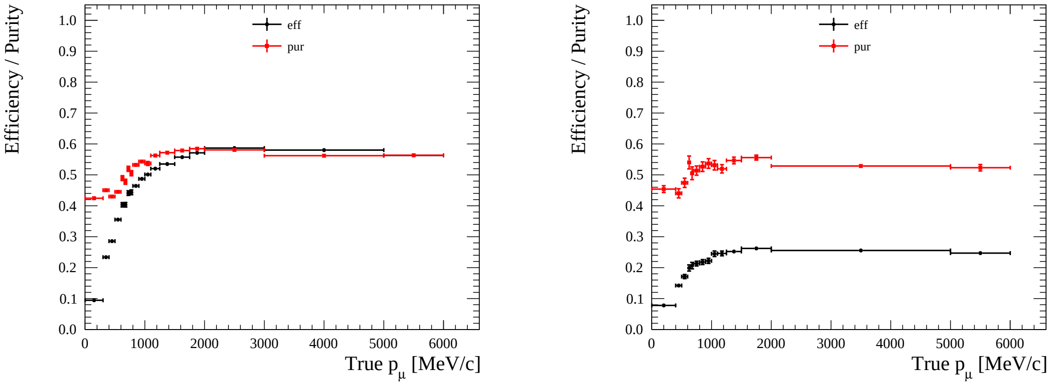

(c) CC-Photon (d) CC-Other

Figure 3.20: Selection efficiency (black dots) and purity (red dots) for ν_μ CC0π (a), CC1π^+ (b), CC-Photon (c) and CC-Other (d) samples in FGD1, plotted against true muon momentum. The last bin in momentum includes all events with p_μ greater than 5000 MeV/c.

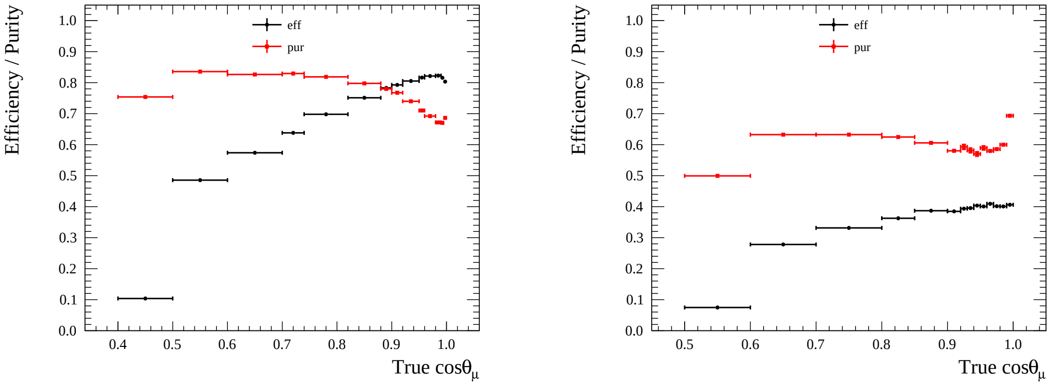

(a) CC0π (b) CC1π^+

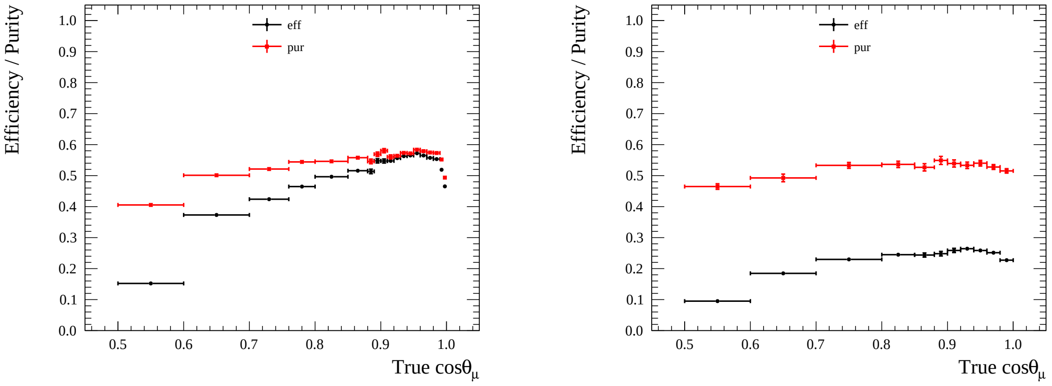

(c) CC-Photon (d) CC-Other

Figure 3.21: Selection efficiency (black dots) and purity (red dots) for ν_μ CC0π (a), CC1π^+ (b), CC-Photon (c) and CC-Other (d) samples in FGD1, plotted against true muon $\cos\theta$. The first bin in $\cos\theta_\mu$ includes all events with $\cos\theta_\mu$ below 0.6.

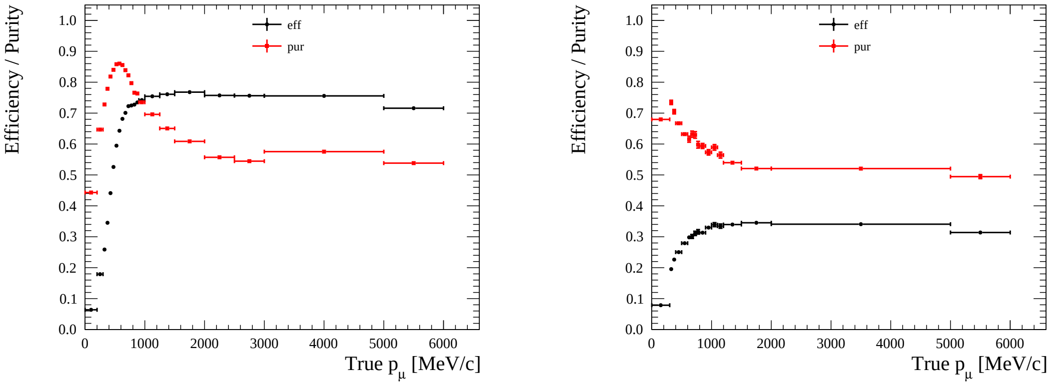

(a) CC0π (b) CC1π^+

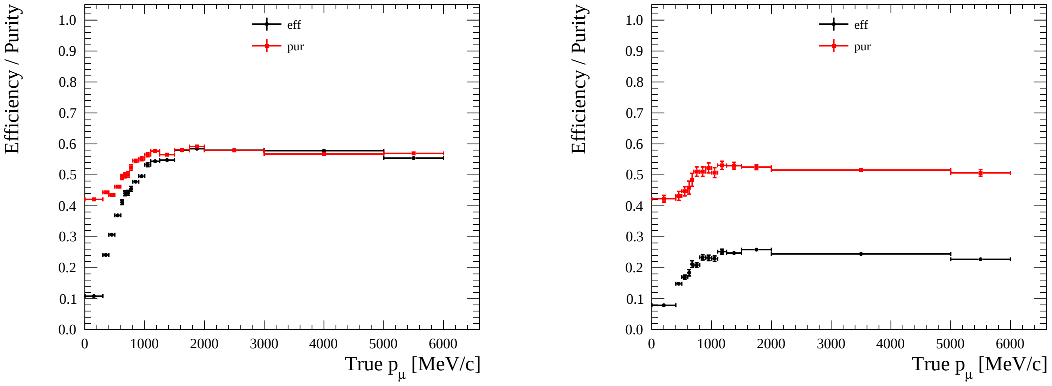

(c) CC-Photon (d) CC-Other

Figure 3.22: Selection efficiency (black dots) and purity (red dots) for ν_μ CC0π (a), CC1π^+ (b), CC-Photon (c) and CC-Other (d) samples in FGD2, plotted against true muon momentum. The last bin in momentum includes all events with p_μ greater than 5000 MeV/c.

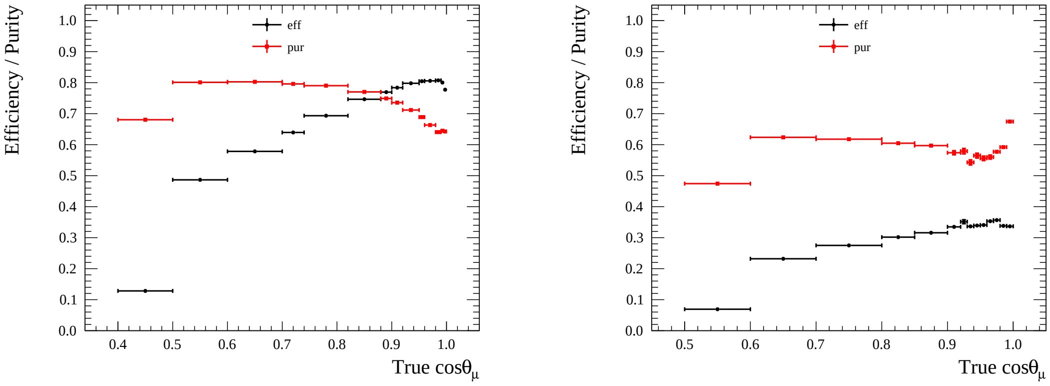

(a) CC0π (b) CC1π^+

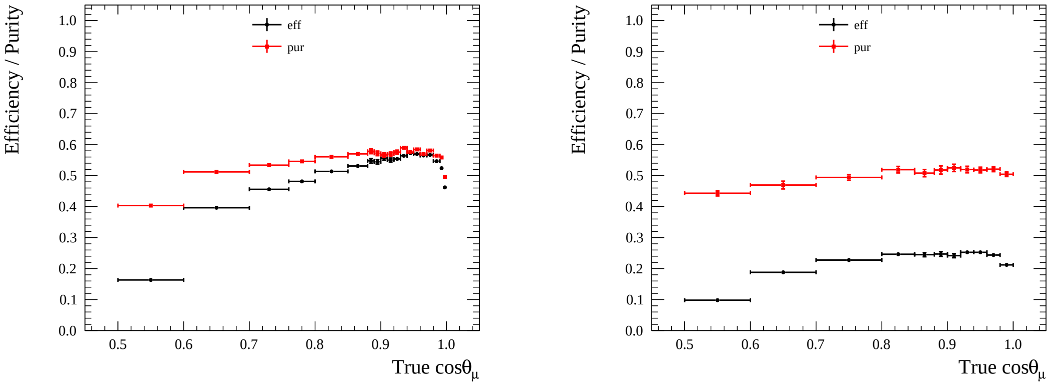

(c) CC-Photon (d) CC-Other

Figure 3.23: Selection efficiency (black dots) and purity (red dots) for ν_μ CC0π (a), CC1π^+ (b), CC-Photon (c) and CC-Other (d) samples in FGD2, plotted against true muon $\cos\theta$. The first bin in $\cos\theta_\mu$ includes all events with $\cos\theta_\mu$ below 0.6.

Sample	**Efficiency(%)**		**Purity(%)**	
	FGD1	FGD2	FGD1	FGD2
CC0π	46.86 ± 0.05	47.47 ± 0.05	76.3 ± 0.1	72.8 ± 0.1
CC1π^+	27.06 ± 0.08	23.03 ± 0.08	60.2 ± 0.2	58.5 ± 0.2
CC-Photon	43.0 ± 0.1	43.9 ± 0.1	53.9 ± 0.2	54.2 ± 0.2
CC-Other	21.1 ± 0.1	20.6 ± 0.1	52.2 ± 0.4	50.3 ± 0.4

Table 3.8: Final selection efficiencies and purities for each sample in FGD1 and FGD2 in the selection. Statistical uncertainties on these values are also included.

In order to make use of the selections described in this chapter, the uncertainties associated with making these selections must be understood. Each variable used in the selection must be compared to data and differences in the variables for data and MC must be accounted for. This is the subject of Chapter 4.

Chapter 4

ND280 Detector Systematics

The MC simulation uses the best understanding of the detector response, however simulation does not perfectly reproduce data. Differences between the true detector response and that simulated in MC introduce systematic errors. The uncertainty in the modelling of sub-detector responses and of neutrino interactions outside of the FGD FV are quantified through the use of control samples. These are dedicated data and MC samples that are different to those used in the analysis, containing a minimal number of signal events to avoid potential biases. The differences between data and MC observed in control samples are applied as correction factors to the nominal MC to take into account the observed discrepancies, while the error on these correction factors is propagated as a detector systematic uncertainty.

In this chapter, the impact of the detector systematics on the presented analysis is described. Most of the systematics are common with the previous iteration of the analysis [80, 95] which categorised ν_μ CC events into just three samples: CC0π, CC1π^+, and CC-Other. This old categorisation of events is referred to as the "MultiPi" selection. Only an overview of these systematics is included below, and any changes are highlighted. Plots of the relative errors for each of these systematics are shown in Appendix A. The relative error is calculated by running toy experiments for each systematic. A Gaussian distribution is defined using the central value of the systematic as the mean and the uncertainty on the systematic as the width. Each toy experiment uses a value of the systematic taken from this Gaussian distribution, which results in a different number of events in each sample for each toy. The relative error is defined as the Root Mean Square (RMS) of the toy distribution divided by the mean of the distribution, and can be calculated for each bin in p_μ or $\cos\theta_\mu$, or for the sample as a whole. The relative error calculated for the whole sample is referred to as the integrated relative error. Four additional systematics have been introduced which are associated with the selection of photons in the ECal, these are discussed in detail in this chapter.

4.1 ν_μ CC MultiPi Systematics

The systematic uncertainties used in this analysis that are in common with the ν_μ CC MultiPi selection are:

B field distortions: This systematic uncertainty is due to the modelling of distortions in the non-uniform TPC magnetic field [95]. A correction is applied in the reconstruction to shift clusters back to the ionisation point based on the map of the magnetic field. This map was produced with a granularity of 10 cm, which limits the resolution of these corrections. Incorrect modelling of the magnetic field could lead to biases in momentum measurements.

TPC momentum resolution: The TPC momentum resolution has an associated systematic uncertainty due to how well it is modelled in the MC [80]. To compute the uncertainty, the momentum component transverse to the magnetic field is measured for data and MC. The difference between data and MC is approximately Gaussian, and the width is taken as the systematic uncertainty.

TPC momentum scale: There is a systematic uncertainty associated with the TPC momentum scale which comes from uncertainties in the magnetic field map in ND280 discussed above [95]. The size of this uncertainty is estimated to be 0.5% from the field map, and this has been verified through comparisons of data and MC cosmic muon samples.

TPC PID: As described in Section 3.2, the TPC PID is based on measurements of dE/dx, which is used to compute pulls and likelihoods for different particle hypotheses. This systematic estimates the uncertainty on the dE/dx measurements [80]. The difference between data and MC pulls is applied as the systematic uncertainty.

FGD PID: Energy deposited in the FGD is used to define pulls for different particle hypotheses in the FGD PID. This systematic uncertainty is the difference between the pulls for data and MC for a control sample of tracks stopping in the FGD that contain a TPC segment [80].

Charge identification efficiency: This systematic describes the efficiency of the TPC charge identification algorithm in the TPC, which uses the curvature of the track to distinguish positive and negative tracks [95]. For tracks that have segments in multiple TPCs, the charge is computed for each segment individually and for the global track as a whole. The segments are given relative weights based on the number of hits in each segment. The efficiency represents the probability of selecting the correct charge in each segment and global track.

TPC cluster efficiency: A TPC cluster is defined as a collection of contiguous pads containing hits. Depending on the track angle, a cluster will have several hits in the same column, for horizontal tracks, or in the same row, for vertical tracks. Since the beam direction is essentially horizontal, most clusters will contain several hits in the same column. The cluster efficiency is defined as the probability of finding a reconstructed cluster at a given column where the particle should have produced one. The data-MC difference in this efficiency is used as the systematic uncertainty and is applied to FGD-TPC objects that pass the TPC track quality cut described in Section 3.2 which relies on the number of reconstructed TPC clusters [80].

TPC tracking efficiency: This systematic describes the efficiency with which the TPCs successfully reconstruct tracks from particles that enter them [80]. This includes evaluation for the TPC pattern recognition algorithm and the likelihood calculation. Failure in reconstruction leads to the wrong classification of the event topology, resulting in fewer events being selected and migration between sub-samples.

FGD-TPC matching efficiency: This systematic accounts for the efficiency of matching TPC tracks to FGD tracks left by the same particles [80]. A control sample of muons going through two consecutive TPCs is selected and an efficiency is defined as the number of events with a corresponding FGD component matched between the TPC components divided by the total number of selected muons. The efficiency is calculated for data and MC separately and the difference is propagated as the systematic uncertainty.

FGD tracking efficiency: This systematic uncertainty describes differences in the data and MC reconstruction efficiencies in the FGD [95]. TPC tracks entering the FGDs are selected, and efficiencies are defined as the number of tracks reconstructed in the FGD divided by the number of tracks entering the FGD. It has been re-evaluated using more recent MC for this analysis, leading to a slightly reduced uncertainty [96].

Michel electron efficiency: The signal of Michel electrons is based on activity in delayed time bins (see Section 3.3), and an uncertainty is introduced due to the ability to correctly tag such signals [95]. A control sample of cosmic-triggered muons that stop in the FGD was selected for data and MC, and the Michel electron cut was applied. The systematic uncertainty applied is the difference in data and MC efficiencies of this cut.

Pion secondary interaction: In simulation, after pions leave the nucleus they are propagated through the detector using GEANT4 in steps of 0.1 mm. At each step the probability of the pion undergoing an interaction is calculated. The systematic uncertainties on these processes are calculated by comparing the GEANT4 cross sections for each simulated interaction type to external data for interactions. The weights applied have been updated for this analysis [81].

Proton secondary interaction: This systematic uncertainty is due to the modelling of proton interactions after they leave the nucleus and is similar to the equivalent systematic for pions. Protons are propagated through the detector in steps of 0.1 mm and interaction probabilities are calculated at each step. Weights were re-calculated for this analysis [81].

FGD mass: This systematic uncertainty accounts for the difference in the density of the scintillator and water that makes up the FGD target mass in truth compared to in simulation [95]. It was found that the MC overestimates the density of the FGD modules and, combined with the uncertainty on measuring the true densities of the modules, results in a 0.6% uncertainty on the FGD1 mass and 0.4% uncertainty on the FGD2 mass.

Sand muon background: A dedicated MC sample is used to simulate neutrino interactions in the rock surrounding the ND280 cavern, referred to as "sand". The MultiPi selection was applied to this Monte Carlo sample and data events identified as sand interactions to calculate the rate at which these interactions enter the selected samples. The data-MC difference is used as the uncertainty and was found to be 10% in FHC and 30% in RHC [95].

OOFV background: Out-Of-Fiducial-Volume events are interactions whose vertices are reconstructed as inside the FGD FV while the true vertices are outside. Using MC truth information, these events are separated into 9 categories corresponding to the reasons they weren't rejected. These categories include high energy neutrons that produce π^- inside the FGD, which can be mis-reconstructed as forward-going muons, and muons passing through the FGD where the TPC-FGD matching fails, which can also look like FV events. A rate uncertainty of 20% is applied for categories where the true interaction vertex is outside the tracker, which comes from data-MC comparisons of event rates in the PØD, ECal and SMRD. Additional reconstruction uncertainties are evaluated for categories where control samples exist to evaluate the corresponding reconstruction failure [95].

Pile-up: The effect of pile up considered here is due to sand muons that are in coincidence with magnet events. Selecting events that fail the TPC veto cut allows calculation of the number of events with activity in TPC1 per bunch. The difference in this number between data and the sand muon MC sample is propagated as the systematic uncertainty [80].

4.2 ECal Systematics for Photon Selection

The selection of photon candidates in the ECal requires additional consideration of systematic uncertainties compared to the previous analysis. When using ECal information, it is necessary to consider the ability to reconstruct objects in the ECal, and the ability to match showers and tracks in the ECal to components in the tracker where appropriate. There are also uncertainties related to the variables used in the selection cuts: PIDEmHip and MostUpStreamLayerHit. These four systematic uncertainties are described in detail below.

4.2.1 ECal Tracking Efficiency

First, the reconstruction efficiency of objects in the ECal must be considered. This systematic was evaluated using the Highland2 framework based on previous work [97], with updates for use with the new selection. The control sample requires a good quality TPC track ending close to the edges of the ECal, where the end of the track points towards the ECal. This provides a sample of tracks and showers entering the ECal that can be used to assess the reconstruction efficiency. To select tracks entering the barrel ECal, the following conditions are applied to the TPC tracks:

- $|$ end position along X $| < 890\,\mathrm{mm}$
- $-980\,\mathrm{mm} <$ end position along $Y < 1085\,\mathrm{mm}$
- $600\,\mathrm{mm} <$ end position along $Z < 2600\,\mathrm{mm}$
- angle w.r.t. Z axis $> 35°$

while for tracks entering the downstream ECal the following conditions are applied:

- $|$ end position along X $| < 920\,\mathrm{mm}$
- $|$ end position along $Y + 10\,\mathrm{mm}$ $| < 920\,\mathrm{mm}$
- end position along $Z > 2665\,\mathrm{mm}$
- angle w.r.t. Z axis $< 40°$

The control sample is then separated into four sub-samples: shower-like objects in the downstream ECal, track-like objects in the downstream ECal, shower-like objects in the barrel ECal, and track-like objects in the barrel ECal.

To separate the TPC tracks into shower-like and track-like, PID is used to select e^+/e^- enhanced and μ^- enhanced samples. The muon PID cut for the track-like sample is the same as that described in Section 3.2, applied to the highest momentum negative track. Electrons are selected by requiring: the track is not the highest momentum negative track, the TPC electron pull satisfies $|\mathrm{Pull}_e| < 2$, and the momentum is less than 700 MeV.

The closest ECal object to the end of the TPC track is then selected if it is no more than 700 mm away from the end of the track. To determine if the ECal object is track-like or shower-like, the ECal PID variable PIDEmHip is used. Objects with PIDEmHip > 0 are taken as tracks, and objects with PIDEmHip < 0 are taken as showers.

To evaluate the systematic, the following efficiencies are defined for showers and tracks:

$$\mathrm{Eff}_{\mathrm{shower}} = \frac{\#(\text{shower-like TPC candidate} \cap \text{ECal shower found})}{\#(\text{shower-like TPC candidate})} \tag{4.1}$$

$$\mathrm{Eff}_{\mathrm{track}} = \frac{\#(\text{track-like TPC candidate} \cap \text{ECal track found})}{\#(\text{track-like TPC candidate})} \tag{4.2}$$

for both downstream and barrel ECals. The total efficiency for each of the four sub-samples is shown in Fig. 4.1. The reconstruction efficiency for tracks is higher than that for showers, most likely because the shower-like control samples are less pure, which changes the value of Pull_e used in the selection. The efficiencies are higher in the downstream ECal than the barrel, which is expected as the bars in the downstream ECal have double-ended readout, whereas those in the barrel do not. The largest data-MC difference is observed for tracks in the barrel ECal, however this difference is small and there is good agreement in all four sub-samples.

The efficiency for each sub-sample as a function of momentum entering the ECal, defined as the momentum at the endpoint of the TPC track, is shown in Fig. 4.2. The behaviour noted for the samples as a whole is observed across the whole momentum range too. The uncertainty applied in the analysis comes from the data-MC difference, which is calculated for each ECal momentum bin separately.

There are two cases in which this systematic is applied, where the event would

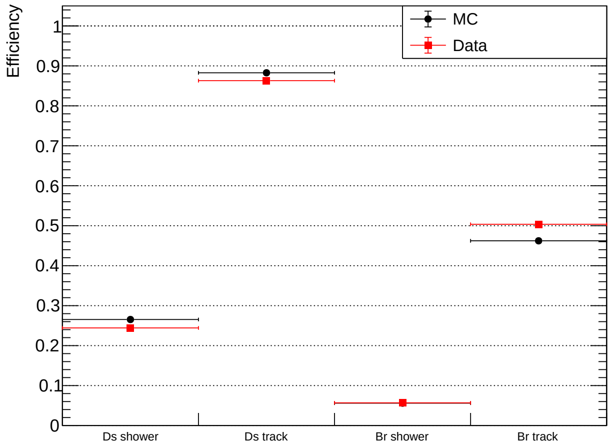

Figure 4.1: Efficiency of shower and track reconstruction in the downstream (Ds) and barrel (Br) ECals. Red points represent the data efficiency, and black points represent the MC efficiency. The points for the data and MC efficiencies for showers in the barrel ECal overlap. Error bars representing the statistical uncertainty on these efficiencies are too small to be visible on this scale.

change sample if an object is reconstructed or not. The first case is where there is one ECal photon identified and no TPC-tagged π^0. The ECal photon is what defines the event categorisation as CC-Photon, and had it not been reconstructed the event would be placed in another sample. The second case is when there is no ECal photon identified and no TPC-tagged π^0, but there is an unreconstructed true particle in the ECal. Had this true particle been reconstructed, it has potential to be identified as an ECal photon and thus would move the event into the CC-Photon sample. Conditions are placed on the true particle to select those which would most likely pass the photon selection. Only true $e^{\pm}$ and true γ with momenta of more than 30 MeV in the ECal are considered, since the ECal reconstruction is unreliable below 30 MeV.

In Figs. 4.3 and 4.4 the relative errors for this systematic for FGD1 and FGD2 are shown. The total integrated relative error for this systematic is 0.34% for CC0π0p, 0.52% for CC0πNp, 1.07% for CC1π^+, 1.00% for CC-Photon and 2.64% for CC-Other in FGD1. The total integrated relative error is 0.38% for CC0π0p, 0.69% for CC0πNp, 1.51% for CC1π^+, 0.89% for CC-Photon and 4.35% for CC-Other in FGD2.

The uncertainty is typically larger in the FGD2 samples than the FGD1 samples,

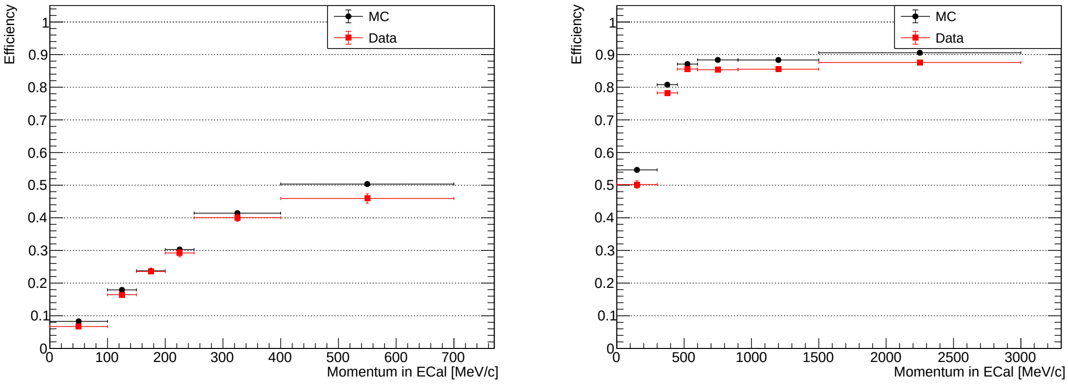

(a) Downstream Shower (b) Downstream Track

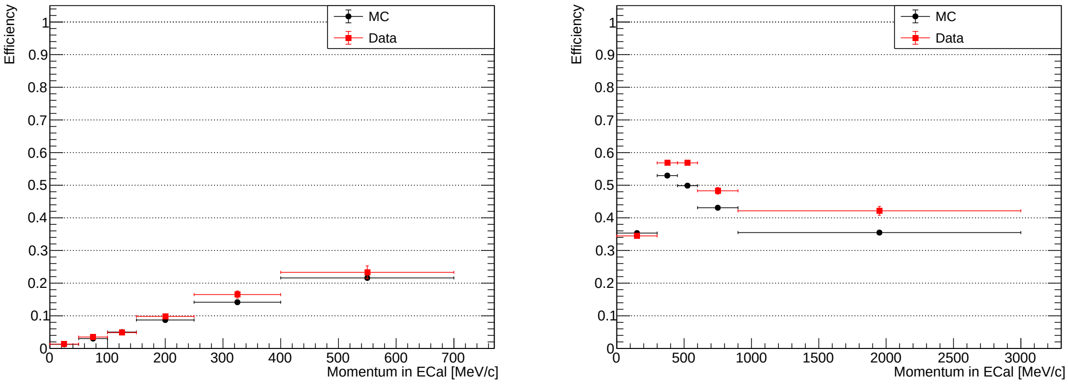

(c) Barrel Shower (d) Barrel Track

Figure 4.2: Efficiency of shower (left) and track (right) reconstruction as a function of reconstructed momentum entering the downstream (top) and barrel (bottom) ECals. Red points represent the data efficiency, and black points represent the MC efficiency. Error bars representing the statistical uncertainty on these efficiencies are generally too small to be visible on this scale.

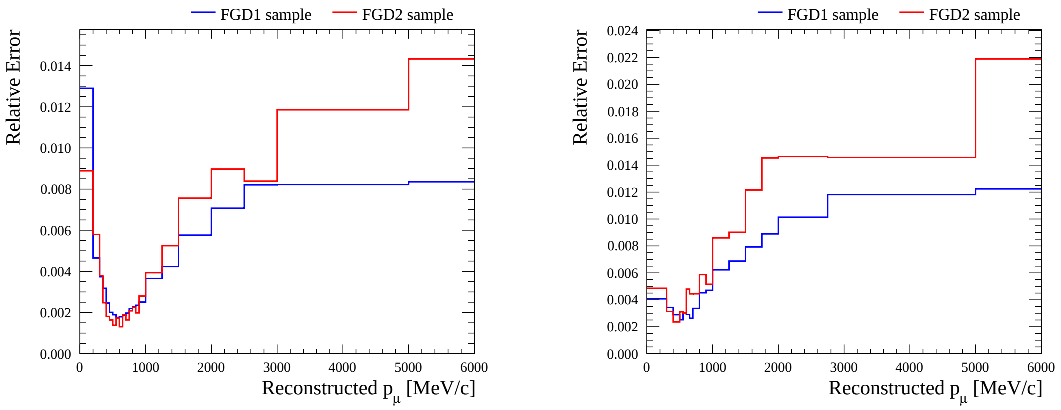

(a) CC0π0p

(b) CC0πNp

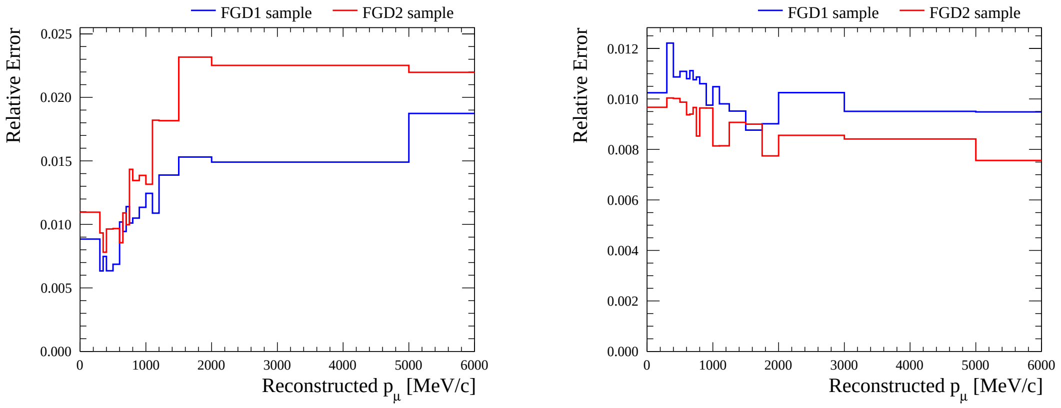

(c) CC1π^+

(d) CC-Photon

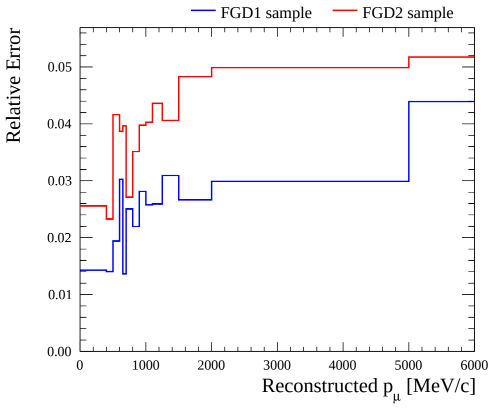

(e) CC-Other

Figure 4.3: Relative error evaluated after the propagation of the uncertainty on the ECal tracking efficiency as function of the reconstructed muon momentum for ν_μ CC0π0p (a), CC0πNp (b), CC1π^+ (c), CC-Photon (d) and CC-Other (e) samples. The blue line shows the relative error for FGD1 while the red line for FGD2. The last bin in momentum includes all events with p_μ greater than 5000 MeV/c.

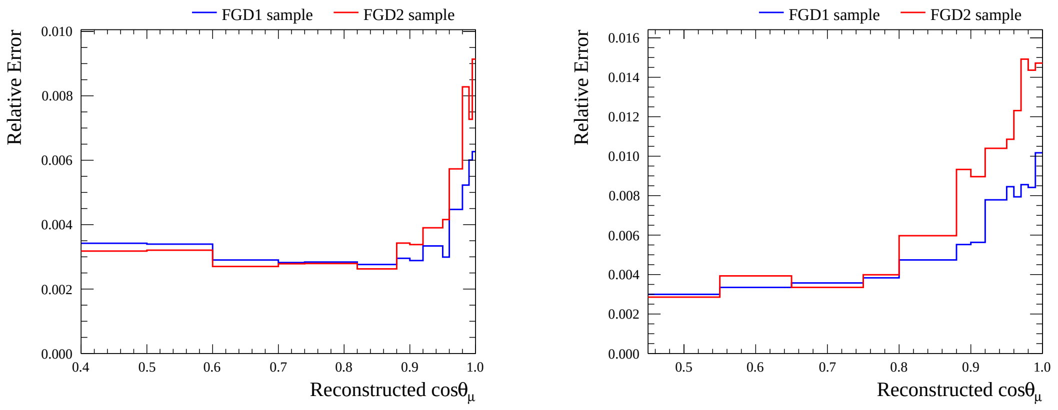

(a) CC0π0p (b) CC0πNp

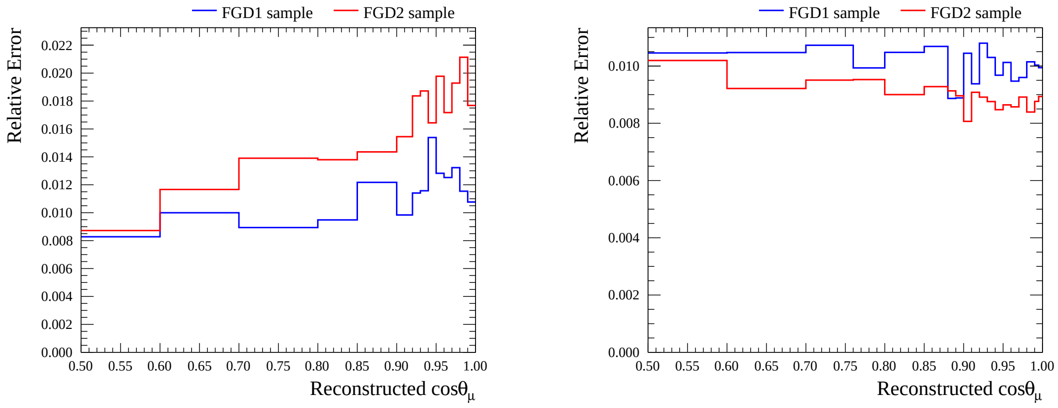

(c) CC1π^+ (d) CC-Photon

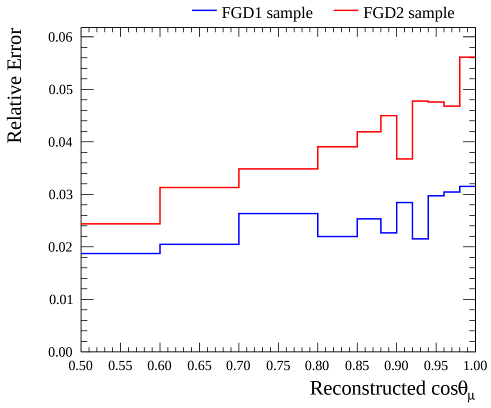

(e) CC-Other

Figure 4.4: Relative error evaluated after the propagation of the uncertainty on the ECal tracking efficiency as function of the reconstructed muon $\cos\theta$ for ν_μ CC0π0p (a), CC0πNp (b), CC1π^+ (c), CC-Photon (d) and CC-Other (e) samples. The blue line shows the relative error for FGD1 while the red line for FGD2. The first bin in $\cos\theta_\mu$ includes all events with $\cos\theta_\mu$ below 0.6.

which can be understood by considering the geometry of the detector. Forward-going photons produced in FGD1 can interact in FGD2 on their path towards the downstream ECal, while those produced in FGD2 have to pass only through TPC3. Therefore it is expected that more photons would reach the downstream ECal in the FGD2 sample. Fig. 4.1 shows that the data-MC difference, which is used as the systematic uncertainty, is larger for showers in the downstream ECal than in the barrel ECal. The combined effect of having more photons reach the downstream ECal and the tracking uncertainty for those being larger than for photons in the barrel, results in the larger relative error on the FGD2 samples.

4.2.2 TPC-ECal Matching Efficiency

The control samples used to evaluate this systematic select TPC tracks entering the barrel and downstream ECals in the way described in Section 4.2.1, and separate the tracks into muon-like, electron-like and proton-like samples. The selection of the muon enhanced sample is identical to that described in Section 4.2.1. The selection of electron-like tracks requires a pair of oppositely charged tracks originating within 10 cm of each other. The negative (positive) track in the pair is selected as the electron (positron) candidate and must be consistent with the electron hypothesis based on TPC pulls. Proton tracks are selected using the same method as the muons, however the track should be positive and should be consistent with the proton hypothesis based on TPC pulls.

The selected tracks should enter the ECal and thus have an ECal segment matched with the selected TPC track. Matching efficiencies are calculated for each sub-sample for data and MC as:

$$\mathrm{Eff}_{\mathrm{match}} = \frac{\#(\text{tracks passing selection with an ECal segment})}{\#(\text{tracks passing selection})} \tag{4.3}$$

and the data-MC difference is used to estimate the systematic uncertainty. As before, this is calculated for momentum bins separately for each sub-sample. An unbinned summary of the systematic uncertainties for each sub-sample is shown in Table 4.1, while a complete bin-by-bin breakdown can be found in [97]. All systematic uncertainties are below 3%, and are consistent with zero at the 2σ level.

Detector	**PID**	σ (%)	$\delta\sigma$ (%)
Downstream	$e^{+/-}$	1.5	$+1.5/-1.5$
Barrel	$e^{+/-}$	0.5	$+2.1/-2.0$
Downstream	μ^-	0.3	$+0.2/-0.2$
Barrel	μ^-	0.6	$+0.9/-0.9$
Downstream	p	-2.4	$+1.6/-1.7$
Barrel	p	1.2	$+1.6/-1.6$

Table 4.1: Unbinned systematic uncertainties for each sub-sample used in the evaluation of the TPC-ECal matching efficiency [97].

In the analysis presented, this systematic uncertainty is applied to any event that does not contain an isolated ECal object, which covers the case where an ECal photon has been wrongly matched to a TPC track. Figs. 4.5 and 4.6 show the resulting relative errors for this systematic for the FGD1 and FGD2 samples.

The total integrated relative error for this systematic is 0.61% for CC0π0p, 1.01% for CC0πNp, 0.74% for CC1π^+, 0.99% for CC-Photon and 1.27% for CC-Other in FGD1. The total integrated relative error for this systematic is 0.32% for CC0π0p, 1.03% for CC0πNp, 0.67% for CC1π^+, 1.04% for CC-Photon and 1.25% for CC-Other in FGD2.

4.2.3 PIDEmHip

Control samples of electrons, muons and protons were used in the evaluation of this systematic. Muons are selected in two groups: horizontally through-going muons, coming mainly from interactions in the rock upstream of ND280, and vertical cosmic muons, which are selected with a different trigger to typical beams events, requiring activity in two independent sides of the SMRD, PØD ECal and downstream ECal. The selections of the control samples require:

Electrons: a pair of oppositely charged tracks starting within 10 cm of each other and beginning in the FGD fiducial volume. Each track must have at least one TPC component with $-2 < \mathrm{Pull}_e < 2$ and the reconstructed invariant mass of the pair must be below 50 MeV/c^2 [98], calculated as:

$$M^2_{Invariant} = 2 \times m^2_{electron} + 2(E_{electron} \times E_{positron} - \boldsymbol{p}_{electron} \cdot \boldsymbol{p}_{positron}) \quad (4.4)$$

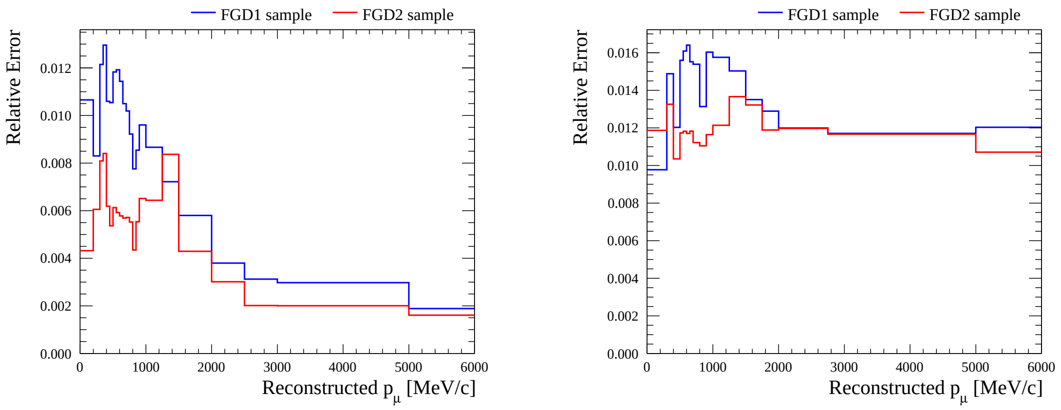

(a) CC0π0p

(b) CC0πNp

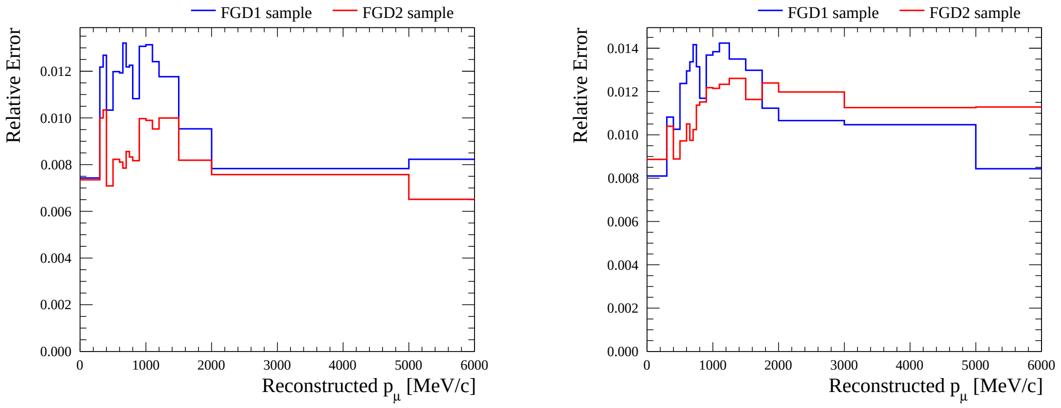

(c) CC1π^+

(d) CC-Photon

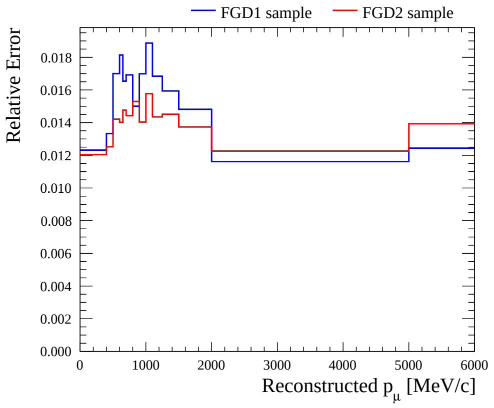

(e) CC-Other

Figure 4.5: Relative error evaluated after the propagation of the uncertainty on the TPC-ECal matching efficiency as function of the reconstructed muon momentum for ν_μ CC0π0p (a), CC0πNp (b), CC1π^+ (c), CC-Photon (d) and CC-Other (e) samples. The blue line shows the relative error for FGD1 while the red line for FGD2. The last bin in momentum includes all events with p_μ greater than 5000 MeV/c.

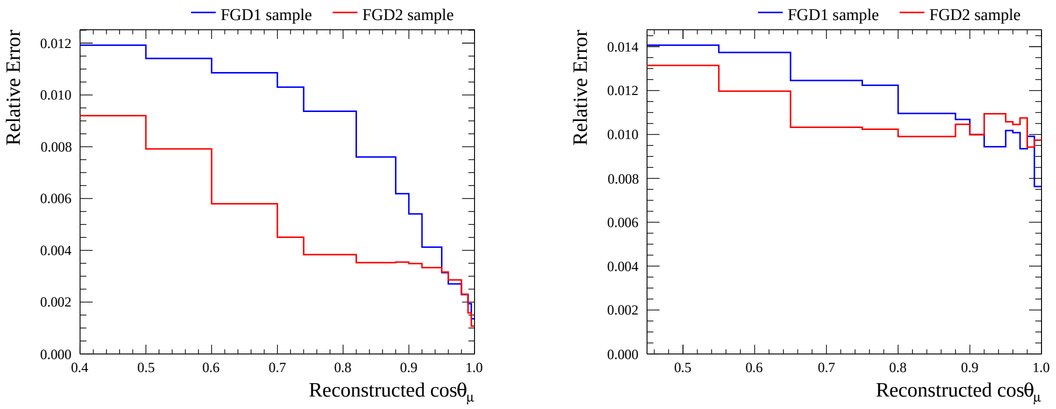

(a) CC0π0p (b) CC0πNp

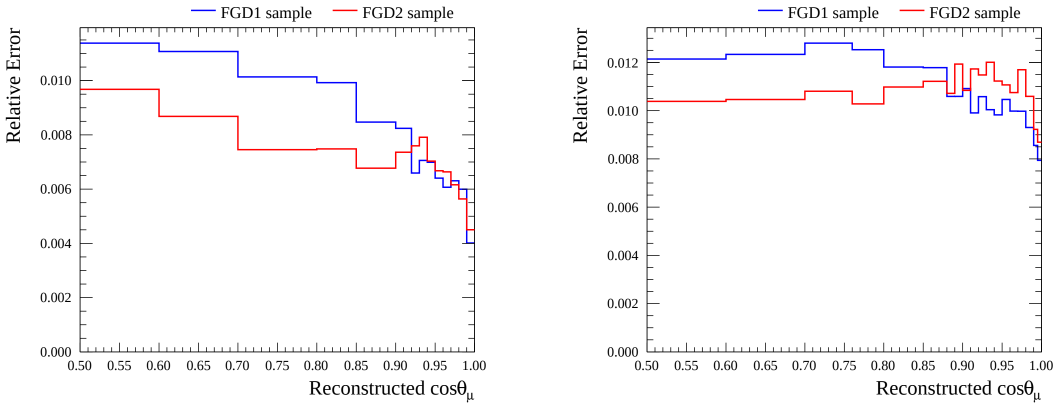

(c) CC1π^+ (d) CC-Photon

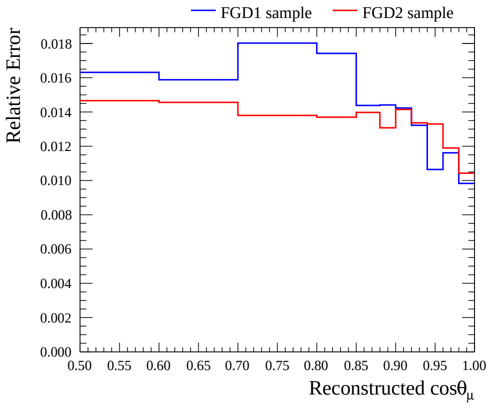

(e) CC-Other

Figure 4.6: Relative error evaluated after the propagation of the uncertainty on the TPC-ECal matching efficiency as function of the reconstructed muon $\cos\theta$ for ν_μ CC0π0p (a), CC0πNp (b), CC1π^+ (c), CC-Photon (d) and CC-Other (e) samples. The blue line shows the relative error for FGD1 while the red line for FGD2. The first bin in $\cos\theta_\mu$ includes all events with $\cos\theta_\mu$ below 0.6.

Sample	**ECal Module**	**Data Efficiency (%)**	**MC Efficiency (%)**
μ^-	Downstream	99.0 ± 0.0	99.2 ± 0.0
μ^-	Barrel	98.8 ± 0.0	99.3 ± 0.0
$e^{+/-}$	Downstream	20.7 ± 1.1	16.8 ± 0.3
$e^{+/-}$	Barrel	62.8 ± 1.5	59.9 ± 0.4
p	Downstream	92.1 ± 0.4	91.4 ± 0.1
p	Barrel	72.9 ± 0.8	74.3 ± 0.2

Table 4.2: Data and MC efficiencies used in the evaluation of the PIDEmHip systematic [97]. Efficiencies correspond to the number of events passing the cut on PIDEmHip divided by the total number of events in the control sample.

where $m_{electron}$ is the mass of the electron and positron, $E_{electron}$ ($E_{positron}$) is the energy of the electron (positron), and $\boldsymbol{p}_{electron}$ ($\boldsymbol{p}_{positron}$) is the momentum of the electron (positron). In addition, at least one of the tracks must enter the ECal.

Through-going muons: a track with three TPC components and one ECal component. Each TPC component must have $-2 < \text{Pull}_\mu < 2$.

Cosmic muons: a track with one TPC component and two ECal components. The TPC component must have at least 18 hits.

Protons: a positive track in the TPC with $0 < \text{Pull}_p < 2$ and $|\text{Pull}_\mu| > 10$.

For each control sample a cut was placed on PIDEmHip > 0. An efficiency for each was defined as the number of events passing this cut divided by the total number of events in the control sample, calculated for both data and MC. These efficiencies are listed in Table 4.2. The difference between data and MC is interpreted as the systematic uncertainty on this variable. The systematic uncertainty was evaluated previously in [97] for the same cut value as used in this analysis, so the numbers calculated in that evaluation are used here.

This uncertainty has the potential to shift objects from one side of the cut value to another. In this case the event could move from one sample to another, thus the uncertainty should be applied to objects close to the cut value. The largest uncertainty on PIDEmHip given in [97] is 3.9%, so objects with very negative values of PIDEmHip are unlikely to experience a variation so extreme as to move them to a positive value. Therefore a range close to the cut value of zero is defined such

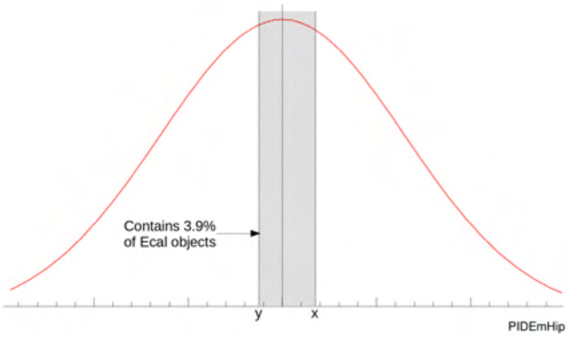

Figure 4.7: A sketch showing how the upper and lower bounds for applying the PIDEmHip systematic is defined. A region around the cut value of 0 is defined such that 3.9% of ECal objects with positive and negative PIDEmHip values are contained within.

that $y <$ PIDEmHip $< x$ contains 3.9% of ECal objects, where the value of x (y) is chosen such that 3.9% of objects with positive (negative) PIDEmHip values are selected. A sketch illustrating this is shown in Fig. 4.7. The values are found to be $x = 0.35$ and $y = -0.25$, so the systematic is applied when there is an object (or objects) with $-0.25 <$PIDEmHip< 0.35, if there is no object with PIDEmHip less than -0.25.

In Figs. 4.8 and 4.9 the relative errors for the systematic uncertainty on PIDEmHip for FGD1 and FGD2 are shown. The total integrated relative error for this systematic is 0.08% for CC0π0p, 0.06% for CC0πNp, 0.10% for CC1π^+, 0.42% for CC-Photon and 0.09% for CC-Other in FGD1. The total integrated relative error for this systematic is 0.06% for CC0π0p, 0.06% for CC0πNp, 0.07% for CC1π^+, 0.33% for CC-Photon and 0.09% for CC-Other in FGD2.

4.2.4 ECal Photon Pile-up

This systematic was evaluated using the Highland2 framework. The control sample requires that the event quality cuts described in Section 3.2 are passed and that there is also no activity recorded in the FGD fiducial volume. Activity outside of the FGD in these events is considered pile-up, and an ECal pile-up efficiency is defined as:

$$\mathrm{Eff}_{\text{pile-up}} = \frac{\#(\text{events with ECal photons} \cap \text{no FGD activity})}{\#(\text{events with no FGD activity})} \tag{4.5}$$

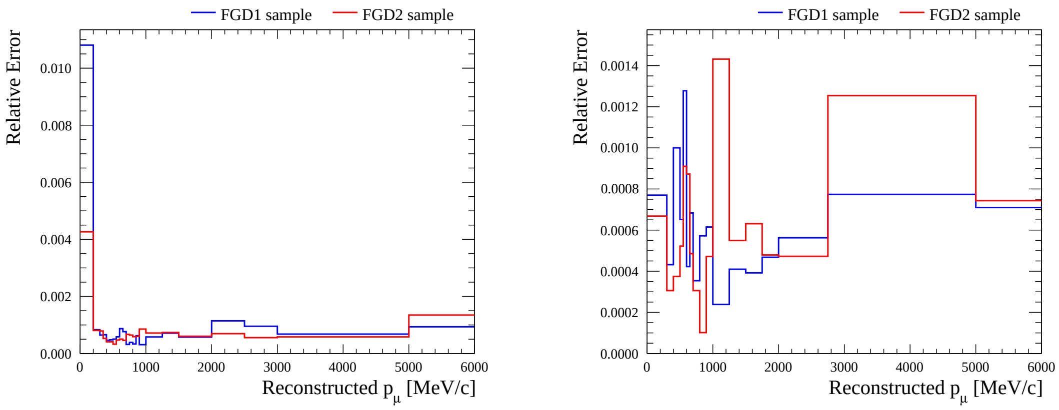

(a) CC0π0p (b) CC0πNp

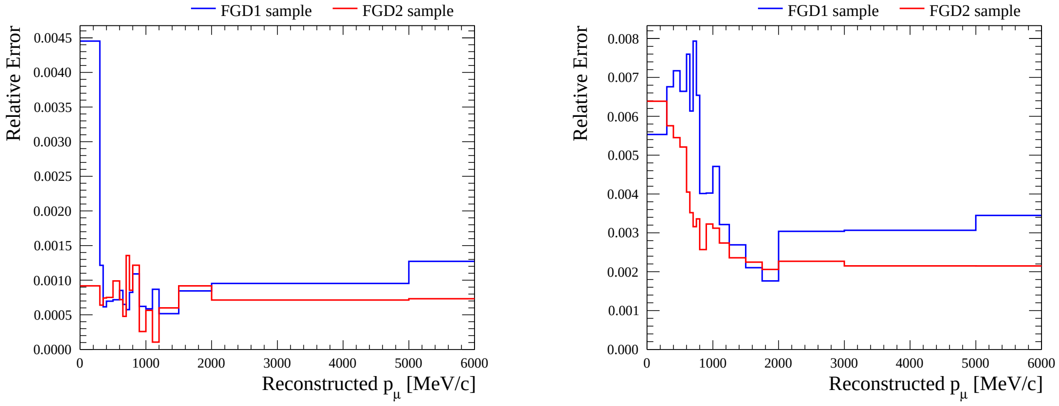

(c) CC1π^+ (d) CC-Photon

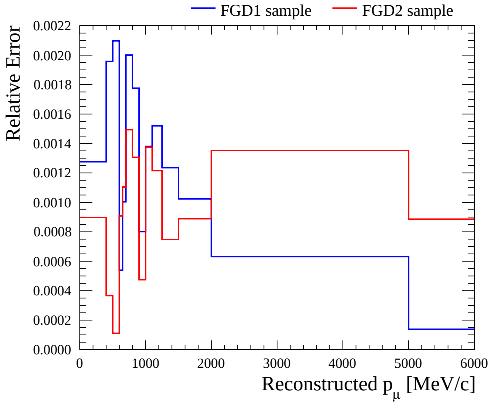

(e) CC-Other

Figure 4.8: Relative error evaluated after the propagation of the uncertainty on the ECal PID variable EmHip as function of the reconstructed muon momentum for ν_μ CC0π0p (a), CC0πNp (b), CC1π^+ (c), CC-Photon (d) and CC-Other (e) samples. The blue line shows the relative error for FGD1 while the red line for FGD2. The last bin in momentum includes all events with p_μ greater than 5000 MeV/c.

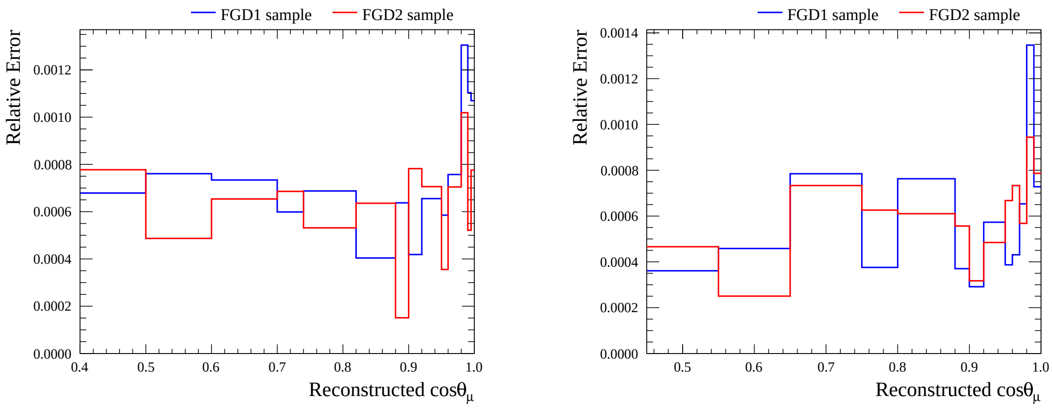

(a) CC0π0p

(b) CC0πNp

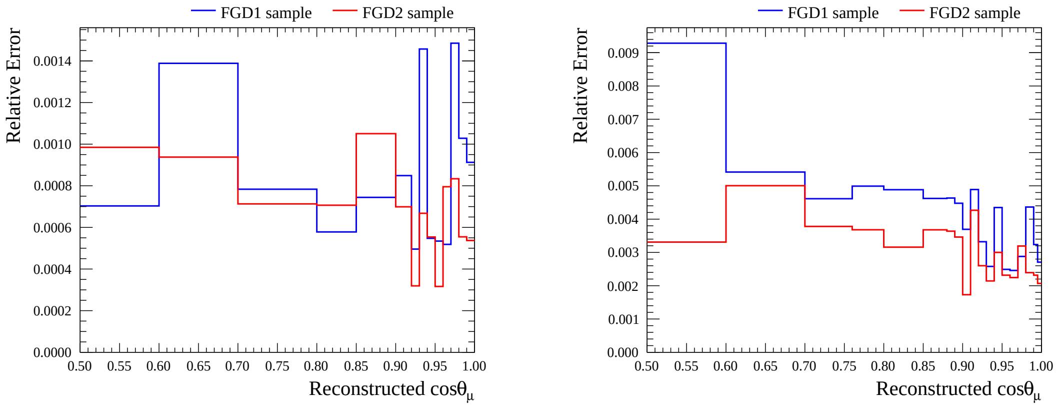

(c) CC1π^+

(d) CC-Photon

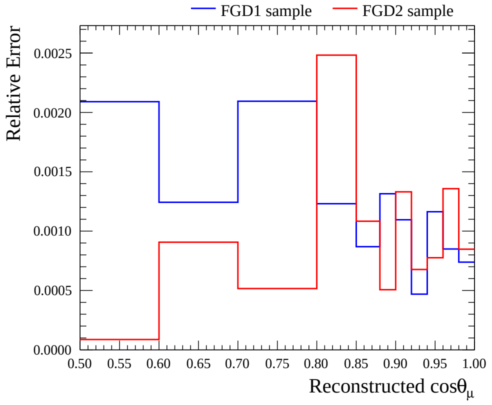

(e) CC-Other

Figure 4.9: Relative error evaluated after the propagation of the uncertainty on the ECal PID variable EmHip as function of the reconstructed muon $\cos\theta$ for ν_μ CC0π0p (a), CC0πNp (b), CC1π^+ (c), CC-Photon (d) and CC-Other (e) samples. The blue line shows the relative error for FGD1 while the red line for FGD2. The first bin in $\cos\theta_\mu$ includes all events with $\cos\theta_\mu$ below 0.6.

	POT per spill in MC / $\times 10^{13}$	**MC Efficiency (%)**		**Data Efficiency (%)**	
		FGD1	FGD2	FGD1	FGD2
run 2	7.99	1.78	1.79	2.16	2.18
run 3	9.46	2.10	2.11	2.49	2.51
run 4	9.46	2.10	2.11	3.00	3.01
run 8	22.70	4.95	4.96	5.80	5.82

Table 4.3: ECal pile-up efficiencies for data and MC and for each FGD. Efficiencies are calculated for each run used in the analysis. The number of POT per spill used in the MC for each run is also shown, reflecting the increase in beam power from run 2 to run 8.

where an ECal photon is defined as an isolated ECal object with PIDEmHip < 0. Efficiencies are calculated for both data and MC, for each FGD separately, and the data-MC difference is used as the systematic uncertainty. The efficiencies for the runs used in this analysis are given in Table 4.3, along with the number of POT per spill in the MC for each run. The number of POT per spill increased from run 2 to run 8 due to an increase in the beam power during that time period. As expected, increasing the POT per spill leads to more pile-up interactions, however the data-MC agreement is comparable for all runs.

There is a possibility that any isolated ECal object could be the product of a pile-up interaction in the ECal, so this systematic is applied to all events with isolated ECal objects. Figs. 4.10 and 4.11 show the relative errors for this systematic for each sample in FGD1 and FGD2.

The total integrated relative error for this systematic is 0.07% for CC0π0p, 0.04% for CC0πNp, 0.08% for CC$1\pi^+$, 1.17% for CC-Photon and 0.05% for CC-Other in FGD1. The total integrated relative error for this systematic is 0.05% for CC0π0p, 0.04% for CC0πNp, 0.04% for CC$1\pi^+$, 1.11% for CC-Photon and 0.04% for CC-Other in FGD2.

4.3 Results of Detector Systematic Propagation

The relative error evaluated for each sample after the simultaneous propagation of all the detector systematics is shown in Figs. 4.12 and 4.13 as function of the reconstructed muon kinematics. The figures compare the relative error for the FGD1

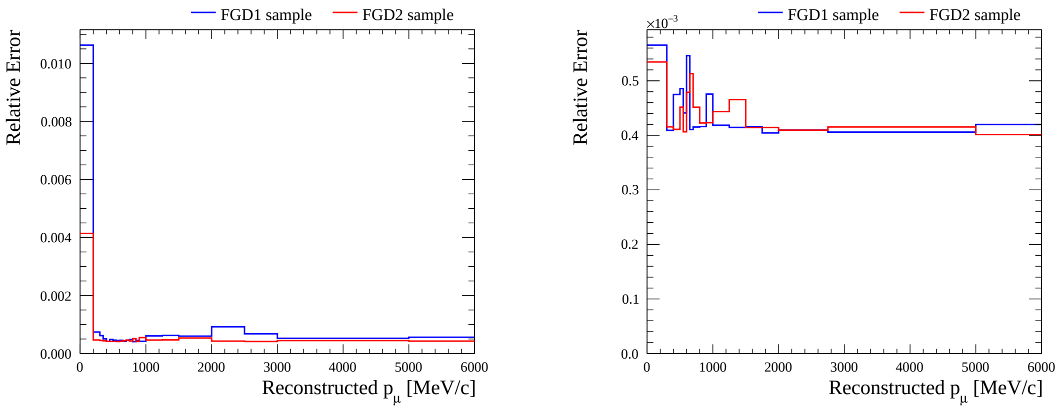

(a) CC0π0p (b) CC0πNp

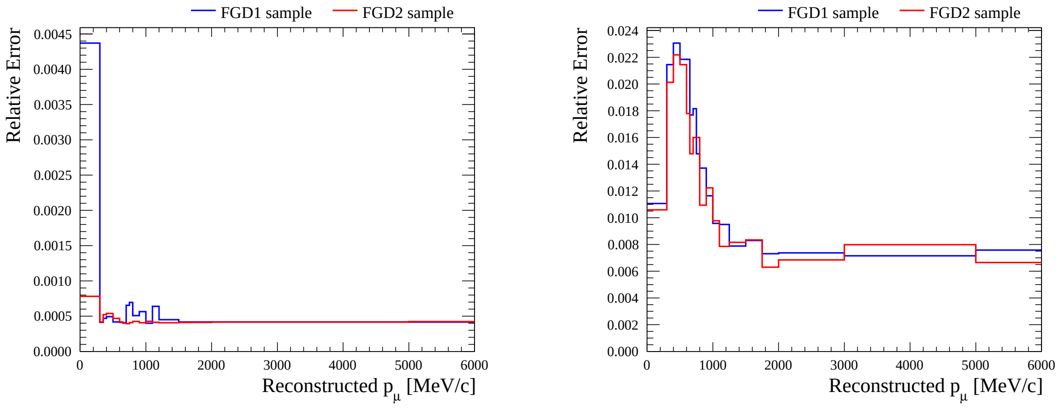

(c) CC1π^+ (d) CC-Photon

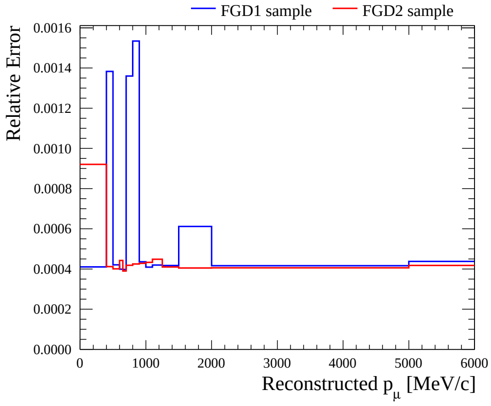

(e) CC-Other

Figure 4.10: Relative error evaluated after the propagation of the uncertainty on pile-up in the ECal as function of the reconstructed muon momentum for ν_μ CC0π0p (a), CC0πNp (b), CC1π^+ (c), CC-Photon (d) and CC-Other (e) samples. The blue line shows the relative error for FGD1 while the red line for FGD2. The last bin in momentum includes all events with p_μ greater than 5000 MeV/c.

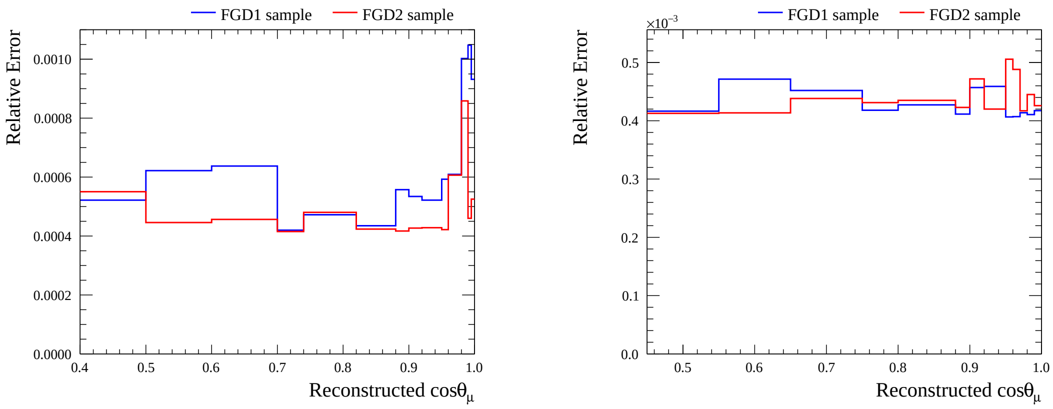

(a) CC0π0p

(b) CC0πNp

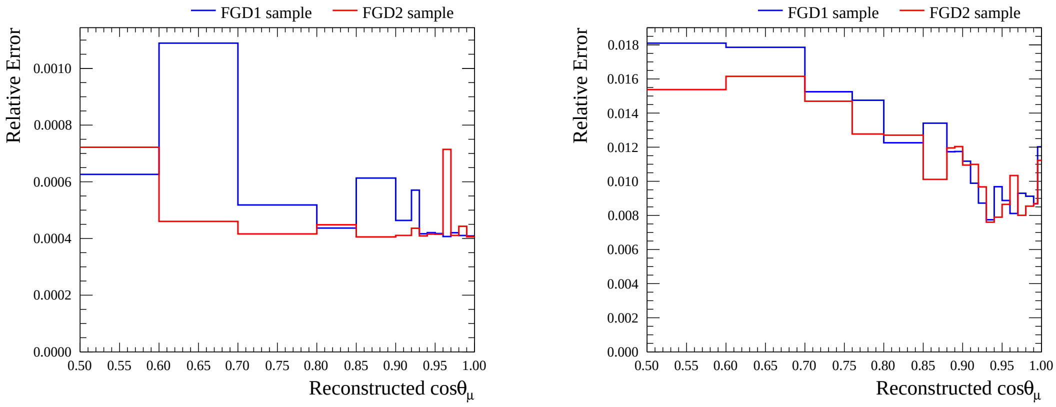

(c) CC1π^+

(d) CC-Photon

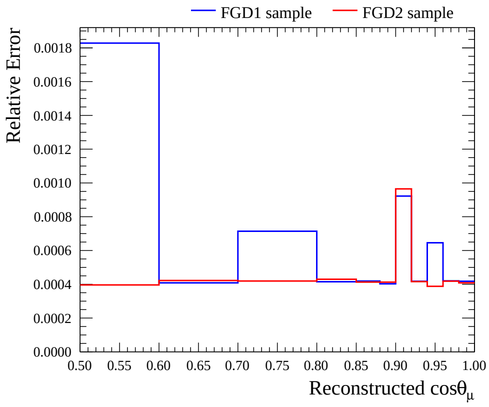

(e) CC-Other

Figure 4.11: Relative error evaluated after the propagation of the uncertainty on pile-up in the ECal as function of the reconstructed muon $\cos\theta$ for ν_μ CC0π0p (a), CC0πNp (b), CC1π^+ (c), CC-Photon (d) and CC-Other (e) samples. The blue line shows the relative error for FGD1 while the red line for FGD2. The first bin in $\cos\theta_\mu$ includes all events with $\cos\theta_\mu$ below 0.6.

and FGD2 event selections. Around the peak of the T2K beam energy spectrum observed by ND280, 600 MeV, the relative error is below 2% for the CC0π0p sample, below 4% for the CC0πNp sample, below 3% for the CC1π^+ sample, below 4% for the CC-Photon sample and below 5% for CC-Other. The impact of the individual detector systematics is discussed in Appendix A.

Figs. 4.14 and 4.15 show the distributions of the reconstructed muon momentum and $\cos\theta$ respectively for each FGD1 sample. Figs. 4.16 and 4.17 show the same for the FGD2 samples. The error bands correspond to the impact of the MC statistical error (magenta) and the quadrature sum of the MC statistical and the detector systematic errors (blue). The statistical error is the dominant uncertainty in every sample, while the systematic uncertainty becomes dominant only at low momentum. While there are still some differences between data and MC, it should be noted that flux and cross section systematics are not considered here. These are applied to the samples in the near detector fit, where better data-MC agreement is observed, this is shown in Chapter 5.

The integrated relative errors for each source of detector systematic uncertainty, sample and selection are reported in Table 4.4. The main systematic errors are proton and pion secondary interactions, ECal tracking, TPC-ECal matching, TPC PID, and TPC tracking efficiency. The TPC PID uncertainty is significantly smaller for the CC-Photon sample than for the CC1π^+ and CC-Other samples. This is expected since only one TPC track (corresponding to the muon) is required for an ECal-tagged CC-Photon event, whereas charged pions are also commonly identified using TPC PID in the CC1π^+ and CC-Other samples. Finally, the integrated total relative errors show a slightly larger impact on selections in FGD2 than in FGD1. This difference is mostly driven by the uncertainties on proton secondary interactions and on the ECal tracking efficiency.

The selections and systematics described in Chapters 3 and 4 are used as input to the near detector fit described in Chapter 5. Categorising the near detector events in the way described allows constraints to be made on the flux and cross section uncertainties used by the far detector in measurements of the oscillation parameters.

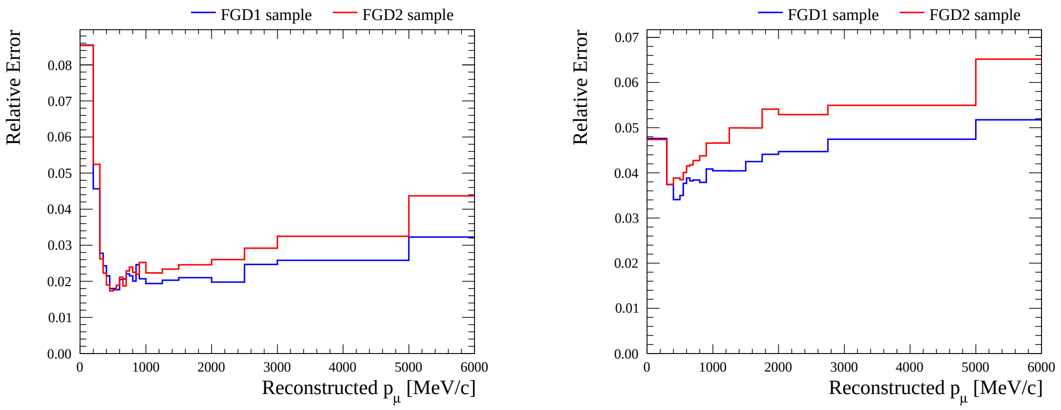

(a) CC0π0p

(b) CC0πNp

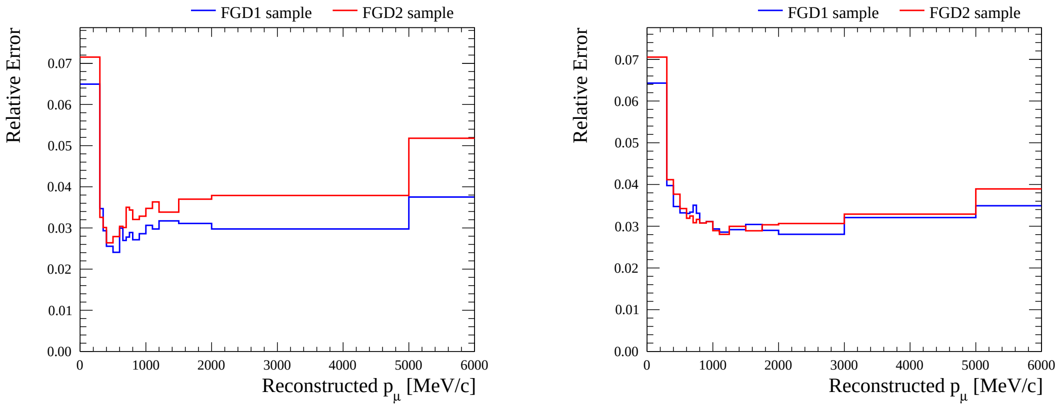

(c) CC1π^+

(d) CC-Photon

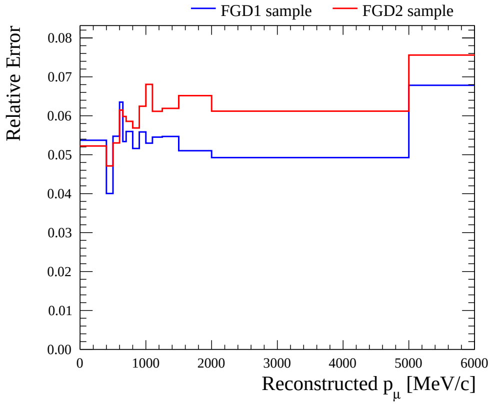

(e) CC-Other

Figure 4.12: Relative error evaluated after the propagation of all the detector systematics as function of the reconstructed muon momentum for ν_μ CC0π0p (a), CC0πNp (b), CC1π^+ (c), CC-Photon (d) and CC-Other (e) samples. The blue line shows the relative error for FGD1 while the red line for FGD2. The last bin in momentum includes all events with p_μ greater than 5000 MeV/c.

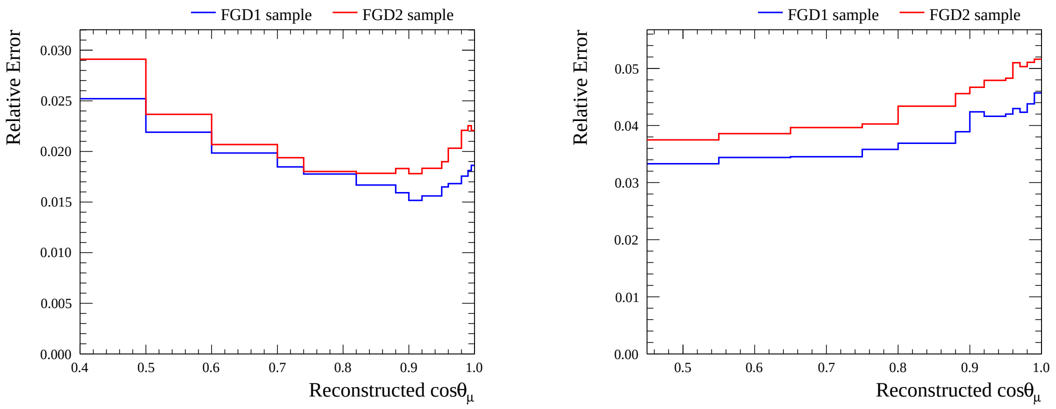

(a) CC0π0p

(b) CC0πNp

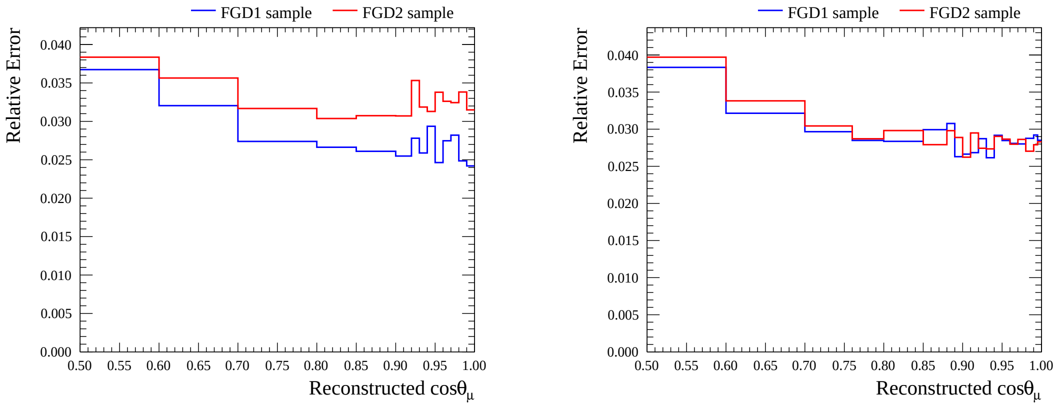

(c) CC1π^+

(d) CC-Photon

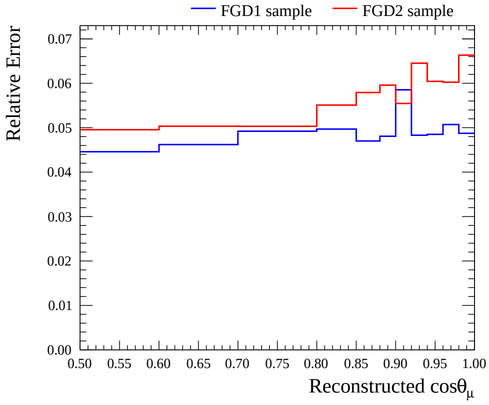

(e) CC-Other

Figure 4.13: Relative error evaluated after the propagation of all the detector systematics as function of the reconstructed muon $\cos\theta$ for ν_μ CC0π0p (a), CC0πNp (b), CC1π^+ (c), CC-Photon (d) and CC-Other (e) samples. The blue line shows the relative error for FGD1 while the red line for FGD2. The first bin in $\cos\theta_\mu$ includes all events with $\cos\theta_\mu$ below 0.6.

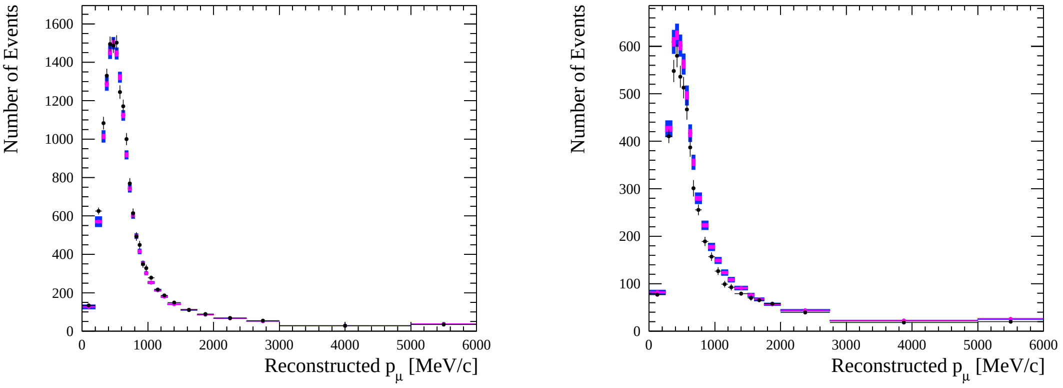

(a) CC0π0p (b) CC0πNp

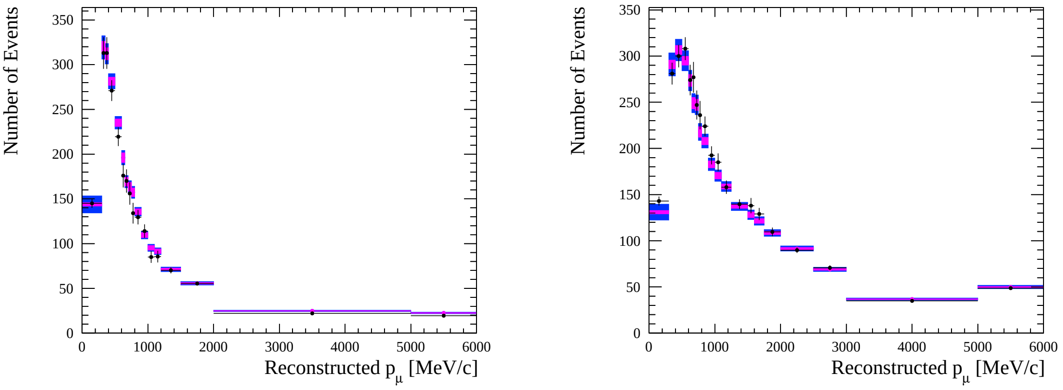

(c) CC1π^+ (d) CC-Photon

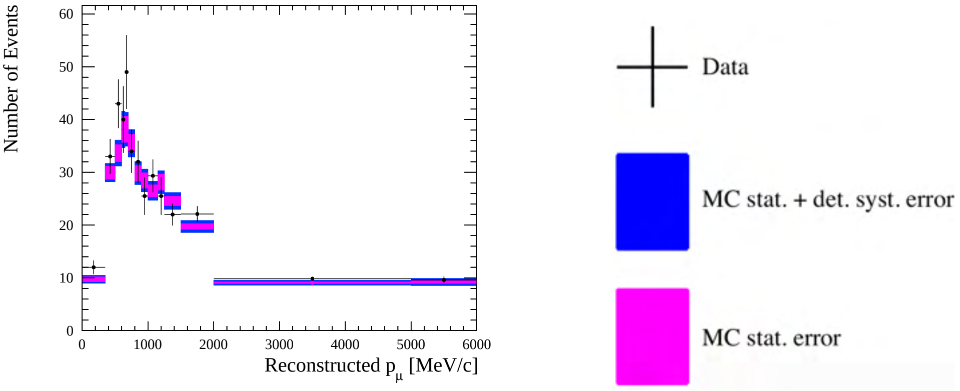

(e) CC-Other

Figure 4.14: Reconstructed muon momentum distributions for ν_μ CC0π0p (a), CC0πNp (b), CC1π^+ (c), CC-Photon (d) and CC-Other (e) FGD1 samples. The error bands refer to MC statistical error (magenta) and the sum in quadrature of the MC statistical and the detector systematic errors (blue). The last bin in momentum includes all events with p_μ greater than 5000 MeV/c.

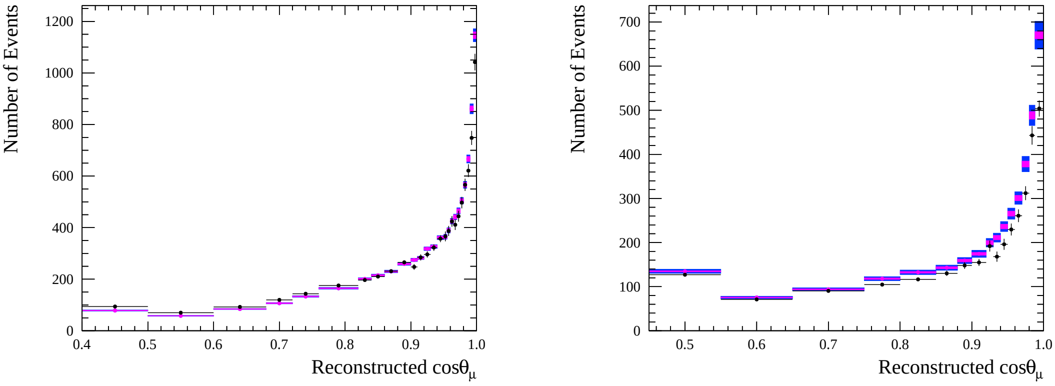

(a) CC0π0p (b) CC0πNp

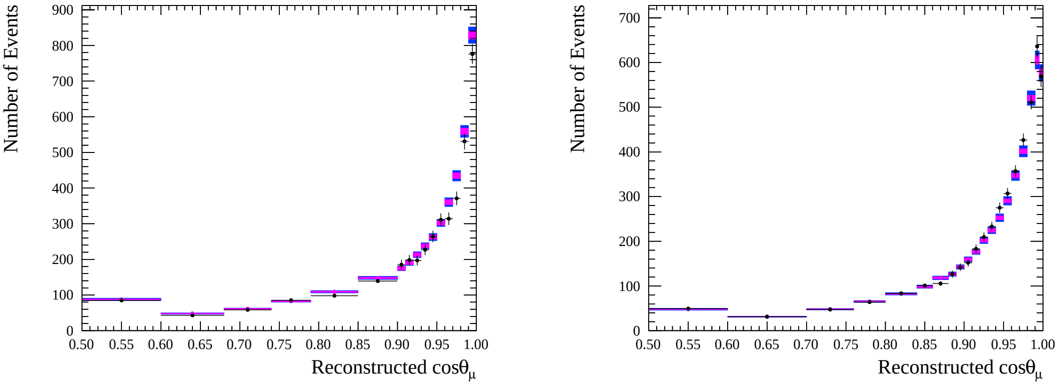

(c) CC1π^+ (d) CC-Photon

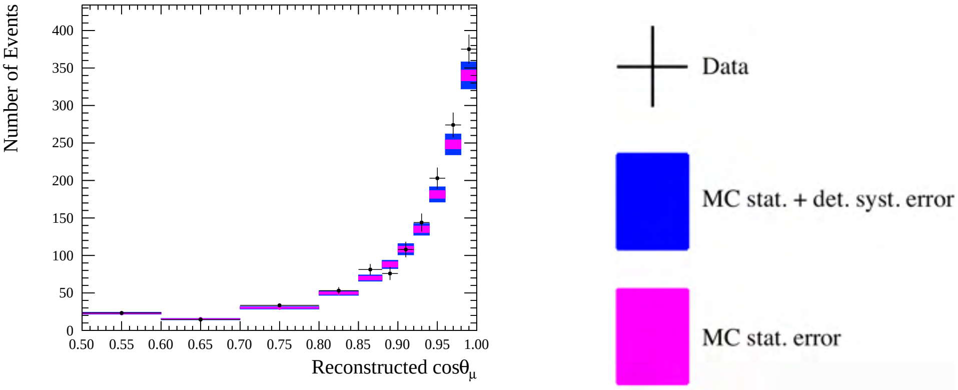

(e) CC-Other

Figure 4.15: Reconstructed muon $\cos\theta$ distributions for ν_μ CC0π0p (a), CC0πNp (b), CC1π^+ (c), CC-Photon (d) and CC-Other (e) FGD1 samples. The error bands refer to MC statistical error (magenta) and the sum in quadrature of the MC statistical and the detector systematic errors (blue). The first bin in $\cos\theta_\mu$ includes all events with $\cos\theta_\mu$ below 0.6.

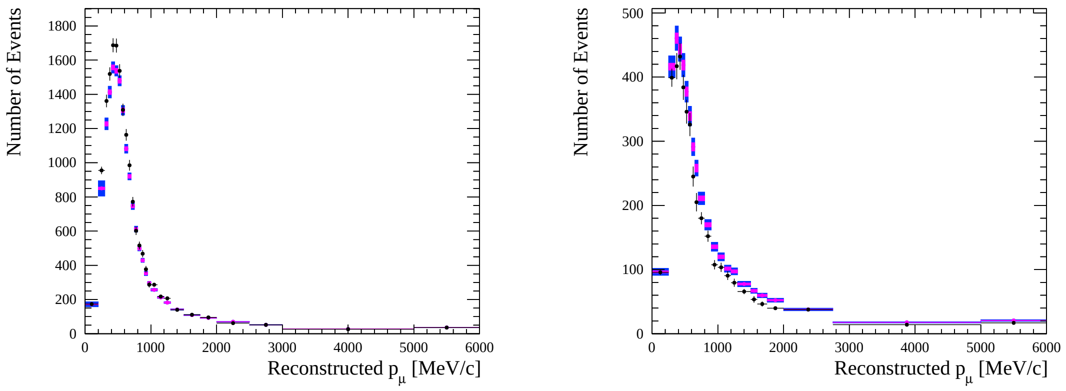

(a) CC0π0p (b) CC0πNp

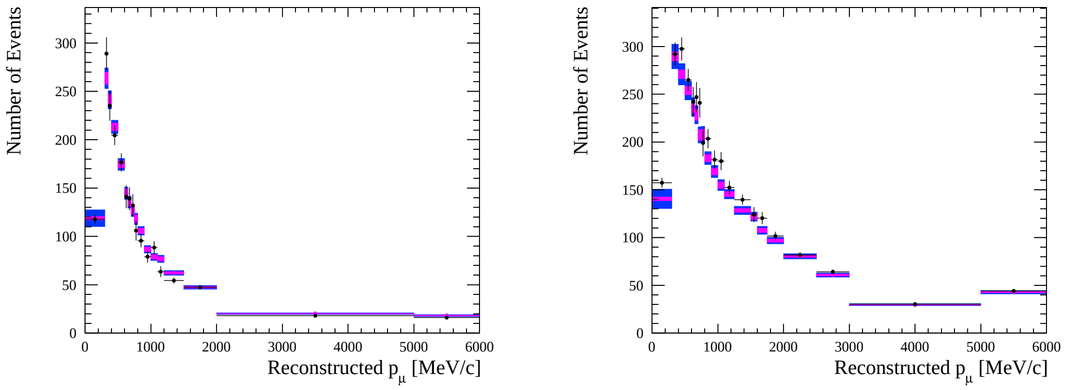

(c) CC1π^+ (d) CC-Photon

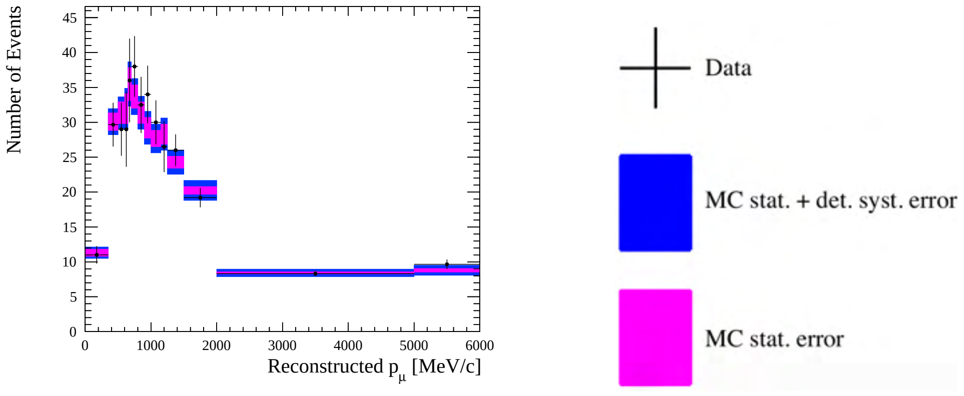

(e) CC-Other

Figure 4.16: Reconstructed muon momentum distributions for ν_μ CC0π0p (a), CC0πNp (b), CC1π^+ (c), CC-Photon (d) and CC-Other (e) FGD2 samples. The error bands refer to MC statistical error (magenta) and the sum in quadrature of the MC statistical and the detector systematic errors (blue). The last bin in momentum includes all events with p_μ greater than 5000 MeV/c.

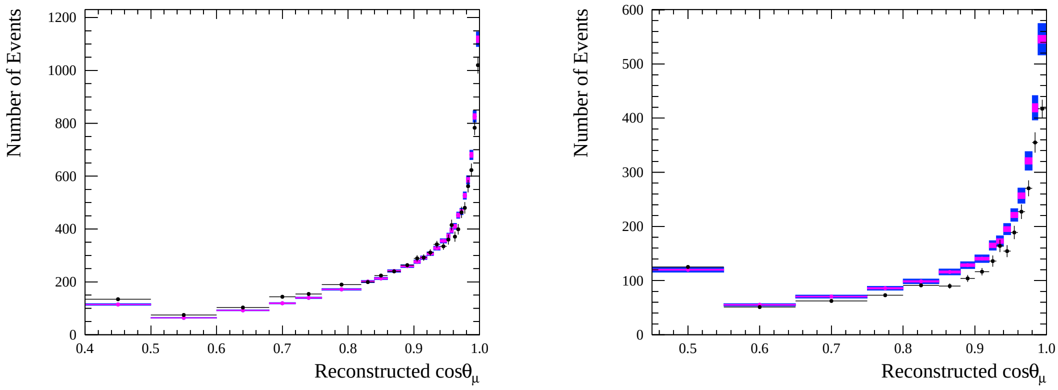

(a) CC0π0p (b) CC0πNp

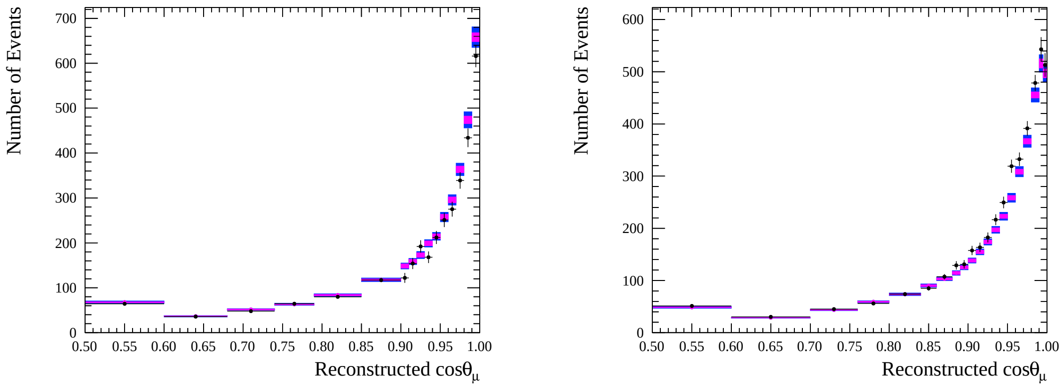

(c) CC1π^+ (d) CC-Photon

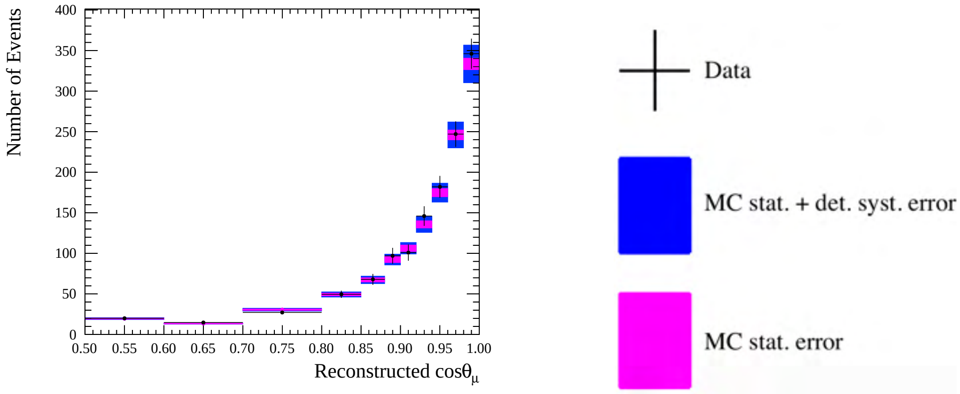

(e) CC-Other

Figure 4.17: Reconstructed muon $\cos\theta$ distributions for ν_μ CC0π0p (a), CC0πNp (b), CC1π^+ (c), CC-Photon (d) and CC-Other (e) FGD2 samples. The error bands refer to MC statistical error (magenta) and the sum in quadrature of the MC statistical and the detector systematic errors (blue). The first bin in $\cos\theta_\mu$ includes all events with $\cos\theta_\mu$ below 0.6.

Systematic error source	**Total error in [%]**									
	CC0π0p		CC0πNp		CC1π^+		CC-Photon		CC-Other	
	FGD1	FGD2	FGD1	FGD2	FGD1	FGD2	FGD1	FGD2	FGD1	FGD2
Observable-like systematics										
Magnetic field distortions	0.003	0.007	0.003	0.009	0.004	0.02	0.007	0.03	0.02	0.02
Momentum resolution	0.005	0.004	0.008	0.008	0.01	0.01	0.03	0.04	0.04	0.07
Momentum scale	0.01	0.02	0.01	0.02	0.02	0.02	0.02	0.04	0.04	0.04
TPC PID	0.31	0.45	0.62	0.79	0.88	1.18	0.48	0.43	1.27	1.40
FGD PID	0.09	0.04	0.18	0.10	0.03	0.04	-	-	0.03	0.03
Efficiency-like systematics										
Charge ID efficiency	0.08	0.20	0.24	0.37	0.11	0.32	0.03	0.17	0.07	0.16
TPC cluster efficiency	0.01	0.01	0.02	0.02	0.02	0.02	0.03	0.03	0.03	0.03
TPC tracking efficiency	0.30	0.74	0.75	1.38	0.67	1.40	0.49	0.89	0.66	1.62
TPC-FGD matching efficiency	0.08	0.16	0.19	0.33	0.15	0.23	0.09	0.14	0.14	0.18
FGD tracking efficiency	0.26	0.05	0.82	0.16	0.27	0.03	0.27	0.05	0.30	0.07
Michel electron	0.05	0.08	0.08	0.17	0.28	0.52	0.06	0.06	0.10	0.15
ECal tracking efficiency	0.34	0.38	0.52	0.69	1.07	1.51	1.00	0.89	2.64	4.35
TPC-ECal matching efficiency	0.61	0.32	1.01	1.03	0.74	0.67	0.99	1.04	1.27	1.25
ECal PID EmHip	0.08	0.06	0.06	0.06	0.10	0.07	0.42	0.33	0.09	0.09
ECal photon pile-up	0.07	0.05	0.04	0.04	0.08	0.04	1.17	1.11	0.05	0.04
Normalization systematics										
OOFV background	0.54	0.72	0.14	0.20	0.80	0.67	0.70	0.76	0.17	0.17
Pile-up	0.18	0.17	0.18	0.17	0.18	0.17	0.19	0.18	0.18	0.18
FGD mass	0.57	0.39	0.58	0.40	0.56	0.38	0.54	0.37	0.58	0.40
Pion secondary interactions	0.36	0.38	1.38	1.33	1.31	1.47	1.62	1.21	3.48	3.18
Proton secondary interactions	1.06	1.26	2.61	3.08	0.59	0.75	0.64	0.73	0.84	1.04
Sand muon background	0.06	0.03	0.01	0.01	0.07	0.02	0.02	0.01	0.02	0.006
All										
Total systematic uncertainty	1.68	1.97	3.66	4.25	2.56	3.06	2.75	2.82	4.72	5.69

Table 4.4: Integrated relative errors (in %) for each source of detector systematic uncertainty, in each sample. Since the photon tag is applied before the charged pion tag, where FGD PID is used, the FGD PID uncertainty is not applied to the CC-Photon samples.

Chapter 5

The Near Detector Fit in the T2K Oscillation Analysis

As stated in Chapter 2, the T2K experiment was designed to measure the neutrino oscillation parameters θ_{13}, θ_{23}, Δm^2_{23} and δ_{CP}. To do this, T2K performs multiple oscillation analyses using different fitting frameworks and statistical approaches. The neutrino oscillation parameters are extracted by performing a fit to the oscillated data at the far detector, which requires a good understanding of the unoscillated data at ND280. The event rates at the near and far detectors can be written as a function of neutrino energy, E_ν, as:

$$N^{ND}_{\nu_\alpha}(E_\nu) = \Phi^{ND}_{\nu_\alpha}(E_\nu) \times \epsilon^{ND}(E_\nu) \times \sigma^{ND}_{\nu_\alpha}(E_\nu) \tag{5.1}$$

and

$$N^{FD}_{\nu_\beta}(E_\nu) = \Phi^{FD}_{\nu_\beta}(E_\nu) \times \epsilon^{FD}(E_\nu) \times \sigma^{FD}_{\nu_\beta}(E_\nu) \times P_{\nu_\alpha \to \nu_\beta}(E_\nu) \tag{5.2}$$

respectively, where Φ_{ν_α} is the flux distribution of α flavour (anti)neutrinos; ϵ is the detector reconstruction efficiency of neutrino interactions; σ_{ν_α} is the total cross section of α flavour (anti)neutrinos; and $P_{\nu_\alpha \to \nu_\beta}$ is the probability of an α flavour (anti)neutrino oscillating to a β flavour (anti)neutrino. Eqs. (5.1) and (5.2) highlight that the measurement of the neutrino oscillation probability is dependent on the best understanding of the flux, detector and cross section models, and each is a source of systematic uncertainty that must be constrained as much as possible. To this end, the T2K experiment uses data from the near detector to constrain the flux and cross section systematic uncertainties at the far detector in the oscillation analyses.

This chapter begins with an overview of the T2K analysis strategy used to extract the oscillation parameters, and the flux, detector and cross section models used in the analysis presented in this thesis. The near detector fitting framework of interest for this thesis is then described in detail along with validations that are performed before fitting to data. Finally the results of the near detector fit to data are discussed, and the constraints passed to the far detector groups are presented.

5.1 The T2K Oscillation Analysis

T2K performs three oscillation analyses at the far detector using frameworks called P-Theta [99], VaLOR [100] and MaCh3 [101]. P-Theta and VaLOR are semi-frequentist fitting frameworks that use gradient descent minimisation algorithms to find the best-fit point for the oscillation parameters θ_{13}, θ_{23}, Δm^2_{23} and δ_{CP}. They then marginalise over the “nuisance parameters”: those that describe sources of systematic uncertainty on the result (flux, detector and cross section parameters), but whose final values are not of direct interest. This marginalisation is essentially an integration over the whole range of values for each nuisance parameter, and is achieved by summing over a set of parameter throws. The results obtained from the fits to the data are frequentist confidence limits on the oscillation parameters. The main implementation difference between these two fitters is the choice of variable in which the far detector samples are binned. In VaLOR, the far detector samples are binned in reconstructed neutrino energy, E_{rec}, and the reconstructed angle of the lepton with respect to the beam axis, θ. The P-Theta fitter can use either the $E_{rec} - \theta$ binning used by VaLOR, or a separate binning in reconstructed lepton momentum, p, and reconstructed lepton angle, θ.

The third method, MaCh3, is a Bayesian fitting framework that uses a Markov Chain Monte Carlo (MCMC) to sample the parameter space. The results of this fit are posterior probability distributions for the oscillation parameters. The oscillation parameter results are then expressed as Bayesian credible intervals, with the best-fit point being at the maximum of the posterior distribution. In the MaCh3 method, the far detector samples are only binned in one dimension, the reconstructed neutrino

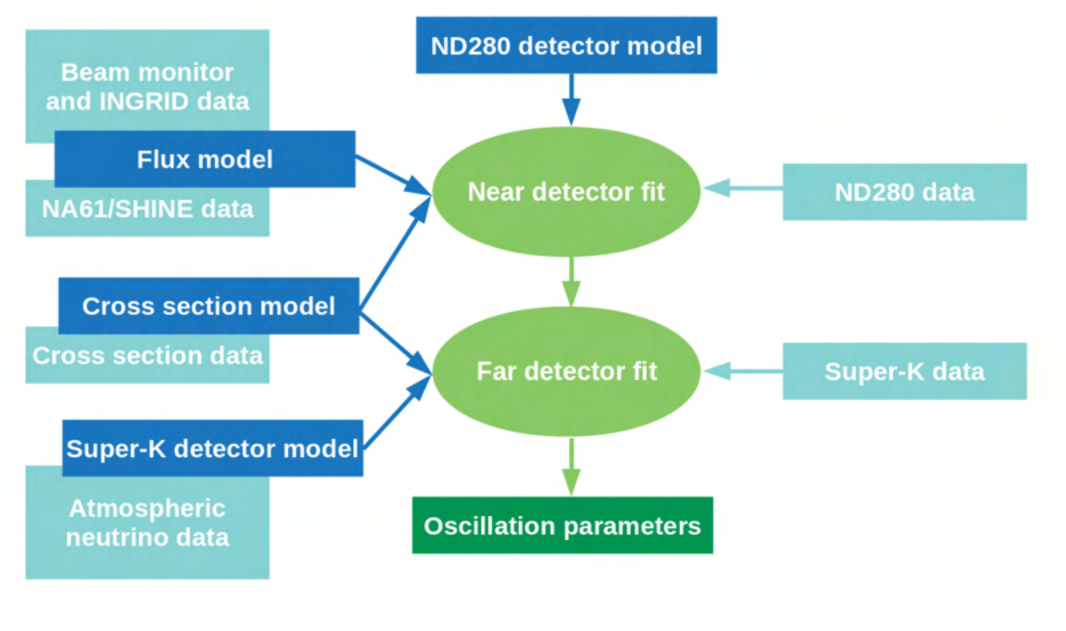

Figure 5.1: An overview of the semi-frequentist oscillation analyses performed by T2K. The near detector fit is performed using the BANFF fitting framwork, while two independent far detector fits are performed using the P-Theta and VaLOR frameworks.

energy, E_{rec}.

The three far detector fitting frameworks have different methods for including the near detector constraints on the flux and cross section parameters. To extract the oscillation parameters, MaCh3 performs a simultaneous fit to near and far detector data. However, P-Theta and VaLOR use near detector constraints provided by a separate near detector fitting framework: BANFF (Beam And ND280 Flux extrapolation task Force). The BANFF fitting framework is semi-frequentist and uses a gradient descent algorithm to find the best-fit point. Although MaCh3 extracts the oscillation parameters in a joint near and far detector fit, it is also able to perform near detector only fits. In both the MaCh3 and BANFF near detector fits, the selected samples are binned in reconstructed muon momentum, p_μ, and the cosine of the reconstructed muon angle with respect to the beam axis, $\cos\theta_\mu$. An overview of the semi-frequentist oscillation analysis strategy, which uses the P-Theta, VaLOR and BANFF fitting frameworks, is given in Fig. 5.1.

5.1.1 Neutrino Flux Model

The T2K flux model is tuned using NA61/SHINE data taken with a replica of the T2K beam target [102]. This helps account for re-interactions occurring in the 90 cm T2K target that were missing in the previously used thin target data [103]. Since the 2020 oscillation results [45] more replica target data from NA61/SHINE has been included, which improves measurements of pions and kaons produced in interactions in the target material, allowing further constraint of the flux parameters. A summary of the flux parameters used in the oscillation analysis is given below, while full details of the flux tuning using NA61/SHINE replica-target data can be found in [65].

The flux model has separate parameters for each beam mode, for different neutrino flavours (ν_μ, $\bar{\nu}_\mu$, ν_e and $\bar{\nu}_e$), and for each detector. For each beam mode, neutrino flavour and detector, the flux parameters are binned in true (anti)neutrino energy. The different contributions to the flux uncertainty obtained with the replica target tuning are presented in Fig. 5.2 for the ND280 parameters and Fig. 5.3 for the Super-Kamiokande (SK) parameters. They are also compared to the flux model used in the 2020 analysis [45], showing how the new tuning reduces the uncertainties on these parameters.

The main sources of uncertainty in the flux model are:

- Interactions of protons and produced hadrons with the beam target.
- Mismodeling of materials in the beam target and decay volume.
- Alignment of the proton beam with the graphite target.
- The horn current and magnetic field.
- Alignment of the target with the focusing horns.
- The number of protons on target.

The total uncertainty on the flux at the peak beam energy of 600 MeV is ∼5% for the right-sign neutrino flavours, with the hadron interaction contribution dominating for the majority of the parameters. The proton beam alignment is the second largest

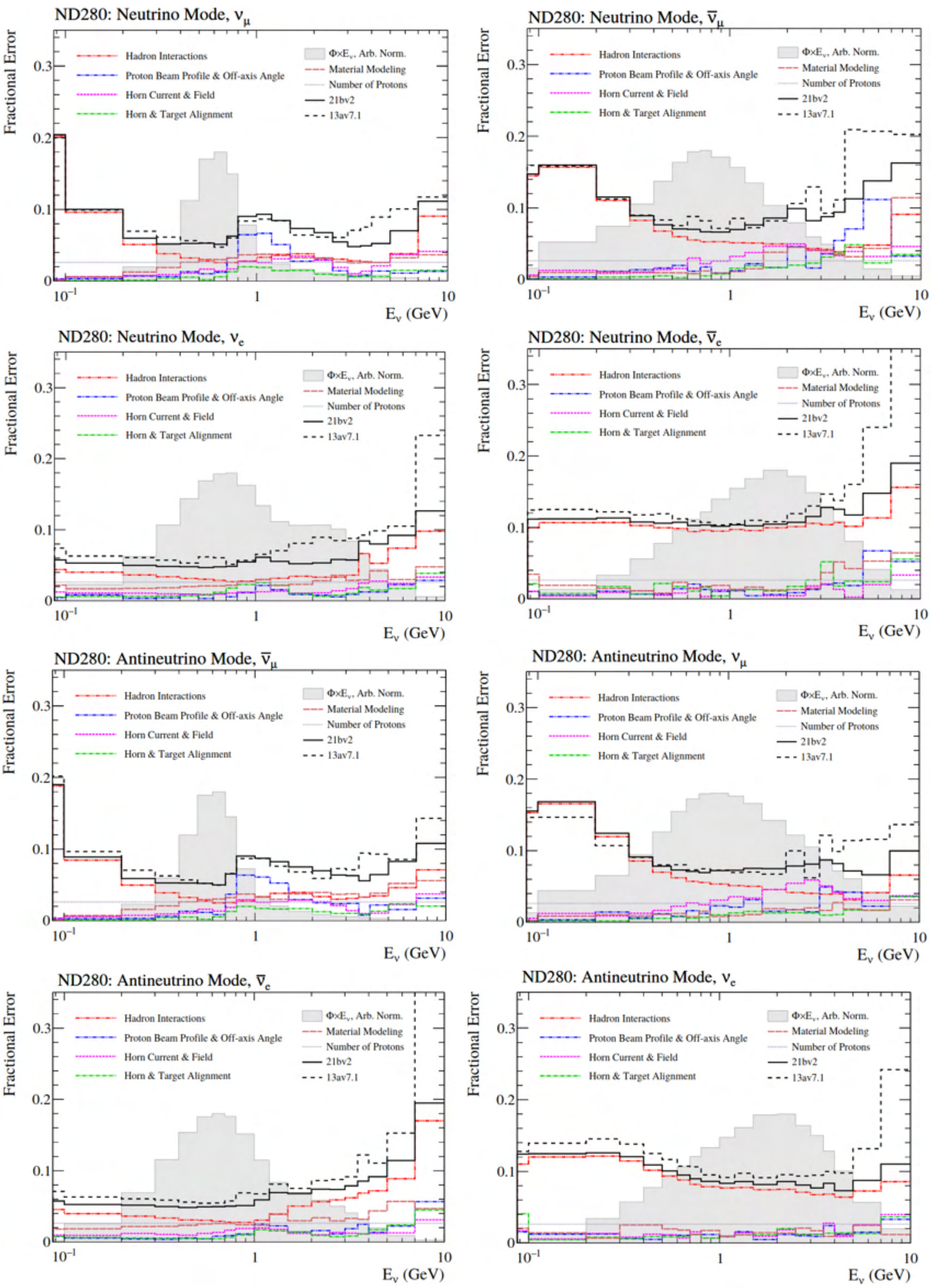

Figure 5.2: Total flux uncertainty as a function of true neutrino energy at ND280 [65]. 21bv2 corresponds to the flux model used in this analysis, while 13av7.1 corresponds to the flux model of the previous analysis [104]. An arbitrary normalisation of the energy spectrum is also shown as a filled shaded grey area.

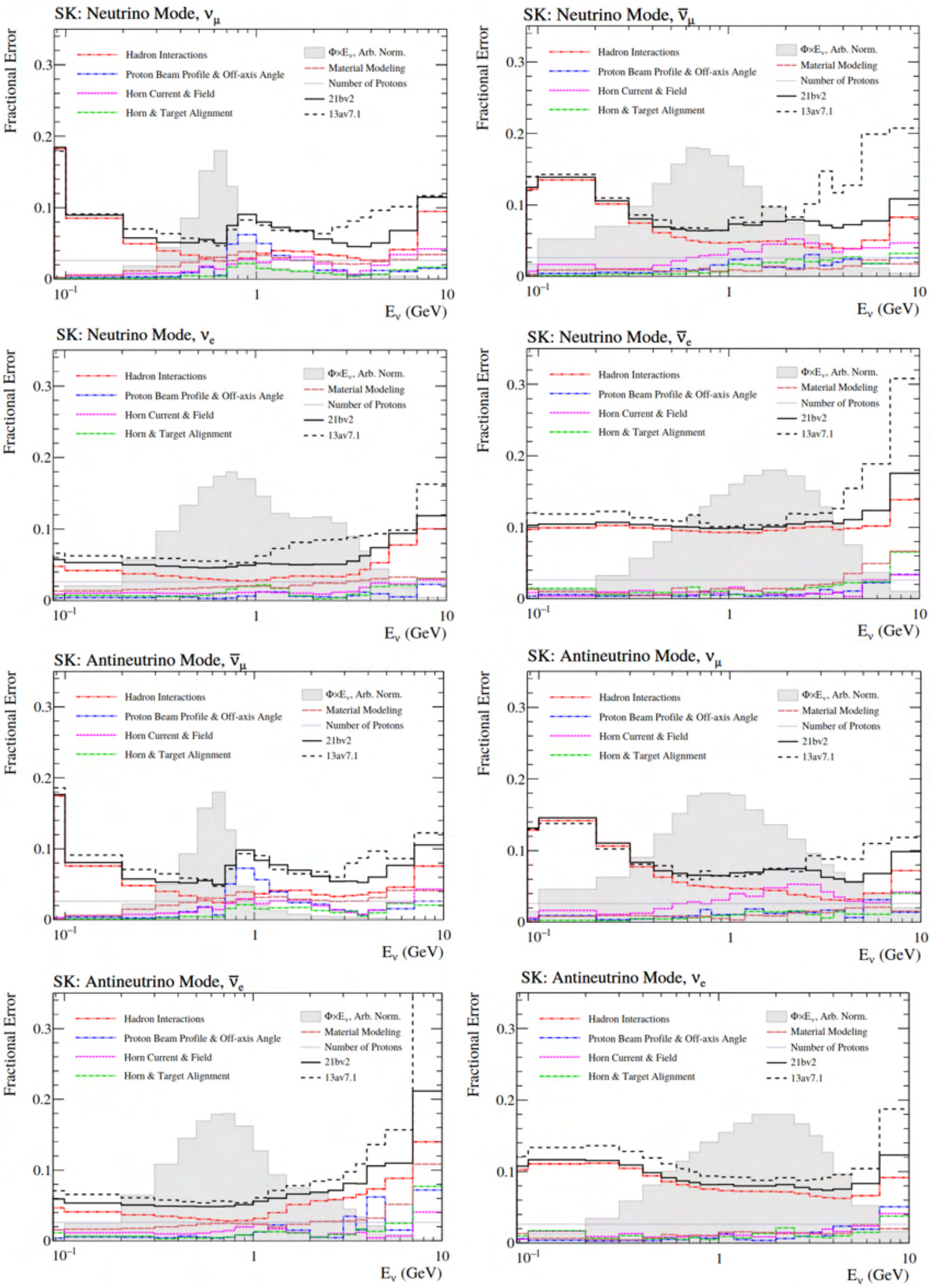

Figure 5.3: Total flux uncertainty as a function of true neutrino energy at Super-Kamiokande [65]. 21bv2 corresponds to the flux model used in this analysis, while 13av7.1 corresponds to the flux model of the previous analysis [104]. An arbitrary normalisation of the energy spectrum is also shown as a filled shaded grey area.

contribution to the flux uncertainties, becoming particularly significant at around 1 GeV.

The flux parameters use the following binning in true (anti)neutrino energy in this analysis:

FHC ν_μ + **RHC** $\bar{\nu}_\mu$:

E_ν^{true} (GeV): 0, 0.4, 0.5, 0.6, 0.7, 1, 1.5, 2.5, 3.5, 5, 7, 30

FHC $\bar{\nu}_\mu$ + **RHC** ν_μ :

E_ν^{true} (GeV): 0, 0.7, 1, 1.5, 2.5, 30

FHC ν_e + **RHC** $\bar{\nu}_e$:

E_ν^{true} (GeV): 0, 0.5, 0.7, 0.8, 1.5, 2.5, 4, 30

FHC $\bar{\nu}_e$ + **RHC** ν_e :

E_ν^{true} (GeV): 0, 2.5, 30

where the numbers presented are the bin edges. The same binning is used for the ND280 and Super-K flux parameters, giving a total of 100 flux parameters. The flux parameters are applied as normalisation parameters, scaling events whose true (anti)neutrino energy sits in the corresponding bin. The prior uncertainties are Gaussian and are centred on the nominal values, with widths coming from the diagonal of a covariance matrix of the flux parameters.

5.1.2 Neutrino Cross Section Model

Contributions to the total ν_μ cross section are shown in Fig. 5.4 alongside the neutrino flux seen by ND280. The dominant interaction type at T2K energies is CCQE, with the next largest contributions coming from CC resonant interactions and CC deep inelastic scattering. Other contributions come from NC interactions and wrong-sign backgrounds ($\bar{\nu}_\mu$ in FHC and ν_μ in RHC). Since the observed event rate is the product of the flux and cross section, and the cross section of each interaction type is not the same, individual parameters are needed to describe uncertainties associated with the cross section model used in the analysis.

The majority of the cross section parameters used in the oscillation analysis can be categorised as either normalisation or shape parameters. Normalisation parame-

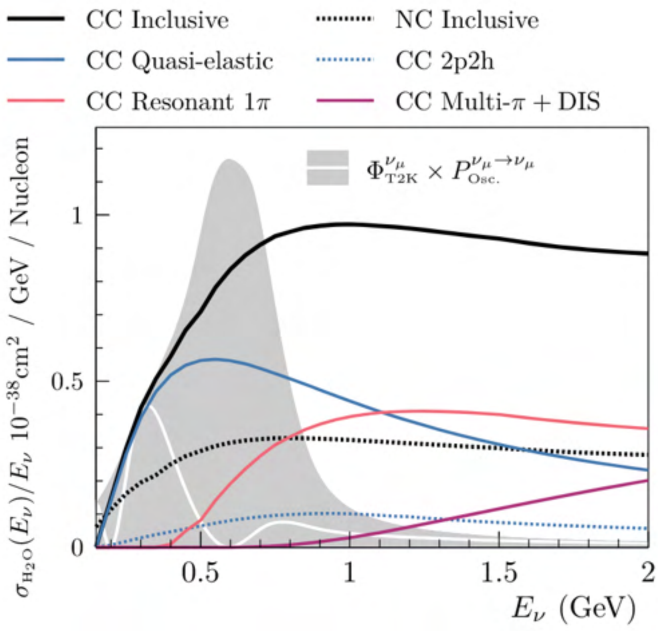

Figure 5.4: Contributions to the total cross section for ν_μ interactions in water predicted by NEUT as a function of neutrino energy. The oscillated ν_μ flux as seen by SK is shown with a white line, and the unoscillated ν_μ flux as seen by ND280 is shown in gray. The figure is adapted from [105].

ters are applied as weights which affect all events defined by a particular interaction type, increasing or decreasing the contribution from a given mode. For this reason, normalisation parameters are not sensitive to event kinematics. Shape parameters, on the other hand, are applied using response functions, with weights given as a function of the parameter value for each event. In this way shape parameters are sensitive to individual event kinematics. The response functions corresponding to cross section shape-like parameters are commonly referred to as splines.

A summary of the cross section systematic parameters used in this analysis is given below; more details can be found in [106].

CCQE Parameters

The nuclear ground state model used for CCQE interactions is the Benhar Spectral Function (SF) model [16]. The analysis includes several sets of uncertainties to account for imperfections in the model:

Axial mass, M_A^{QE}: This is a splined parameter for the axial mass in the dipole form factor for CCQE interactions. The prior value and uncertainty is informed by bubble chamber data [107].

Q^2 normalisation: There are three normalisation parameters (indexed 5, 6 and 7 in Table 5.1 and later figures) for three bins in the square of the four momentum transfer, Q^2: 0.25-0.50 GeV^2, 0.50-1.00 GeV^2, and >1.00 GeV^2. The prior values and uncertainties are tuned to MINERνA [108] data to account for differences between the nominal NEUT model and experimental observations.

Spectral function shell model modifications: Several parameters were introduced in this analysis to give more flexibility to the physical features of the SF model. First, a set of Mean Field (MF) parameters that describe the nucleus in the shell model. There are normalisation and splined parameters for the P and S shells of the carbon nucleus, and for the $P_{1/2}$, $P_{3/2}$ and S shells of the oxygen nucleus. The is also an additional splined parameter for both carbon and oxygen nuclei describing Short Range Correlations (SRC) between nucleon pairs that may be produced. This gives a total of five parameters for carbon nuclei and seven parameters for oxygen nuclei, greatly increasing the flexibility and sophistication of the model compared to the 2020 analysis [45, 109].

Pauli Blocking: The NEUT model uses a Fermi Gas (FG) inspired approach to Pauli Blocking (defined in Section 1.3), where the cross section is set to 0 in regions of phase space where the outgoing primary nucleon has a lower value than some Fermi momentum, k_F, taken to be 209 MeV for carbon and oxygen in the MC used in this analysis. Four splined Pauli Blocking parameters are introduced to give freedom to this effect, separating ν and $\bar{\nu}$ interactions on carbon and oxygen.

Optical Potential: The SF model implemented in NEUT does not account for Final State Interactions (FSI, defined in Section 1.3). FSI corrections are applied in two splined Optical Potential dials for carbon and oxygen, which use histograms in energy, q_0, and the magnitude of the three momentum transfer, q_3, to reweight between the model with and without these FSI corrections.

Binding Energy: These parameters allow for shifts in the energy required to remove a nucleon from a nucleus. The effect of these parameters would ideally be implemented as direct shifts to lepton kinematics, corresponding to the change in binding energy. However, such shifts can cause events to move from one kinematic bin to another during the fit, which is problematic for the BANFF minimisation algorithm. Instead of shifting the kinematics, the BANFF fit applies an effective reweighting of CCQE events on a bin-by-bin basis. The MC prediction at various values of the binding energy parameters are compared to the MC prediction when the parameters are at their nominal values. In this way binned splines are produced that can be applied to average the effect of kinematic shifts. This is done for four binding energy parameters for carbon and oxygen, and for ν and $\bar{\nu}$. In addition to these parameters, fits to electron scattering data [106] suggest an additional q_3-dependent term is included in the binding energy, this is referred to as the α correction.

2-particle-2-hole Parameters

2-particle-2-hole (2p2h) interactions, where neutrinos interact with a bound pair of nucleons, are generated using the Nieves model [84], with the following parameters accounting for uncertainties in the model:

2p2h normalisation: Three normalisation parameters are applied to 2p2h events, one for ν events, one for $\bar{\nu}$ events, and one for carbon to oxygen scaling, which is applied to events on oxygen multiplicatively with the ν and $\bar{\nu}$ parameters. The parameter scaling the 2p2h cross section on carbon to that on oxygen is required for extrapolation to the far detector where all of the target nuclei are oxygen.

Nucleon pair shape corrections: These splined parameters account for changes in the distribution of energy and momentum transfer. At one extreme of the parameter value, the distribution consists entirely of Δ-decay-like processes with an associated pion produced, in agreement with the Nieves model, while at the other extreme it is entirely pionless-Δ-decay-like, in agreement with the Martini model [110]. Separate parameters are applied for carbon and oxygen, and for np and nn pairs.

PNNN shape: For neutrinos, 2p2h interactions can occur on either a pn or nn nucleon pair, while for antineutrinos they can occur on np or pp pairs. Which pair the interaction occurs on is particularly important for the FHC CC0π0p and CC0πNp samples. This splined parameter changes the ratio of pn and nn (np or pp) pairs produced in (anti)neutrino 2p2h interactions.

Energy dependent shape corrections: Four additional splined parameters account for the energy dependence of 2p2h interactions. The two extremes of the parameter value again correspond to the Nieves and Martini models. Separate parameters are applied for ν and $\bar{\nu}$, and for high and low energy (anti)neutrinos.

Single Pion Production (SPP) Parameters

Resonant pion production is described by the Rein-Sehgal model [85]. The following uncertainties are applied to this model:

Axial mass, M^{A}_{RES}: This splined parameter allows for changes in the axial mass for resonant interactions. The NEUT nominal value of this parameter is 0.95 GeV, however this was found to be too low when comparing to external data [106]. Therefore the nominal MC is reweighted to a value of 1.07 GeV and a Gaussian uncertainty of 0.15 GeV is applied.

Axial form factor, C^{A}_{5}: This splined parameter describes the normalisation of the axial form factor, C^{A}_{5}, at $Q^2 = 0$ in the Graczyk-Sobczyk parameterisation [86]. The NEUT nominal value of this parameter, 1.01, was found to be too high compared to external data [106], so it has been reweighted to 0.95. A Gaussian uncertainty of 0.15 is applied.

Isospin 1/2 ($I_{1/2}$) background: Additional parameters are included to account for backgrounds to resonant pion production channels. The main source of background is non-resonant isospin 1/2 pion production, where a nucleon is excited but does not produce a resonance, and then emits a final state pion. This splined parameter gives the relative size of the isospin 1/2 non-resonant background compared to resonant isospin 3/2 interactions.

Isospin 1/2 ($I_{1/2}$) background for low momentum pions: An additional parameter is included to account for antineutrino events that produce a single low momentum negative pion, which is likely to be reconstructed as a 0π event at the far detector.

Resonant binding energy: The binding energy applied for resonant interactions, unlike for CCQE, is not applied as direct lepton kinematic shifts in the reweighting software. Instead, these parameters are implemented as standard event-by-event splines similar to other shape parameters. There are separate parameters for carbon and oxygen, and for ν_μ and $\bar{\nu}_\mu$.

Rein-Sehgal Δ decay: This splined parameter allows the fit to move between two methods of pion ejection from the nucleus, from one extreme of the parameter value to the other. The first method isotropically ejects the pion and the nucleon back to back in the resonance rest frame, with no preferred direction for either particle. The second method calculates matrix elements for the nucleon to Δ resonance transition and contracts them with the relevant spherical harmonics.

π^0 normalisation: Two normalisation parameters are applied to resonant interactions that produce a single π^0. Separate parameters are included for ν_μ and $\bar{\nu}_\mu$ interactions.

CC coherent: Separate normalisation parameters are applied to coherent scattering events on carbon and oxygen to account for cross section differences on the two target nuclei. Such events are described by the Rein-Sehgal model [111], however measurements from MINERνA show a difference of 30% in the cross section of this process compared to the Rein-Sehgal model [112]. For this reason a 30% prior uncertainty is applied to these parameters.

Deep Inelastic Scattering Parameters

Deep inelastic scattering (DIS) corresponds to neutrino interactions with quarks inside nucleons. The nucleon is usually broken in such an interaction producing a range of hadronic states. In the MC generation a custom hadronisation model is used. For invariant hadronic masses $1.3 < W < 2.0\,\text{GeV}$, interactions are modelled with NEUT's multiple-pion (multi-π) production mode and Bodek-Yang [88] corrections are applied, while for $W > 2.0\,\text{GeV}$, PYTHIA 5.7 [89] is used to model interactions. The following parameters account for uncertainties in this hybrid model:

CC Bodek-Yang DIS: DIS interactions in NEUT are modelled using parton distribution functions from the GRV98 model [113], with corrections from Bodek and Yang [88]. This splined parameter accounts for difference between the NEUT model with and without these corrections.

Multi-π multiplicity total cross section: This splined parameter changes the total cross section for multi-π interactions to account for differences in the pion multiplicity models in different generators. The two extremes of the parameters correspond to the AGKY hadronic multi-particle production model [114] which has a smooth transition between low and high regions of W^2, and the nominal NEUT model including the hard transition between low and high W^2.

Multi-π multiplicity shape: An additional splined parameter is added in this analysis that allows shape changes in the cross section, binned in W and $N\pi$, between the NEUT and AGKY models, while the total cross section remains fixed.

Multi-π BY vector and axial parameters: These splined parameters account for differences between an updated Bodek-Yang low Q^2 neutrino DIS model [115] and the older model implemented in NEUT.

CC multi-π normalisation: Two normalisation parameters are included to modify the number of CC multi-π interactions, with separate parameters for ν and $\bar{\nu}$ interactions.

Other DIS parameters: Other DIS event topologies including the production of particles such as η and K are all covered by a single splined parameter referred to as CC Miscellaneous (CC Misc.).

Neutral Current Parameters

Neutral current (NC) processes that produce a photon or π^0 can be misreconstructed at the far detector as electron-like events. The following parameters are implemented to constrain these backgrounds:

NC coherent normalisation: These interactions are modelled in the same way as the CC coherent interactions. Here only one normalisation parameter is applied, without separating by target nucleus, since there aren't sufficient statistics at the near detector to constrain differences between NC interactions on carbon and oxygen.

NC 1γ normalisation: This normalisation parameter is applied to interactions that involve a single photon emission during a non-resonant NC scattering.

NC other normalisation: All other NC interactions, including multi-π and DIS interactions, are grouped together into two normalisation parameters, one for the near detector and one for the far detector.

Coulomb Correction Normalisation

Two normalisation parameters are included to account for the "Coulomb correction". This is the change in momentum experienced by the outgoing charged lepton in a neutrino interaction due to the Coulomb potential of the charged nucleus in which the interaction occurred. Separate parameters are applied to ν and $\bar{\nu}$ interactions.

ν_e/ν_μ and $\bar{\nu}_e/\bar{\nu}_\mu$ differences

Two normalisation parameters are included to account for differences in the ν_e/ν_μ and $\bar{\nu}_e/\bar{\nu}_\mu$ cross sections. These differences are a result of two main effects. First, due to the mass difference of the outgoing lepton the interaction phase space is different, since more of the momentum transferred in a given interaction will be needed to produce the muon mass. Second, the full cross section computation would include many radiative corrections that are not included in the simulation (only leading-order terms are included). These parameters allow for an effective description of these differences.

Final State Interactions

Final state interactions (FSI) are modelled by intranuclear cascade models in NEUT [116]. A pion produced in a neutrino interaction is propagated through the nucleus,

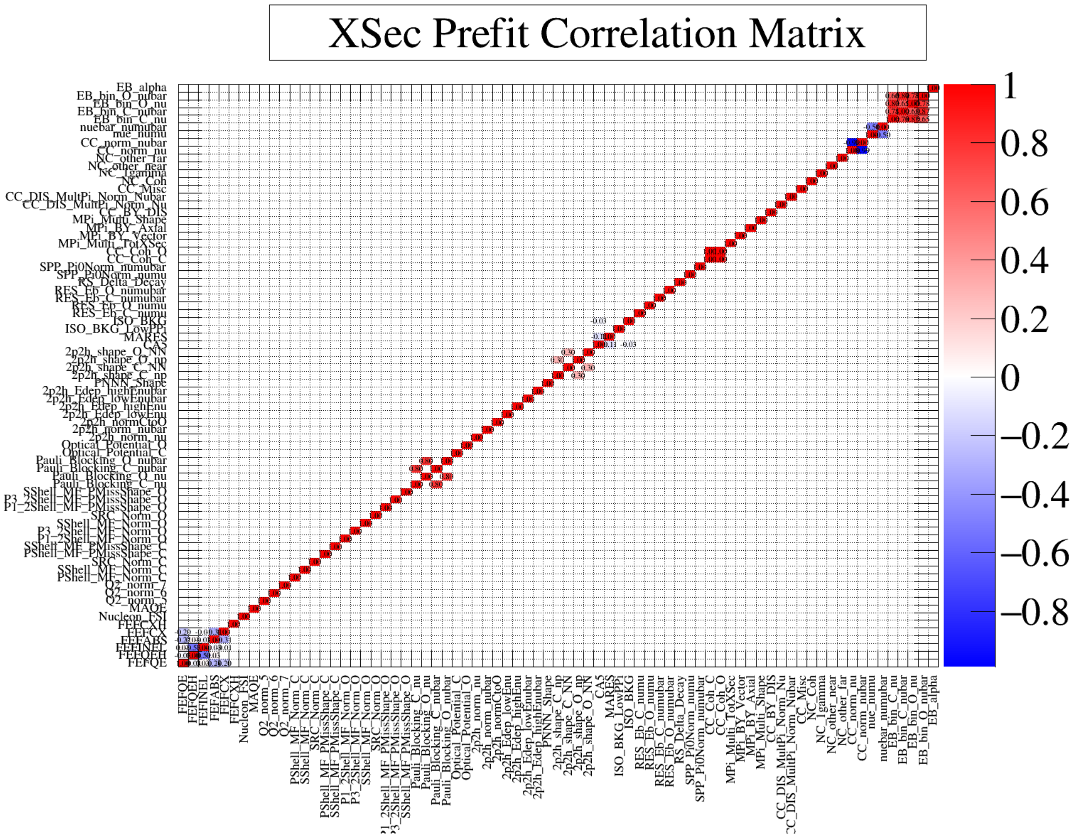

Figure 5.5: The prefit correlation matrix showing the cross section parameters used in this analysis. The axes show the different cross section parameters described in this chapter.

and at each step the probability of each of the following process is calculated: quasi-elastic (QE) scattering, charge exchange, absorption, hadron production. This is repeated, allowing for multiple (possibly different) interactions, until the pion either leaves the nucleus or is absorbed. Separate splined parameters are applied for each of these processes, with quasi-elastic scattering and charge exchange having separate parameters for low and high energy pions.

A single additional FSI parameter was included in this analysis to account for nucleon FSI. The parameter covers several FSI processes and has no requirement on the nucleon momentum.

Summary of Cross Section Model Uncertainties

The cross section model uncertainties detailed above are summarised in Tables 5.1 and 5.2, and the cross section correlation matrix used as input to the near detector fit is shown in Fig. 5.5.

Parameter	Type	Nominal	Uncertainty
M_A^{QE}	Shape	1.03	0.06
Q^2 norm 5	Norm	1	0.11
Q^2 norm 6	Norm	1	0.18
Q^2 norm 7	Norm	1	0.40
P shell MF norm ^{12}C	Norm	0	0.2
S shell MF norm ^{12}C	Norm	0	0.45
SRC norm ^{12}C	Norm	1	2
P shell MF p_{miss} Shape ^{12}C	Shape	0	1
S shell MF p_{miss} Shape ^{12}C	Shape	0	1
P 1/2 shell MF norm ^{16}O	Norm	0	0.2
P 3/2 shell MF norm ^{16}O	Norm	0	0.45
S shell MF norm ^{16}O	Norm	0	0.75
SRC norm ^{16}O	Norm	1	2
P 1/2 shell MF p_{miss} Shape ^{16}O	Shape	0	1
P 3/2 shell MF p_{miss} Shape ^{16}O	Shape	0	1
S shell MF p_{miss} Shape ^{16}O	Shape	0	1
Pauli Blocking ^{12}C ν	Shape	0	1
Pauli Blocking ^{16}O ν	Shape	0	1
Pauli Blocking ^{12}C $\bar{\nu}$	Shape	0	1
Pauli Blocking ^{16}O $\bar{\nu}$	Shape	0	1
Optical Potential ^{12}C	Shape	0	1
Optical Potential ^{16}O	Shape	0	1
2p2h norm ν	Norm	1	1
2p2h norm $\bar{\nu}$	Norm	1	1
2p2h norm C to O	Norm	1	0.2
2p2h E_{dep} low E_ν	Shape	1	1
2p2h E_{dep} high E_ν	Shape	1	1
2p2h E_{dep} low $E_{\bar{\nu}}$	Shape	1	1
2p2h E_{dep} high $E_{\bar{\nu}}$	Shape	1	1
PNNN Shape	Shape	0	0.33
2p2h shape C np	Shape	0	3
2p2h shape C NN	Shape	0	3
2p2h shape O np	Shape	0	3
2p2h shape O NN	Shape	0	3
Eb C ν	Mom Shift	2	6
Eb C $\bar{\nu}$	Mom Shift	0	6
Eb O ν	Mom Shift	4	6
Eb O $\bar{\nu}$	Mom Shift	0	6
Eb α	Mom Shift	0	1

Table 5.1: CC0π cross-section parameters, with the implementation method, prior values and prior uncertainties.

Parameter	Type	Nominal	Uncertainty
FEFQE	Shape	1.069	0.313
FEFQEH	Shape	1.824	0.859
FEFINEL	Shape	1.002	1.101
FEFABS	Shape	1.404	0.432
FEFCX	Shape	0.697	0.305
FEFCXH	Shape	1.8	0.288
Nucleon FSI	Shape	0	0.3
C_A^5	Shape	1.06	0.1
M_A^{RES}	Shape	0.91	0.1
ISO BKG Low p_π	Shape	1.3	1.3
ISO BKG	Shape	1.21	0.27
RES Eb C ν_μ	Shape	25	25
RES Eb O ν_μ	Shape	25	25
RES Eb C $\bar{\nu}_\mu$	Shape	25	25
RES Eb O $\bar{\nu}_\mu$	Shape	25	25
RS Delta Decay	Shape	1	1
SPP π^0 Norm ν_μ	Norm	1	0.3
SPP π^0 Norm $\bar{\nu}_\mu$	Norm	1	0.3
CC Coh C	Norm	1	0.3
CC Coh O	Norm	1	0.3
MPi Multi TotXSec	Shape	0	1
MPi BY Vector	Shape	0	1
MPi BY Axial	Shape	0	1
MPi Multi Shape	Shape	0	1
CC BY DIS	Shape	0	1
CC DIS MultPi Norm ν	Norm	1	0.035
CC DIS MultPi Norm $\bar{\nu}$	Norm	1	0.065
CC Misc	Norm	1	1
NC Coh	Norm	1	0.3
NC 1γ	Norm	1	1
NC other near	Norm	1	0.3
NC other far	Norm	1	0.3
CC norm ν	Norm	1	0.020025
CC norm $\bar{\nu}$	Norm	1	0.0100499
ν_e/ν_μ	Norm	1	0.0282843
$\bar{\nu}_e/\bar{\nu}_\mu$	Norm	1	0.0282843

Table 5.2: Other cross-section parameters, with the implementation method, prior values and prior uncertainties.

5.1.3 Event Selections

Below, the selections used to categorise the FHC (neutrino mode) and RHC (antineutrino mode) samples used in the near detector fit are briefly described. The performance of each selection is discussed and the nominal predictions at ND280 are presented. A brief description of the far detector selections is given at the end of this section.

ND280 FHC ν_μ Selections

The separation of ND280 FHC ν_μ CC events into the 10 samples used in the near detector fit for this oscillation analysis are described in detail in Chapter 3, however a brief summary is given here. For both FGD1 and FGD2, events with a reconstructed μ^- candidate are separated into five samples:

- FHC ν_μ CC0π0p: Events containing no reconstructed protons, pions or photons.
- FHC ν_μ CC0πNp: Events containing no reconstructed pions or photons and one or more reconstructed protons.
- FHC ν_μ CC1π^+: Events containing only one reconstructed pion which is positively charged, and no reconstructed photons.
- FHC ν_μ CC-Photon: Events containing one or more reconstructed photons or neutral pions.
- FHC ν_μ CC-Other: Events containing no reconstructed photons or neutral pions, with more than one postively charged pion and/or any number of negatively charged pions.

ND280 RHC $\bar{\nu}_\mu$ Selections

The cuts applied in the FHC selection of the μ^- can be applied to select the μ^+ in RHC simply by reversing the charge selection of the highest momentum track. The newly implemented photon and proton selections in FHC have not been implemented in RHC, meaning there are six RHC $\bar{\nu}_\mu$ samples, three in each FGD:

- RHC $\bar{\nu}_\mu$ CC0π: Events containing no reconstructed pions.
- RHC $\bar{\nu}_\mu$ CC1π^-: Events containing only one reconstructed negatively charged pion.
- RHC $\bar{\nu}_\mu$ CC-Other: Events containing more than one negatively charged pion and/or any number of positively charged or neutral pions.

ND280 RHC ν_μ Selections

The cuts applied in the FHC selection of the μ^- can also be applied to the select the ν_μ background in RHC. The six RHC ν_μ samples are analogous to the RHC $\bar{\nu}_\mu$ samples, similarly split into FGD1 and FGD2 selections:

- RHC ν_μ CC0π: Events containing no reconstructed pions.
- RHC ν_μ CC1π^+: Events containing only one reconstructed positively charged pion.
- RHC ν_μ CC-Other: Events containing more than one positively charged pion and/or any number of negatively charged or neutral pions.

ND280 Selection Performance

A summary of the efficiency and purity of each of the near detector samples is given in Table 5.3. The FHC ν_μ and RHC $\bar{\nu}_\mu$ CC0π samples have the highest efficiencies and purities in their respective beam modes. The efficiencies of the RHC $\bar{\nu}_\mu$ CC0π samples are higher than those of the corresponding FHC samples since the final state nucleon is a neutron rather than a proton. The neutrons are essentially invisible in the tracking detectors, however the protons do produce tracks, which may be misreconstructed as pions and result in the event being placed in the wrong sample. The RHC $\bar{\nu}_\mu$ CC-Other samples have the lowest purities of all samples, since high pion-multiplicity events have several candidates that may be constructed as muons. In all cases there is no significant difference in the efficiency or purity when comparing the FGD1 selections to those of FGD2.

Interaction	Topology	Target	Efficiency (%)	Purity (%)
FHC ν_μ CC	0π0p	FGD1	46.9	76.3
		FGD2	47.5	72.8
	0πNp	FGD1	46.9	76.3
		FGD2	47.5	72.8
	$1\pi^+$	FGD1	27.1	60.2
		FGD2	23.0	58.5
	Other	FGD1	21.1	52.2
		FGD2	20.6	50.3
	Photon	FGD1	43.0	53.9
		FGD2	43.9	54.2
RHC $\bar{\nu}_\mu$ CC	0π	FGD1	70.0	74.5
		FGD2	69.0	72.7
	$1\pi^-$	FGD1	19.3	45.4
		FGD2	17.2	41.0
	Other	FGD1	26.5	26.3
		FGD2	25.2	26.0
RHC ν_μ CC	0π	FGD1	60.3	55.9
		FGD2	60.3	52.8
	$1\pi^+$	FGD1	30.3	44.4
		FGD2	26.0	44.8
	Other	FGD1	27.4	68.3
		FGD2	27.1	69.5

Table 5.3: The efficiency and purity of each near detector sample used in the oscillation analysis presented in this thesis. The efficiency and purity of the FHC ν_μ CC0π0p and CC0πNp samples are calculated as a combined CC0π sample.

Nominal ND280 Prediction

In the near detector fit, the ND280 samples are binned in reconstructed muon momentum, p_μ, and reconstructed angle of the muon with respect to the beam axis, $\cos\theta_\mu$. The binning for each sample is optimised such that each bin in $p_\mu - \cos\theta_\mu$ contains at least one data event and at least 20 MC events. The requirement of having one data event in each bin is necessary to avoid discontinuities in the likelihood function that is minimised during the BANFF fit. The same binning is used for both the FGD1 samples and FGD2 samples. Optimising the binning scheme in this way results in a total of 4952 sample bins. The nominal MC predictions using this optimised binning are shown as a function of p_μ in Figs. 5.6 to 5.8 and as a function of $\cos\theta_\mu$ in Figs. 5.9 to 5.11. The MC distributions in these figures include nominal flux, cross section and detector weights, calculated at the prior central values of the parameters.

In the FHC ν_μ CC0π0p samples (Fig. 5.6), the MC underestimates the data by 10-20% across the whole range of p_μ. The RHC CC0π samples (Figs. 5.7 and 5.8) are also underestimated, however the discrepancy is significantly smaller, at 5-10%. The discrepancy is visible across the whole $\cos\theta_\mu$ range (Figs. 5.9 to 5.11), but is largest for higher angle muons. The FHC ν_μ CC1π^+ samples are overestimated by the MC (Fig. 5.6), at a level of ∼5%. The FHC ν_μ CC-Other and CC-Photon samples (Fig. 5.6), as well as the RHC $\bar{\nu}_\mu$ CC-Other samples (Fig. 5.7), are all underestimated by around 5-10% in the MC.

Super-Kamiokande Selections

For the oscillation analysis, events at the far detector are separated into six samples. A summary of these samples is given here; for full details of the selection criteria see [117, 118].

- FHC 1Rμ: Events with a single reconstructed lepton ring (1R) which is muon-like in the FHC beam mode.
- FHC 1Re: Events with a single reconstructed electron-like ring in the FHC beam mode.
- FHC 1Re1de: Events with a single reconstructed electron-like ring in the FHC

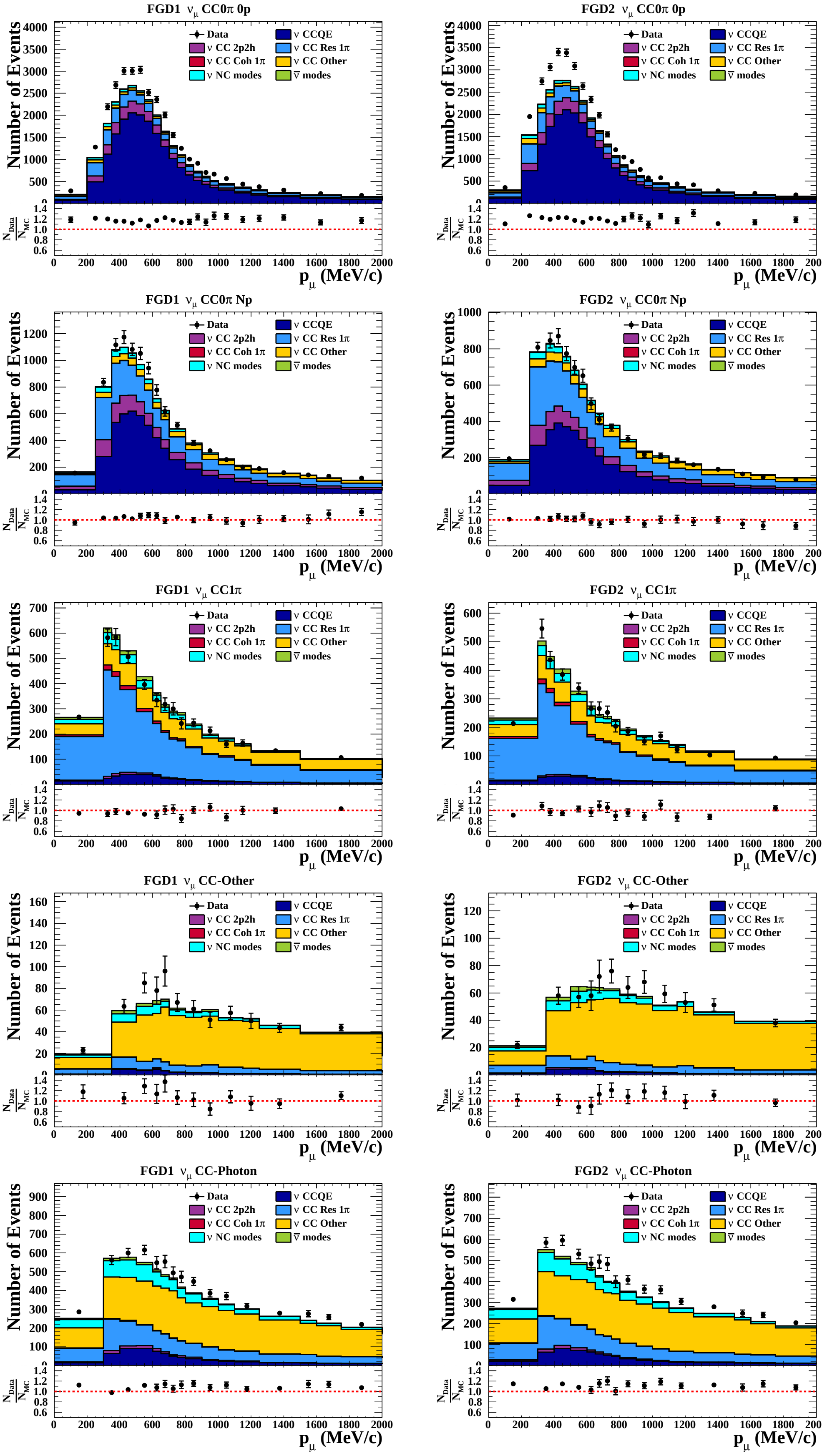

FGD1 ν_μ CC0π 0p

FGD2 ν_μ CC0π 0p

FGD1 ν_μ CC0π Np

FGD2 ν_μ CC0π Np

FGD1 ν_μ CC1π

FGD2 ν_μ CC1π

FGD1 ν_μ CC-Other

FGD2 ν_μ CC-Other

FGD1 ν_μ CC-Photon

FGD2 ν_μ CC-Photon

Figure 5.6: Projections of data and the prefit MC prediction in p_μ broken down by interaction mode for the FHC samples in BANFF.

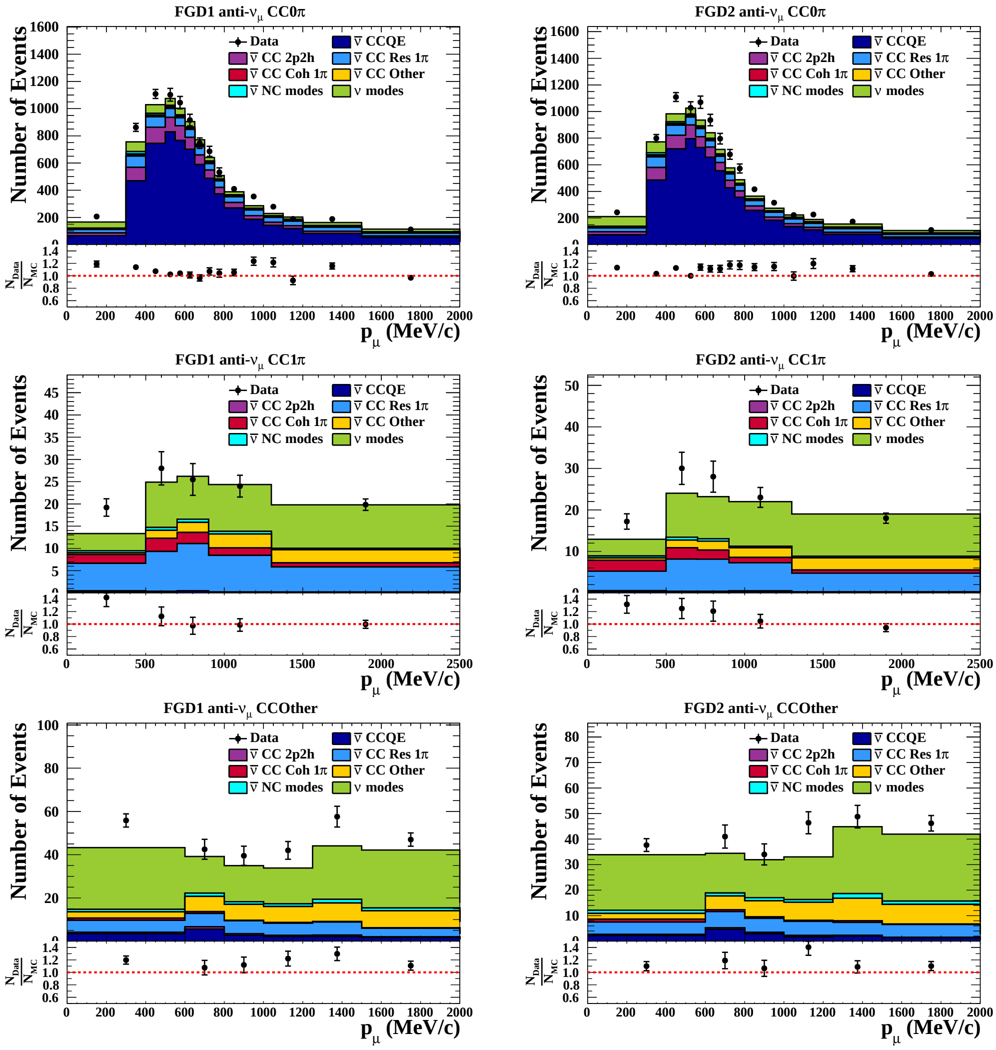

Figure 5.7: Projections of data and the prefit MC prediction in p_μ broken down by interaction mode for the RHC $\bar{\nu}_\mu$ samples in BANFF.

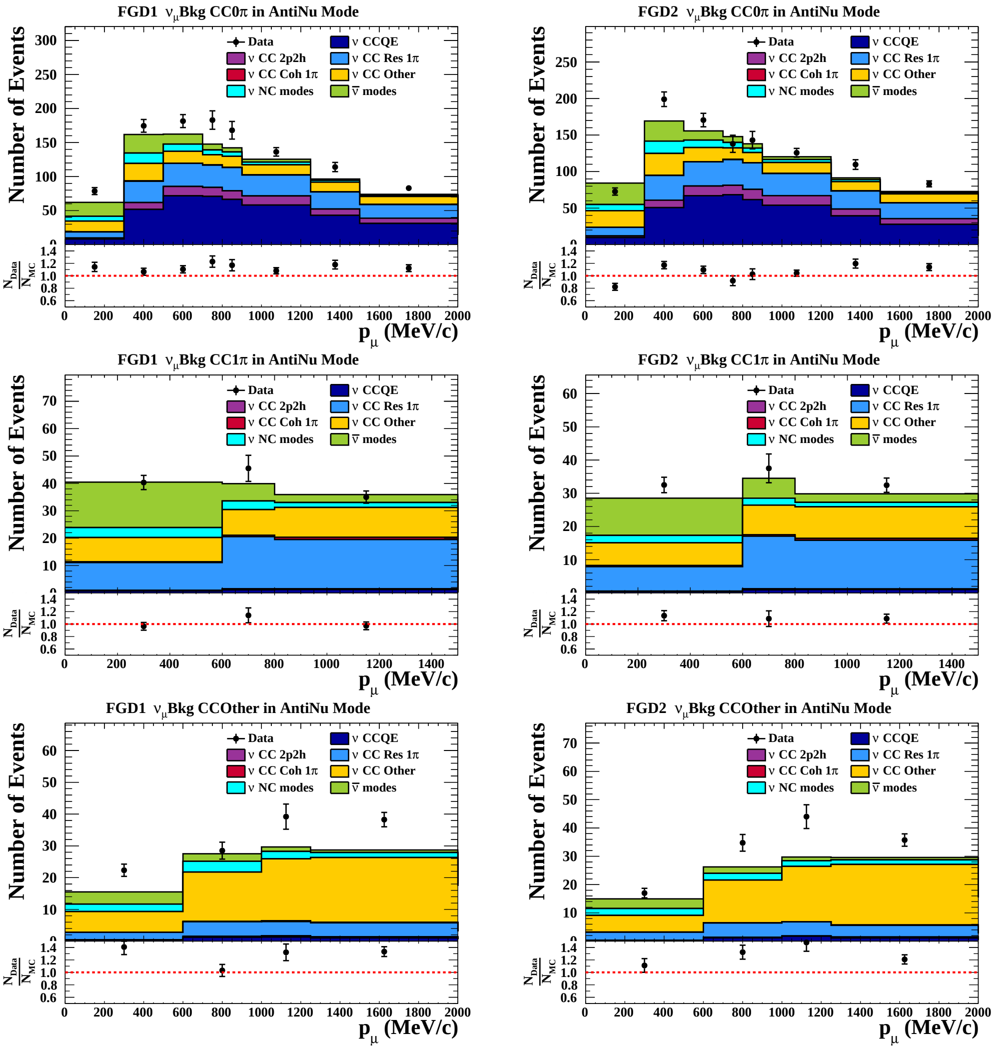

Figure 5.8: Projections of data and the prefit MC prediction in p_μ broken down by interaction mode for RHC ν_μ samples in BANFF.

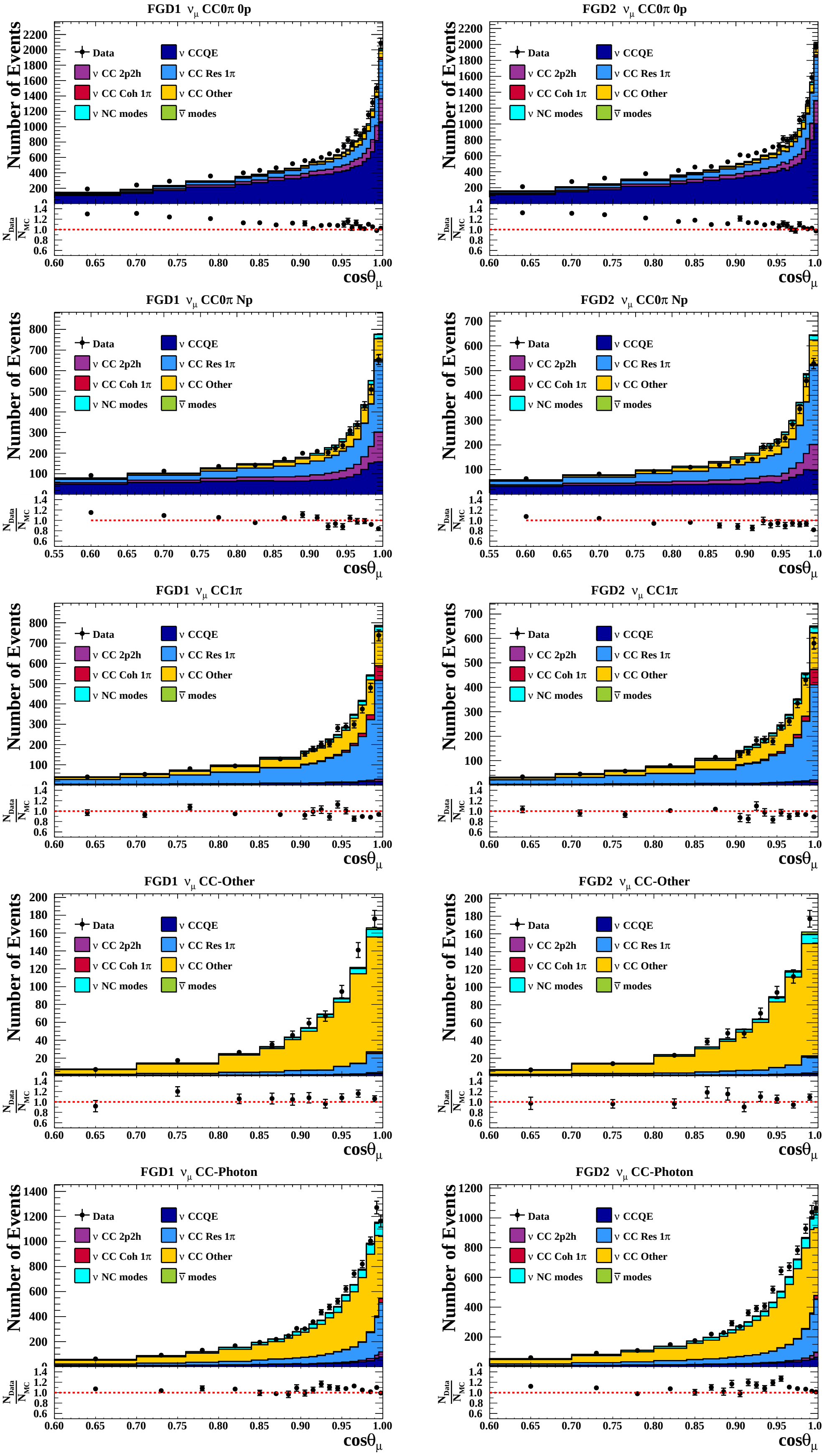

Figure 5.9: Projections of data and the prefit MC prediction in $\cos\theta_\mu$ broken down by interaction mode for the FHC samples in BANFF.

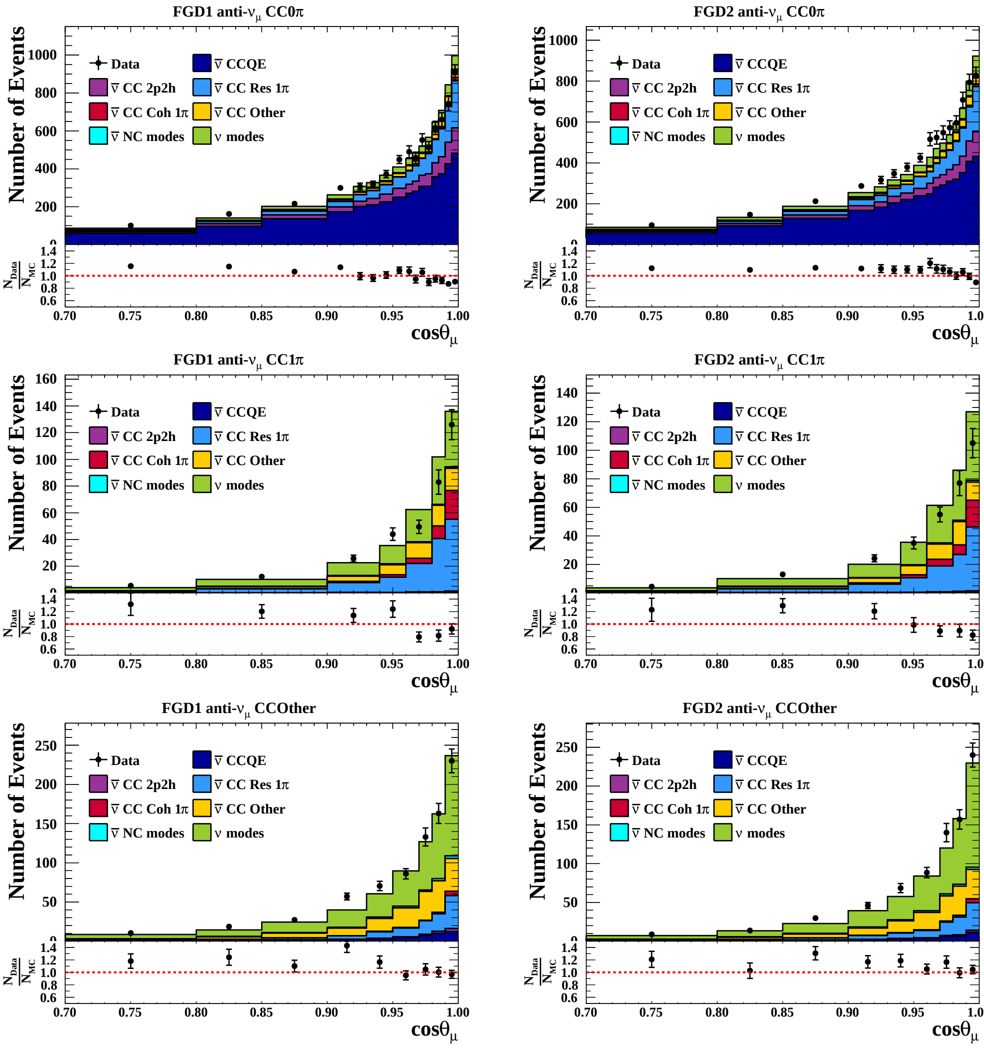

Figure 5.10: Projections of data and the prefit MC prediction in $\cos\theta_\mu$ broken down by interaction mode for the RHC $\bar{\nu}_\mu$ samples in BANFF.

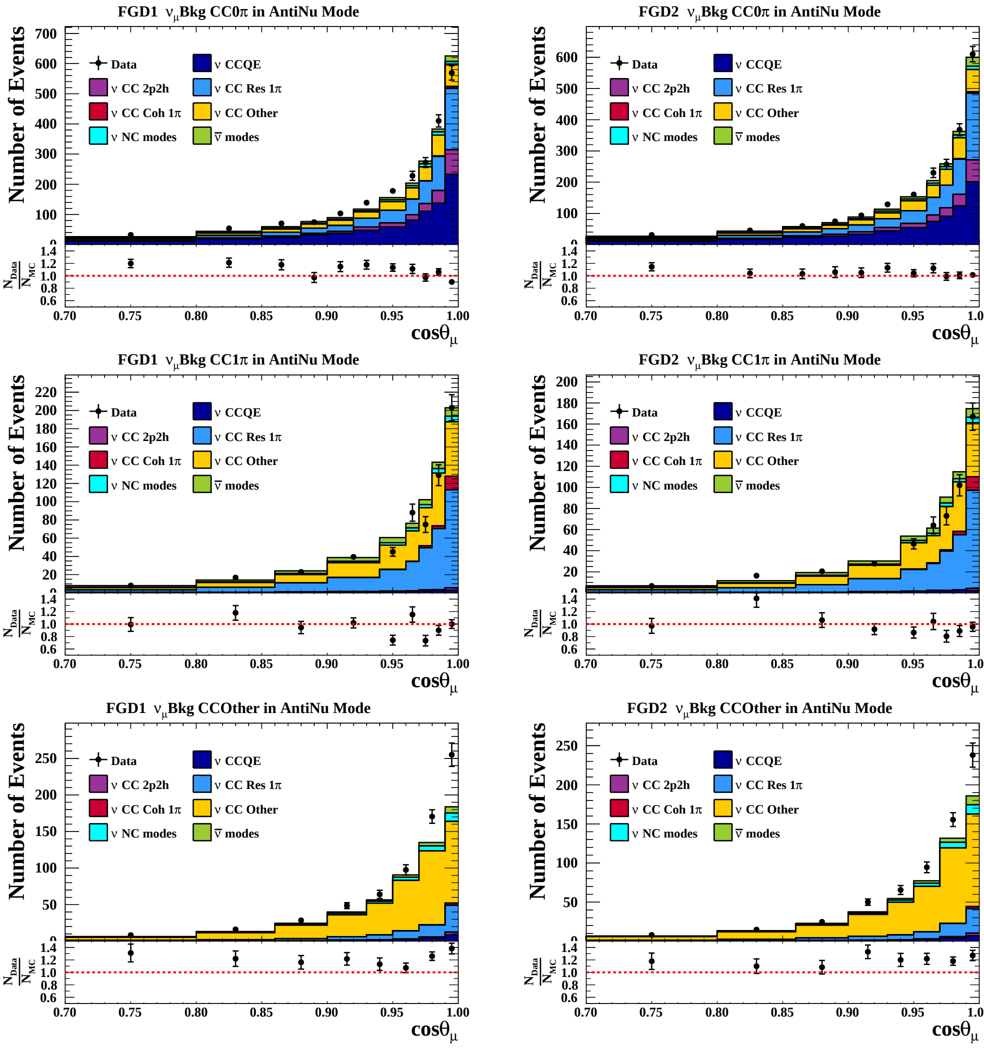

Figure 5.11: Projections of data and the prefit MC prediction in $\cos\theta_\mu$ broken down by interaction mode for the RHC ν_μ selections in BANFF.

beam mode and an additional delayed electron-like ring (1de) which comes from a Michel electron.

- FHC ν_μ CC1π: Events with either two reconstructed muon-like rings and an additional delayed electron-like ring, or one or two reconstructed muon-like rings and two additional delayed electron-like rings.
- RHC 1Rμ: Events with a single reconstructed muon-like ring in the RHC beam mode.
- RHC 1Re: Events with a single reconstructed electron-like ring in the RHC beam mode.

Samples containing a single lepton ring are analogous to the near detector CC0π samples targeting CCQE interactions. The FHC samples containing decay electron rings are analogous to the near detector CC1π^+ samples targeting resonant pion production.

5.1.4 Detector Systematic Uncertainties

The detector systematics associated with the near detector FHC event selections are described in detail in Chapter 4. The same detector systematics are applied to the RHC event selections, with the exception of the ECal systematics introduced for the FHC CC-Photon selection, since the photon tag is not currently used in the RHC selections. The fully correct way of simulating the effect of these detector systematic uncertainties would be to evaluate these on an event-by-event basis during the near detector fit. This is, however, a very computationally expensive endeavour, and varying systematics that can lead to event migration from one fit bin to another could lead to discontinuities in the likelihood.

For this reason, the detector systematic uncertainties are applied in the form of bin normalisation parameters. To produce these detector normalisation parameters, the underlying detector systematic uncertainties are varied in 2000 toy experiments in Psyche (defined in Section 3.1). The resulting variations on the nominal MC prediction are used to calculate the size of the systematic effect on each bin. Varying the detector systematics simultaneously introduces correlations between samples and adjacent kinematic bins within each sample.

Applying a normalistaion parameter to each of the 4952 kinematic bins used in the fit is also computationally intensive, so the binning for the detector systematic parameters applied in the fit is coarser to reduce computation time. The coarser binning definition for the detector normalisation parameters is defined by first producing a detector covariance matrix for all 4952 kinematic bins. Then, adjacent bins are merged iteratively if the systematic uncertainties are within 5% of each other. In this analysis, the process led to a detector normalisation binning with 552 bins. Both the binning used during the fit and the reduced binning used in the detector covariance matrix can be found in [119].

Super-Kamiokande Detector Systematics

Only a summary of the detector systematic treatment at SK is provided here, full details can be found in [117, 120]. Sources of detector systematic uncertainty at the far detector include the water transparency, the PMT timing resolution and the PMT gain. The uncertainties are estimated in a manner similar to the ND280 detector uncertainties, using control samples and comparing data to MC. Three main control samples are used: cosmic muons stopping in the detector, atmospheric neutrino interactions and a π^0 sample. A detector covariance matrix is produced using toy experiments, in a method similar to that of ND280 using toy experiments. There are detector parameters for each neutrino flavour and interaction type in each sample, which are applied as normalisation parameters in the far detector fit.

The SK detector matrix also has two additional contributions included. Uncertainties on hadron secondary interactions (SI) and on photo-nuclear reactions, where photons are absorbed by surrounding nuclei, are computed. The two effects are evaluated separately and produce two additional covariance matrices. These are combined with the detector covariance matrix to produce the final matrix used in the fit.

5.2 The BANFF Near Detector Fit

The BANFF framework uses a gradient-descent algorithm in the MINUIT package of ROOT [121] to minimise the χ^2 test-statistic with respect to the flux, detector and cross section parameters. The fit finds a global minimum of the test-statistic, which maximises the likelihood of having a model that matches the observed data.

The results of the fit are constraints on the flux, detector and cross section parameters, which are summarised with central values and a covariance matrix relating them. The parameters' probability distributions are assumed to be well-modelled by a correlated multi-dimensional Gaussian distribution. The parameter constraints are propagated to the far detector oscillation analyses performed by P-Theta and VaLOR, however parameters that have an effect only at the near detector are not propagated. Parameters that are not propagated include the ND280 detector parameters and cross section parameters only affecting interactions on carbon.

The goodness-of-fit is evaluated by producing toy experiments using the prior constraints on the parameters, statistical fluctuations, and using the nominal MC to fit to the toy experiments. The test-statistic is saved for each toy fit and is used to build a distribution of χ^2 for the prior model. The test-statistic obtained from the finalised data fit is compared to the distribution and a p-value is calculated.

5.2.1 Fitter Framework

The aim of the near detector fit is to maximise a global likelihood such that the near detector event rate prediction matches the data as closely as possible. BANFF uses the MIGRAD gradient descent minimisation algorithm available in MINUIT to find the values of the systematic parameters that produce this best-fit point.

The likelihood calculated in the fit has several separate contributions from systematic and statistical uncertainties. Each source of systematic uncertainty contributes a multivariate Gaussian penalty term defined as:

$$\pi(\boldsymbol{s}) = (2\pi)^{n_s/2}|V_s|^{1/2}e^{-\frac{1}{2}\Delta\boldsymbol{s}(V_s)^{-1}\Delta\boldsymbol{s}^T}. \tag{5.3}$$

$\boldsymbol{s}$ is a vector of systematic parameters, with $\boldsymbol{s} \in \boldsymbol{b}, \boldsymbol{x}, \boldsymbol{d}$ where $\boldsymbol{b}$, $\boldsymbol{x}$ and $\boldsymbol{d}$ correspond to the flux, cross section and detector systematic parameters respectively; n_s is the number of systematic parameters in a given category; $\Delta\boldsymbol{s}$ is a vector containing the differences between the nominal values of the systematic parameters and the values being considered in the given iteration of the fit; and V_s is a covariance matrix for each set of systematic uncertainties.

In each bin the number of events is distributed according to a Poisson distribution:

$$P(N_i^{\text{obs}}|N_i^{\text{pred}}) = \frac{(N_i^{\text{pred}})^{N_i^{\text{obs}}} e^{-N_i^{\text{pred}}}}{N_i^{\text{obs}}!} \tag{5.4}$$

where $P(N_i^{\text{obs}}|N_i^{\text{pred}})$ is the probability of observing N_i^{obs} events in the i-th bin, given the number of events predicted in that bin, N_i^{pred}. The product of these terms over all fit bins represents the statistical contribution to the likelihood.

The quantity that is maximised in the fit is the ratio of the likelihood at a given point in parameter space to the likelihood of the nominal model:

$$\mathscr{L}_{\text{ND280}} = \frac{\pi(\boldsymbol{b})\pi(\boldsymbol{x})\pi(\boldsymbol{d}) \prod_{i=1}^{N_{\text{bins}}} \left((N_i^{\text{pred}})^{N_i^{\text{obs}}} e^{-N_i^{\text{pred}}} / N_i^{\text{obs}}! \right)}{\pi(\boldsymbol{b}_{\text{nom}})\pi(\boldsymbol{x}_{\text{nom}})\pi(\boldsymbol{d}_{\text{nom}}) \prod_{i=1}^{N_{\text{bins}}} \left((N_i^{\text{obs}})^{N_i^{\text{obs}}} e^{-N_i^{\text{obs}}} / N_i^{\text{obs}}! \right)}, \tag{5.5}$$

where $\boldsymbol{b}_{\text{nom}}$, $\boldsymbol{x}_{\text{nom}}$ and $\boldsymbol{d}_{\text{nom}}$ are the Gaussian penalty terms evaluated at the nominal values of the systematic parameters, and N_{bins} is the total number of bins.

In the development of the fitter it was found that, rather than maximising the likelihood itself, it is easier to minimise the negative logarithm of the likelihood, given by:

$$\begin{aligned} -2\log\mathscr{L}_{\text{ND280}} =& 2\sum_{i=0}^{N_{\text{bins}}} \left(N_i^{\text{pred}}(\boldsymbol{b},\boldsymbol{x},\boldsymbol{d}) - N_i^{\text{obs}} + N_i^{\text{obs}} \log \frac{N_i^{\text{obs}}}{N_i^{\text{pred}}(\boldsymbol{b},\boldsymbol{x},\boldsymbol{d})} \right) \\ &+ \sum_{i=0}^{N_b} \sum_{j=0}^{N_b} \Delta\boldsymbol{b}_i \left(V_b^{-1}\right)_{ij} \Delta\boldsymbol{b}_j^T \\ &+ \sum_{i=0}^{N_x} \sum_{j=0}^{N_x} \Delta\boldsymbol{x}_i \left(V_x^{-1}\right)_{ij} \Delta\boldsymbol{x}_j^T \\ &+ \sum_{i=0}^{N_d} \sum_{j=0}^{N_d} \Delta\boldsymbol{d}_i \left(V_d^{-1}\right)_{ij} \Delta\boldsymbol{d}_j^T \\ &\equiv \Delta\chi^2_{\text{ND280}} \end{aligned} \tag{5.6}$$

where N_b, N_x and N_d are the numbers of flux, cross section and detector parameters respectively. With sufficient statistics, $-2\log\mathscr{L}_{\text{ND280}}$ resembles a χ^2 distribution, and is therefore referred to as $\Delta\chi^2_{\text{ND280}}$ for the rest of this thesis.

The nominal values of the systematic parameters are referred to as the pre-fit values, while the set of parameters which minimise $\Delta\chi^2_{\mathrm{ND280}}$ are referred to as the post-fit values. Before the fit, no prior correlations are assumed between the flux, detector and cross section parameters, though correlations exist within each source of systematic uncertainty. After the fit, correlations exist between the systematic sources, since all of the systematic parameters are varied simultaneously. These correlations are calculated from a post-fit covariance matrix which contains the second derivatives of the parameters at the fit minimum. This matrix is the inverse of the Hessian matrix obtained using the HESSE algorithm in MINUIT.

5.2.2 Fitter Validation

Before the near detector fit can be performed on data, it is essential that changes to the fitting framework are well validated. Three sets of validations performed for this analysis are presented below, but a full and detailed account of all validations of the near detector fit can be found in [119].

Likelihood Scans

The BANFF fit, or more accurately, the minimisation algorithm used in the fit, is particularly sensitive to the smoothness of the likelihood surface in the parameter space, as discontinuities in the derivative of the likelihood surface commonly lead to minimisation failures. It is thus important at an early stage in the validation to check how the likelihood of individual parameters varies. To do this likelihood scans are performed, where parameters are varied individually to 50 equally spaced points between -3σ and $+3\sigma$[1] while all other parameters remain fixed at their pre-fit values. The likelihood is calculated as a function of the parameter, and the resulting functions are visually inspected for discontinuities.

As well as identifying discontinuities, the likelihood scans provide some indication as to which parameters the fit is able to constrain. Fig. 5.12 shows likelihood scans for one of the ND280 FHC ν_μ flux parameters and M_A^{QE} to illustrate this. The scan for the flux parameter shows the Poisson term to the likelihood, labelled as

---

[1] For parameters with a physical boundary less than 3σ away from the nominal value, the scan is performed up to the boundary.

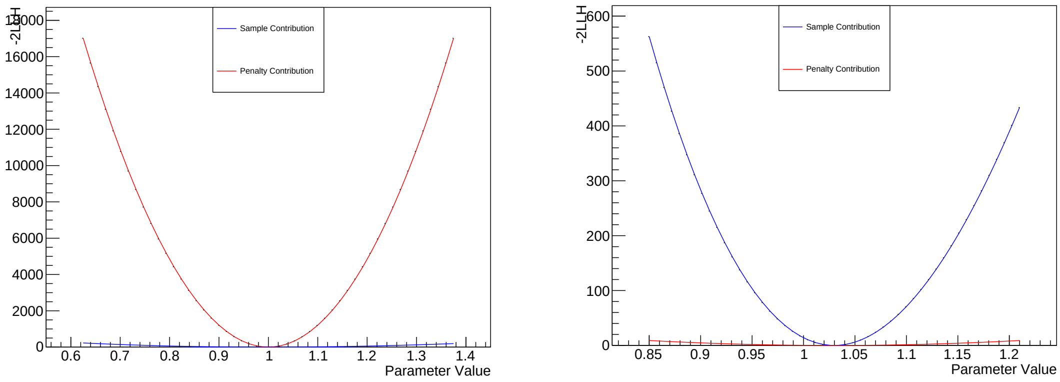

(a) ND280 FHC ν_μ flux parameter 2

(b) M_A^{QE}

Figure 5.12: The sample and penalty contributions to the likelihood for (a) one of the ND280 FHC ν_μ flux parameters and (b) M_A^{QE}.

the sample contribution, is much smaller than the penalty term applied. This flux parameter affects a region of phase space that has low statistics, so it is unsurprising that the fit may be unable to constrain this parameter. Conversely, the scan for M_A^{QE}, which affects a region of phase space with much higher statistics, shows a significantly larger sample contribution to the likelihood than the penalty term. This suggests the fit should be able to constrain this parameter relatively well.

In the BANFF fit, all parameters are assumed to have Gaussian uncertainties around the prior central value. For this reason, all of the penalty contributions to the likelihood, which describe the uncertainties, are also Gaussian. The contribution to the $\Delta\chi^2$ from a Gaussian parameter is quadratic, reflecting the fact that event rate changes in the samples are symmetric around the likelihood maximum. Although the Gaussian approximation is valid for many of the parameters used in the near detector fit, there are some for which it is not a good approximation, for example Fig. 5.13 shows likelihood scans for Nucleon FSI and Pauli Blocking O ν. In both cases, the non-Gaussian behaviour is due to the physical implementation of these parameters in the NEUT model. The non-Gaussian sample contributions do not cause problems for the fitting machinery.

Although the likelihood scans provide indications of parameters that may be well-constrained by the fit, it is not possible to extract constraints from the scan itself, since parameters are varied individually and no correlations between parameters are taken into account. In order to extract constraints on the parameters, all must be

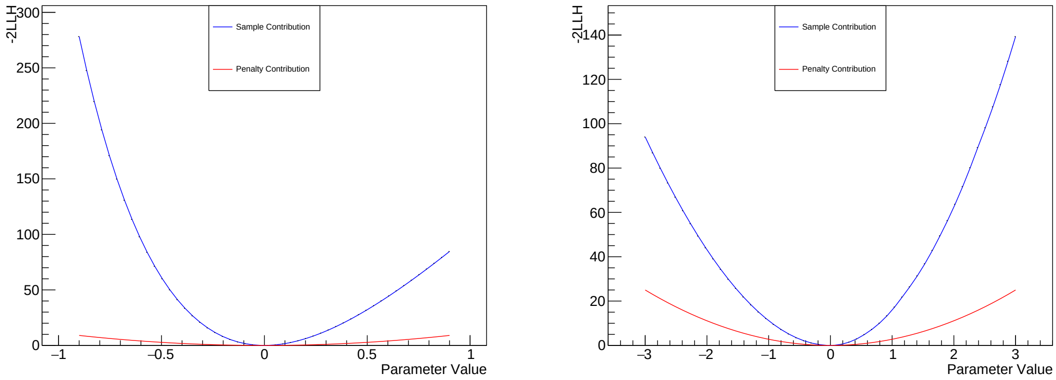

(a) Nucleon FSI

(b) Pauli Blocking O ν

Figure 5.13: The sample and penalty contributions to the likelihood for (a) Nucleon FSI and (b) Pauli Blocking O ν, showing the non-Gaussian behaviour of their sample contributions.

varied simultaneously.

Asimov Fits

In an Asimov fit, the “data” is set to be the nominal MC prediction for each sample, with all systematic parameters at their central values. The nominal MC is then fitted to this “data”, varying all systematic parameters simultaneously, and taking into account correlations between parameters, to give some indication of the expected constraints. Fitting in this way is unphysical, since the number of “data” events can be non-integer as pre-fit weights are applied to the MC to produce the nominal prediction, and there are also no statistical fluctuations in the “data”. The results can however be used to estimate the maximum possible sensitivity of the true fit to data, since the constraints achieved in the Asimov fit show the reduction in systematic uncertainties that would be observed if the model perfectly described the data.

Asimov fits also provide a means to validate the full fitting machinery, and identify parameters that may cause problems for the algorithms used in the fit. A common problem in the BANFF fit occurs during the calculation of the Hessian matrix, after the minimisation is complete. Since the fit assumes all systematic parameters are Gaussian, the errors associated with the post-fit values are always symmetric. However, when the post-fit value of a parameter sits on, or close to, a boundary in parameter space, the HESSE algorithm is unable to sample both sides

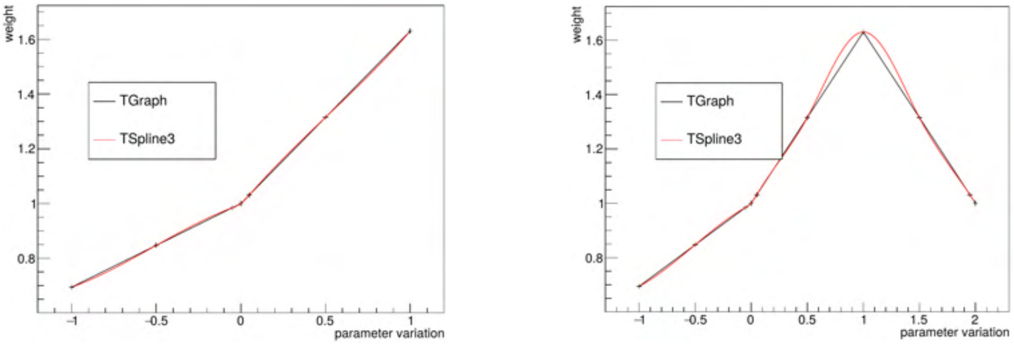

(a) without mirroring (b) with mirroring

Figure 5.14: Examples of linear (TGraph) and cubic (TSpline3) interpolation using ROOT [121] for a parameter (a) without and (b) with mirroring.

of the parameter. This leads to the post-fit uncertainty being reduced, often to unphysically small values, and the Hessian matrix has to be forced positive definite by adding an element to the diagonal. If the Hessian matrix is forced positive definite, the post-fit uncertainties and correlations are no longer valid, and cannot be passed on to the next stage of the oscillation analysis, i.e. the far detector fits.

To avoid this problem, parameters that end up being close to the boundary have their splines mirrored. The spline is reflected at the boundary, thus allowing the HESSE algorithm to sample both sides. It is difficult to predict which parameters will require mirroring in the data fit. In the Asimov fit, all parameters whose prior central values sit on or near to the boundary of the parameter space have their splines mirrored. Although mirroring is an effective way of avoiding the Hessian matrix calculation problem, it does introduce some problems of its own. The spline response becomes distorted around the mirroring point, leading to different weights being applied in this region. An example of this is shown in Fig. 5.14 for one of the 2p2h shape parameters. Without mirroring the spline response closely resembles linear interpolation between the spline knots, however when mirroring is used the spline produces slightly larger weights around the mirrored point. This distortion of the splines for mirrored parameters leads to a reduction in the post-fit correlations between these parameters and others, however previous analyses have shown this has a minimal impact on the analysis [109].

The output from the BANFF Asimov fit for the flux parameters is shown in Fig. 5.15. In the Asimov fit, the post-fit parameter values should be equal to the pre-fit parameter values, for the flux parameters these are all 1.0. Since the near detector

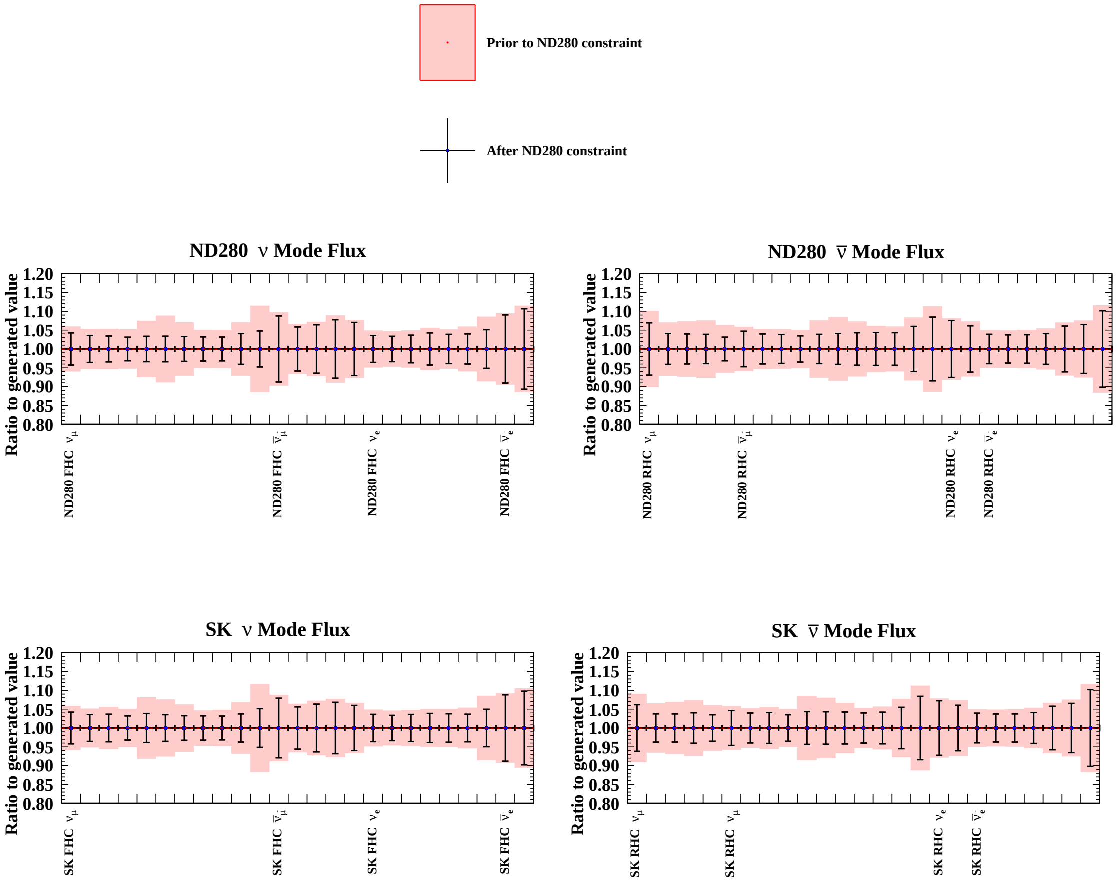

Figure 5.15: The flux parameters used in the oscillation analysis presented in this thesis, and the constraints on these parameters obtained in the BANFF Asimov fit. All parameter values remain at 1.0 as expected in the Asimov fit.

samples all aim to select ν_μ or $\bar{\nu}_\mu$ interactions, the flux parameters corresponding to these neutrino flavours get the greatest constraints. However there is no selection of $\bar{\nu}_\mu$ interactions in FHC, so those flux parameters are mostly constrained by the penalty term, leading to relatively little constraint on those parameters. Similarly, there are no selections of ν_e or $\bar{\nu}_e$ interactions used in the near detector fit, and the corresponding flux parameters are only weakly constrained. Constraints on the far detector flux parameters come from correlations with the near detector flux parameters, so these parameters show the same behaviour.

Fig. 5.16 shows the Asimov fit results for the cross section parameters. The majority of the parameters see a reduced uncertainty after the fit, with the CCQE parameters generally seeing the largest reductions. Several parameters are not varied in the near detector fit, either because there is limited sensitivity to the parameters due to limited statistics, or because the parameter only affects the far detector (e.g. NC other far). The parameters which are not varied in the fit are: the nuclear shell model shape parameters; the 2p2h energy dependent parameters; the low pion momentum $I_{1/2}$ parameter; the NC coherent, NC 1γ and NC other far parameters; and the ν_e/ν_μ and $\bar{\nu}_e/\bar{\nu}_\mu$ normalisation parameters.

Likelihood scans and Asimov studies can indicate which parameters see the largest impact from the addition of the new photon and proton selections described in Chapter 3. Due to the necessarily different detector parameterisation, drawing quantitative comparisons between fits with and without the photon selection is difficult, however some qualitative statements can be made about its impact. Since the CC-Photon sample is dominated by events containing π^0s, it is unsurprising that improvement is seen on the constraint of the SPP π^0 normalisation parameter for ν_μ events when the CC-Photon sample is included. Similarly, improvement is seen on the constraint of the RS delta decay parameter, which also includes π^0 production. The CC misc parameter primarily targets η-producing processes and, since there is also significant η contribution to the CC-Photon sample, improvement is seen here too. Since the photon selection improves the purities of the other samples, small improvements are also seen across a wide range of parameters from the CCQE, 2p2h, FSI and DIS parameter categories.

The Asimov fit results for the detector parameters corresponding to the FHC FGD1 samples are shown in Fig. 5.17. These parameters are not propagated to the far detector, and are simply shown to illustrate the fit's response to the binned normalisation approach used to describe the detector systematic parameters. As expected, the samples and bins with the largest numbers of events see the largest constraints on the uncertainties. This behaviour is seen across all 22 near detector samples.

Fig. 5.18 shows the correlation matrix for all fit parameters before and after the Asimov fit. The flux and detector parameters show strong internal correlations both before and after the fit. Anti-correlations between different sources of systematic uncertainty (flux, cross section and detector) are observed after the fit. Fig. 5.19 shows the correlation matrix for only the flux and cross section parameters. Since the

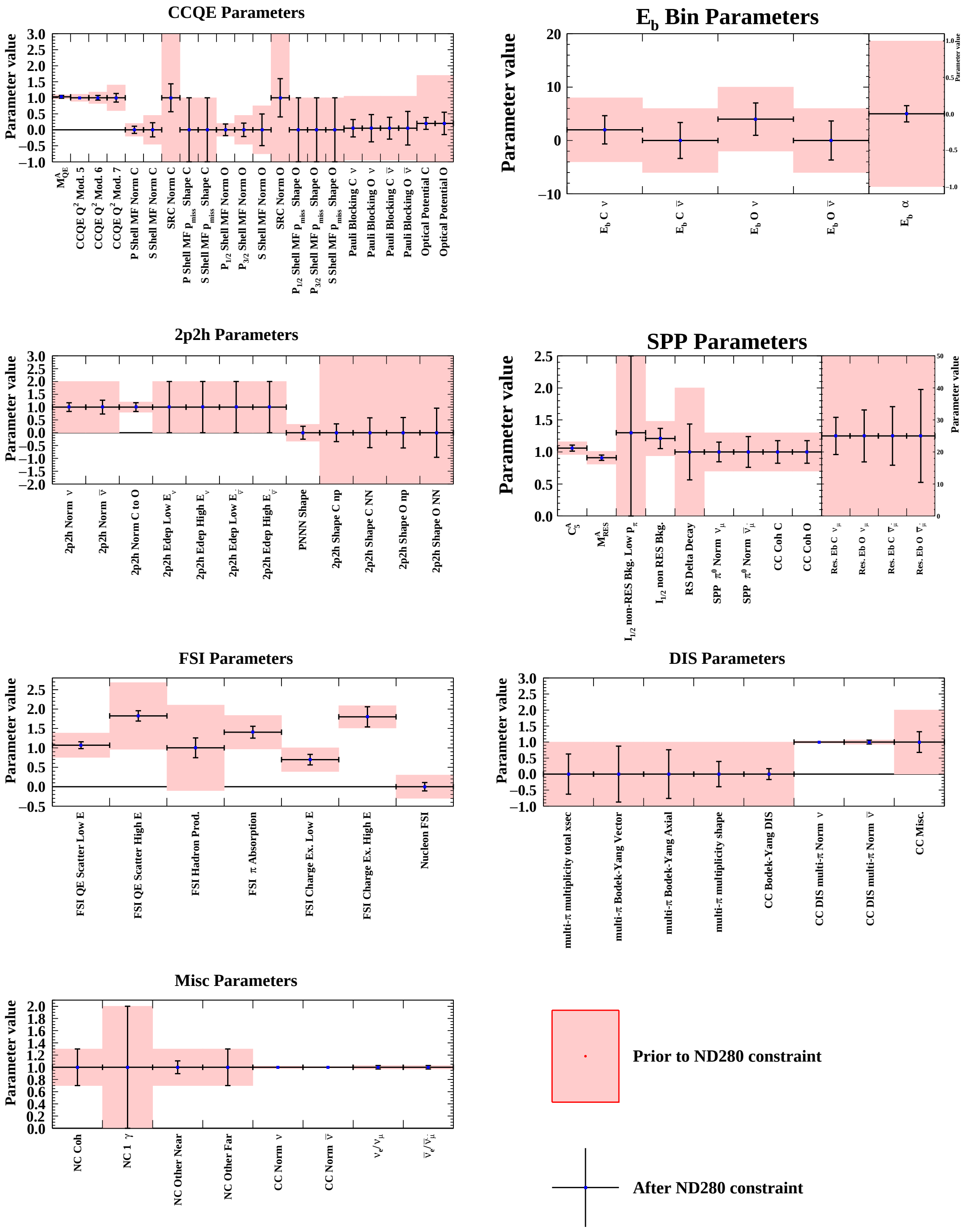

Figure 5.16: The cross section parameters used in the oscillation analysis presented in this thesis, and the constraints on these parameters obtained in the BANFF Asimov fit.

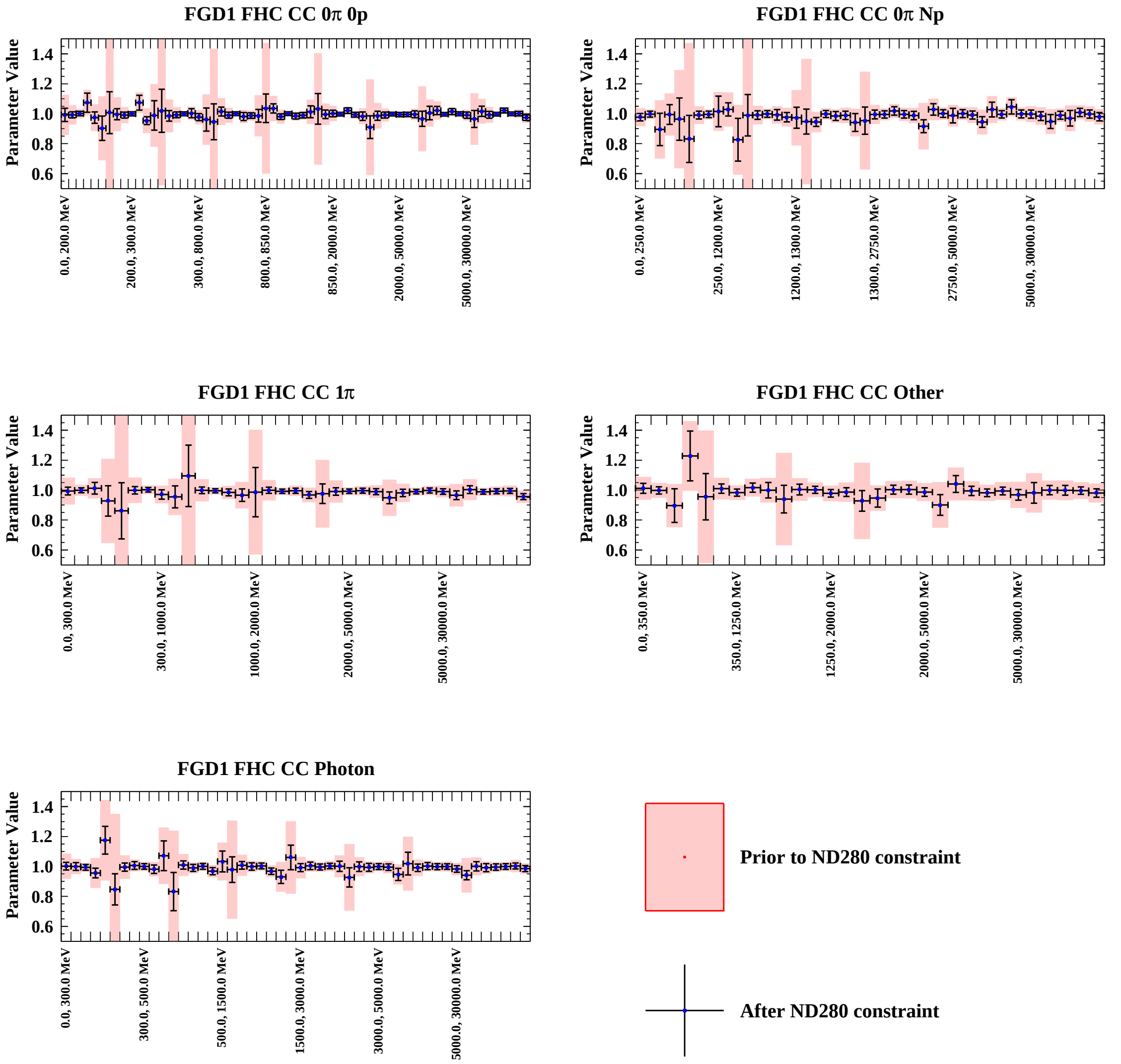

Figure 5.17: The detector parameters for the FHC FGD1 samples used in the oscillation analysis presented in this thesis, and the constraints on these parameters obtained in the BANFF Asimov fit. The two-dimensional binning used in the fit has been linearised for presentation purposes, with labels indicating the first bin in $\cos\theta_\mu$ for each slice in p_μ.

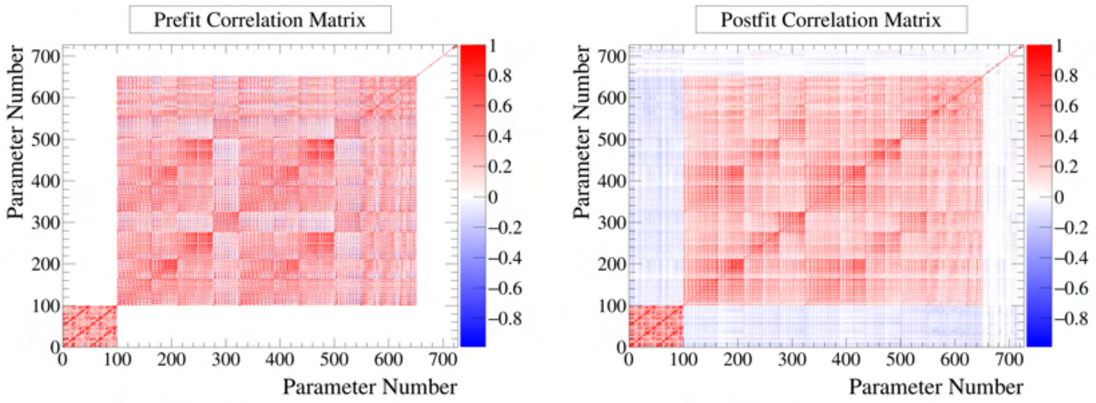

Figure 5.18: The prefit (left) and postfit (right) correlation matrices showing all fit parameters from the BANFF Asimov fit. Parameters 0-99 correspond to the flux parameters; parameters 100-651 correspond to the detector parameters; and parameters 652-726 correspond to the cross section parameters.

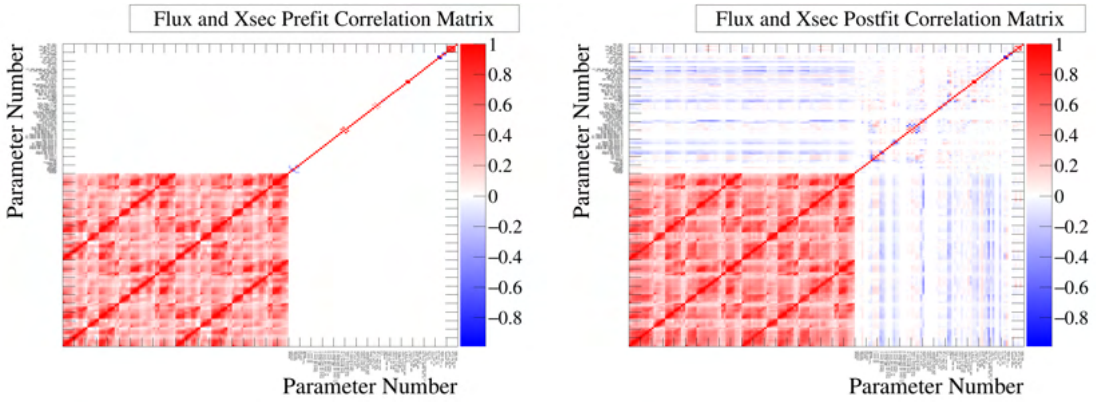

Figure 5.19: The prefit (left) and postfit (right) correlation matrices showing the flux and cross section parameters from the BANFF Asimov fit.

flux parameters are normalisation parameters, they show stronger anti-correlations with the cross section normalisation parameters.

The correlation matrix for only the cross section parameters is shown in Fig. 5.20. The Q^2 normalisation parameters are correlated with each other, and show anti-correlations with M_A^{QE} which is applied to many events in the same region of high Q^2. The S and P shell MF normalisations for carbon and oxygen are strongly anti-correlated. This is not hugely surprising since both parameters work as normalisations of CCQE interactions, differing only in the shell that is affected, which ND280 has limited sensitivity to. Similar behaviour is seen in the oxygen equivalent parameters. The Pauli Blocking and Optical Potential parameters are strongly anti-correlated with each other; a consequence of both sets of parameters affecting the low Q^2 region. The 2p2h shape parameters for carbon are anti-correlated with

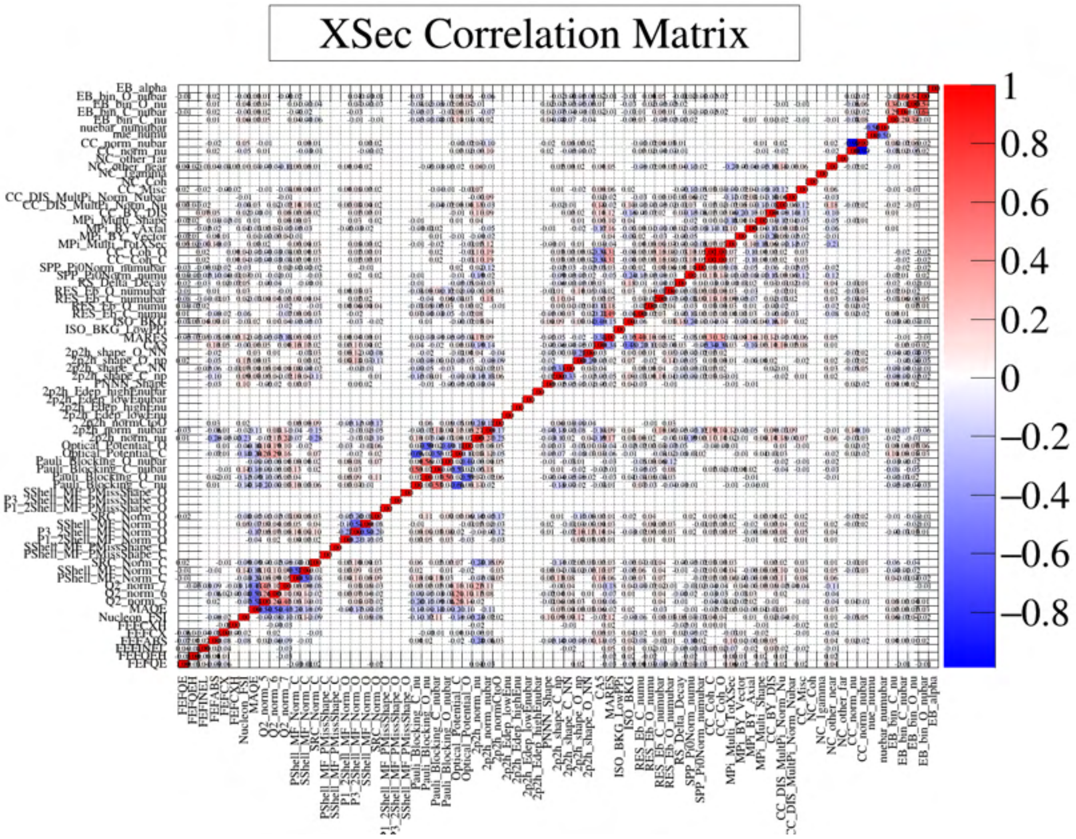

Figure 5.20: The postfit correlation matrix showing the cross section parameters from the BANFF Asimov fit.

each other, as are the 2p2h shape parameters for oxygen.

There is anti-correlation between C_A^5 and M_A^{RES}. These parameters show anti-correlations and correlations with the CC coherent parameters respectively. Similar behaviour is seen between C_A^5 and M_A^{RES} and the resonant binding energy parameters.

Other correlations observed are driven in part, or entirely, by input correlations in the cross section model. The CC coherent parameter for carbon is 100% correlated with the equivalent oxygen parameter. The CC normalisations for ν and $\bar{\nu}$ are strongly anti-correlated, as are the ν_e/ν_μ and $\bar{\nu}_e/\bar{\nu}_\mu$ parameters. The binned CCQE binding energy parameters are correlated with each other.

To generalise the trends above, there are strong (anti-)correlations between parameters affecting similar event topologies, e.g. between M_A^{QE} and the Q^2 normalisations which both affect CCQE events that most commonly get reconstructed as CC0π events, either with or without a proton. There are also small correlations between parameters that affect different types of events, since the event selections used aren't perfect and some events with final state pions will be reconstructed as CC0π events.

Bias Studies

To assess biases in the fitter, the ability of the fitter to explore the parameter space is tested. The flux, cross section and detector parameters are thrown in BANFF according to their prior uncertainties and covariances. A "toy" data set is created by applying a statistical variation to each bin of the nominal Asimov prediction and, using the thrown parameter values as the new prior central values, a fit is performed to the toy data set. For each parameter the fit should return a value of that parameter matching the prior central value, within the uncertainties of the fit.

The pull of a parameter p is defined as the difference between the prior central value of the parameter, p_{prior}, and the fitted value of the parameter, p_{fit}, normalised by its uncertainty, σ_{fit}. Expressed mathematically, this is:

$$\text{pull} = \frac{p_{\text{fit}} - p_{\text{prior}}}{\sigma_{\text{fit}}}. \tag{5.7}$$

If the parameters have been thrown according to their priors, the pulls for a given parameter should be distributed according to a Gaussian. Deviation of the mean from zero suggests a bias in the parameter, whilst a width other than one indicates the uncertainties have been incorrectly estimated. A width greater than one suggests an underestimated uncertainty, while a width below one suggests an overestimated uncertainty on the fitted parameter.

At the time of writing these bias studies are in progress, so no results are presented here. However the p-value calculation discussed in Section 5.3.5 can also identify similar biases, and results are presented in that section.

5.3 Results of the Near Detector Fit

Following extensive validation of the fitting framework, a reliable fit to the ND280 data can be performed. This section details the results of this fit and the impact the results have in the oscillation analysis.

Table 5.4 shows the predicted MC event rates before and after the fit to ND280

Interaction	Topology	Target	Prefit	Postfit	Data	$\Delta\chi^2$	Bins
FHC ν_μ CC	$0\pi0$p	FGD1	18312.50	21112.10	21329	706.83	650
		FGD2	19406.40	22778.60	22935	697.94	
	0πNp	FGD1	9027.02	9268.07	9257	378.36	352
		FGD2	7403.13	7487.09	7373	341.28	
	$1\pi^+$	FGD1	6491.09	6323.92	6224	315.90	272
		FGD2	5311.48	5094.53	5099	284.26	
	Other	FGD1	1621.02	1725.77	1737	145.30	154
		FGD2	1560.34	1590.59	1620	151.83	
	Photon	FGD1	10521.10	11310.80	11156	489.43	400
		FGD2	9537.12	10233.00	10460	425.87	
RHC $\bar{\nu}_\mu$ CC	0π	FGD1	8172.58	8665.70	8676	376.05	306
		FGD2	7815.33	8511.22	8608	373.28	
	$1\pi^-$	FGD1	699.84	716.78	719	65.98	48
		FGD2	654.47	679.99	660	56.08	
	Other	FGD1	1370.95	1478.87	1533	99.82	80
		FGD2	1230.61	1329.42	1396	98.62	
RHC ν_μ CC	0π	FGD1	3444.80	3788.83	3714	144.48	120
		FGD2	3361.06	3719.68	3537	142.26	
	$1\pi^+$	FGD1	1212.63	1228.41	1147	59.87	40
		FGD2	974.48	970.12	955	61.48	
	Other	FGD1	1164.15	1295.52	1425	68.05	54
		FGD2	1101.66	1201.26	1334	60.83	

Table 5.4: Event rates for each of the ND280 samples used in the near detector fit for data and the Monte Carlo predictions before and after the fit. The $\Delta\chi^2$ and number of bins for each sample is also given.

data. It is clear that the postfit event rates show much better agreement to the data than the prefit event rates. The postfit data-MC agreement is also significantly better on a bin-by-bin basis, as seen in Figs. 5.21 to 5.26 which compare the data distributions of p_μ and $\cos\theta_\mu$ to the postfit MC prediction. Substantial improvement is seen when compared with the prefit comparison made in Section 5.1.3. In order to understand why this is the case, the postfit values of the flux, cross section and detector parameters must be considered.

5.3.1 Flux Parameters

Fig. 5.27 shows the postfit values of the near and far detector flux parameters. The FHC ν_μ and FHC ν_e flux parameters, for both the near and far detectors, show energy-dependent pulls away from the nominal model. At low energies the

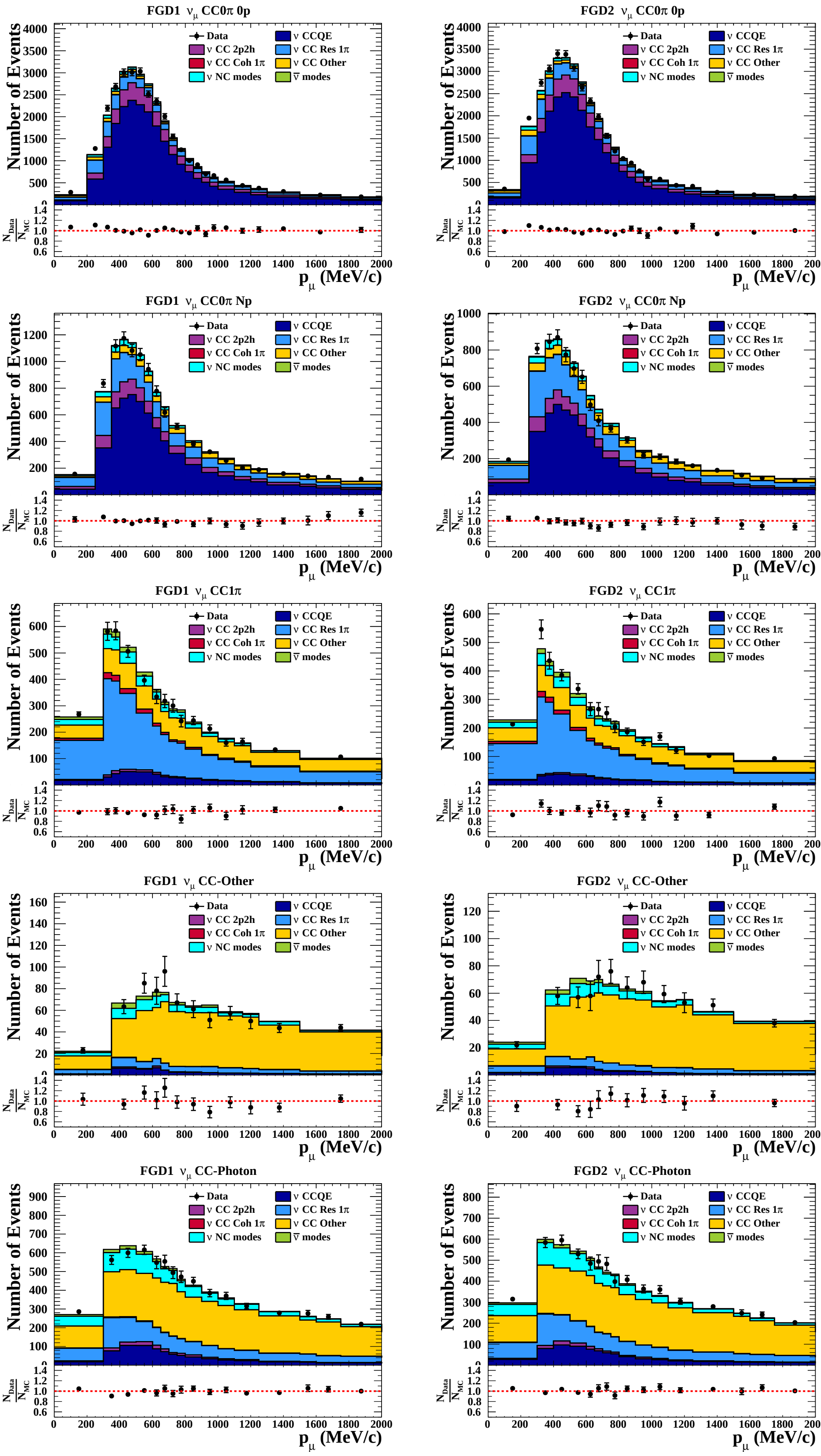

Figure 5.21: p_μ projections of data and the postfit MC prediction broken down by interaction mode for the FHC samples in BANFF.

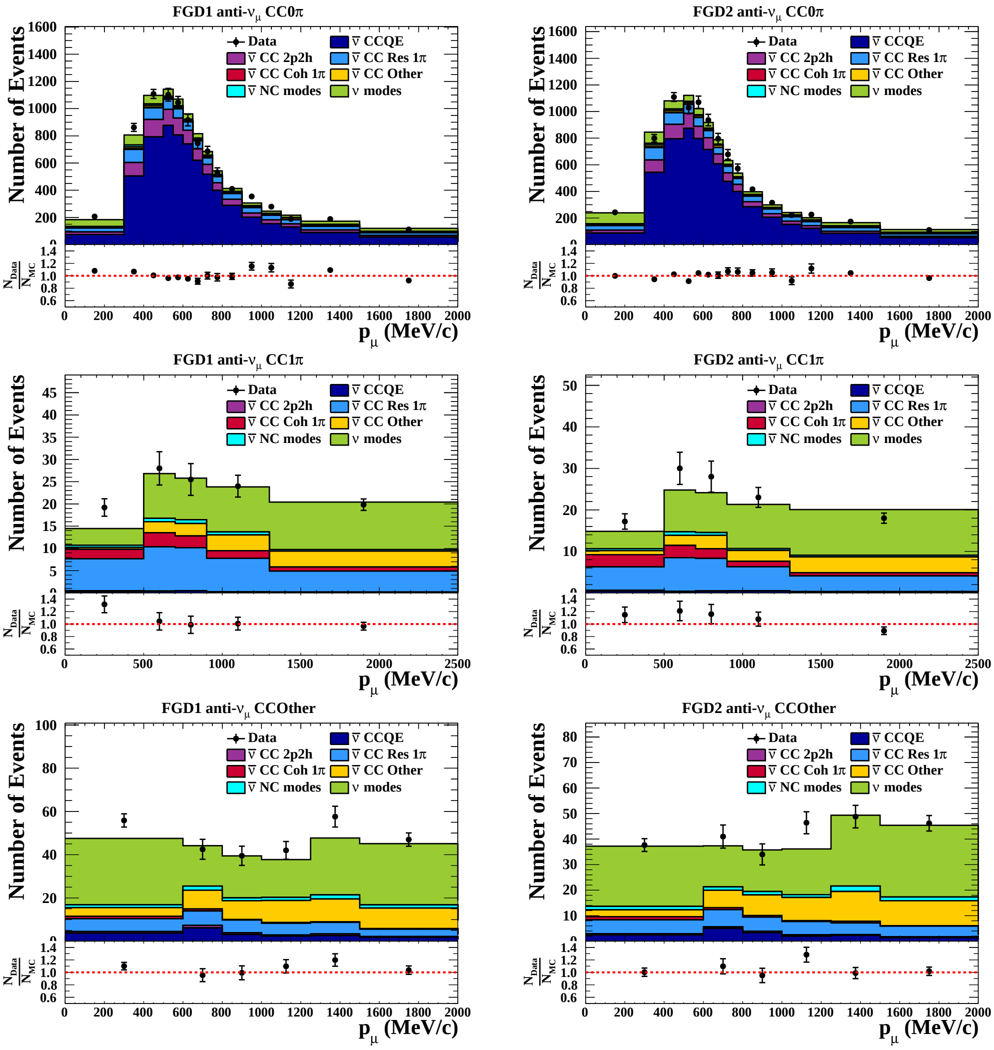

Figure 5.22: p_μ projections of data and the postfit MC prediction broken down by interaction mode for the RHC $\bar{\nu}_\mu$ samples in BANFF.

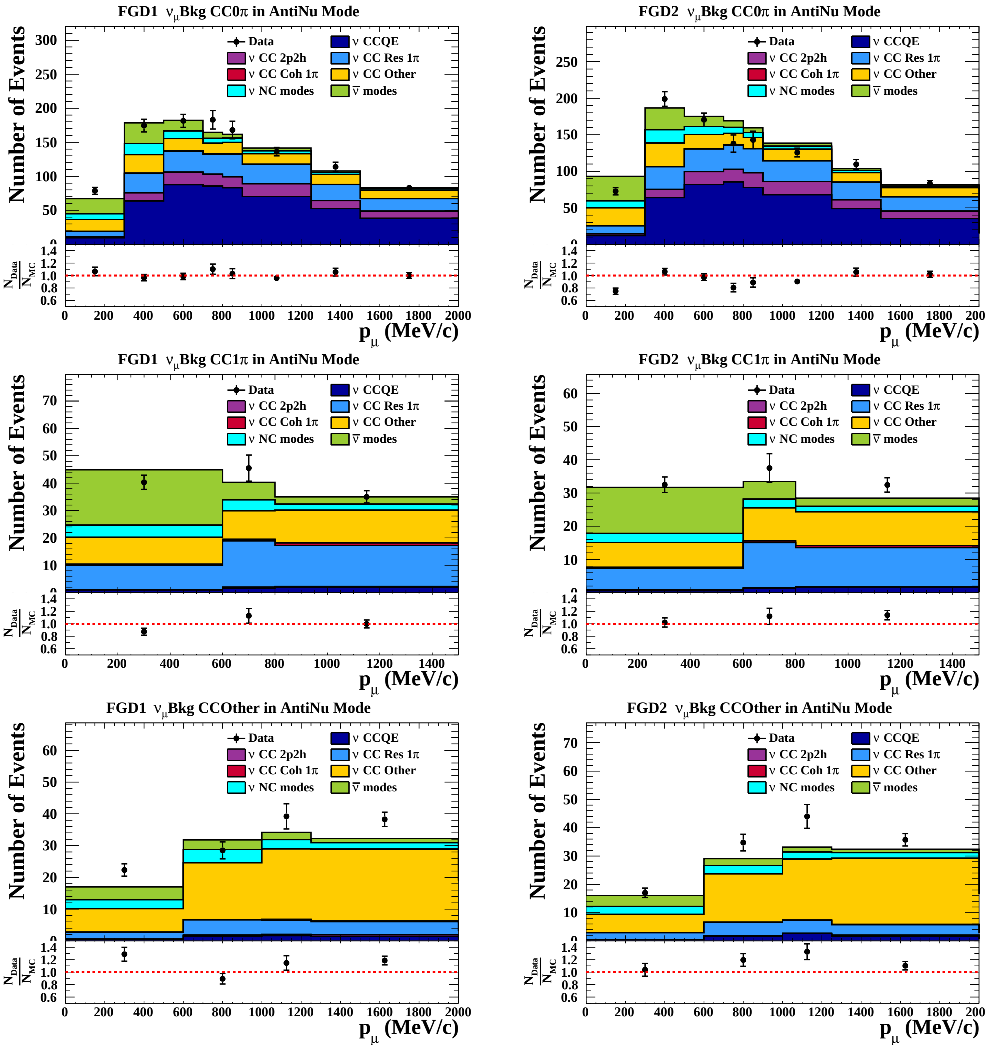

Figure 5.23: p_μ projections of data and the postfit MC prediction broken down by interaction mode for RHC ν_μ samples in BANFF.

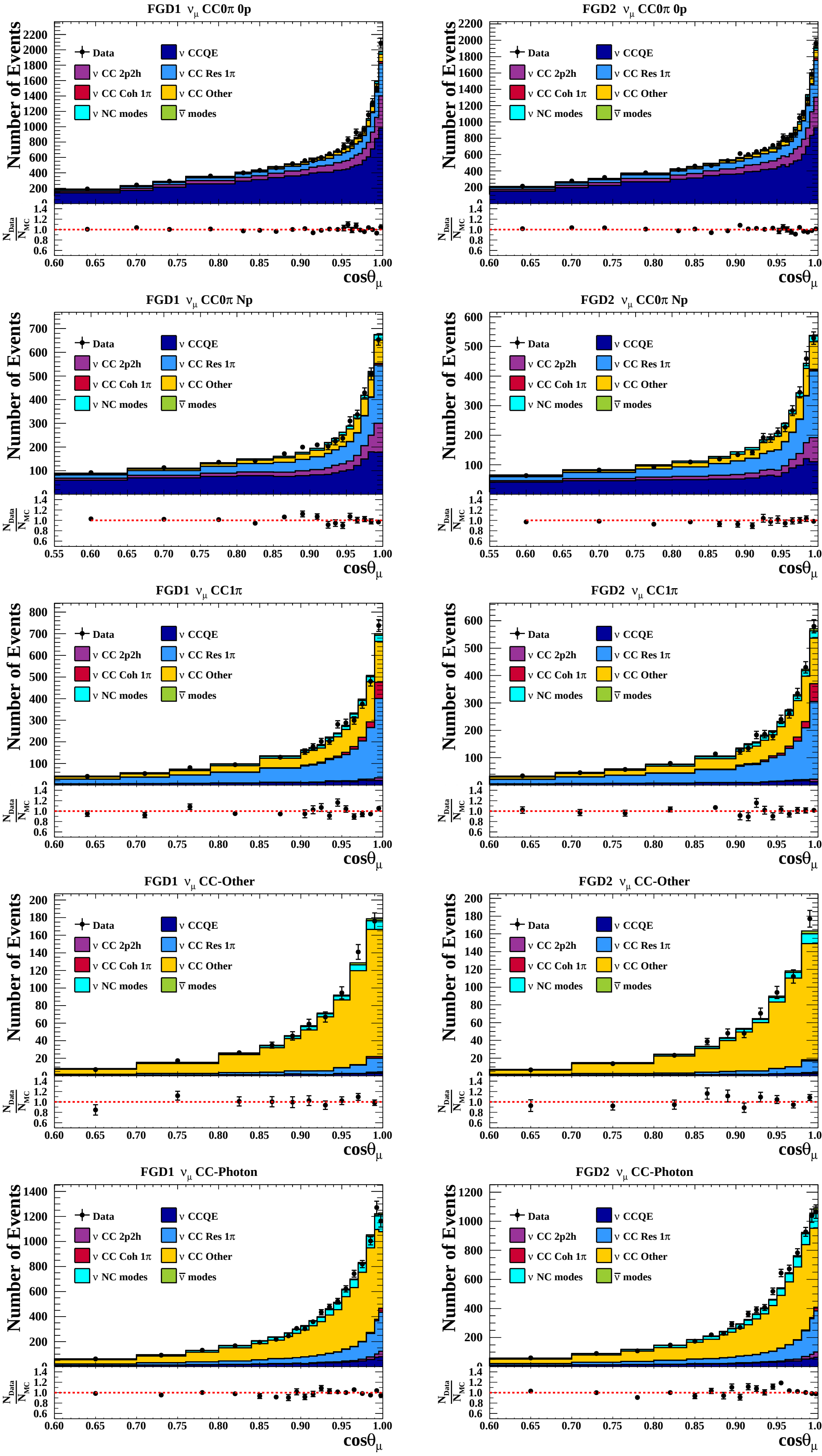

Figure 5.24: $\cos\theta_\mu$ projections of data and the postfit MC prediction broken down by interaction mode for the FHC samples in BANFF.

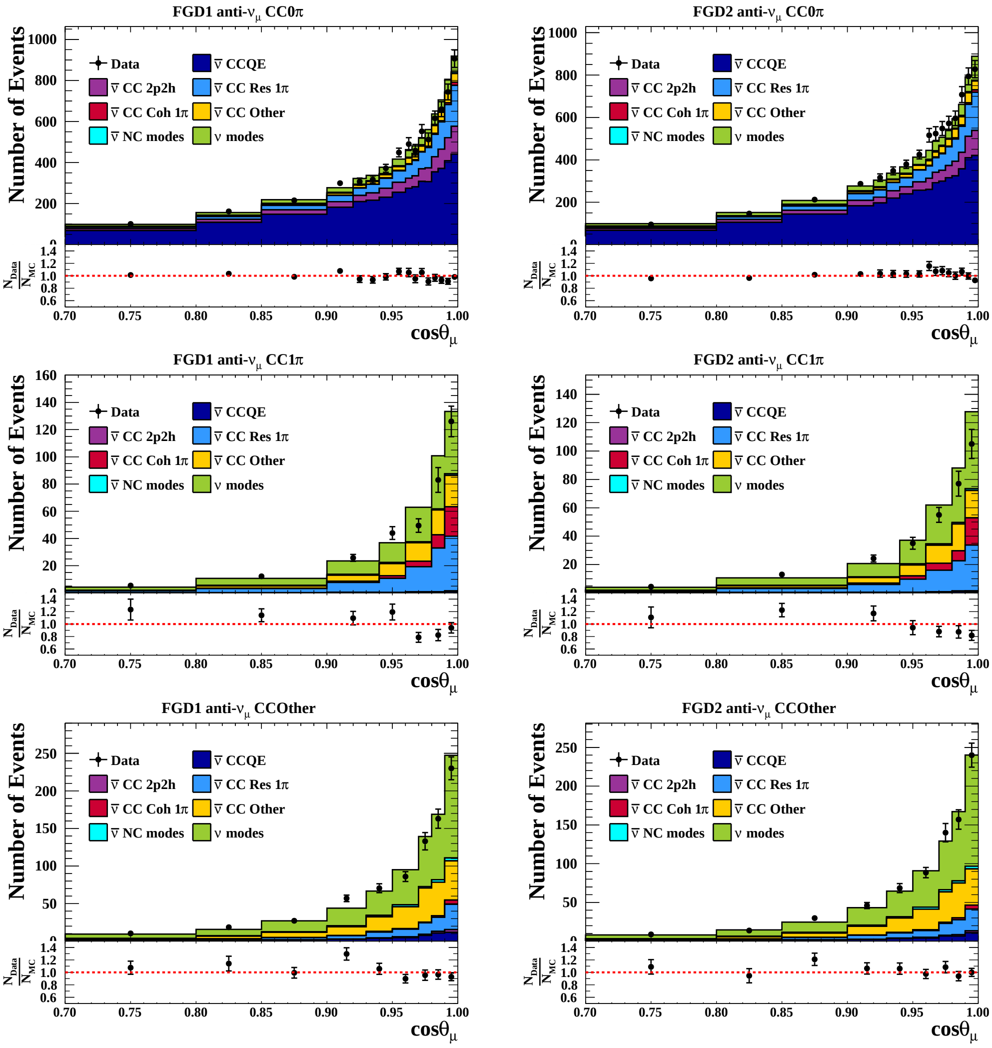

Figure 5.25: $\cos\theta_\mu$ projections of data and the postfit MC prediction broken down by interaction mode for the RHC $\bar{\nu}_\mu$ samples in BANFF.

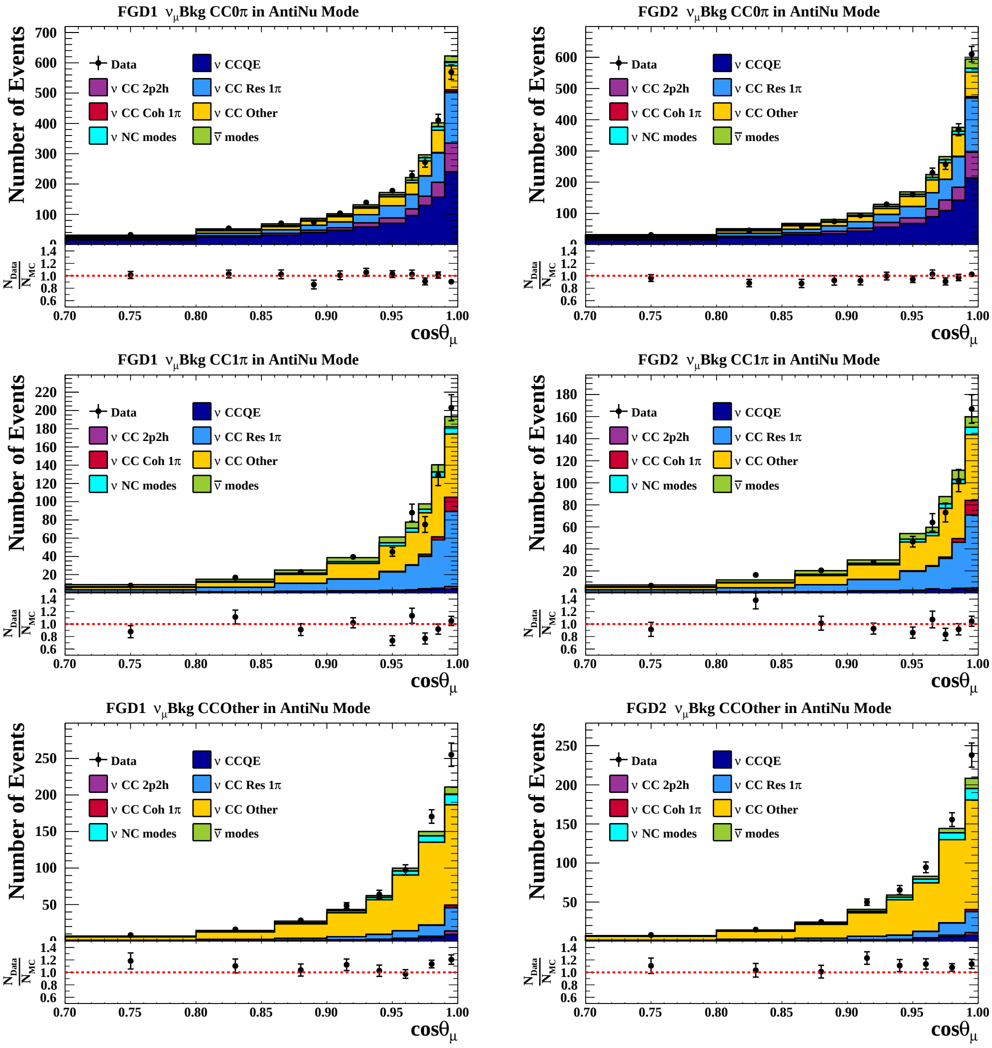

Figure 5.26: $\cos\theta_\mu$ projections of data and the postfit MC prediction broken down by interaction mode for the RHC ν_μ selections in BANFF.

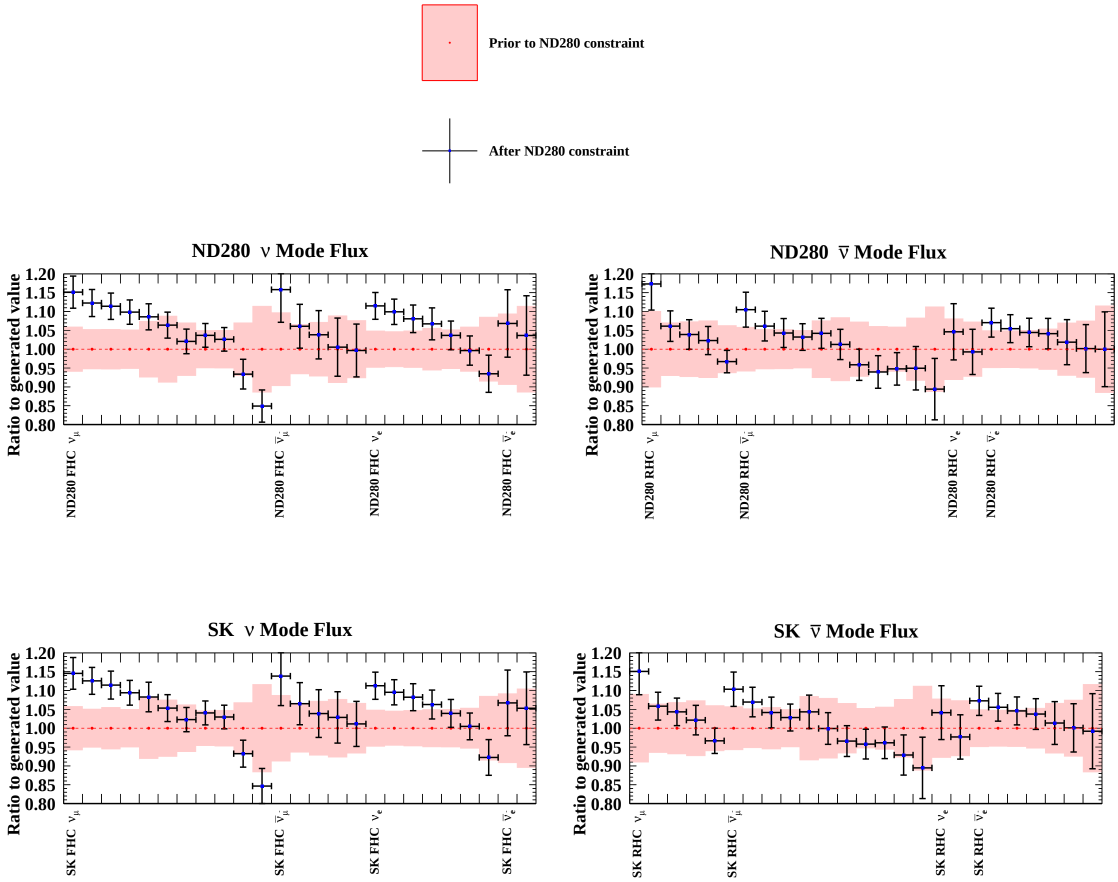

Figure 5.27: The flux parameters used in the oscillation analysis presented in this thesis, and the constraints on these parameters obtained in the BANFF fit to the near detector data.

parameters are pulled up by ∼15%, while at high energies the parameters are pulled down by a similar amount. The RHC $\bar{\nu}_\mu$ parameters see similar shape changes, though the pulls are to values of around ±10% at the high and low energy ends of the spectrum. The FHC $\bar{\nu}_\mu$ and FHC $\bar{\nu}_e$ parameters are generally pulled to values higher than the nominal values, with increases ranging from 0-15%. Similar behaviour is observed for the RHC ν_μ and RHC ν_e parameters, though the highest energy parameters in each case are pulled slightly below the nominal values. The postfit values of all flux parameters are within 1-2σ of their prior uncertainties.

Although many of the individual flux parameters are pulled away from their prior central values, and beyond the prefit $\pm 1\sigma$ range, these results do not represent a strong bias in the fit. As the flux parameters are strongly correlated, a pull in one translates to many of them moving in similar ways. The shift of the flux parameters from their nominal values is the result of two effects. First, is that the flux model itself is not perfect, and shifting parameters is the easiest way for the fit to correct for this. Second, there are (anti-)correlations between the flux and cross section parameters, which means that any cross section mismodelling can also be absorbed by the flux parameters in the fit.

Comparing the size of the uncertainties to their prior constraints, similar results to the Asimov studies are observed. The fit does not have much ability to constrain the parameters beyond the prior uncertainty for $E_\nu < 0.8$ GeV; only to shift them, as this incurs a lower penalty during the fit. At higher E_ν, the fit is able to constrain the parameters more than the priors, reducing the uncertainty by up to 50%. Since there are no ν_e or $\bar{\nu}_e$ samples in the fit, the uncertainties on these parameters see the smallest constraints. The high statistics of the FHC ν_μ selections are likely why the FHC ν_μ flux parameters see the most significant shape change.

Although only the ND280 flux parameters can be varied in the near detector fit, the Super-K errors can be inferred and constrained through prior correlations to the near detector parameters. This is particularly true at lower energies where the correlations between near and far detectors is strongest. However, at higher angles the correlations become weaker due to the different angular acceptance of the two detectors.

5.3.2 Cross Section Parameters

Fig. 5.28 shows the postfit values of the cross section parameters used in the near detector fit. M_A^{QE} is pulled $\sim 2\sigma$ above its prior central value, moving much closer to the nominal generated value of 1.21 GeV, which has been seen in previous iterations of the analysis [109]. The Q^2 normalisation parameters are also pulled above their prior values.

The S shell MF normalisation for carbon is pulled in the opposite direction to the P shell MF normalisation for carbon, though both remain within 1σ of the prior central value. The $P_{1/2}$ and $P_{3/2}$ shell MF normalisations for oxygen are slightly increased, but remain close to the prior, however the S shell MF normalisation for oxygen is pulled 1σ above the prior. The SRC normalisation for carbon is pulled

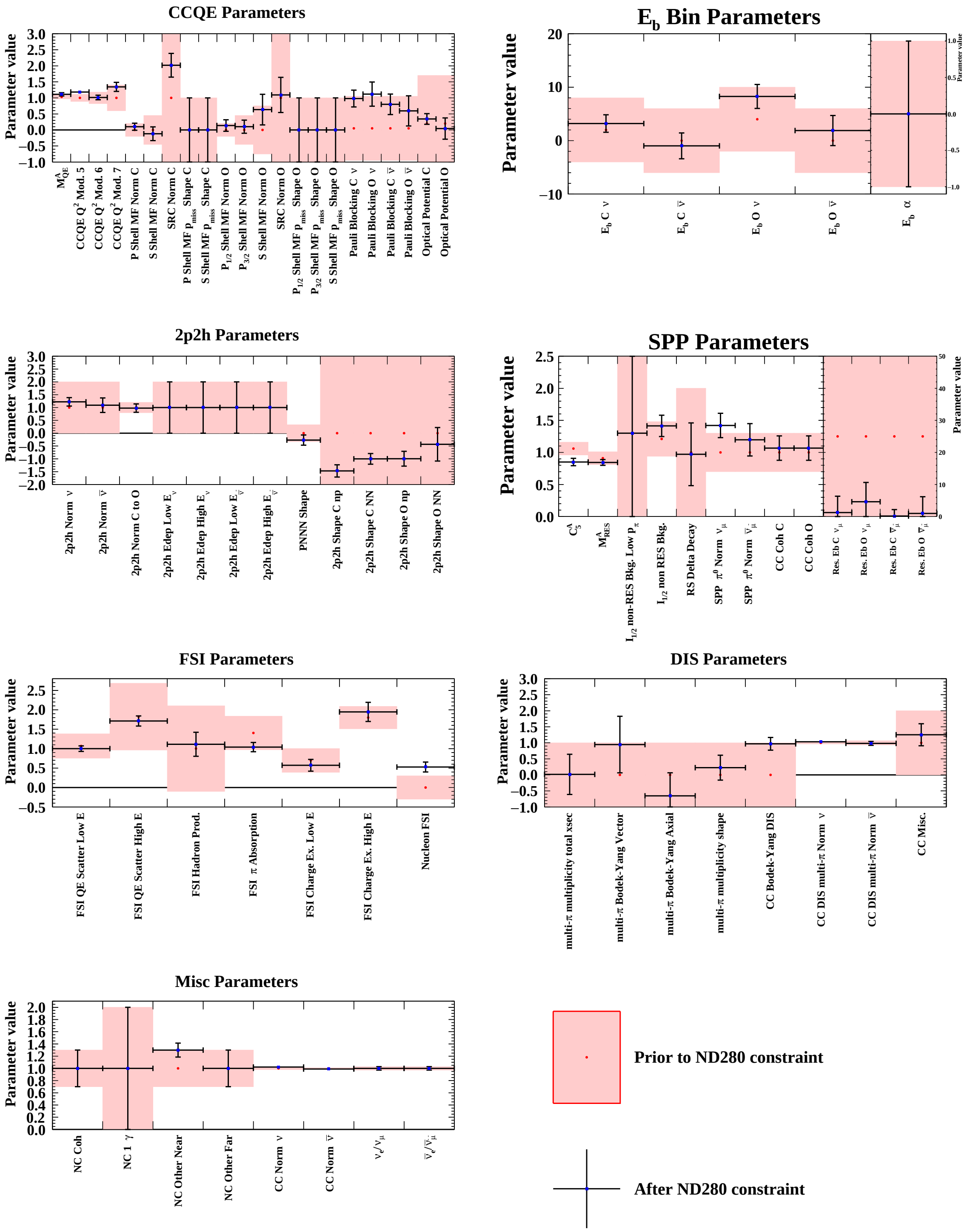

Figure 5.28: The cross section parameters used in the oscillation analysis presented in this thesis, and the constraints on these parameters obtained in the BANFF fit to the near detector data.

relatively strongly above its prior central value, while the SRC normalisation for oxygen remains close to its prior. Both remain within the prior uncertainties.

The Pauli Blocking parameters are pulled above the prior central values, favouring suppression of the low Q^2 region. The Optical Potential parameters account for similar effects as Pauli Blocking and don't move far from the priors, suggesting most of the impact on the low Q^2 region is being absorbed by the Pauli Blocking parameters.

The binned CCQE binding energy parameters show some pulls away from the prior central values, generally increasing the binding energy. However the 1σ postfit uncertainty still encompasses the prior values for three of the four parameters, and all postfit central values are within the prior uncertainties.

The 2p2h normalisation parameters move slightly above the prior value, but remain compatible with the prior within uncertainties. The PNNN shape parameter is shifted below the prior, favouring nn pairs over pn pairs. The 2p2h shape parameters are all shifted to lower values, in favour of Δ-decay-like processes that include the production of an associated pion. This movement of the 2p2h shape parameters is the opposite of the effect seen in the previous analysis [109], but the fit now has explicit sensitivity to these parameters through the CC0πNp samples.

The C_A^5 parameter is pulled almost 2σ away from it's prior central value, while M_A^{RES} remains close to its prior. The $I_{1/2}$ non-resonant background parameter is shifted slightly above the prior. RS Delta Decay remains at the prior central value, which corresponds to a flat decay process. The SPP π^0 normalisation for ν_μ is pulled above the 1σ prior uncertainty, while the $\bar{\nu}_\mu$ parameter remains closer to its prior central value and see a smaller constraint on it's uncertainty. These differences between the ν_μ and $\bar{\nu}_\mu$ parameters is likely due to the new photon sample added to the FHC selections. The CC coherent parameters for both carbon and oxygen are pulled slightly above the prior central values. The resonant binding energy parameters are strongly pulled from the prior central value of 25 MeV towards 0 MeV, which is the generated value. Since 0 MeV is a physical boundary for these parameters, the associated splines are mirrored at this point.

The pion FSI parameters generally stay close to their prior central values, except for the pion absorption parameter which is pulled 1σ below its prior. The nucleon

FSI parameter is pulled almost 2σ above its prior value, increasing the number of nucleons undergoing final state interactions.

The multi-π Bodek-Yang (BY) vector parameter is pulled in the opposite direction to the multi-π BY axial parameter, both being pulled $\sim 1\sigma$ away from the prior central value. The pion multiplicity parameter for the total cross section and shape remain close to their prior values. The CC BY DIS parameter is pulled to the edge of its 1σ prior uncertainty. The CC DIS normalisation parameters remain close to the prior values. The postfit value of the CC misc. parameter is about 1σ above its prior central value. Since η production is included in this parameter, the new photon selection may be driving this shift.

The NC other near parameter is pulled above its prior central value, while the CC normalisation parameters remain close to their prior values.

Overall, shifts away from the pre-fit cross section model are generally small, indicating that the model is fairly good at describing the data. The compatibility of the model with the data is studied in more detail in Section 5.3.5.

5.3.3 Detector Parameters

Figs. 5.29 to 5.32 show the postfit values and uncertainties of the ND280 detector parameters varied in the BANFF fit. Since the BANFF detector parameterisation is an effective bin-by-bin normalisation, rather than varying the underlying detector uncertainties described in Chapter 4, interpreting these results is extremely difficult. However, the vast majority of the postfit parameter values are within the 1σ prior uncertainties, which gives some validation to this approach for parameterising the detector systematics.

5.3.4 Parameter Correlations

Fig. 5.33 shows the correlation matrix for all fit parameters before and after the data fit. As was observed for the Asimov fit in Section 5.2.2, anti-correlations between different sources of systematic uncertainty are introduced by the fit. The anti-correlations between flux and detector parameters are fairly uniform across the whole range of parameters, having anti-correlations of around 20%. The internal correlations of the flux and detector parameters are also present in the data fit.

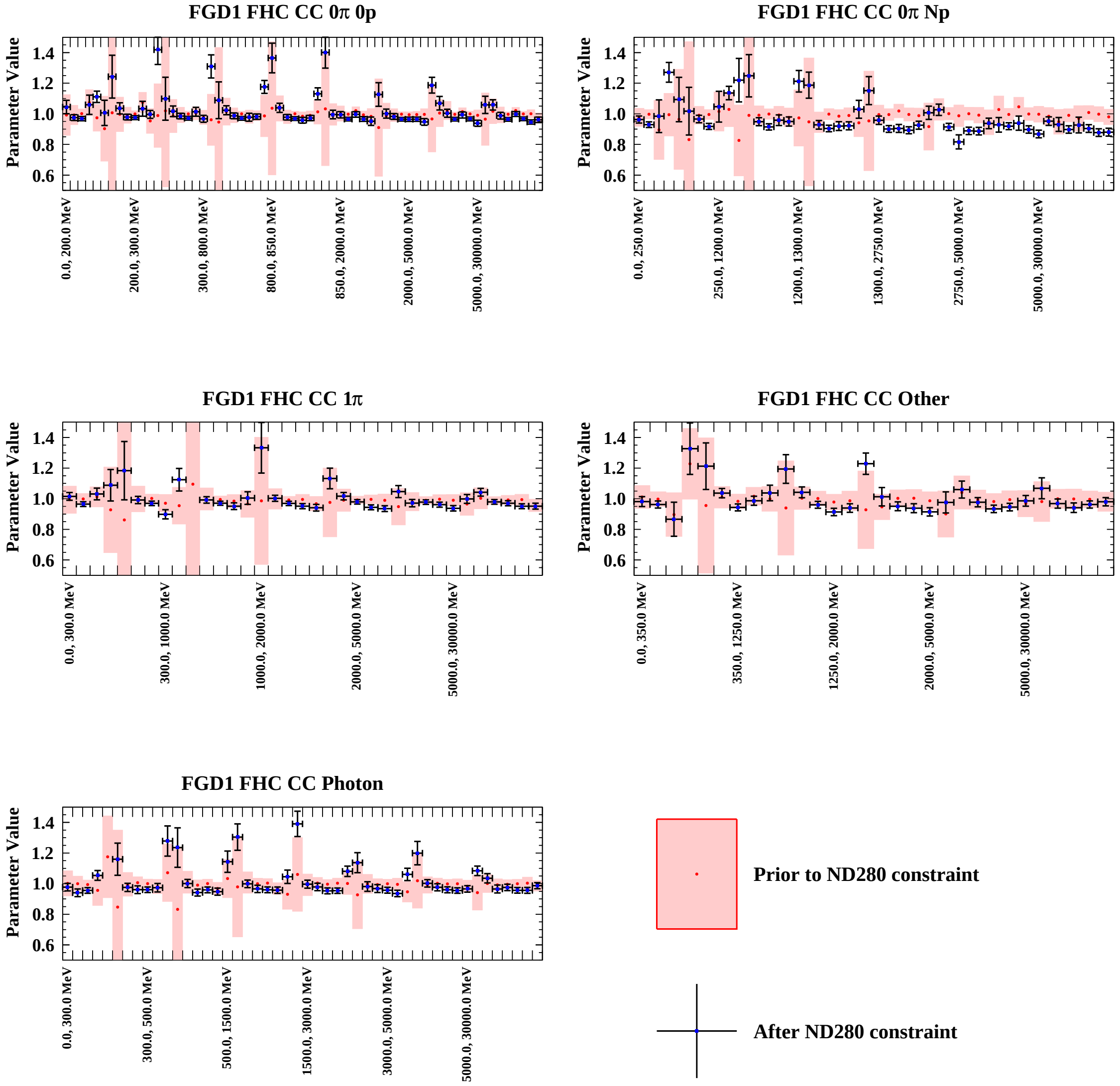

Figure 5.29: The detector parameters for the FHC FGD1 samples used in the oscillation analysis presented in this thesis, and the constraints on these parameters obtained in the BANFF fit to the near detector data.

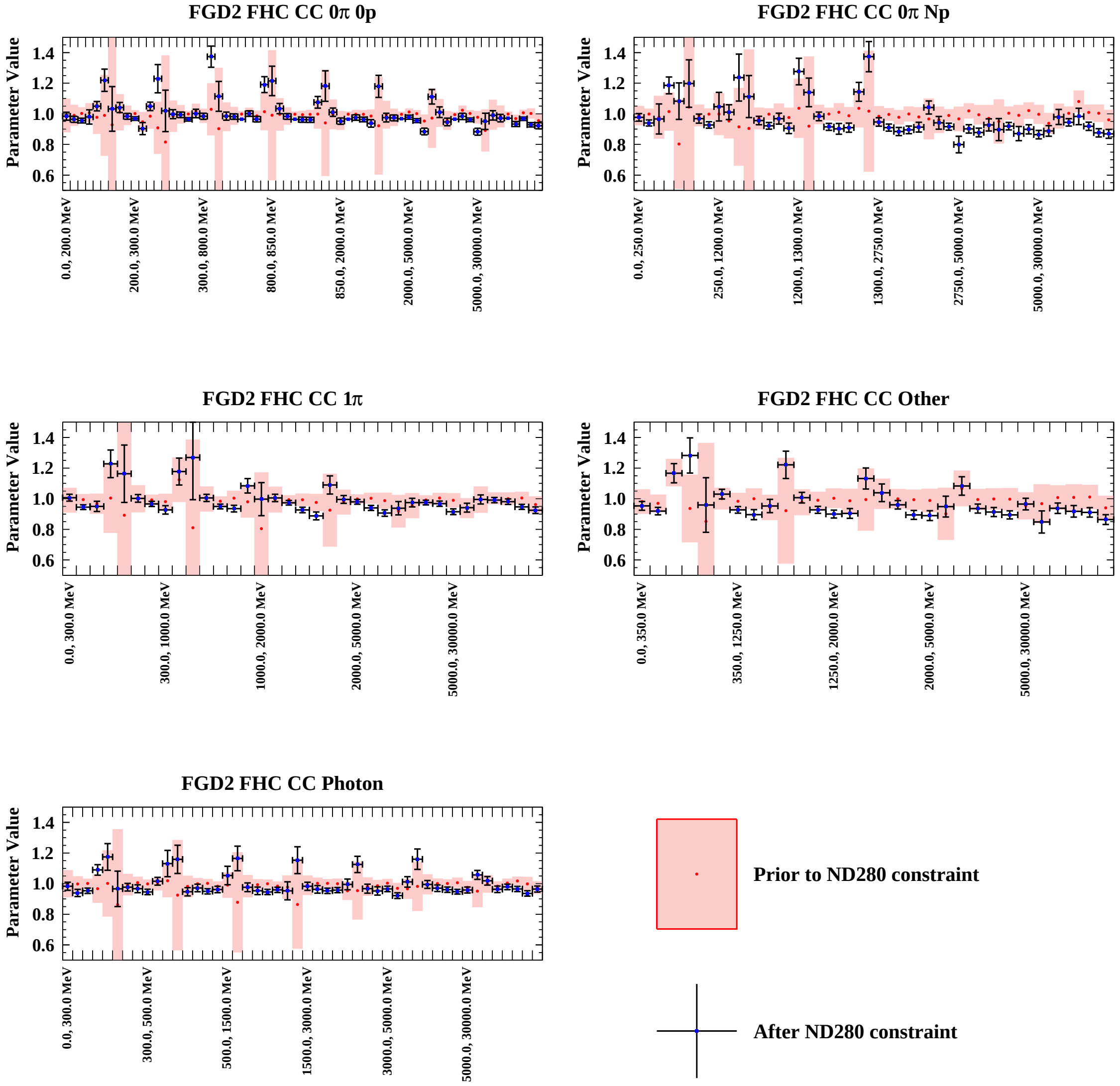

Figure 5.30: The detector parameters for the FHC FGD2 samples used in the oscillation analysis presented in this thesis, and the constraints on these parameters obtained in the BANFF fit to the near detector data.

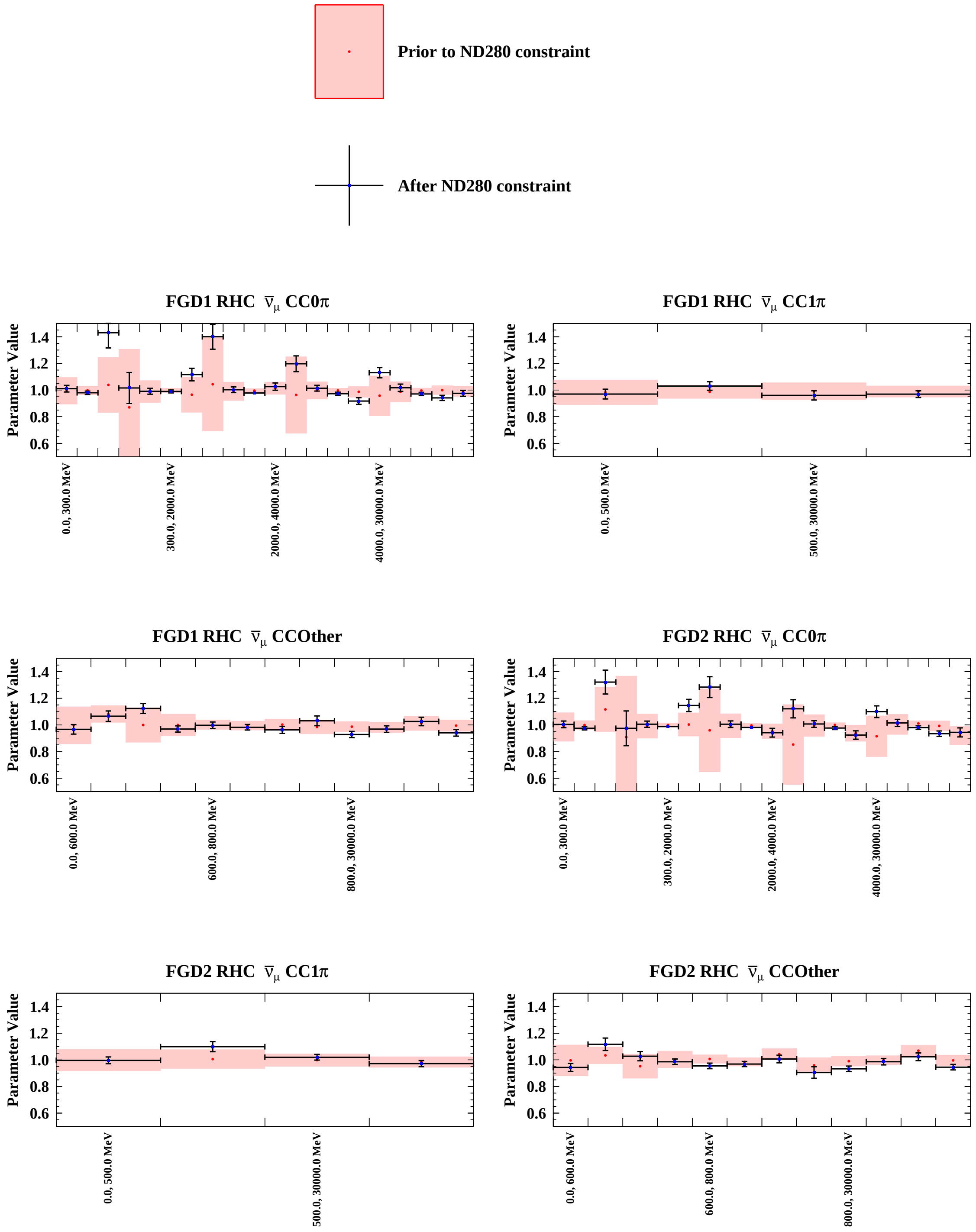

Figure 5.31: The detector parameters for the RHC $\bar{\nu}_\mu$ samples used in the oscillation analysis presented in this thesis, and the constraints on these parameters obtained in the BANFF fit to the near detector data.

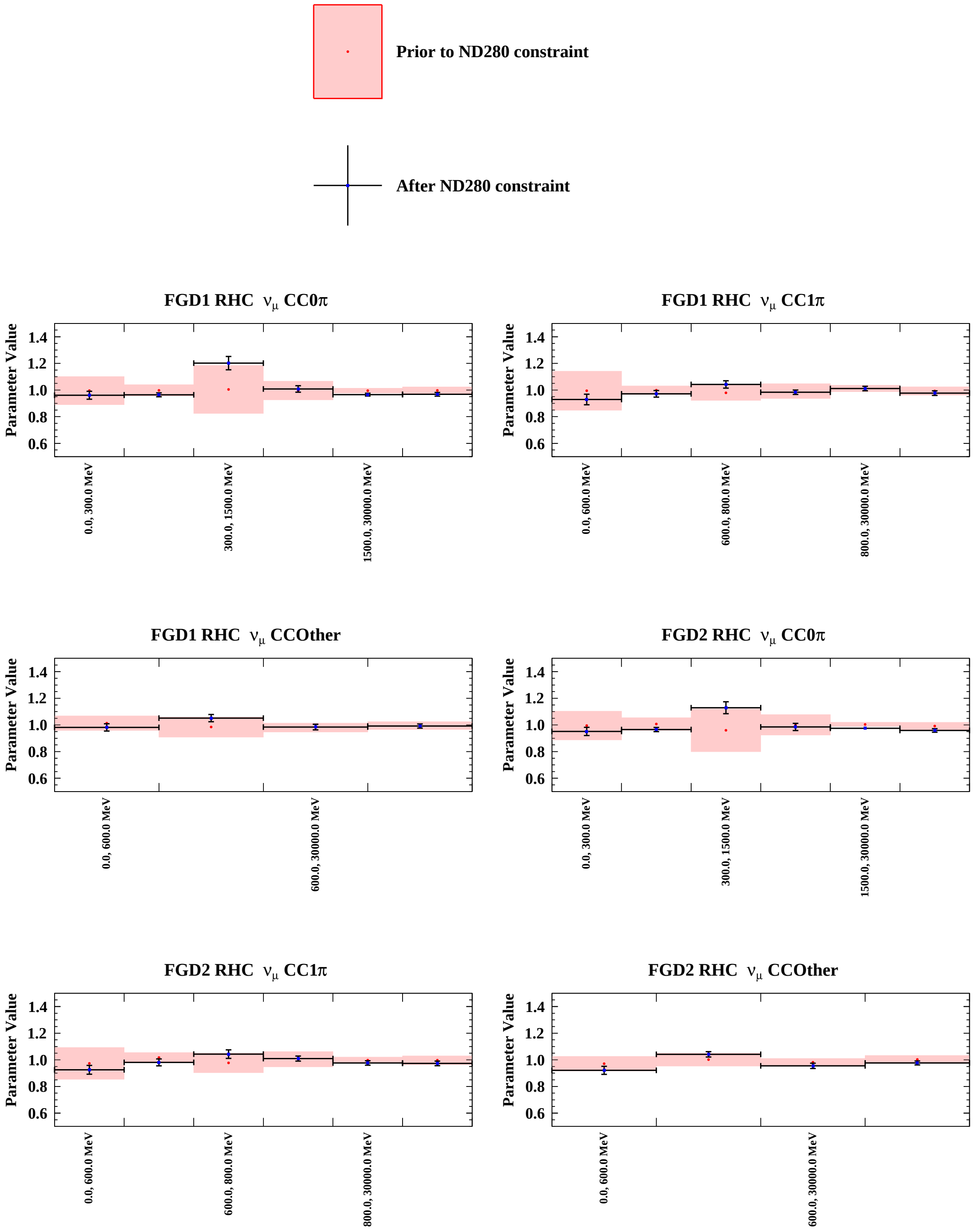

Figure 5.32: The detector parameters for the RHC ν_μ samples used in the oscillation analysis presented in this thesis, and the constraints on these parameters obtained in the BANFF fit to the near detector data.

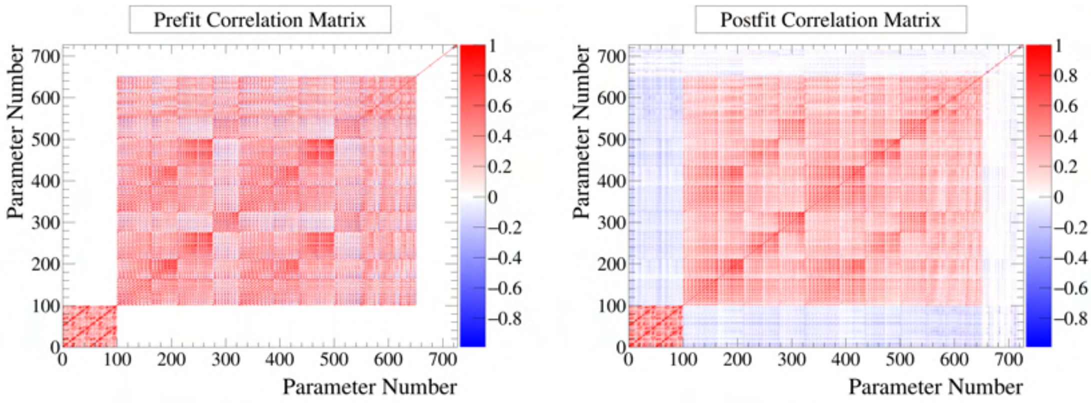

Figure 5.33: The prefit (left) and postfit (right) correlation matrices showing all fit parameters from the BANFF fit to the near detector data. Parameters 0-99 correspond to the flux parameters; parameters 100-651 correspond to the detector parameters; and parameters 652-726 correspond to the cross section parameters.

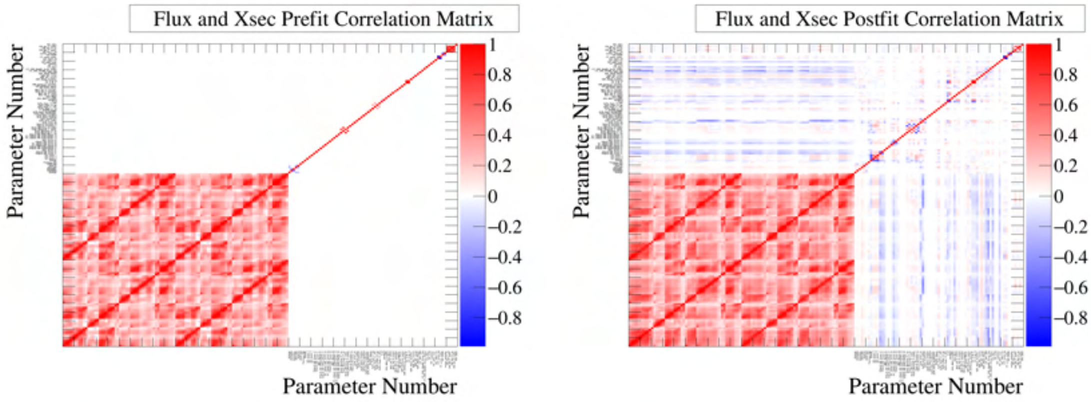

Figure 5.34: The prefit (left) and postfit (right) correlation matrices showing the flux and cross section parameters from the BANFF fit to the near detector data.

The correlation matrix for the flux and cross section parameters only is shown in Fig. 5.34. Again, similar behaviour is seen as that in the Asimov fit, with the strongest anti-correlations with the flux parameters being from the cross section normalisation parameters.

Finally, the cross section correlation matrix is shown in Fig. 5.35. The same general trends from the Asimov fit are observed here too, with the strongest (anti-) correlations being between parameters affecting similar event topologies. Since the conclusions drawn are very similar to before, the reader is directed to Section 5.2.2 for a discussion of the cross section parameter correlations.

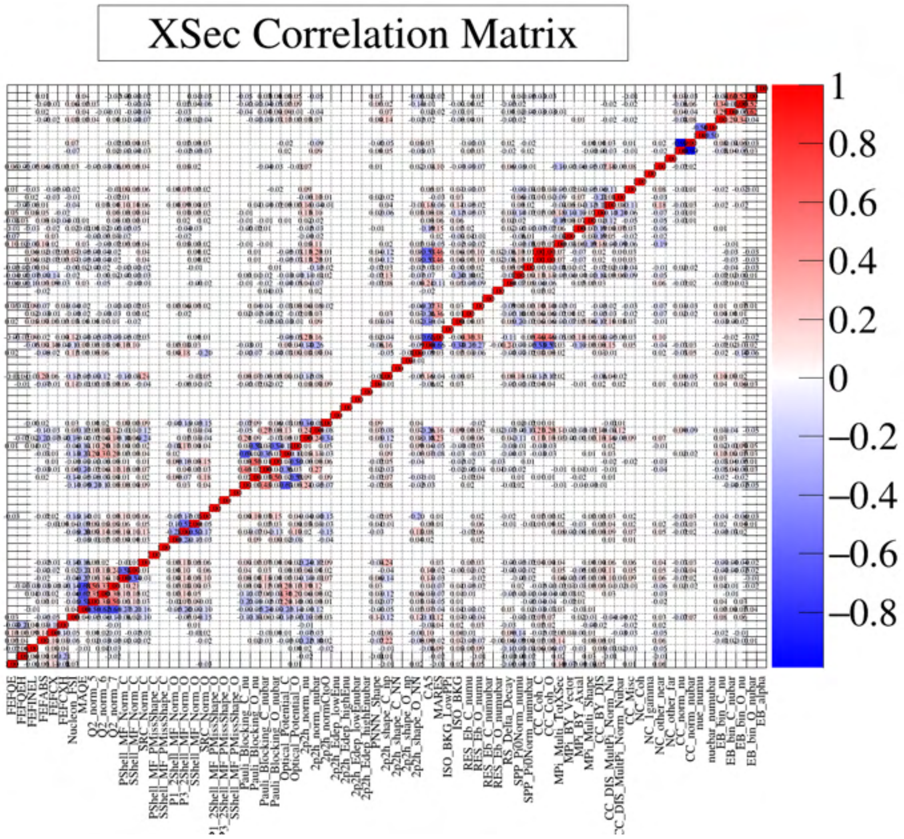

Figure 5.35: The postfit correlation matrix showing the cross section parameters from the BANFF fit to the near detector data.

5.3.5 p-value Calculation

To demonstrate that the fit behaves well over the parameter space covered by the model, and that the model properly covers the parameter space which best describes the data, a p-value study is performed. The null hypothesis is defined as $\mathbb{H}$ = "The model is compatible with the ND280 data", and a number of "toy" experiments are conducted to test this hypothesis. Each toy corresponds to a different possible set of the model parameters from all classes of systematics: flux, detector and cross section. Additionally, the toys include statistical variations in the form of Poisson fluctuations. Values of the parameters are thrown randomly according to their prior covariances to take into account both their uncertainties and any correlations between parameters; i.e. more probable regions of parameter space, according to the prior model, will be more densely populated by the toys.

Toys for the detector systematics described in Chapter 4 are thrown directly in the Psyche software framework, instead of throwing uncertainties from the binned normalisation used in the standard BANFF fit. Each toy is then loaded into the BANFF interface as the input to a fit. Toys for the flux and cross section parameters are thrown according to their respective covariances internally in BANFF. Monte Carlo predictions are built for each toy, using the thrown values of each parameter as the prior in place of the nominal values given in Section 5.1.2. A bin-by-bin Poisson fluctuation is applied to the final prediction for each toy to include statistical effects. Each toy data set is then fitted instead of the data or nominal Monte Carlo.

Each fit to a toy data set will give a minimum $\Delta\chi^2$ according to Eq. (5.6), which can then be compared to the value from the fit to real data, $\Delta\chi^2_{\text{Data}}$. A p-value is defined as the probability of an observation as or more extreme than the data, relative to the nominal model. This can be calculated by comparing $\Delta\chi^2_{\text{Data}}$ to the distribution of $\Delta\chi^2$ from the toy experiments as:

$$p = \mathbb{P}(\Delta\chi^2 > \Delta\chi^2_{\text{Data}}|\mathbb{H}) = \frac{\int_{\Delta\chi^2_{\text{Data}}}^{+\infty} d\Delta\chi^2}{\int_0^{+\infty} d\Delta\chi^2}. \tag{5.8}$$

The distribution of $\Delta\chi^2$ for the convergent toy fits is shown in Fig. 5.36, and $\Delta\chi^2_{\text{Data}}$ is shown as a vertical line at $\Delta\chi^2 = 5543.81$. From this, the total p-value for the BANFF data fit is calculated using Eq. (5.8) as $p = 0.109$, above the threshold of

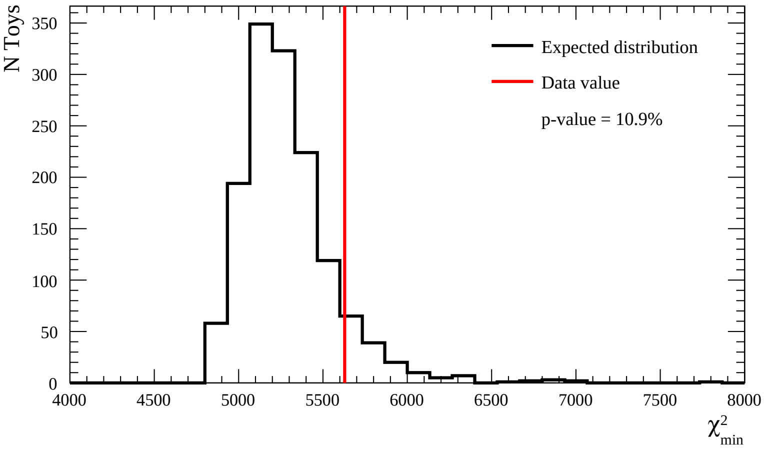

Figure 5.36: Total $\Delta\chi^2$ for each successful toy fit in BANFF. The p-value is constructed from the number of fits with a $\Delta\chi^2$ (relative to the nominal MC) greater than or equal to that of the data as a fraction of the total number of fits.

0.05 set internally by the ND280 group, demonstrating that the data is consistent with the prefit model.

Below the χ^2 distribution is broken down into contributions from each sample and systematic error source to probe possible tensions explored in the fit. While these breakdowns are informative, it is not unexpected that the p-values will show large variations, and they are not held to the same threshold as the total p-value for the fit. This is because of the correlations that exist between the samples and the sources of systematic uncertainty, which make it difficult to separate each to give reliable individual p-values.

Fig. 5.37 shows the χ^2 distributions for the FHC and RHC FGD1 samples. The FHC FGD1 ν_μ CC0π0p ($p = 0.134$), FHC FGD1 ν_μ CC-Photon ($p = 0.080$) and RHC FGD1 ν_μ CC1π^+ ($p = 0.112$) samples show the lowest p-values.

Fig. 5.38 shows the χ^2 distributions for the FHC and RHC FGD2 samples. The RHC FGD2 $\bar{\nu}_\mu$ CC0π ($p = 0.097$) and RHC FGD2 ν_μ CC1π^+ ($p = 0.099$) samples show the lowest p-values.

Fig. 5.39 shows the total sample likelihood contribution ($p = 0.143$), and breaks down the prior likelihood into flux ($p = 0.045$), cross-section ($p = 0.735$) and ND280 detector ($p = 0.036$) systematics.

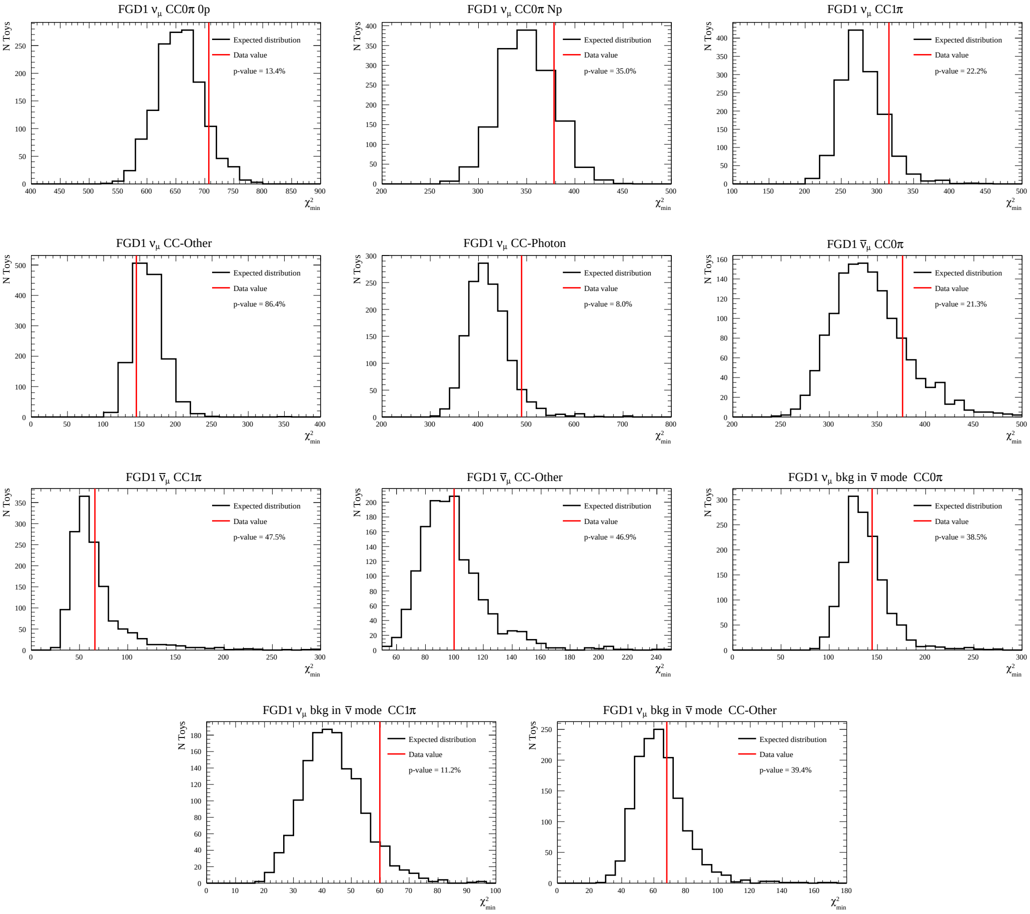

Figure 5.37: Toy fit $\Delta\chi^2$ distributions for the FHC and RHC FGD1 samples and their p-values.

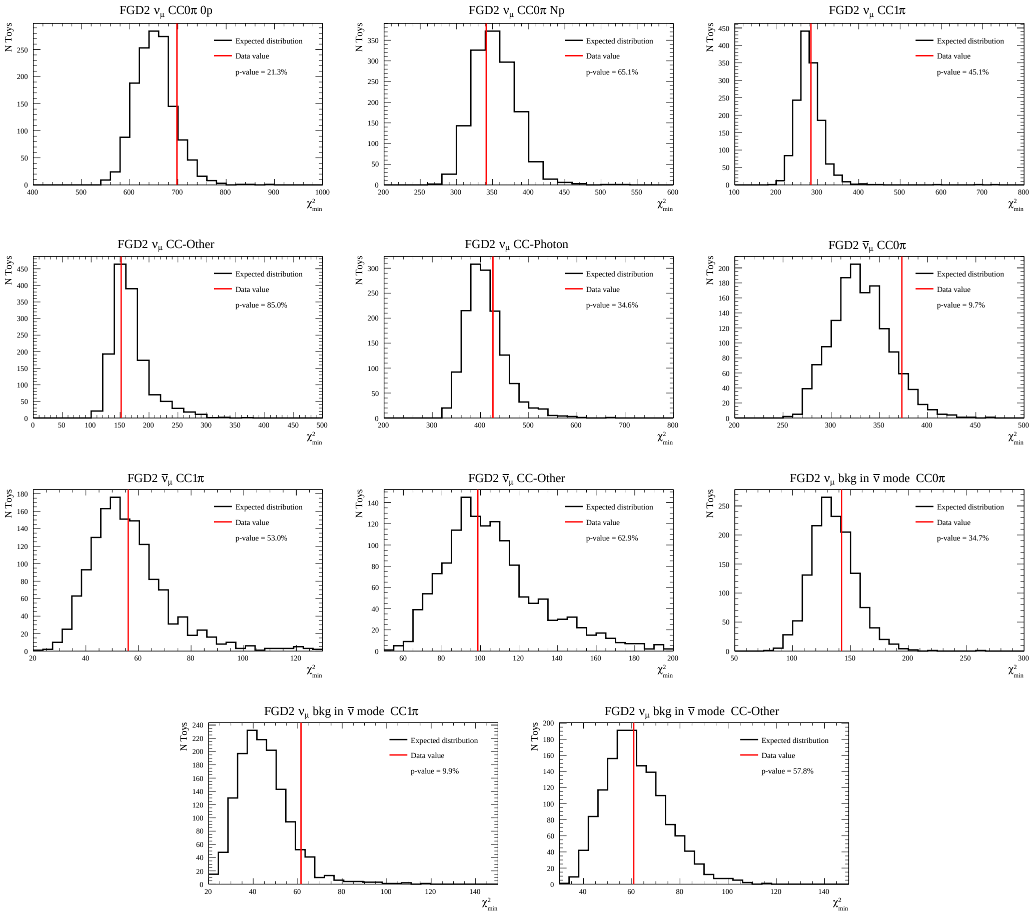

Figure 5.38: Toy fit $\Delta\chi^2$ distributions for the FHC and RHC FGD2 samples and their p-values.

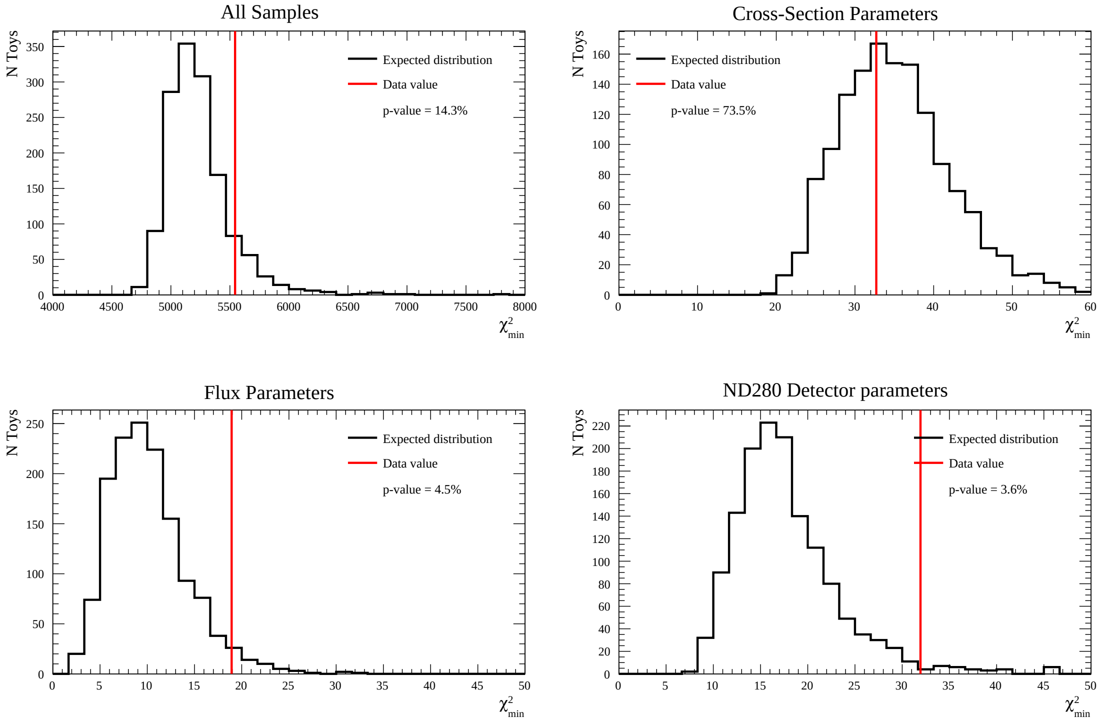

Figure 5.39: Total sample and parameter type contributions to toy $\Delta\chi^2$ distributions.

Fit Failures in the p-Value Calculation

As described above, the p-value for the BANFF fit is calculated by throwing a series of toy experiments, however not all of the toy data sets produce convergent fits. Out of the 2000 toys thrown in this analysis, 28.8% of the fits failed to converge properly - a failure rate which is consistent with the previous analysis [109]. Having failures in the fits is not necessarily surprising, since detector throws are created with Psyche but are then fitted using BANFF's effective binned normalisation parameterisation of those systematics. During the Psyche throws an event can change from one sample to another or the reconstructed muon kinematics can change, and the effective normalisation parameters are produced without taking this into account. There may also be degeneracies between parameters that are being fit and, as noted previously, fitting to points close to the physical boundaries of the parameter space is problematic for BANFF. However, it is important to check that the toys of the failed fits show no biases, which would indicate some region of parameter space is not being correctly covered. Fig. 5.40 shows some selected parameters' throws, including breakdowns for converging and failing fits. No particular bias has been

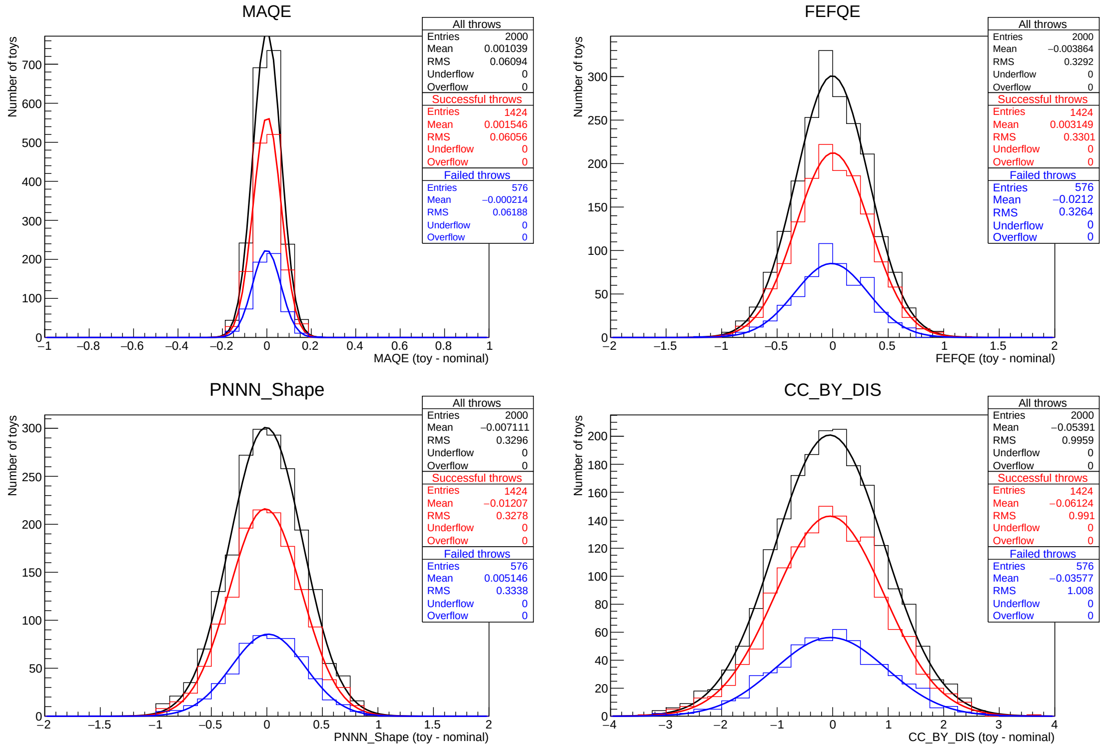

Figure 5.40: Throws of cross section model parameters indicating the distributions of successfully (red) and unsuccessfully (blue) fitted throws shown as a deviation from the nominal value. Checking the mean of both the successfully fitted and failed throws are consistent with the overall distribution (black) can identify biases in the fitter.

identified in any of the parameters, with the means and widths of the distributions for converging and failing fits being in good agreement for all parameters.

It is also possible to study the failing fits as a function of the parameter values that built the toy distributions in Fig. 5.41, showing some selected parameters. Fits to more extreme parameter values, or values close to the physical boundaries, fail more frequently, but failure rates are within statistical uncertainties.

In addition to looking at the parameter values in the toys, the spread of event rates across the toys for different selections is also considered; these are shown for two samples in Fig. 5.42. These plots also give an estimate of the prior uncertainty on the event rates for the ND280 selections, for instance 11.6% for FGD1 ν_μ CC0π0p. The FGD2 ν_μ CC-Other distribution appears slightly non-Gaussian, which is expected from the effects of pion secondary interactions.

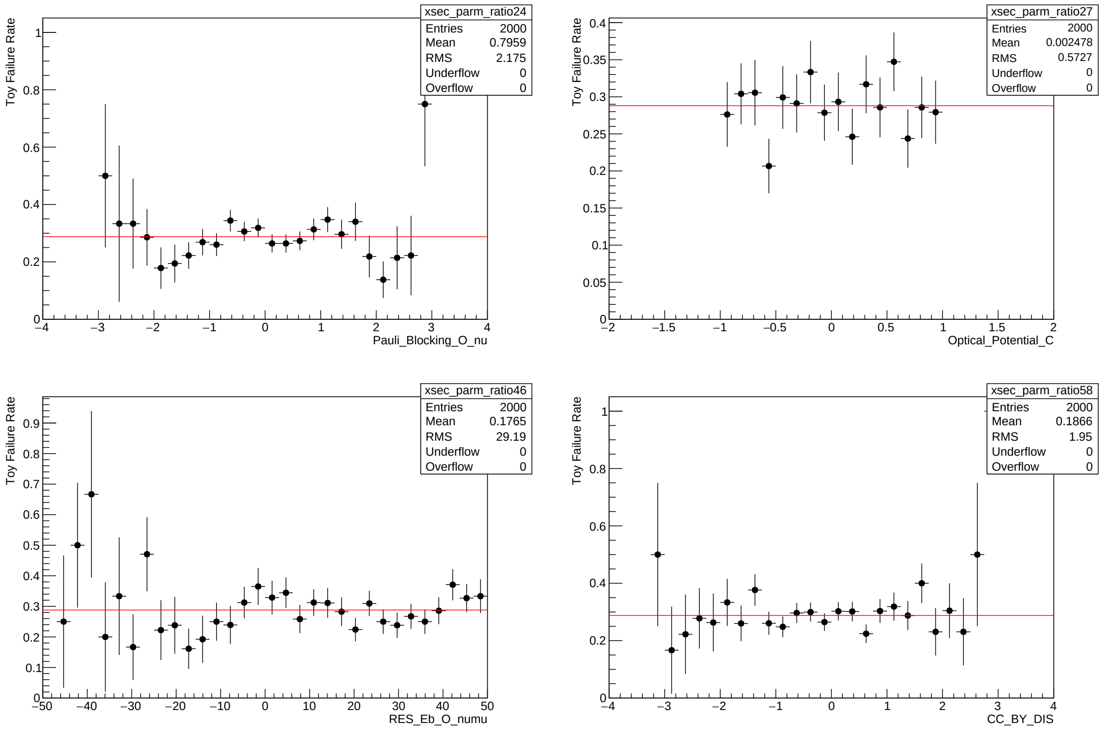

Figure 5.41: Ratio of the number of failed toy fits to the total number of toys as a function of the thrown parameter values. Fits to parameter values far from the prior central value or close to the parameter boundaries fail more frequently, but are within statistical uncertainties.

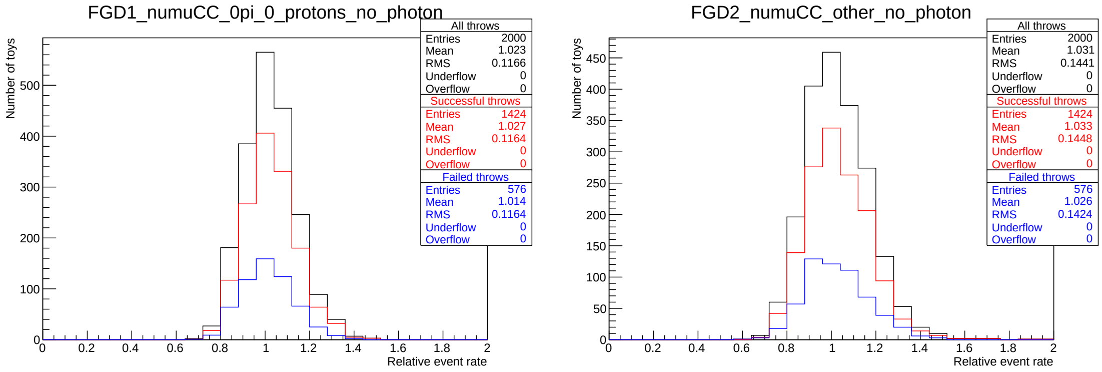

Figure 5.42: Spread of toy event rates relative to the nominal event rates for the FGD1 FHC CC0π0p and FGD2 FHC CC-Other samples. The CC0π0p sample has a narrower, more symmetric spread with most toys lying within 20% of the nominal rate; the CC-Other sample is somewhat non-Gaussian, with a more prominent tail to higher event rates than the nominal model, as well as a broader spread of rates.

5.3.6 Effect on the Far Detector Samples

The results of the BANFF fit are propagated to the far detector as a covariance matrix that includes the best-fit values, uncertainties and correlations between parameters obtained in the fit. The near detector flux and detector systematic parameters are not propagated, nor are the near detector specific cross section parameters. The best-fit values and uncertainties of the propagated parameters are used to reweight the far detector MC prediction in each sample. The SK MC predictions for each sample before and after the BANFF fit are shown in Fig. 5.43. The event rate increases in the CCQE-like (single ring) samples, and decreases in the FHC 1Re1de and ν_μ CC1π samples. This is consistent with the changes observed in the BANFF fit and those observed in the previous analysis [99, 109].

This process leads to the reduction of the systematic uncertainties associated with all of the far detector samples. In the previous analysis [45, 99], the flux uncertainty was reduced from ∼5% to ∼3% for all samples after the near detector constraint. Due to the constraint on the event rate from the BANFF fit, the detector parameters at Super-Kamiokande were also slightly reduced despite not being constrained directly in the BANFF fit. The cross section parameters saw the largest reduction in uncertainties, going from >10% to 3-4% in all samples. The overall effect of the BANFF fit on the total systematic uncertainty at the far detector was a reduction from 12-14% to 3-6% for the CCQE-like samples. The 1Re1de sample systematic uncertainty was reduced from 18.7% to 14.3%, however the uncertainty on this sample is dominated by the detector uncertainties which are not directly constrained in the BANFF fit. At the time of writing, the systematic uncertainties on the far detector samples have not been finalised, however similar trends are expected in this analysis with respect to reduction in systematic uncertainties following the near detector fit.

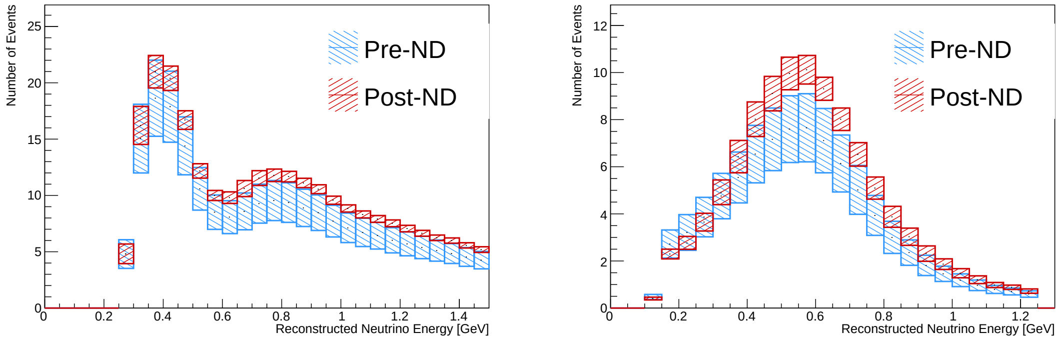

(a) FHC 1Rμ (b) FHC 1Re

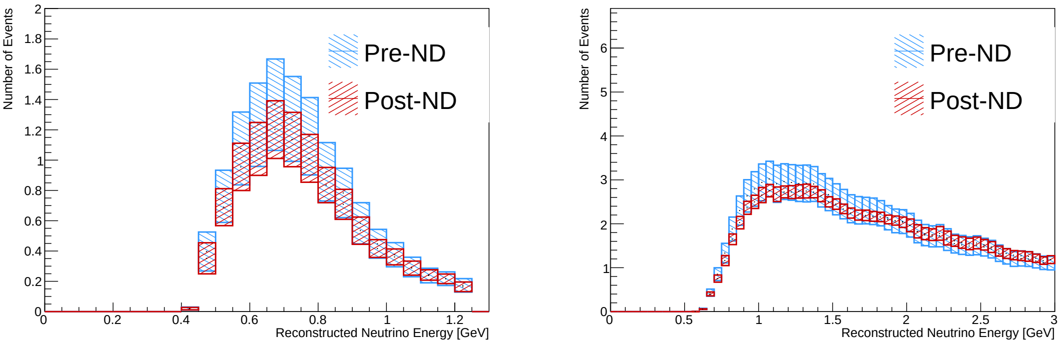

(c) FHC 1Re1de (d) FHC ν_μ CC1π

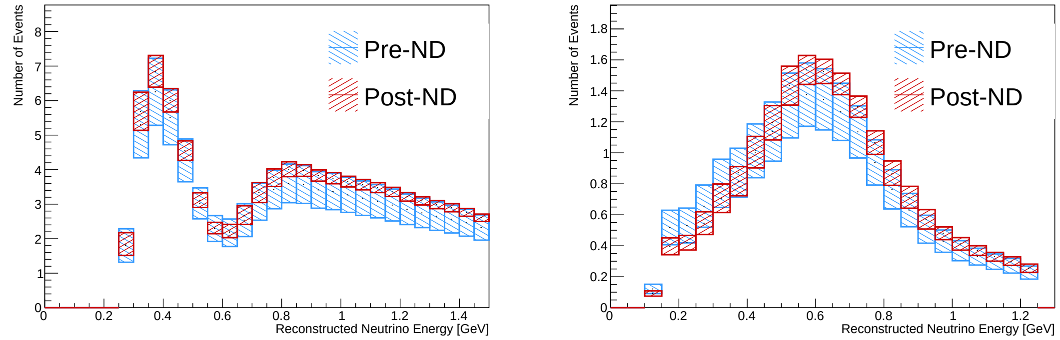

(e) RHC 1Rμ (f) RHC 1Re

Figure 5.43: The SK pre-fit MC as a function of reconstructed neutrino energy before (blue) and after (red) the BANFF fit for the (a) FHC 1Rμ, (b) FHC 1Re, (c) FHC 1Re1de, (d) FHC ν_μ CC1π, (e) RHC 1Rμ and (f) RHC 1Re samples [122]. The shaded regions show the 1σ uncertainty including all systematic uncertainties.

Chapter 6

Discussion and Conclusions

The T2K experiment is a long-baseline neutrino oscillation experiment that uses a beam of muon (anti)neutrinos produced at J-PARC to make measurements of the neutrino oscillation parameters. The beam is directed 2.5° away from the far detector, Super-Kamiokande, and is sampled by the ND280 detector at the same off-axis angle before oscillations occur. The oscillation analysis results published in 2020 [45] saw the systematic uncertainty on the far detector sample event rates reduced significantly compared to previous analyses, to less than 5% for most samples. The work presented in this thesis introduces a new selection of near detector events containing final state photons, with the aim of reducing the systematic uncertainties obtained in the near detector fit, thus reducing the uncertainties at the far detector.

The selection of photons in the ECal described in Chapter 3 provides a π^0 enhanced sample for the near detector fit described in Chapter 5, marking the first use of near detector photon information in the T2K oscillation analysis. The resulting sample has an efficiency of $\sim$43% and purity of $\sim$54%, numbers comparable to the well-established CC0π and CC1π^+ samples. In addition, the introduction of the photon tag improves the purity of the CC0π and CC1π^+ samples by 5-7%, at minimal cost to efficiency. The new sample required the introduction of ECal-related systematic uncertainties, as described in Chapter 4. However, through careful evaluation of each systematic, the resulting increase in uncertainty on the near detector samples has been kept to a minimum.

Together with a split in the CC0π sample, based on the presence or absence of protons, the new photon sample provides increased sensitivity to the flux and cross section parameters described in Chapter 5, allowing systematic uncertainties to be reduced. The constraints obtained in the near detector fit are propagated to the far detector, reducing the systematic uncertainties on the event rates of the far detector samples. This will, in turn, lead to improved measurements of the neutrino oscillation parameters in the far detector analysis.

Other improvements to the near detector event categorisation are being considered that could improve the near detector constraints without taking any additional data. These include the extension of the photon selection to RHC events, and the introduction of a full solid angular acceptance selection of muon candidates in FHC events. Both of these improvements are expected to be included in the next iteration of the near detector fit for the oscillation analysis.

Several major upgrades are planned for the T2K experiment in the coming years. In 2022/2023, the first of two beamline upgrades will be made, increasing the beam power from the current 515 kW to >700 kW. A second upgrade to the beamline will be made, increasing the beam power further to >1 MW by the time the Hyper-Kamiokande detector starts taking data. Increases in beam power mean more statistics can be collected in the same timescale. Beamline upgrades provided motivation for the ND280 Upgrade project.

The ND280 Upgrade, also planned for 2022, will see the PØD replaced with three new subdetectors: the SuperFGD, horizontal TPCs and a time-of-flight detector. The SuperFGD is composed of 2 million 1 cm cubes, providing an additional 2 tonnes of target material. Each cube is read out by three optical fibres, allowing three-dimensional reconstruction with much improved spatial resolution. This will improve particle detection and identification capabilities, particularly for protons and neutrons. Neutron measurements are of particular importance as they will provide a significant improvement to the reconstruction of antineutrino interactions. Horizontal TPCs will be placed above and below the SuperFGD, and will be equipped with resistive MicroMegas, that will use the spread of charge in a resistive layer to provide much improved particle reconstruction, particularly for high angle tracks. Time-of-flight detectors will surround the four faces of the upgraded tracking region parallel to the beam direction, and will improve the ability to determine a tracks direction. Together, the ND280 Upgrade subdetectors will improve the angular acceptance of the near detector, bringing it much closer to the full solid angular acceptance of the far detector.

Inclusion of photon information has already provided improvements to the oscillation analysis, and with the ND280 Upgrade even greater improvements will be achievable. Additionally, the T2K-NOνA joint oscillation analysis currently underway [49] uses the near detector event categorisation of the previous analysis, without the proton and photon information included in this analysis. Future iterations of the joint analysis will also benefit from the work presented in this thesis.

Bibliography

[1] W. Pauli. Dear radioactive ladies and gentlemen. *Phys. Today*, 31(9):27, 1978.

[2] C.L. Cowan *et al.* Detection of the Free Neutrino: a Confirmation. *Science*, 124:103–104, 1956.

[3] P. Pontecorvo. Mesonium and anti-mesonium. *Sov. Phys. JETP*, 6:429, 1957.

[4] P. Pontecorvo. Inverse beta processes and nonconservation of lepton charge. *Sov. Phys. JETP*, 7:172–173, 1958.

[5] S. Sakata Z. Maki, M. Nakagawa. Remarks on the unified model of elementary particles. *Prog. Theor. Phys.*, 28:870–880, 1962.

[6] Y. Fukuda *et al.* Evidence for Oscillation of Atmospheric Neutrinos. *Phys. Rev. Lett.*, 81:1562–1567, 1998.

[7] J. Chadwick. Intensitätsverteilung im magnetischen Spectrum der β-Strahlen von radium B + C. *Verhandl. Dtsc. Phys. Ges.*, 16:383, 1914.

[8] J. Chadwick. Possible Existence of a Neutron. *Nature*, 129:312, 1932.

[9] E. Fermi. Versuch einer Theorie der β-Strahlen. I. *Zeitschrift für Physik*, 88:161–177, 1934.

[10] G. Danby *et al.* Observation of high-energy neutrino reactions and the existence of two kinds of neutrinos. *Phys. Rev. Lett.*, 9:36–44, 1962.

[11] K. Kodama *et al.* Observation of tau neutrino interactions. *Phys. Lett. B*, 504:218–224, 2001.

[12] S. Schael *et al.* Precision electroweak measurements on the Z resonance. *Physics Reports*, 427:257–454, 2006.

[13] A.W. Sunyar M. Goldhaber, L. Grodzins. Helicity of neutrinos. *Phys. Rev.*, 109:1015–1017, 1958.

[14] G.P. Zellar J.A. Formaggio. From eV to EeV: Neutrino Cross Sections Across Energy Scales. *Rev. Mod. Phys.*, 84:1307–1341, 2012.

[15] L. Pickering. Examining Nuclear Effects in Neutrino Interactions With Transverse Kinematic Imbalance. Proc. 10th Int. Workshop on Neutrino-Nucleus Interactions in Few-GeV Region (NuInt15) `https://journals.jps.jp/doi/pdf/10.7566/JPSCP.12.010032`, 2016.

[16] O. Benhar, A. Fabrocini, and S. Fantoni. The Nucleon Spectral Function in Nuclear Matter. *Nuclear Physics A*, 505:267–299, 1989.

[17] C. Giganti, S. Lavignac, and M. Zito. Neutrino oscillations: The rise of the PMNS paradigm. *Progress in Particle and Nuclear Physics*, 98:1–54, 2018.

[18] C. Riccio. Mesure du flux et de la section efficace des antineutrinos dans le détecteur proche de l'expérience T2K. PhD Thesis `https://www.t2k.org/docs/thesis/113/riccioc_phdthesis`, 2018.

[19] L. Wolfenstein. Neutrino oscillations in matter. *Phys. Rev. D*, 17:2369–2374, 1978.

[20] A.Y. Smirnov S.P. Mikheev. Neutrino Oscillations in an Inhomogeneous Medium: Adiabatic Regime. *Sov. Phys. JETP*, 65:230–236, 1987.

[21] A. Bellerive *et al.* The Sudbury Neutrino Observatory. *Nucl. Phys. B*, 908:30–51, 2016.

[22] M.P. Decowski *et al.* KamLAND's precision neutrino oscillation measurements. *Nucl. Phys. B*, 908:52–61, 2016.

[23] J.N. Bahcall *et al.* Solar neutrino flux. *Astrophys. J.*, 137:344–346, 1963.

[24] K.C. Hoffman R. Davis, D.S. Harmer. Search for neutrinos from the sun. *Phys. Rev. Lett.*, 20:1205–1209, 1968.

[25] M. Cribier. Results of the whole GALLEX experiment. *Nucl. Phys. B Proc. Suppl.*, 70:284–291, 1999.

[26] J.N. Abdurashitov *et al.* Solar neutrino flux measurements by the Soviet-American Gallium Experiment (SAGE) for half the 22 year solar cycle. *J. Exp. Theor. Phys.*, 95:181–193, 2002.

[27] K.S. Hirata *et al.* Observation of 8B solar neutrinos in the Kamiokande-II detector. *Phys. Rev. Lett.*, 63:16–19, 1989.

[28] P.F. de Salas *et al.* 2020 global reassessment of the neutrino oscillation picture. *Journal of High Energy Physics*, 71, 2021.

[29] T.J. Haines *et al.* Calculation of Atmospheric Neutrino Induced Backgrounds in a Nucleon Decay Search. *Phys. Rev. Lett.*, 57, 1986.

[30] K.S. Hirata *et al.* Observation of a small atmospheric muon-neutrino / electron-neutrino ratio in Kamiokande. *Phys. Rev. Lett. B*, 280:146–152, 1992.

[31] Y. Fukuda *et al.* Atmospheric muon-neutrino / electron-neutrino ratio in the multiGeV energy range. *Phys. Rev. Lett. B*, 335:237–245, 1994.

[32] Y. Fukuda *et al.* Evidence for oscillation of atmospheric neutrinos. *Phys. Rev. Lett.*, 81:1562–1567, 1998.

[33] K. Abe *et al.* Atmospheric neutrino oscillation analysis with external constraints in Super-Kamiokande I-IV. *Phys. Rev. D*, 97, 2018.

[34] M.G. Aartsen *et al.* Measurement of Atmospheric Neutrino Oscillations at 6-56 GeV with IceCube DeepCore. *Phys. Rev. Lett.*, 120, 2018.

[35] K. Abe *et al.* Improved constraints on neutrino mixing from the T2K experiment with 3.13×10^{21} protons on target. *Phys. Rev. D*, 103, 2021.

[36] M. Acero *et al.* First measurement of neutrino oscillation parameters using neutrinos and antineutrinos by NOvA. *Phys. Rev. Lett.*, 123, 2019.

[37] Y. Abe *et al.* Measurement of θ_{13} in Double Chooz using neutron captures on hydrogen with novel background rejection techniques. *JHEP*, 163, 2016.

[38] F.P. An *et al.* New Measurement of Antineutrino Oscillation with the Full Detector Configuration at Daya Bay. *Phys. Rev. Lett.*, 115, 2015.

[39] J.H. Choi *et al.* Observation of Energy and Baseline Dependent Reactor Antineutrino Disappearance in the RENO Experiment. *Phys. Rev. Lett.*, 116, 2016.

[40] M.H. Ahn *et al.* Measurement of Neutrino Oscillation by the K2K Experiment. *Phys. Rev. D*, 74, 2006.

[41] P. Adamson *et al.* Combined analysis of ν_μ disappearance and $\nu_\mu \to \nu_e$ appearance in MINOS using accelerator and atmospheric neutrinos. *Phys. Rev. Lett.*, 112, 2014.

[42] N. Agafonova *et al.* Discovery of tau neutrino appearance in the CNGS neutrino beam with the OPERA experiment. *Phys. Rev. Lett.*, 115, 2015.

[43] K. Abe *et al.* The T2K Experiment. *Nuclear Instruments and Methods in Physics Research Section A: Accelerators, Spectrometers, Detectors and Associated Equipment*, 659(1):106–135, 2011.

[44] P. Adamson *et al.* Constraints on Oscillation Parameters from ν_e Appearance and ν_μ Disappearance in NOvA. *Phys. Rev. Lett.*, 118, 2017.

[45] K. Abe *et al.* Constraint on the matter–antimatter symmetry-violating phase in neutrino oscillations. *Nature*, 580(7803):339–344, 2020.

[46] T.A. Doyle. T2K Status and Plans. 30th International Symposium on Lepton Photon Interactions at High Energies (LeptonPhoton2021) `https://indico.cern.ch/event/949705/contributions/4555528/attachments/2370865/4049119/TDoyle_LP2021_T2K_Status_and_Plans.pdf`, 2022.

[47] K. Abe *et al.* Hyper-Kamiokande Design Report. `https://arxiv.org/abs/1805.04163`, 2018.

[48] B. Abi *et al.* DUNE Far Detector Technical Design Report, Volume I. *JINST*, 15, 2020.

[49] P.B. Denton. Snowmass Neutrino Frontier: NF01 Topical Group Report Three-Flavor Neutrino Oscillations. Snowmass 2021, NF01: Neutrino Oscillations `https://snowmass21.org/neutrino/start/drafts`, 2022.

[50] M.G. Aartsen *et al.* Development of an analysis to probe the neutrino mass ordering with atmospheric neutrinos using three years of IceCube DeepCore data. *The European Physical Journal C*, 80(9), 2020.

[51] KTeV Collaboration. Observation of Direct CP Violation in $K_{S,L} \to \pi\pi$ Decays. *Phys. Rev. Lett.*, 83, 1999.

[52] BABAR Collaboration. Observation of CP Violation in the B^0 Meson System. *Phys. Rev. Lett.*, 87, 2001.

[53] F. Betti *et al.* Observation of CP Violation in Charm Decays. *Phys. Rev. Lett.*, 122, 2019.

[54] KATRIN Collaboration. Direct neutrino-mass measurement with sub-electronvolt sensitivity. *Nature Physics*, 18:160–166, 2022.

[55] A.A. Aguilar-Arevalo *et al.* Evidence for neutrino oscillations from the observation of $\bar{\nu}_e$ appearance in a $\bar{\nu}_\mu$ beam. *Phys. Rev. D*, 64, 2001.

[56] A.A. Aguilar-Arevalo *et al.* Significant Excess of Electronlike Events in the MiniBooNE Short-Baseline Neutrino Experiment. *Phys. Rev. Lett.*, 121, 2018.

[57] P. Adamson *et al.* Search for Sterile Neutrinos in MINOS and MINOS+ Using a Two-Detector Fit. *Phys. Rev. Lett.*, 122, 2019.

[58] R. Acciarri *et al.* Design and Construction of the MicroBooNE Detector. *JINST*, 12, 2017.

[59] P. Abratenko *et al.* Search for Neutrino-Induced Neutral-Current Δ Radiative Decay in MicroBooNE and a First Test of the MiniBooNE Low Energy Excess under a Single-Photon Hypothesis. *Phys. Rev. Lett.*, 128, 2022.

[60] P. Abratenko *et al.* Search for an anomalous excess of charged-current ν_e interactions without pions in the final state with the MicroBooNE experiment. `https://arxiv.org/abs/2110.14065`, 2021.

[61] P. Abratenko *et al.* Search for an anomalous excess of inclusive charged-current ν_e interactions in the MicroBooNE experiment using Wire-Cell reconstruction. `https://arxiv.org/abs/2110.13978`, 2021.

[62] P. Abratenko *et al.* Search for an anomalous excess of charged-current quasi-elastic ν_e interactions with the MicroBooNE experiment using Deep-Learning-based reconstruction. `https://arxiv.org/abs/2110.14080`, 2021.

[63] K. Matsuoka *et al.* Design and performance of the muon monitor for the T2K neutrino oscillation experiment. *Nuclear Instruments and Methods in Physics Research Section A: Accelerators, Spectrometers, Detectors and Associated Equipment*, 624(3):591–600, 2010.

[64] S. Bhadra *et al.* Optical transition radiation monitor for the T2K experiment. *Nuclear Instruments and Methods in Physics Research Section A: Accelerators, Spectrometers, Detectors and Associated Equipment*, 703:45–58, 2013.

[65] L. Berns et al. Flux Prediction and Uncertainty with NA61/SHINE 2010 Replica Target Mesaurements. Technical Report TN-401, T2K, 2021.

[66] K. Abe *et al.* Measurements of the T2K neutrino beam properties using the INGRID on-axis near detector. *Nuclear Instruments and Methods in Physics Research Section A: Accelerators, Spectrometers, Detectors and Associated Equipment*, 694:211–223, 2012.

[67] K. Abe *et al.* Measurement of neutrino and antineutrino oscillations by the T2K experiment including a new additional samples of ν_e interactions at the far detector. *Physical Review D*, 96, 2017.

[68] S. Assylbekov *et al.* The T2K ND280 off-axis pi-zero detector. *Nuclear Instruments and Methods in Physics Research Section A: Accelerators, Spectrometers, Detectors and Associated Equipment*, 686:48–63, 2012.

[69] P.A. Amaudruz *et al.* The T2K fine-grained detectors. *Nuclear Instruments and Methods in Physics Research Section A: Accelerators, Spectrometers, Detectors and Associated Equipment*, 696:1–31, 2012.

[70] N. Abgrall *et al.* Time projection chambers for the T2K near detectors. *Nuclear Instruments and Methods in Physics Research Section A: Accelerators, Spectrometers, Detectors and Associated Equipment*, 637(1):25–46, 2011.

[71] D. Allan *et al.* The electromagnetic calorimeter for the T2K near detector ND280. *Journal of Instrumentation*, 8, 2013.

[72] S. Aoki *et al.* The T2K side muon range detector (SMRD). *Nuclear Instruments and Methods in Physics Research Section A: Accelerators, Spectrometers, Detectors and Associated Equipment*, 698:135–146, 2013.

[73] J. Estrada, C. Garcia, B. Hoeneisen, and P. Rubinov. MCM II and the Trip chip. Technical Report FERMILAB-TM-2226, Fermilab, 2002.

[74] T. Ovsiannikova *et al.* The new experiment WAGASCI for water to hydrocarbon neutrino cross section measurement using the J-PARC beam. *Journal of Physics: Conference Series*, 675, 2016.

[75] M. Antonova *et al.* Baby MIND: a magnetized segmented neutrino detector for the WAGASCI experiment. *Journal of Instrumentation*, 12, 2017.

[76] T. Odagawa *et al.* Prospect and status of the physics run of the NINJA experiment. *Proceedings of Science (NuFact2019)*, 144, 2020.

[77] S. Jenkins. T2K latest results on neutrino-nucleus cross sections. 17th International Conference on Topics in Astroparticle and Underground Physics (TAUP 2021) `https://indico.ific.uv.es/event/6178/contributions/15576/attachments/9273/12402/TAUP_T2Kxsec_SJenkins_v1.pdf`, 2021.

[78] S. Fukuda *et al.* The Super-Kamiokande detector. *Nuclear Instruments and Methods in Physics Research Section A: Accelerators, Spectrometers, Detectors and Associated Equipment*, 501:418–462, 2003.

[79] C. Simpson *et al.* Sensitivity of Super-Kamiokande with Gadolinium to Low Energy Antineutrinos from Pre-supernova Emission. *Astrophysical Journal*, 885(2), 2019.

[80] K. Fusshoeller et al. FHC muon neutrino charged current multiple pion samples in the ND280 tracker for the 2020 oscillation analysis inputs: Run $2 + 3 + 4 + 8$ with P6T NEUT_D MC. Technical Report TN-407, T2K, 2020.

[81] T. A. Doyle et al. ND280 FHC samples with Photon and Proton information for the 2021 Oscillation Analysis. Technical Report TN-421, T2K, 2021.

[82] Y. Hayato. A neutrino interaction simulation program library NEUT. *Acta Physica Polonica B*, 40(9):2477–2489, 2009.

[83] R.A. Smith and E.J. Moniz. Neutrino reactions on nuclear targets. *Nuclear Physics B*, 43:605, 1972.

[84] R. Gran, J. Nieves, F. Sanchez, and M.J.V. Vacas. Neutrino-nucleus quasi-elastic and 2p2h interactions up to 10 GeV. *Physical Review D*, 88:113007, 2013.

[85] D. Rein and L.M. Sehgal. Neutrino Excitation of Baryon Resonances and Single Pion Production. *Annals of Physics*, 133(1):79–153, 1981.

[86] K.M. Graczyk and J.T. Sobczyk. Form factors in the quark resonance model. *Physical Review D*, 77:053001, 2008.

[87] C. Berger and L.M. Seghal. PCAC and coherent pion production by low energy neutrinos. *Physical Review D*, 79:053003, 2009.

[88] A. Bodek and U.K. Yang. Update to the Bodek-Yang Unified Model for Electron- and Neutrino- Nucleon Scattering Cross Sections. *Proceedings of Science (ICHEP2010)*, page 292, 2010.

[89] T. Sjostrand. High-energy physics event generation with PYTHIA 5.7 and JETSET 7.4. *Computer Physics Communications*, 82:74–90, 1994.

[90] S. Agostinelli *et al.* GEANT4-a simulation toolkit. *Nuclear Instruments and Methods in Physics Research Section A: Accelerators, Spectrometers, Detectors and Associated Equipment*, 506:250–303, 2003.

[91] C. Bojechko et al. CC-multiple-pion ν_μ event selections in the ND280 tracker using Run 1+2+3+4 data. Technical Report TN-152, T2K, 2013.

[92] A. Cervera et al. CC-0Pi Multi-Topology Selection and Systematics in FGD1. Technical Report TN-216, T2K, 2015.

[93] P.A. Zyla *et al.* (Particle Data Group). Review of Particle Physics 083C01 (2020) and 2021 update. *Prog. Theor. Exp. Phys.*, 2020.

[94] G. Barker et al. Implementation of the Second Generation PID for the ND280 Tracker ECals. Technical Report TN-111, T2K, 2012.

[95] P. Bartet et al. ν_μ CC event selections in the ND280 tracker using Run 2+3+4 data. Technical Report TN-212, T2K, 2015.

[96] J. Lagoda K. Skwarczynski. IsoRecon hybrid efficiency for FHC and RHC using production 6T. Technical Report TN-410, T2K, 2020.

[97] D. Brailsford et al. Study of the tracker ECal systematic uncertainties. Technical Report TN-279, T2K, 2017.

[98] P. Lasorak. A search for neutrino-induced single photons and measurement of oscillation analysis systematic errors with electron and anti-electron neutrino selections, using the off-axis near detector of the Tokai to Kamioka experiment. PhD Thesis `https://www.t2k.org/docs/thesis/088/Theesis`, 2018.

[99] L. Berns et al. Five Sample Joint Oscillation Analysis with T2K Run1–10 Data. Technical Report TN-397, T2K, 2021.

[100] C. Andreopoulos et al. T2K Neutrino and Anti-Neutrino 3-Flavour Joint Analysis of Run 1-10 (1.4938×10^{21}-POT ν 1.6346×10^{21}-POT $\bar{\nu}$) data sets. Technical Report TN-394, T2K, 2022.

[101] E. Atkin et al. Measuring PMNS parameters in a joint ND280-SK analysis using MCMC. Technical Report TN-393, T2K, 2021.

[102] N. Abgrall *et al.* Measurements of $\pi^\pm$, $k^\pm$ and proton double differential yields from the surface pf the t2k replica target for incoming 31 gev/c protons with the NA61/SHINE spectrometer at the CERN SPS. *Eur. Phys. J. C*, 79(2):100, 2019.

[103] N. Abgrall *et al.* Measurements of $\pi^{\pm}$, $K^{\pm}$, K^0_S, Λ and proton production in proton-carbon interactions at 31 GeV/c with the NA61/SHINE spectrometer at the CERN SPS. *Eur. Phys. J. C*, 76(2):84, 2016.

[104] T. Vladisavljevic et al. Flux Prediction and Uncertainty with NA61/SHINE 2009 Replica-Target Data. Technical Report TN-354, T2K, 2020.

[105] Y. Hayato and L. Pickering. The `NEUT` neutrino interaction simulation program library. *Eur. Phys. J. Spec. Top.*, 6, 2021.

[106] J. Chakrani et al. NIWG model and uncertainties for 2021 oscillation analysis. Technical Report TN-414, T2K, 2022.

[107] E.T. Atkin et al. NIWG model and uncertainties for 2019-2020 oscillation analysis. Technical Report TN-344, T2K, 2020.

[108] L. Aliaga *et al.* Design, Calibration, and Performance of the MINERνA Detector. *Nuclear Instruments and Methods in Physics Research Section A: Accelerators, Spectrometers, Detectors and Associated Equipment*, 743:130–159, 2014.

[109] L. Munteanu et al. Constraining the flux and cross section models with data from ND280 using FGD1 and FGD2 for the 2020 oscillation analysis. Technical Report TN-395, T2K, 2020.

[110] M. Martini *et al.* Unified Approach for Nucleon Knock-Out and Coherent and Incoherent Pion Production in Neutrino Interactions with Nuclei. *Phys. Rev. C*, 80, 2009.

[111] D. Rein and L.M. Sehgal. Coherent π^0 Production in Neutrino Reactions. *Nuclear Physics B*, 223(1):29–44, 1983.

[112] A. Higuera *et al.* Measurement of Coherent Production of $\pi^{\pm}$ in Neutrino and Antineutrino Beams on Carbon from E_ν of 1.5 to 20 GeV. *Phys. Rev. Lett.*, 113(26), 2014.

[113] M. Glück, E. Reya, and A. Vogt. Dynamical parton distributions revisited. *Eur. Phys. J. C*, 5:461–470, 1998.

[114] T. Yang, C. Andreopoulos, H. Gallagher, and P. Kehayias. A Hadronization Model for the MINOS Experiment. *AIP Conf. Proc.*, 967:269–275, 2007.

[115] A. Bodek and U.K. Yang. Axial and Vector Structure Functions for Electron- and Neutrino- Nucleon Scattering Cross Sections at all Q^2 using Effective Leading order Parton Distribution Functions. *arXiv: High Energy Physics - Phenomenology*, 2010.

[116] P. de Perio et al. NEUT Nuclear Effects (FSI). Technical Report TN-033, T2K, 2012.

[117] D. Barrow et al. Super-Kamiokande Data Quality, MC, and Systematics in Run 10. Technical Report TN-399, T2K, 2020.

[118] D. Barrow et al. Super-Kamiokande ν_μ multi-ring samples for the 2021 Oscillation Analysis. Technical Report TN-447, T2K, 2022.

[119] T. A. Doyle et al. Constraining the flux and cross section models for the 2021 oscillation analysis using ND280 data. Technical Report TN-423, T2K, 2022.

[120] D. Barrow et al. Super-Kamiokande detector systematic uncertainty including the multi-ring $1\mu 1\pi^+$ sample. Technical Report TN-448, T2K, 2022.

[121] R. Brun and F. Rademakers. ROOT - an object oriented data analysis framework. *Nuclear Instruments and Methods in Physics Research Section A: Accelerators, Spectrometers, Detectors and Associated Equipment*, 389:81–86, 1997.

[122] L. Berns et al. Six Sample Joint Oscillation Analysis with T2K Run1–10 Data. Technical Report TN-430, T2K, 2022.

[123] C. Bojechko et al. Measurement and Correction of Magnetic Field Distortions in the Time Projection Chambers. Technical Report TN-061, T2K, 2013.

[124] A. Cervera and L. Escudero. Study of momentum resolution and scale using tracks that cross multiple TPCs. Technical Report TN-222, T2K, 2014.

[125] E. Frank et al. B-field calibration and systematic errors. Technical Report TN-081, T2K, 2011.

[126] F. Sanchez and J. vo Medina. ND280 global charge identification systematic error. Technical Report TN-229, T2K, 2016.

Appendix A

Single Detector Systematics

In this appendix, the impact on the final selected samples of every detector systematic uncertainty is discussed.

A.1 B field distortions

This systematic uncertainty is described in detail in [95]. Figs. A.1 and A.2 show the comparison between relative errors for each sample and for FGD1 and FGD2 selections. The difference between FGD1 and FGD2 is related with the large magnetic field distortion in TPC3, as discussed in [123].

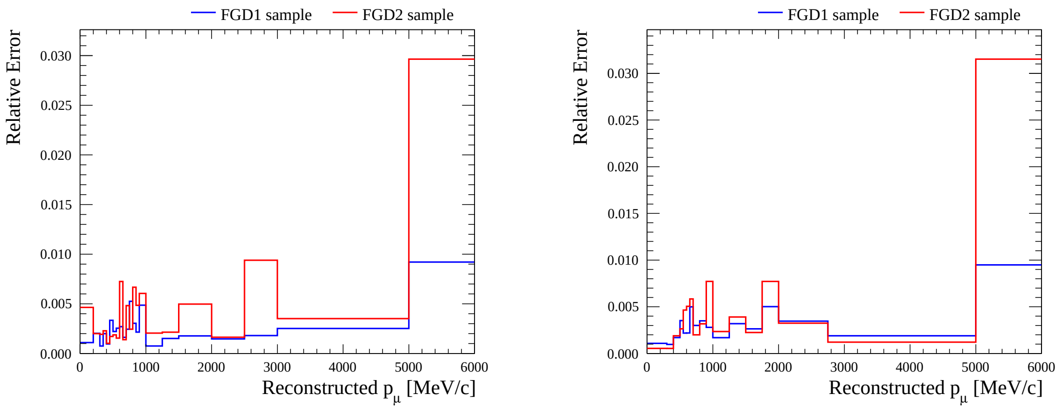

(a) CC0π0p (b) CC0πNp

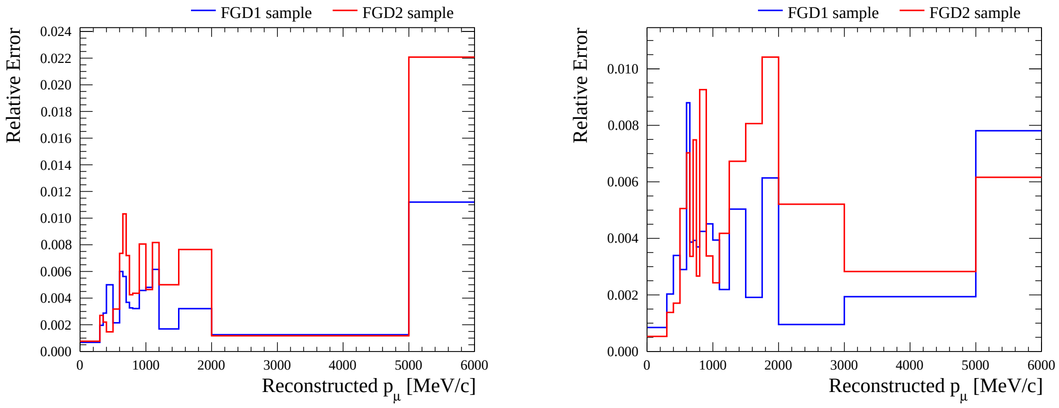

(c) CC1π^+ (d) CC-Photon

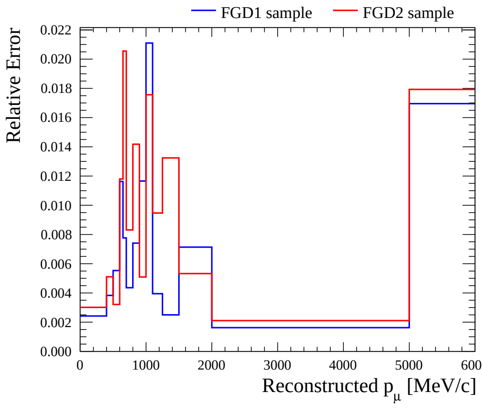

(e) CC-Other

Figure A.1: Relative error evaluated after the propagation the uncertainty on the magnetic field distortion as function of the reconstructed muon momentum for ν_μ CC0π0p (a), CC0πNp (b), CC1π^+ (c), CC-Photon (d) and CC-Other (e) samples. The blue line shows the relative error for FGD1 while the red line for FGD2. The last bin in momentum includes all events with p_μ greater than 5000 MeV/c.

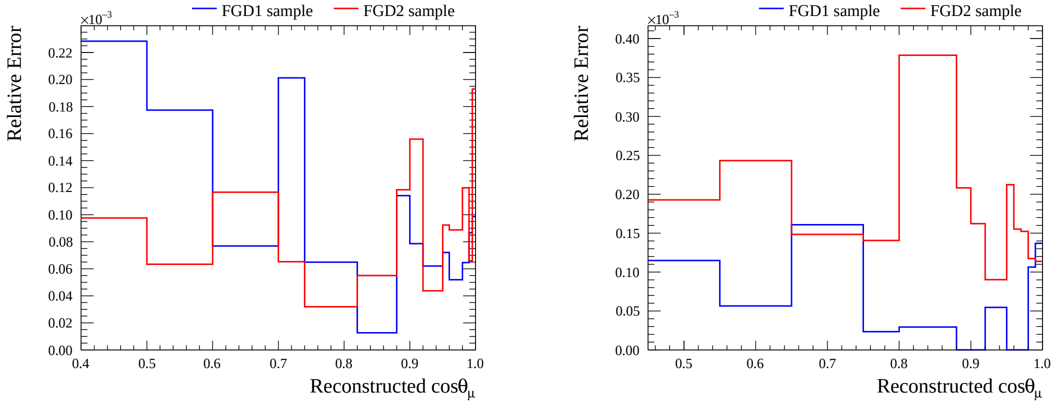

(a) CC0π0p (b) CC0πNp

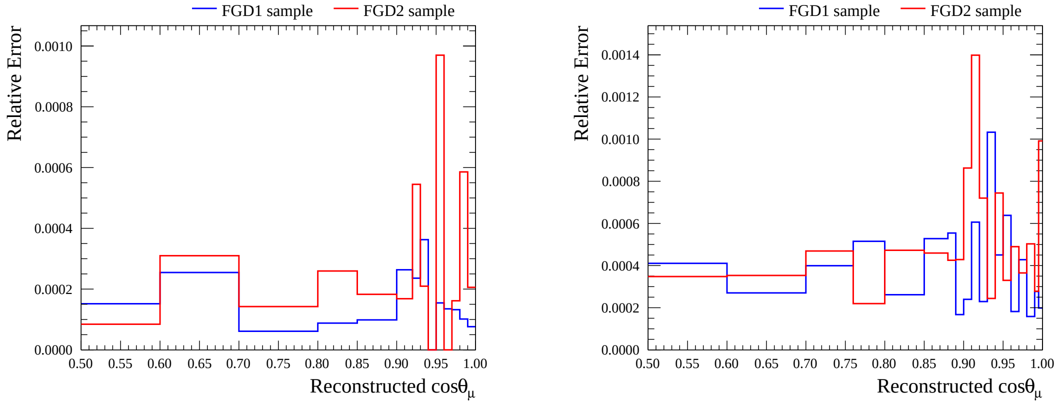

(c) CC1π^+ (d) CC-Photon

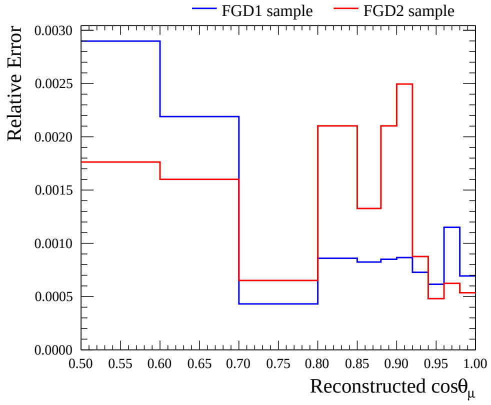

(e) CC-Other

Figure A.2: Relative error evaluated after the propagation the uncertainty on the magnetic field distortion as function of the reconstructed muon $\cos\theta$ for ν_μ CC0π0p (a), CC0πNp (b), CC1π^+ (c), CC-Photon (d) and CC-Other (e) samples. The blue line shows the relative error for FGD1 while the red line for FGD2. The first bin in $\cos\theta_\mu$ includes all events with $\cos\theta_\mu$ below 0.6.

A.2 TPC momentum resolution

This systematic uncertainty is shown in Figs. A.3 and A.4 for each sample and for FGD1 and FGD2. As expected the relative error for both selections has the same behaviour since it depends on the magnetic field. The momentum resolution study is presented in detail in [124].

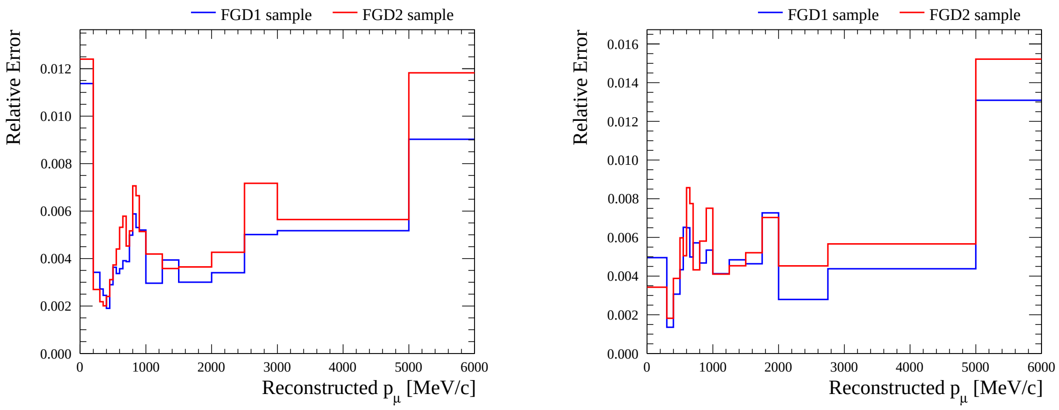

(a) CC0π0p (b) CC0πNp

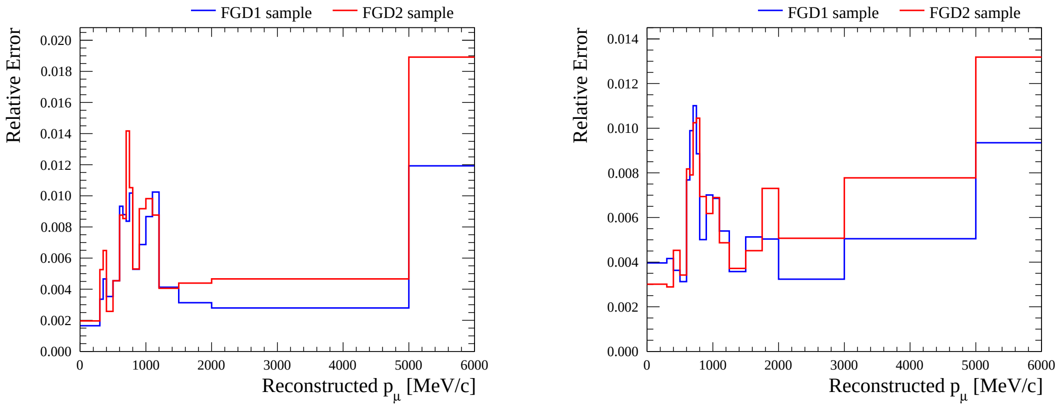

(c) CC1π^+ (d) CC-Photon

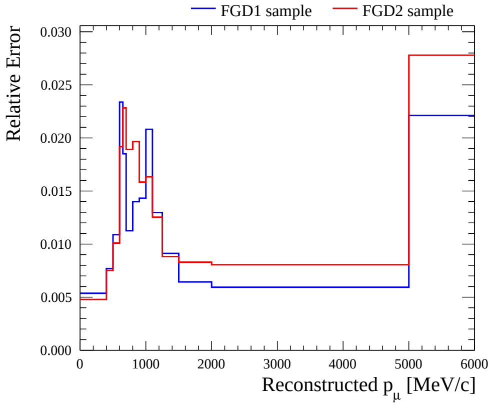

(e) CC-Other

Figure A.3: Relative error evaluated after the propagation the uncertainty on the momentum resolution as function of the reconstructed muon momentum for ν_μ CC0π0p (a), CC0πNp (b), CC1π^+ (c), CC-Photon (d) and CC-Other (e) samples. The blue line shows the relative error for FGD1 while the red line for FGD2. The last bin in momentum includes all events with p_μ greater than 5000 MeV/c.

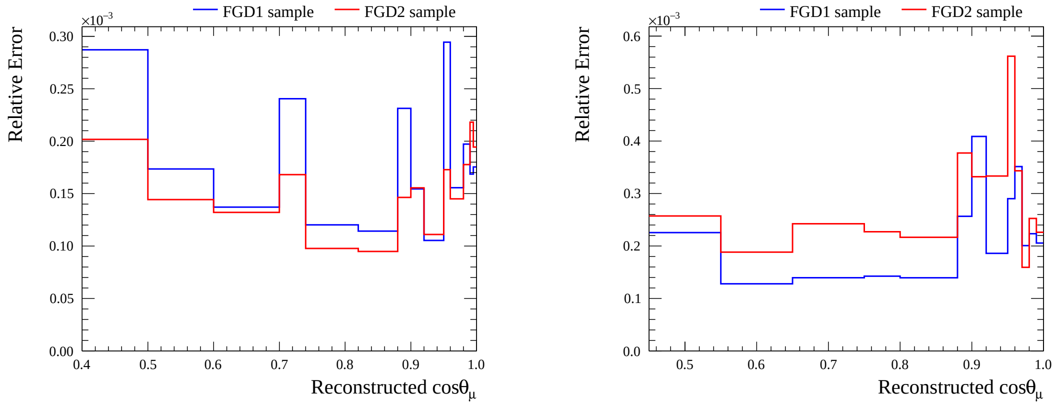

(a) CC0π0p (b) CC0πNp

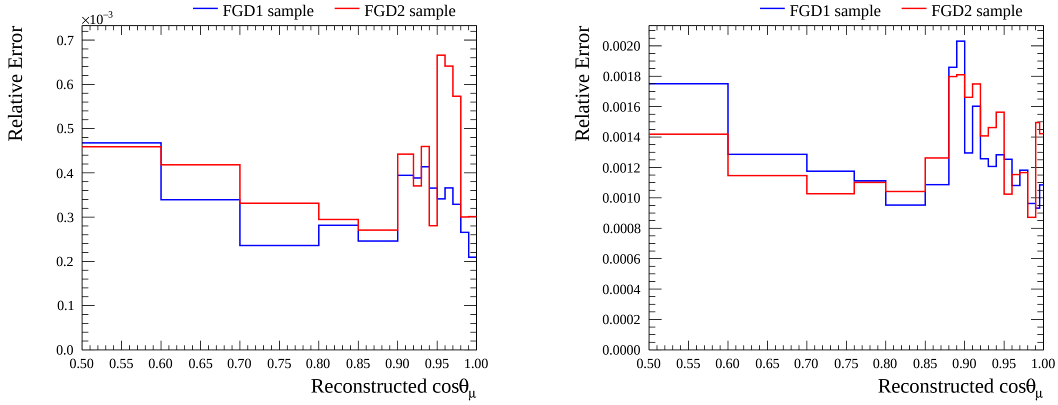

(c) CC1π^+ (d) CC-Photon

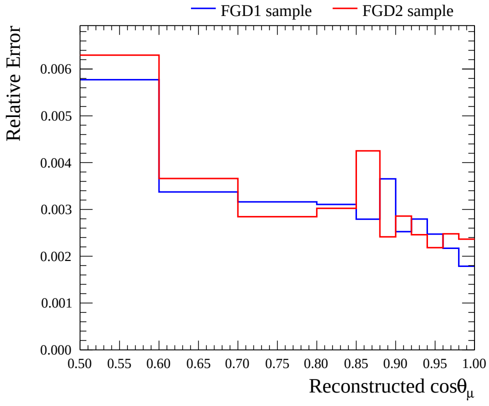

(e) CC-Other

Figure A.4: Relative error evaluated after the propagation the uncertainty on the momentum resolution as function of the reconstructed muon $\cos\theta$ for ν_μ CC0π0p (a), CC0πNp (b), CC1π^+ (c), CC-Photon (d) and CC-Other (e) samples. The blue line shows the relative error for FGD1 while the red line for FGD2. The first bin in $\cos\theta_\mu$ includes all events with $\cos\theta_\mu$ below 0.6.

A.3 TPC momentum scale

The momentum scale uncertainty is evaluated from the B-field measurement described in [125]. The comparison, for this systematic, between relative errors for each sample and for FGD1 and FGD2 selections is shown in Figs. A.5 and A.6. The effect of this uncertainty on the FGD1 and FGD2 selections is very similar; this is because the same systematic is used for all of the TPCs. The effect on the total number of events passing the cuts is small. This is expected as this systematic effects more the migration between bins than the total number of events passing the selection cuts.

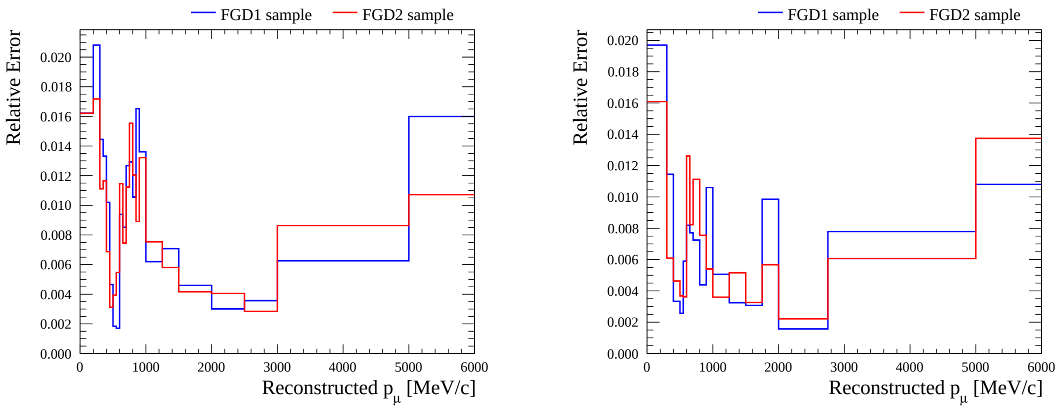

(a) CC0π0p (b) CC0πNp

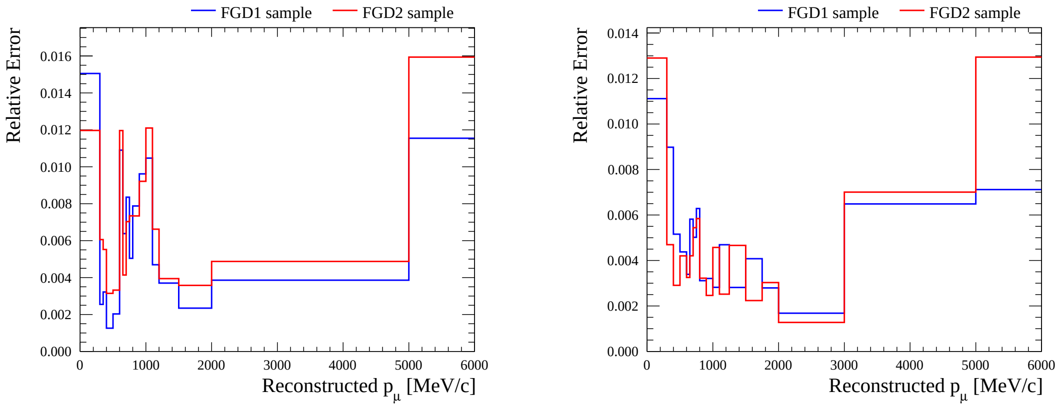

(c) CC1π^+ (d) CC-Photon

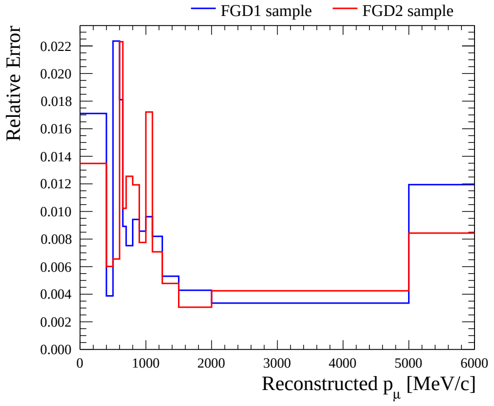

(e) CC-Other

Figure A.5: Relative error evaluated after the propagation of the uncertainty on the momentum scale as function of the reconstructed muon momentum for ν_μ CC0π0p (a), CC0πNp (b), CC1π^+ (c), CC-Photon (d) and CC-Other (e) samples. The blue line shows the relative error for FGD1 while the red line for FGD2. The last bin in momentum includes all events with p_μ greater than 5000 MeV/c.

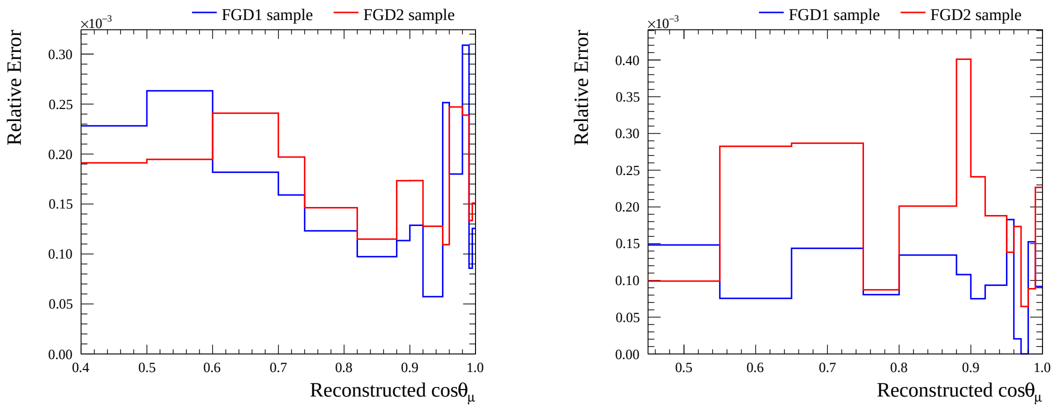

(a) CC0π0p (b) CC0πNp

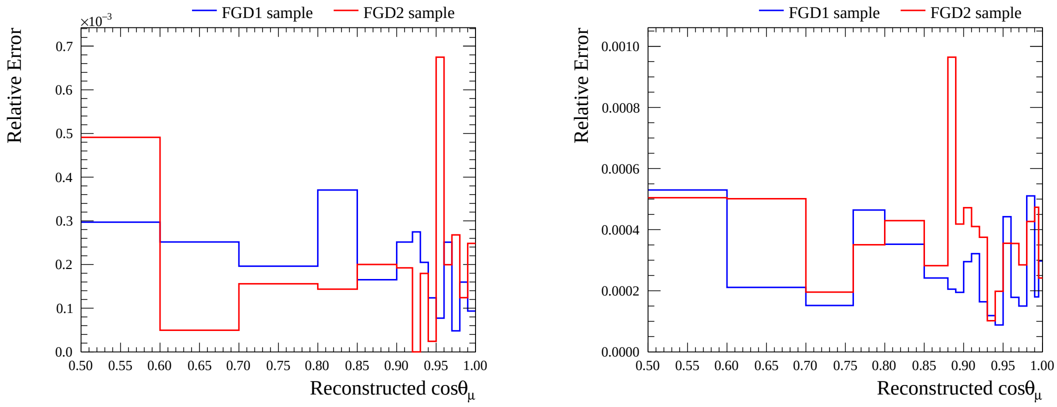

(c) CC1π^+ (d) CC-Photon

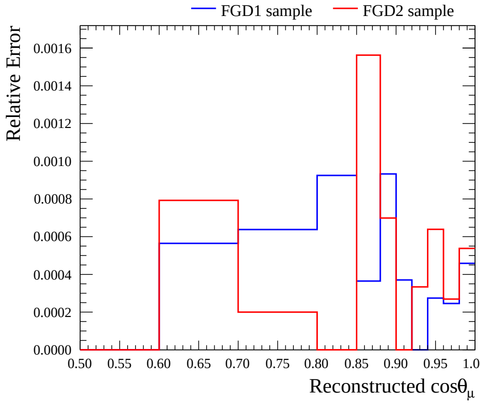

(e) CC-Other

Figure A.6: Relative error evaluated after the propagation of the uncertainty on the momentum scale as function of the reconstructed muon $\cos\theta$ for ν_μ CC0π0p (a), CC0πNp (b), CC1π^+ (c), CC-Photon (d) and CC-Other (e) samples. The blue line shows the relative error for FGD1 while the red line for FGD2. The first bin in $\cos\theta_\mu$ includes all events with $\cos\theta_\mu$ below 0.6.

A.4 TPC PID

The PID is one of the main measurements performed with the TPCs. For the analysis presented in this thesis, the TPC PID systematic is important because of the misidentification between muons and pions that can occur when selecting the muon candidate. The TPC PID relative systematic error is shown in Figs. A.7 and A.8.

The higher value of relative error for each sample at low and high momentum values is due to the failure of TPC PID in this momentum range. At high momentum values, the relative error for FGD2 is higher than for FGD1 because particles with high momentum produce straighter tracks than particles with low momentum. Moreover, in FGD2 only TPC3 is used, lowering the ability to reconstruct the particle charge. This combination causes a failure in TPC PID which is higher in FGD2 than in FGD1.

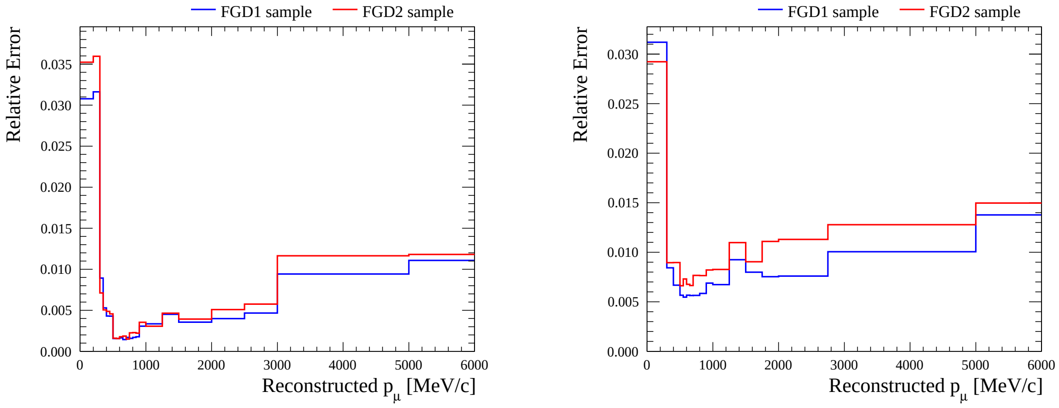

(a) CC0π0p (b) CC0πNp

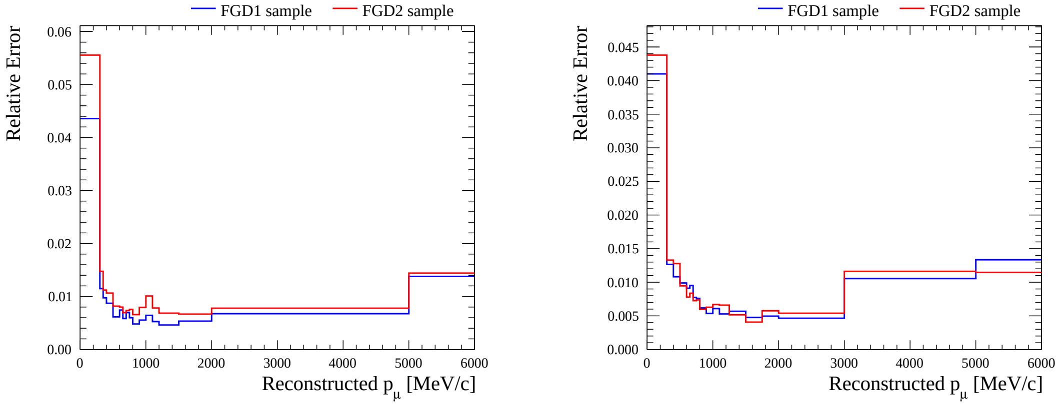

(c) CC1π^+ (d) CC-Photon

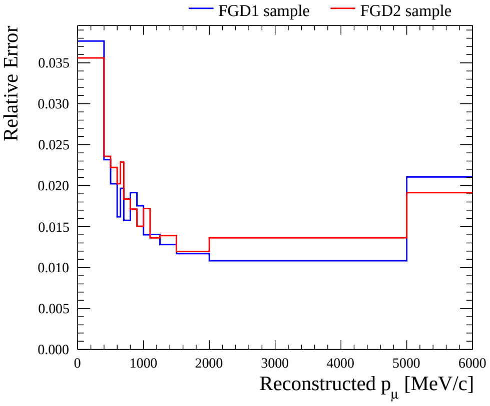

(e) CC-Other

Figure A.7: Relative error evaluated after the propagation of the uncertainty on the TPC PID as function of the reconstructed muon momentum for ν_μ CC0π0p (a), CC0πNp (b), CC1π^+ (c), CC-Photon (d) and CC-Other (e) samples. The blue line shows the relative error for FGD1 while the red line for FGD2. The last bin in momentum includes all events with p_μ greater than 5000 MeV/c.

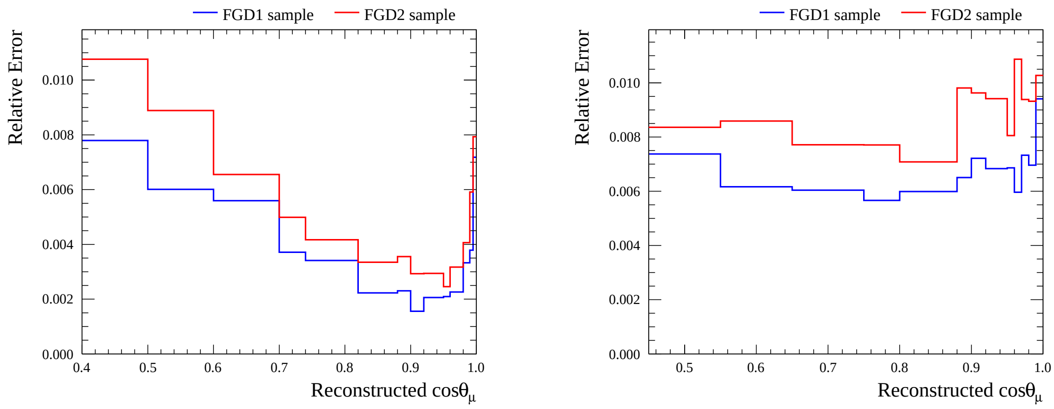

(a) CC0π0p (b) CC0πNp

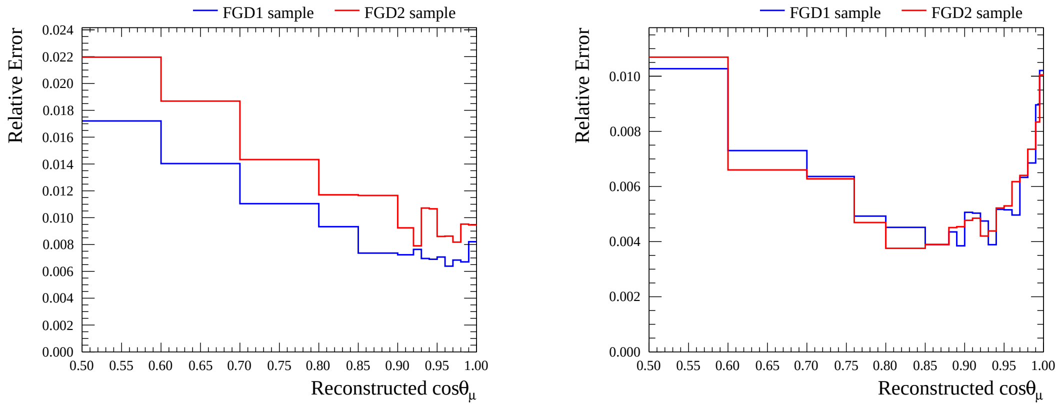

(c) CC1π^+ (d) CC-Photon

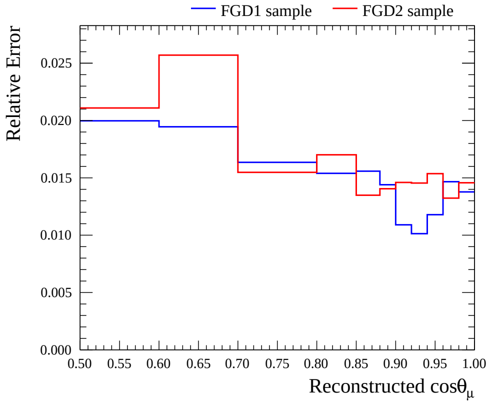

(e) CC-Other

Figure A.8: Relative error evaluated after the propagation of the uncertainty on the TPC PID as function of the reconstructed muon $\cos\theta$ for ν_μ CC0π0p (a), CC0πNp (b), CC1π^+ (c), CC-Photon (d) and CC-Other (e) samples. The blue line shows the relative error for FGD1 while the red line for FGD2. The first bin in $\cos\theta_\mu$ includes all events with $\cos\theta_\mu$ below 0.6.

A.5 FGD PID

In Figs. A.9 and A.10 comparisons between relative errors for each sample and for FGD1 and FGD2 selections are shown. This systematic uncertainty is larger for FGD2 than for FGD1 given the presence of water layers in the former. Furthermore, a sizeable effect can be seen in CC0πNp as proton PID in the FGD is one of the criteria for this sample. This systematic is not applied to the CC-Photon sample, since the photon tag is applied before the charged pion tag which uses FGD PID.

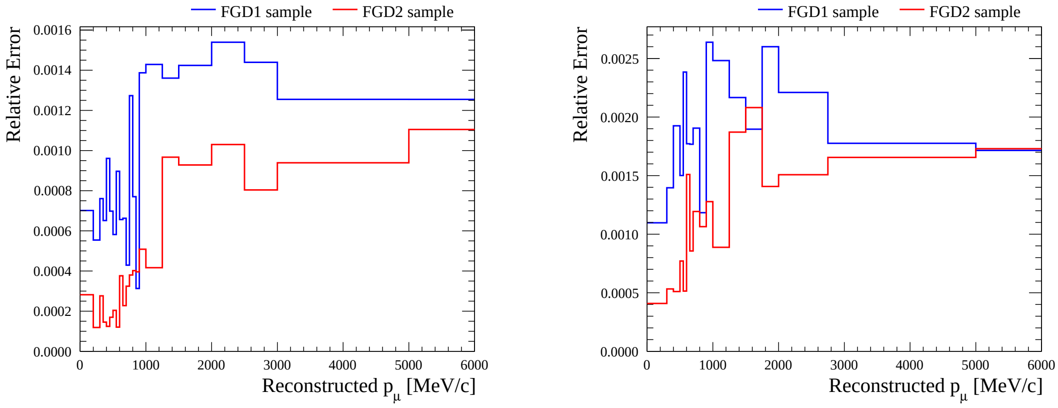

(a) CC0π0p (b) CC0πNp

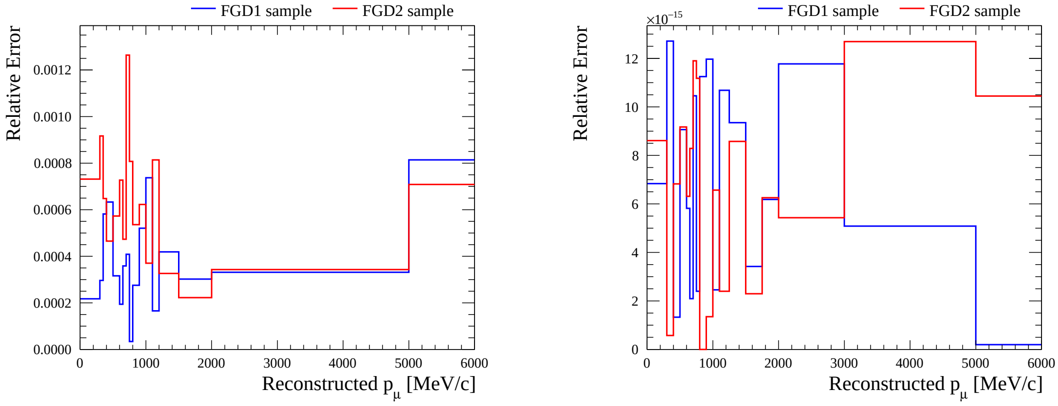

(c) CC1π^+ (d) CC-Photon

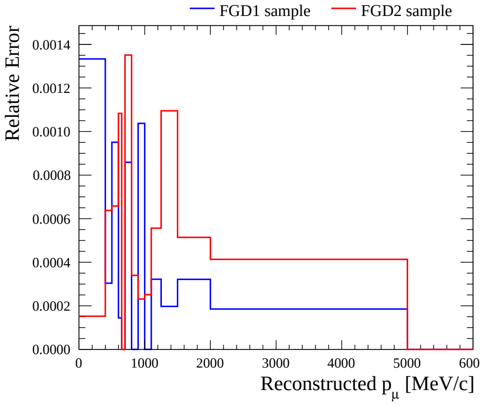

(e) CC-Other

Figure A.9: Relative error evaluated after the propagation of the uncertainty on the FGD PID as function of the reconstructed muon momentum for ν_μ CC0π0p (a), CC0πNp (b), CC1π^+ (c), CC-Photon (d) and CC-Other (e) samples. The blue line shows the relative error for FGD1 while the red line for FGD2. The last bin in momentum includes all events with p_μ greater than 5000 MeV/c.

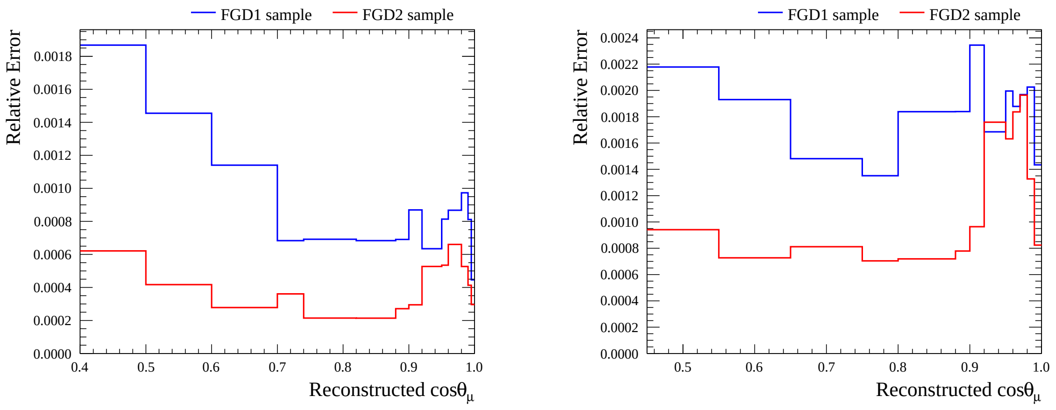

(a) CC0π0p (b) CC0πNp

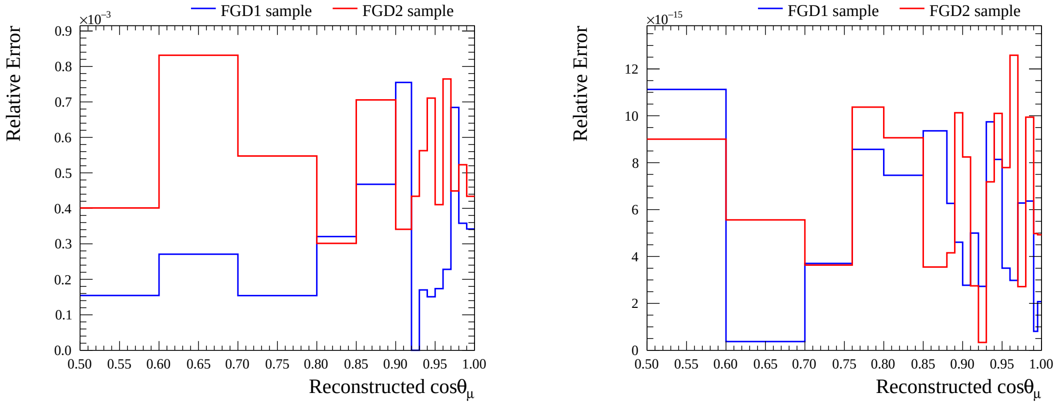

(c) CC1π^+ (d) CC-Photon

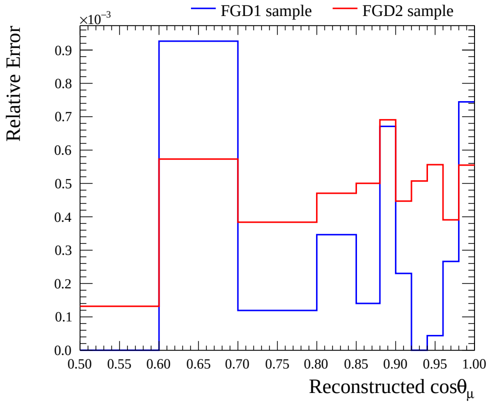

(e) CC-Other

Figure A.10: Relative error evaluated after the propagation of the uncertainty on the FGD PID as function of the reconstructed muon $\cos\theta$ for ν_μ CC0π0p (a), CC0πNp (b), CC1π^+ (c), CC-Photon (d) and CC-Other (e) samples. The blue line shows the relative error for FGD1 while the red line for FGD2. The first bin in $\cos\theta_\mu$ includes all events with $\cos\theta_\mu$ below 0.6.

A.6 Charge identification efficiency

The global charge identification is based on the combination of ND280 sub-detectors. The method used to estimate the systematic uncertainty associated with this is described in [126]. The technique uses the error on momentum to parametrise the differences between data and MC for both the local TPC and the global charge.

In Figs. A.11 and A.12 comparisons between the relative error for FGD1 and FGD2 for each sample are shown. The systematic uncertainty is larger for FGD2 due to TPC3 being located at the edge of the ND280 detector. This results in larger data-MC differences in the performance that can be attributed to difficulties in the simulation of field non-linearities.

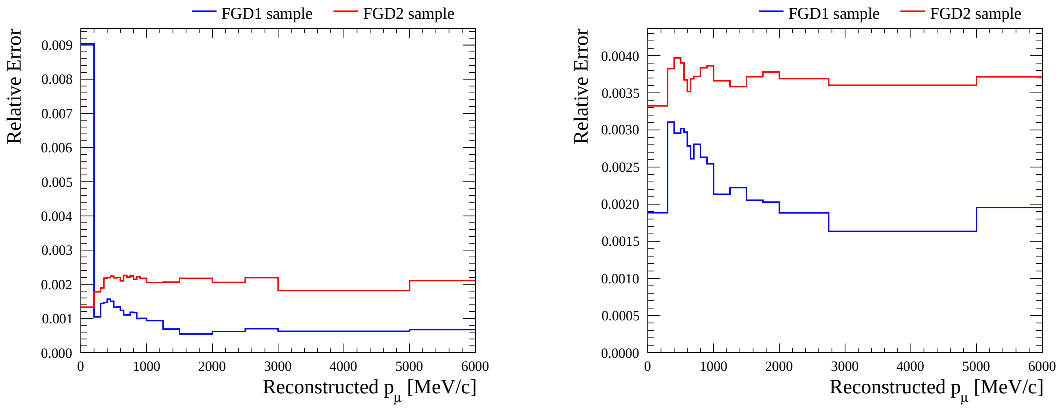

(a) CC0π0p (b) CC0πNp

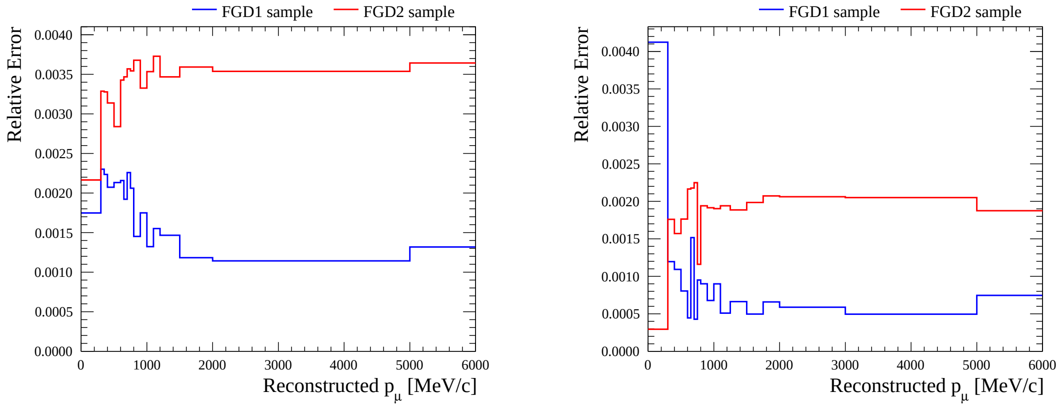

(c) CC1π^+ (d) CC-Photon

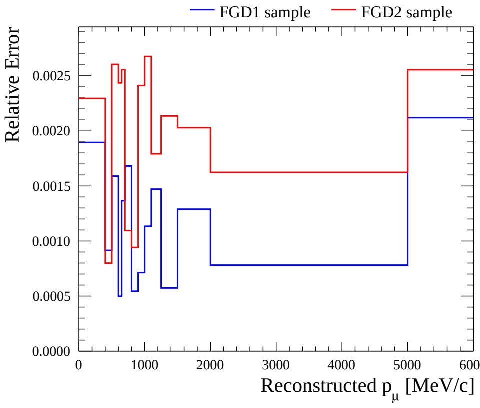

(e) CC-Other

Figure A.11: Relative error evaluated after the propagation of the uncertainty on the charge identification efficiency as function of the reconstructed muon momentum for ν_μ CC0π0p (a), CC0πNp (b), CC1π^+ (c), CC-Photon (d) and CC-Other (e) samples. The blue line shows the relative error for FGD1 while the red line for FGD2. The last bin in momentum includes all events with p_μ greater than 5000 MeV/c.

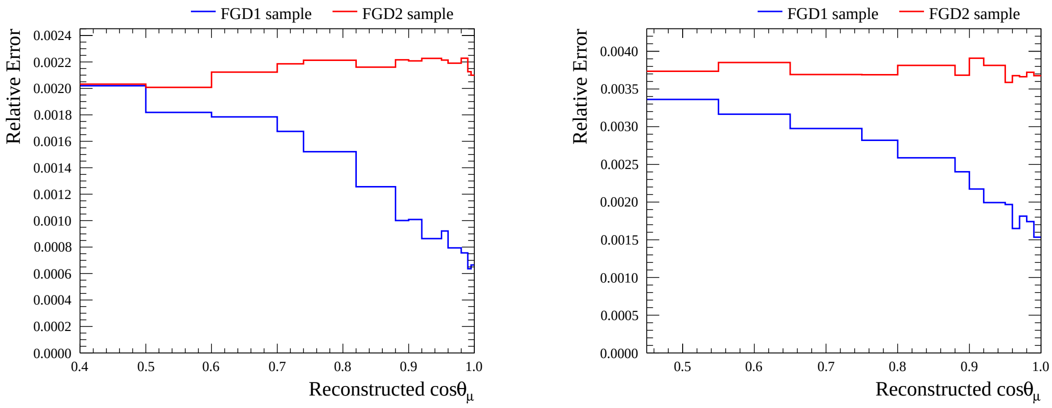

(a) CC0π0p (b) CC0πNp

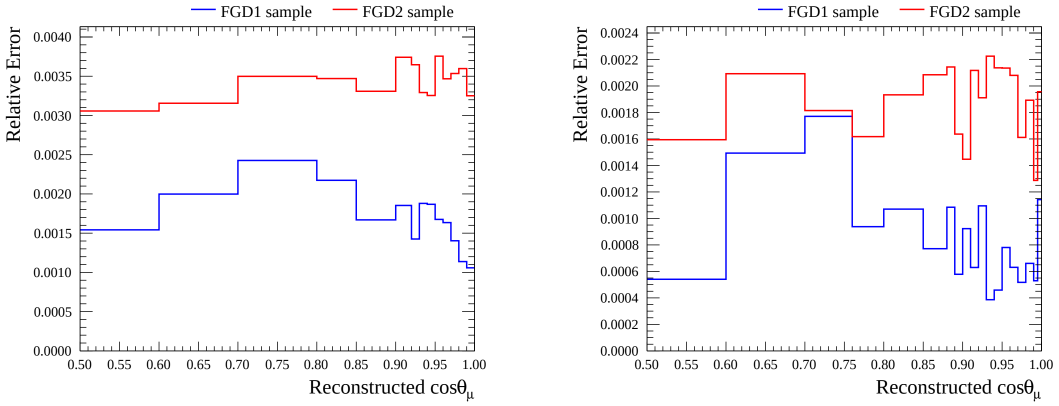

(c) CC1π^+ (d) CC-Photon

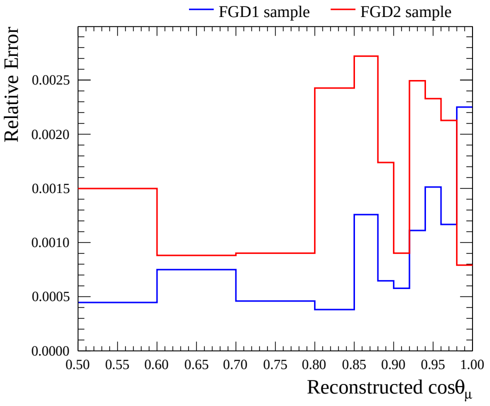

(e) CC-Other

Figure A.12: Relative error evaluated after the propagation of the uncertainty on the charge identification efficiency as function of the reconstructed muon $\cos\theta$ for ν_μ CC0π0p (a), CC0πNp (b), CC1π^+ (c), CC-Photon (d) and CC-Other (e) samples. The blue line shows the relative error for FGD1 while the red line for FGD2. The first bin in $\cos\theta_\mu$ includes all events with $\cos\theta_\mu$ below 0.6.

A.7 TPC cluster efficiency

The difference in TPC cluster efficiency between data and MC is the main source of a different fraction of events in data and MC passing the TPC track quality cut. Details on its evaluation can be found in [95]. In Figs. A.13 and A.14 the relative errors for this systematic for FGD1 and FGD2 are shown.

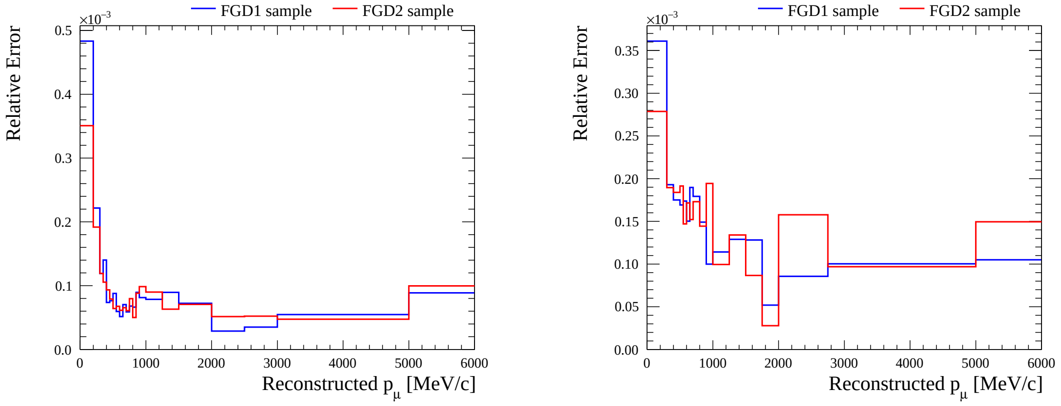

(a) CC0π0p (b) CC0πNp

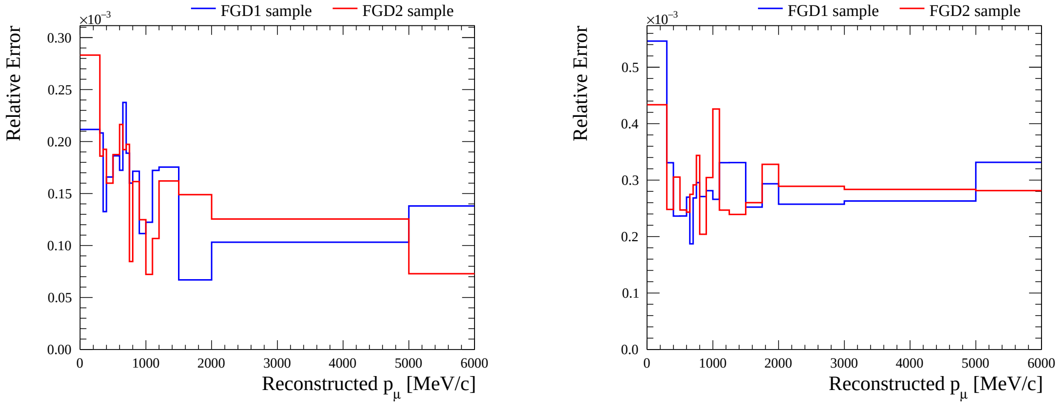

(c) CC1π^+ (d) CC-Photon

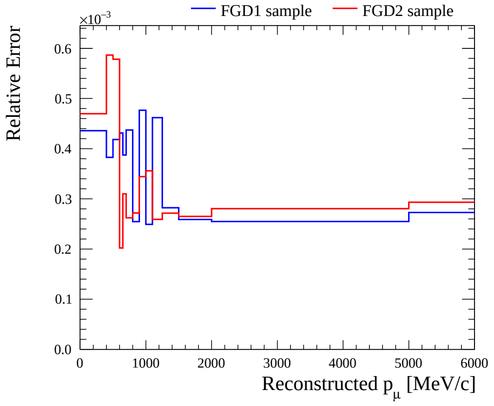

(e) CC-Other

Figure A.13: Relative error evaluated after the propagation of the uncertainty on the TPC cluster efficiency as function of the reconstructed muon momentum for ν_μ CC0π0p (a), CC0πNp (b), CC1π^+ (c), CC-Photon (d) and CC-Other (e) samples. The blue line shows the relative error for FGD1 while the red line for FGD2. The last bin in momentum includes all events with p_μ greater than 5000 MeV/c.

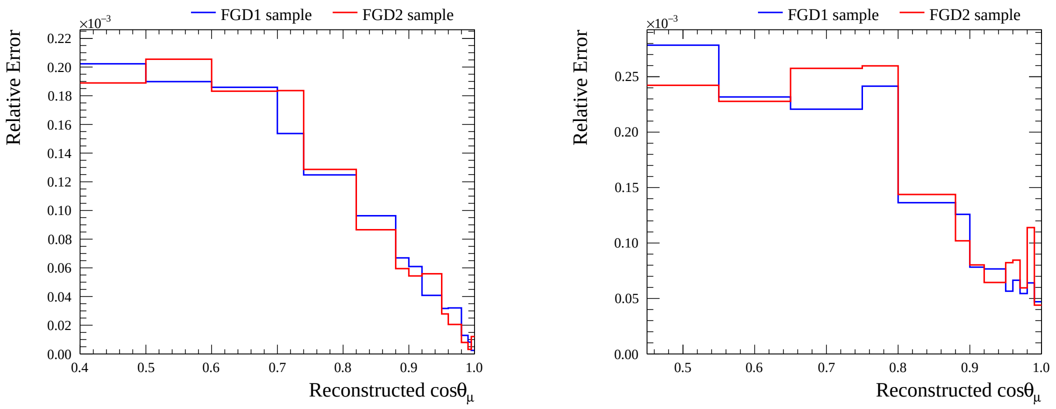

(a) CC0π0p (b) CC0πNp

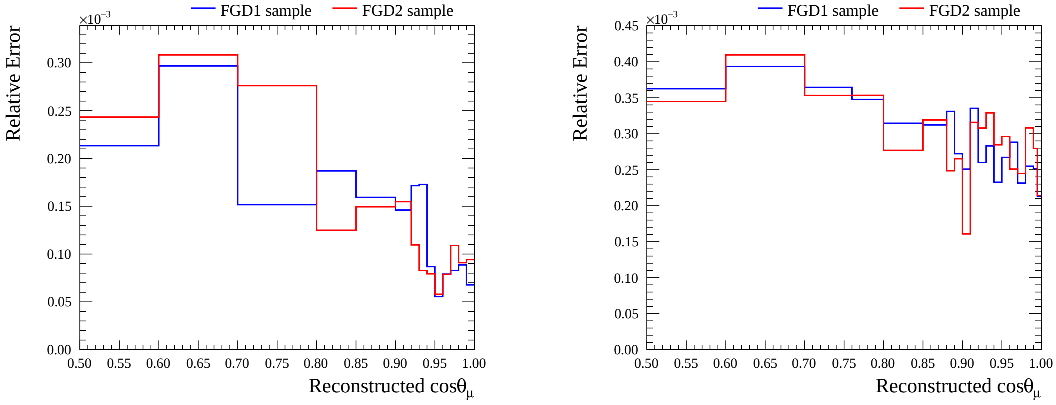

(c) CC1π^+ (d) CC-Photon

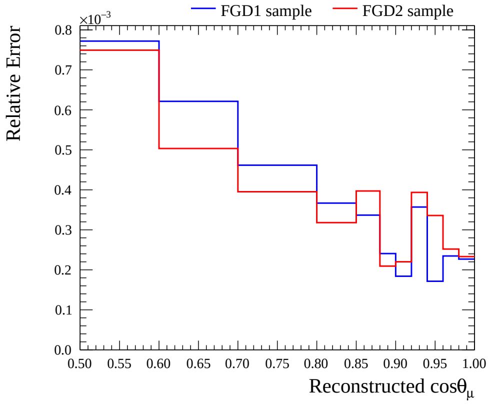

(e) CC-Other

Figure A.14: Relative error evaluated after the propagation of the uncertainty on the TPC cluster efficiency as function of the reconstructed muon $\cos\theta$ for ν_μ CC0π0p (a), CC0πNp (b), CC1π^+ (c), CC-Photon (d) and CC-Other (e) samples. The blue line shows the relative error for FGD1 while the red line for FGD2. The first bin in $\cos\theta_\mu$ includes all events with $\cos\theta_\mu$ below 0.6.

A.8 TPC tracking efficiency

The TPC tracking efficiency includes evaluation for the TPC pattern recognition algorithm and the likelihood fit. This efficiency does not include the hardware efficiency. A failure in the reconstruction leads to the wrong classification of an event topology. The relative errors in case of FGD1 and FGD2 selections are shown in Figs. A.15 and A.16.

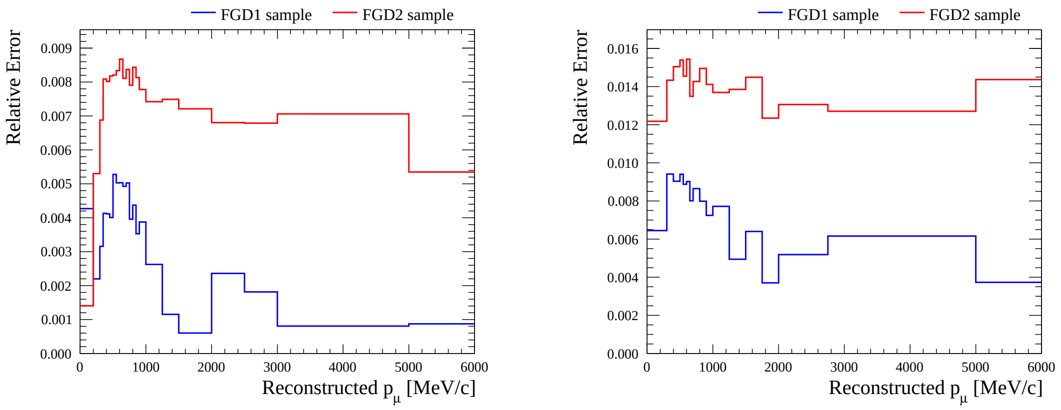

(a) CC0π0p (b) CC0πNp

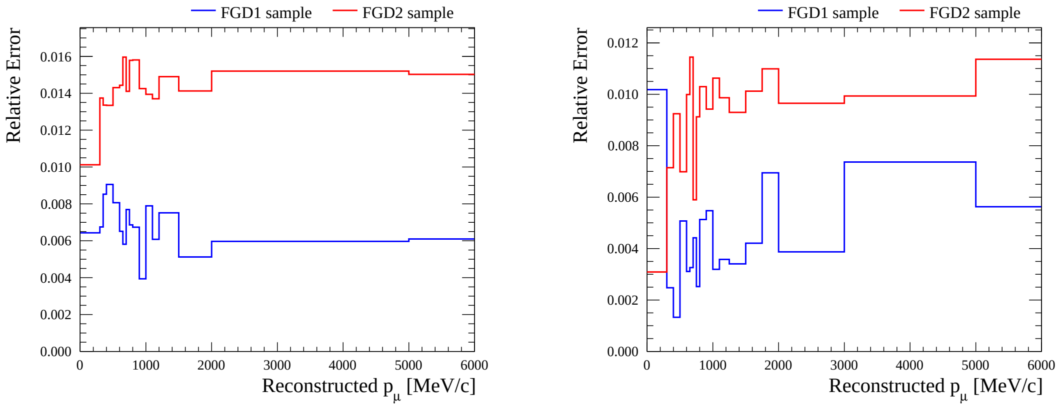

(c) CC1π^+ (d) CC-Photon

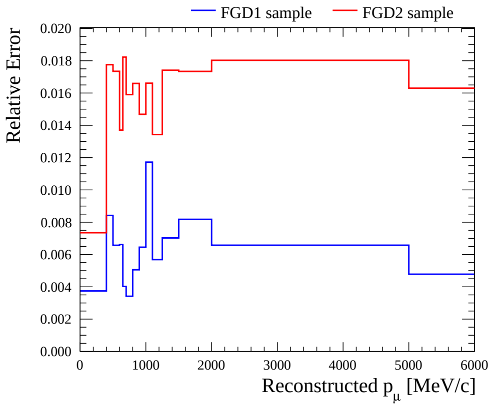

(e) CC-Other

Figure A.15: Relative error evaluated after the propagation of the uncertainty on the TPC track efficiency as function of the reconstructed muon momentum for ν_μ CC0π0p (a), CC0πNp (b), CC1π^+ (c), CC-Photon (d) and CC-Other (e) samples. The blue line shows the relative error for FGD1 while the red line for FGD2. The last bin in momentum includes all events with p_μ greater than 5000 MeV/c.

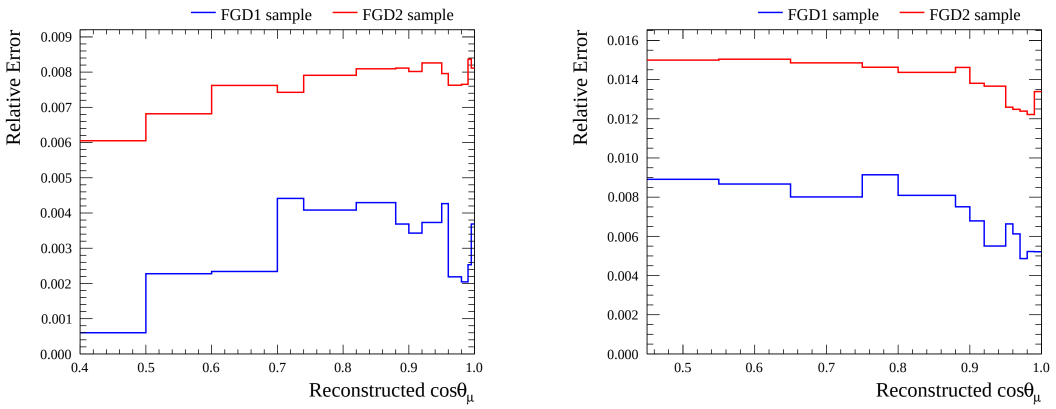

(a) CC0π0p

(b) CC0πNp

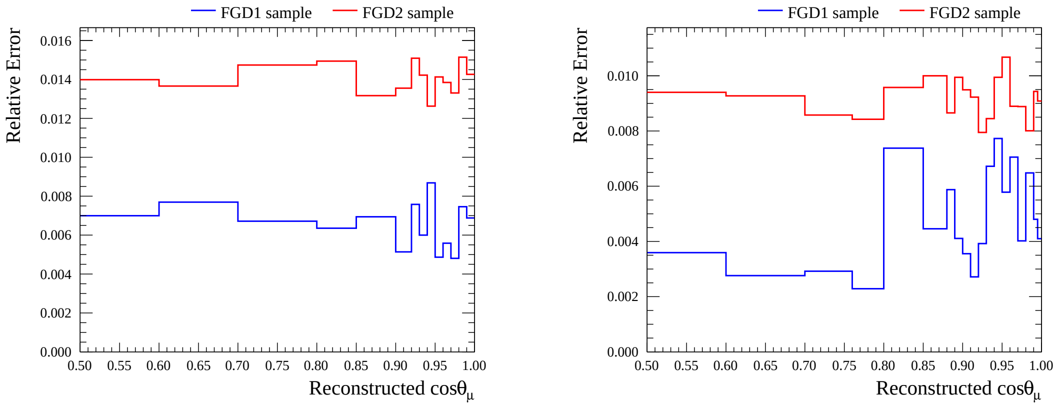

(c) CC1π^+

(d) CC-Photon

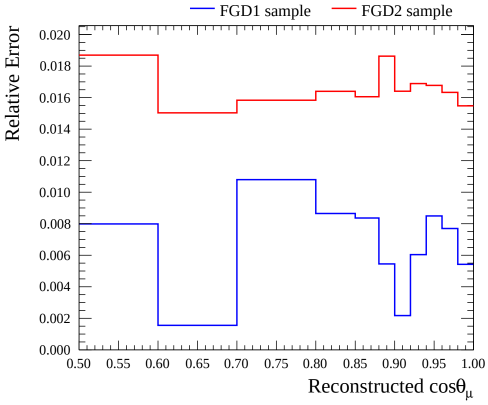

(e) CC-Other

Figure A.16: Relative error evaluated after the propagation of the uncertainty on the TPC track efficiency as function of the reconstructed muon $\cos\theta$ for ν_μ CC0π0p (a), CC0πNp (b), CC1π^+ (c), CC-Photon (d) and CC-Other (e) samples. The blue line shows the relative error for FGD1 while the red line for FGD2. The first bin in $\cos\theta_\mu$ includes all events with $\cos\theta_\mu$ below 0.6.

A.9 FGD-TPC matching efficiency

The TPC-FGD matching systematic method is described in [95]. The comparison between relative errors in the FGD1 and FGD2 selections are shown in Figs. A.17 and A.18.

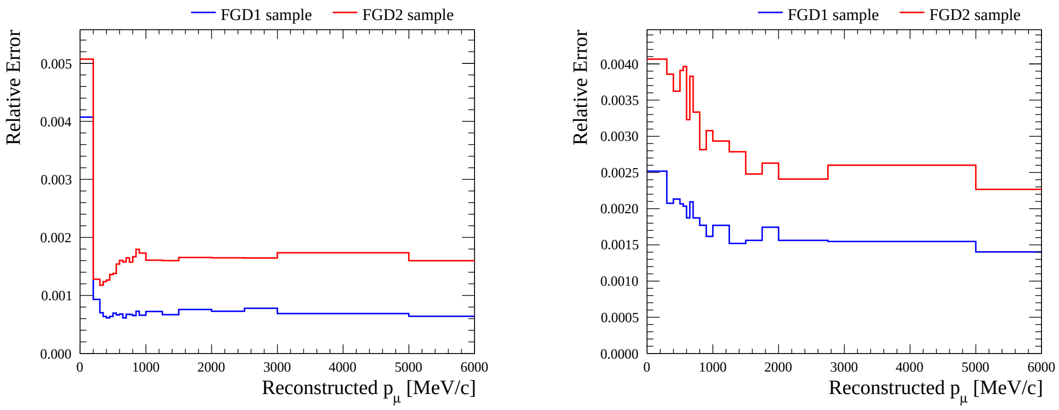

(a) CC0π0p (b) CC0πNp

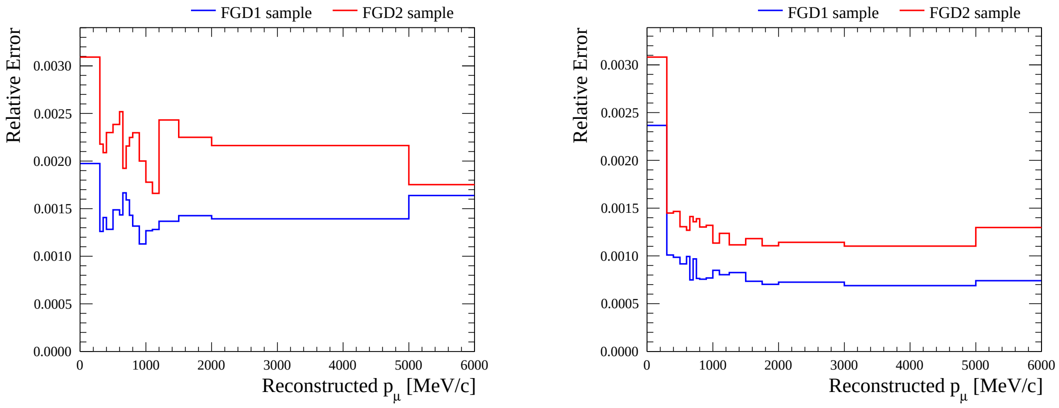

(c) CC1π^+ (d) CC-Photon

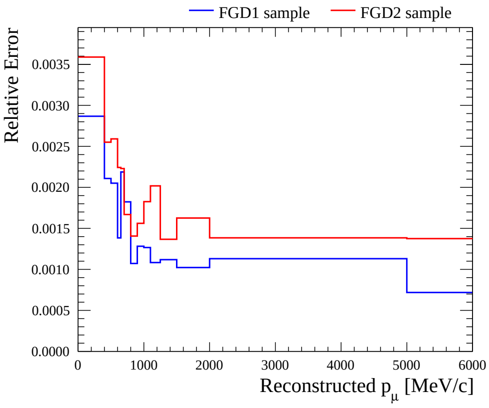

(e) CC-Other

Figure A.17: Relative error evaluated after the propagation of the uncertainty on the TPC-FGD matching efficiency as function of the reconstructed muon momentum for ν_μ CC0π0p (a), CC0πNp (b), CC1π^+ (c), CC-Photon (d) and CC-Other (e) samples. The blue line shows the relative error for FGD1 while the red line for FGD2. The last bin in momentum includes all events with p_μ greater than 5000 MeV/c.

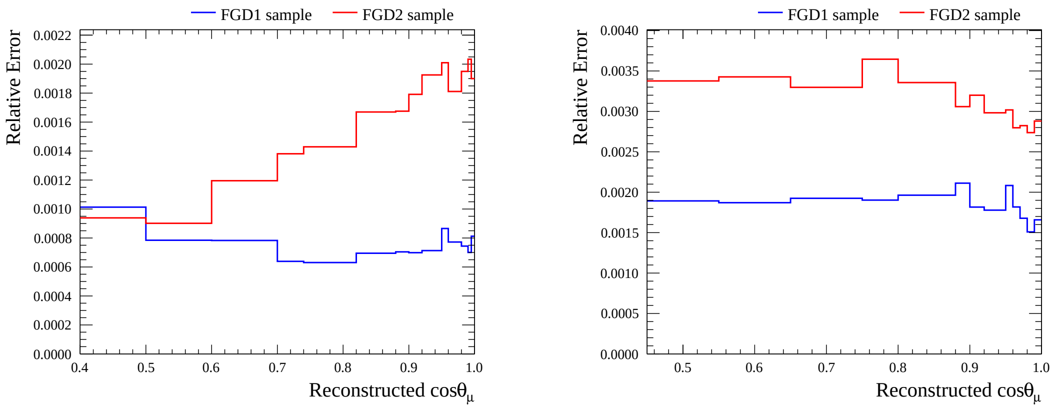

(a) CC0π0p (b) CC0πNp

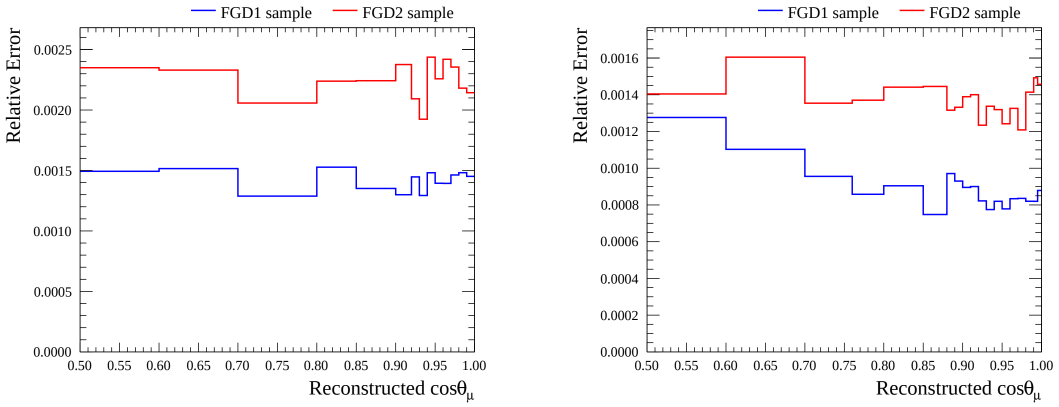

(c) CC1π^+ (d) CC-Photon

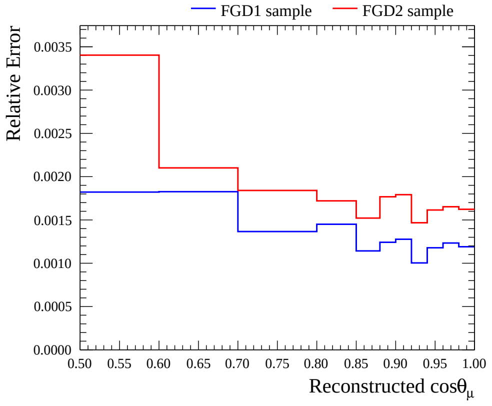

(e) CC-Other

Figure A.18: Relative error evaluated after the propagation of the uncertainty on the TPC-FGD matching efficiency as function of the reconstructed muon $\cos\theta$ for ν_μ CC0π0p (a), CC0πNp (b), CC1π^+ (c), CC-Photon (d) and CC-Other (e) samples. The blue line shows the relative error for FGD1 while the red line for FGD2. The first bin in $\cos\theta_\mu$ includes all events with $\cos\theta_\mu$ below 0.6.

A.10 FGD tracking efficiency

This systematic concerns the tracking efficiency for tracks fully contained in the FGD. A more detailed discussion can be found in [96]. The comparison between relative errors for FGD1 and FGD2 is shown in Figs. A.19 and A.20. The reason for the smaller relative error in FGD2 is not completely understood [95]. One possibility is that the reconstruction cuts on the matching χ^2 are more loose in FGD2 to be able to deal with the more complicated geometry and as a result it fails less often.

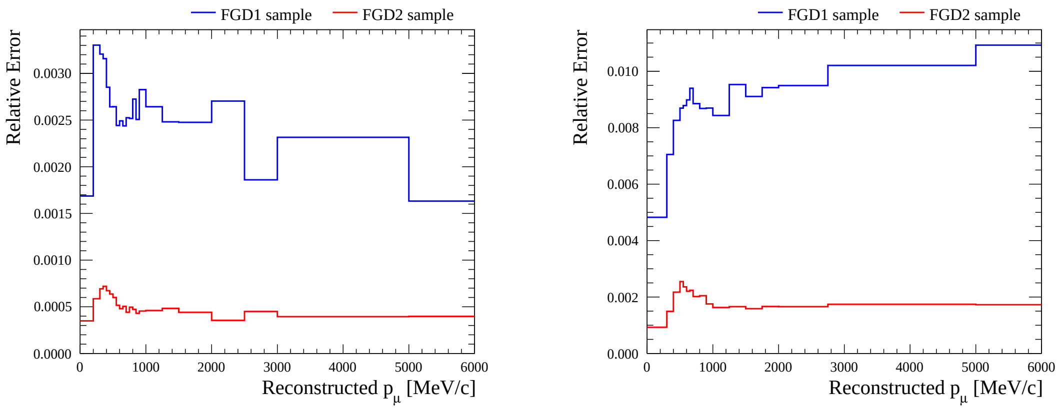

(a) CC0π0p (b) CC0πNp

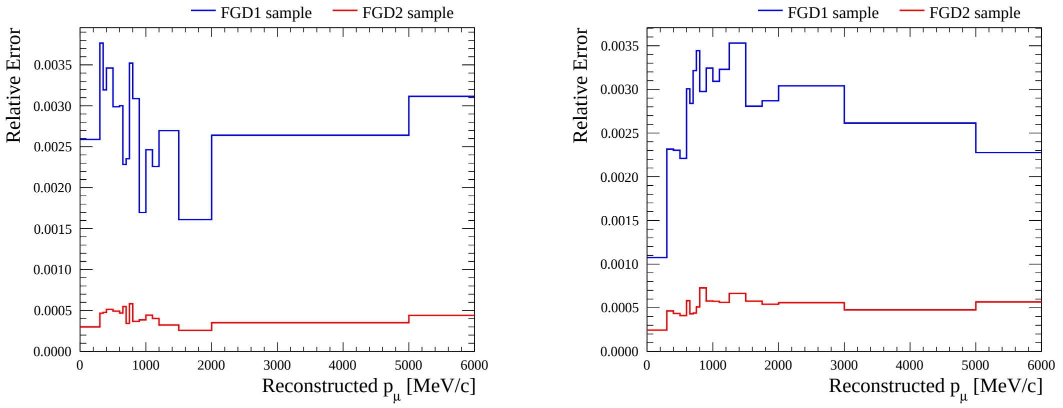

(c) CC1π^+ (d) CC-Photon

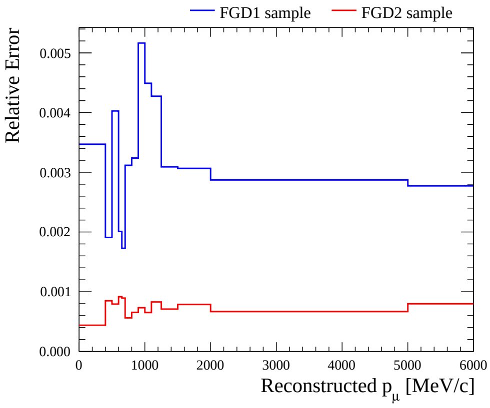

(e) CC-Other

Figure A.19: Relative error evaluated after the propagation of the uncertainty on the FGD hybrid tracking efficiency as function of the reconstructed muon momentum for ν_μ CC0π0p (a), CC0πNp (b), CC1π^+ (c), CC-Photon (d) and CC-Other (e) samples. The blue line shows the relative error for FGD1 while the red line for FGD2. The last bin in momentum includes all events with p_μ greater than 5000 MeV/c.

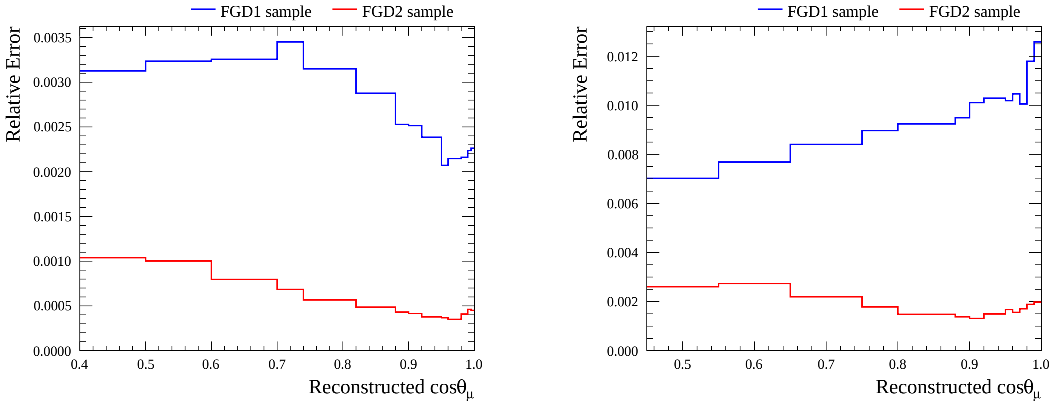

(a) CC0π0p

(b) CC0πNp

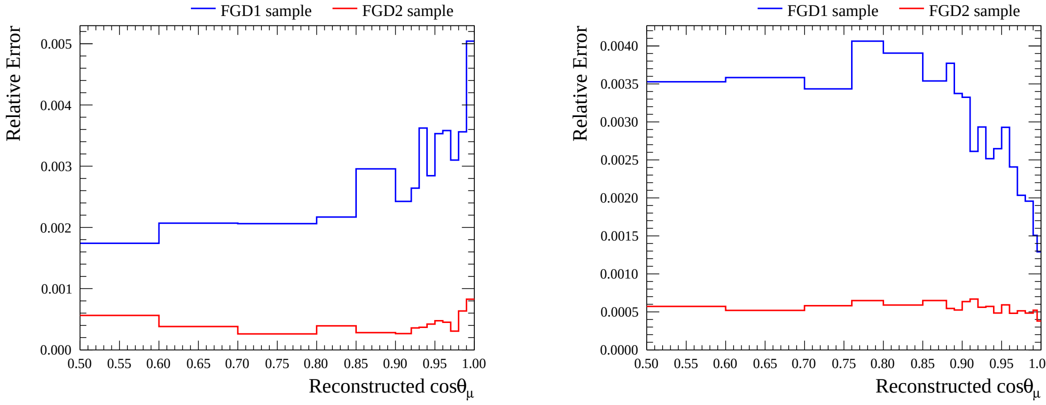

(c) CC1π^+

(d) CC-Photon

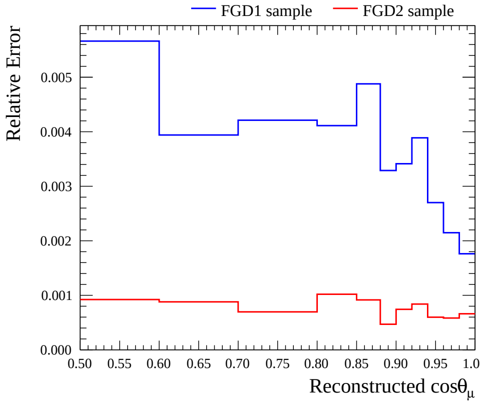

(e) CC-Other

Figure A.20: Relative error evaluated after the propagation of the uncertainty on the FGD hybrid tracking efficiency as function of the reconstructed muon $\cos\theta$ for ν_μ CC0π0p (a), CC0πNp (b), CC1π^+ (c), CC-Photon (d) and CC-Other (e) samples. The blue line shows the relative error for FGD1 while the red line for FGD2. The first bin in $\cos\theta_\mu$ includes all events with $\cos\theta_\mu$ below 0.6.

A.11 Michel electron efficiency

The systematic uncertainty associated with the Michel electron selection arises from the Michel electron detection efficiency and purity. In Figs. A.21 and A.22 comparisons between relative errors in FGD1 and FGD2 are shown. As expected, the relative error is lower in FGD1 than in FGD2.

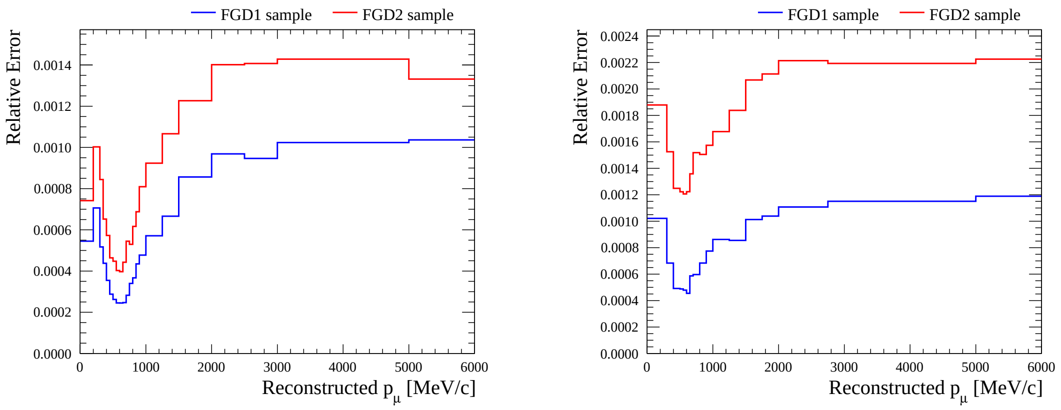

(a) CC0π0p (b) CC0πNp

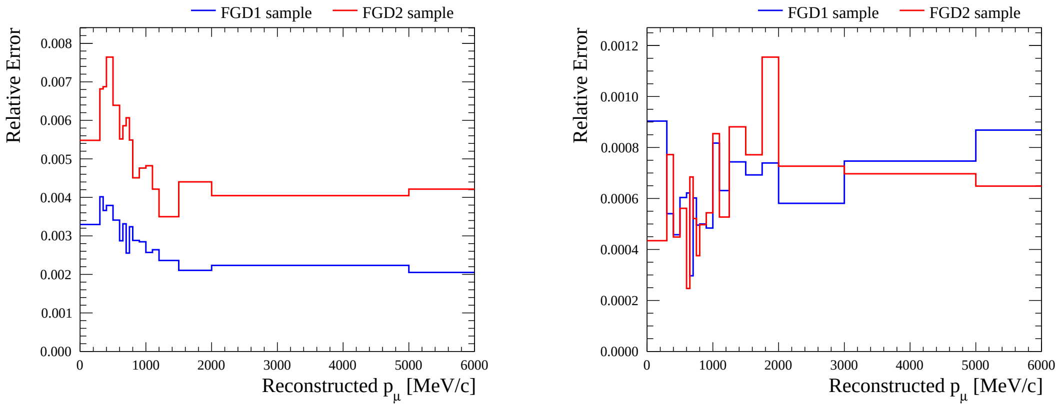

(c) CC1π^+ (d) CC-Photon

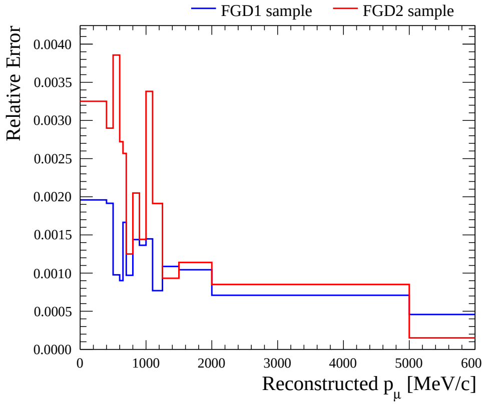

(e) CC-Other

Figure A.21: Relative error evaluated after the propagation of the uncertainty on the michel electron as function of the reconstructed muon momentum for ν_μ CC0π0p (a), CC0πNp (b), CC1π^+ (c), CC-Photon (d) and CC-Other (e) samples. The blue line shows the relative error for FGD1 while the red line for FGD2. The last bin in momentum includes all events with p_μ greater than 5000 MeV/c.

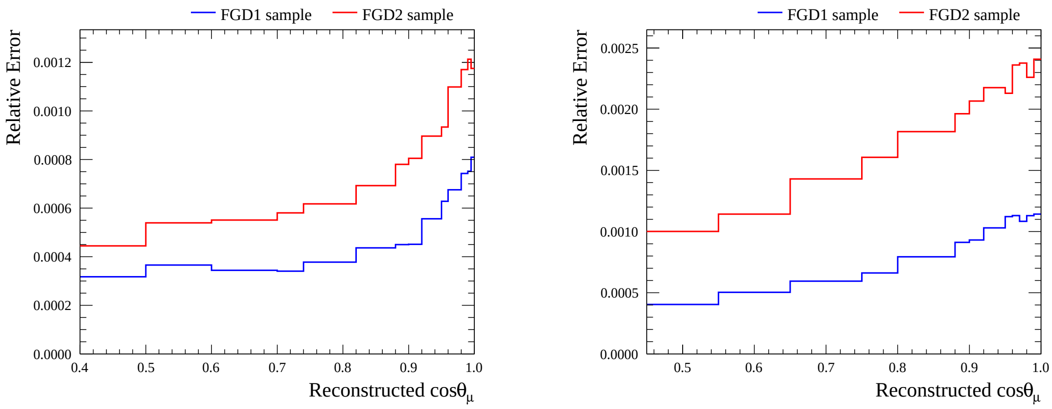

(a) CC0π0p

(b) CC0πNp

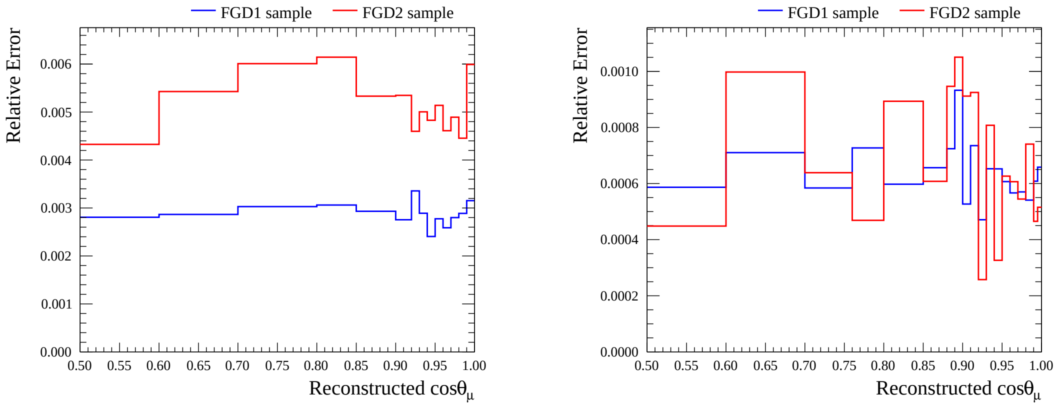

(c) CC1π^+

(d) CC-Photon

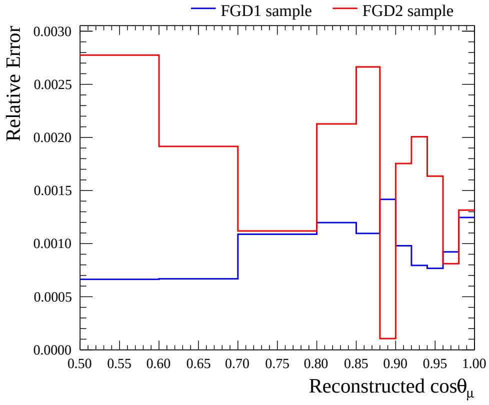

(e) CC-Other

Figure A.22: Relative error evaluated after the propagation of the uncertainty on the michel electron as function of the reconstructed muon $\cos\theta$ for ν_μ CC0π0p (a), CC0πNp (b), CC1π^+ (c), CC-Photon (d) and CC-Other (e) samples. The blue line shows the relative error for FGD1 while the red line for FGD2. The first bin in $\cos\theta_\mu$ includes all events with $\cos\theta_\mu$ below 0.6.

A.12 Pion secondary interaction

Pions undergo secondary interactions outside of the nucleus they were produced in. These processes are modelled in GEANT4; however, the model has been found to differ significantly from existing data and it has been updated using the NEUT cascade model [81, 91, 95]. As described in detail in [95], to take into account the difference between the model and data, a weight is applied to the nominal MC, while the systematic propagation makes use of weights generated using the uncertainty in external data for pion interactions. The comparison between relative errors obtained for FGD1 and FGD2 is shown in Figs. A.23 and A.24.

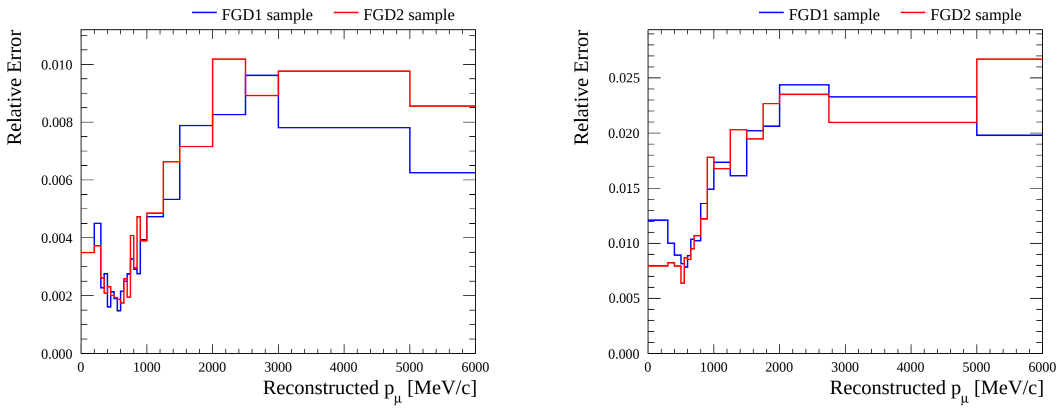

(a) CC0π0p (b) CC0πNp

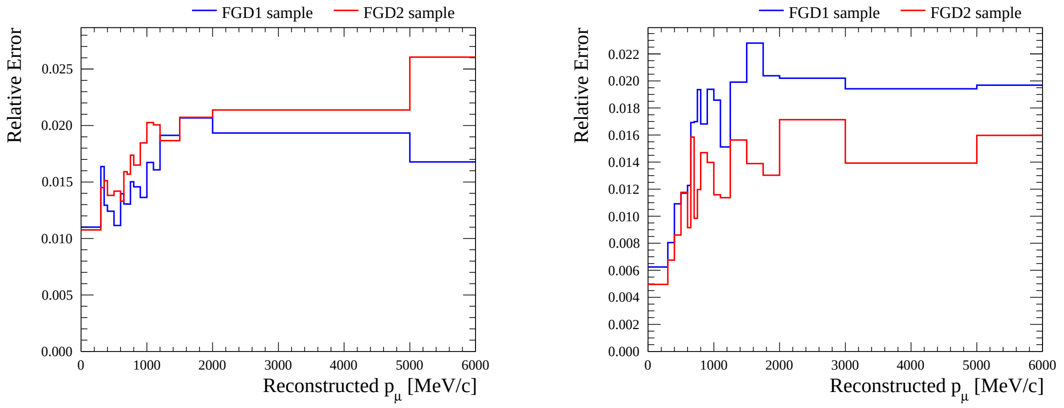

(c) CC1π^+ (d) CC-Photon

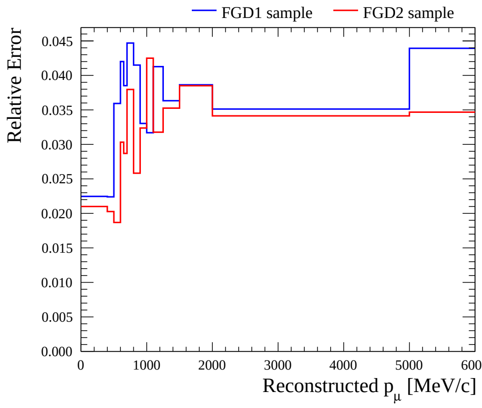

(e) CC-Other

Figure A.23: Relative error evaluated after the propagation of the uncertainty on the secondary pion interactions as function of the reconstructed muon momentum for ν_μ CC0π0p (a), CC0πNp (b), CC1π^+ (c), CC-Photon (d) and CC-Other (e) samples. The blue line shows the relative error for FGD1 while the red line for FGD2. The last bin in momentum includes all events with p_μ greater than 5000 MeV/c.

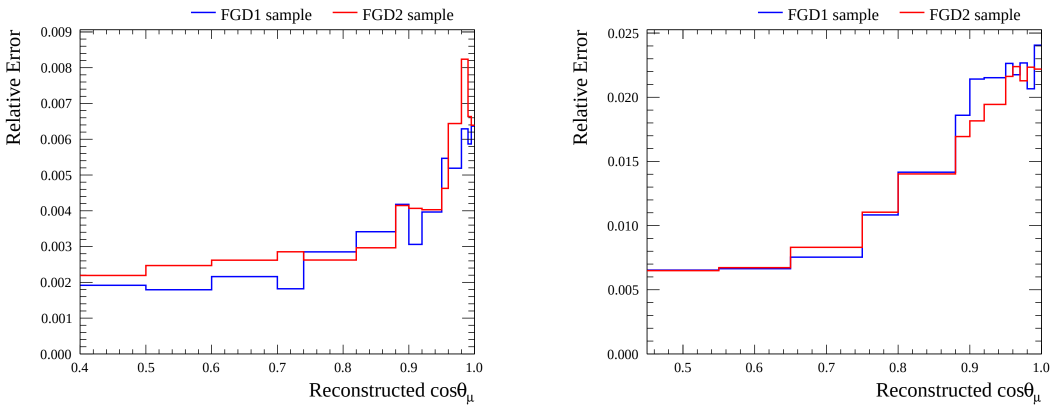

(a) CC0π0p

(b) CC0πNp

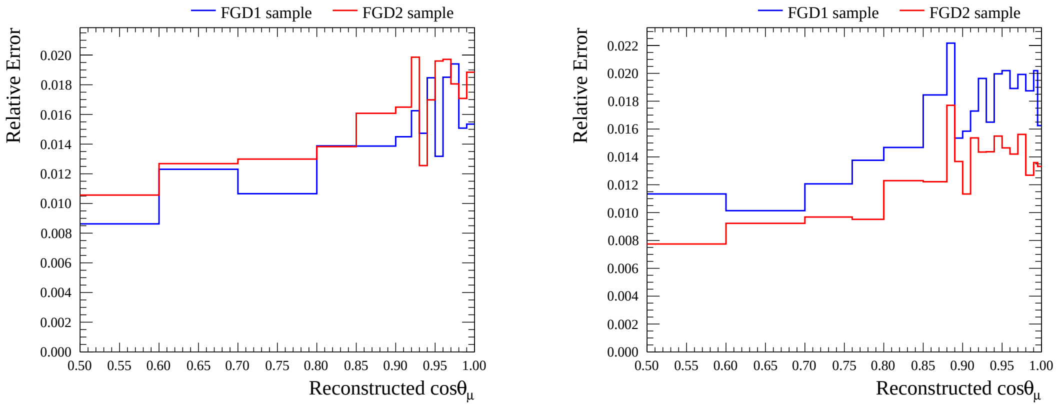

(c) CC1π^+

(d) CC-Photon

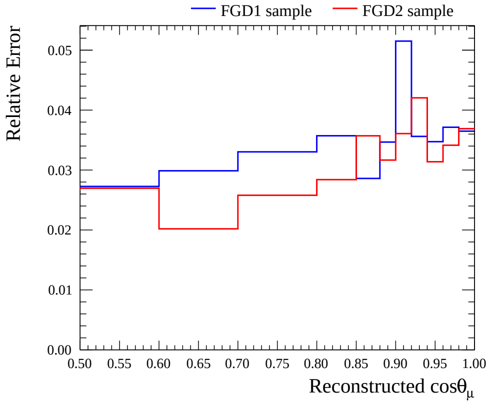

(e) CC-Other

Figure A.24: Relative error evaluated after the propagation of the uncertainty on the secondary pion interactions as function of the reconstructed muon $\cos\theta$ for ν_μ CC0π0p (a), CC0πNp (b), CC1π^+ (c), CC-Photon (d) and CC-Other (e) samples. The blue line shows the relative error for FGD1 while the red line for FGD2. The first bin in $\cos\theta_\mu$ includes all events with $\cos\theta_\mu$ below 0.6.

A.13 Proton secondary interaction

Protons undergo secondary interactions outside of the nucleus they were produced in. The implementation of this systematic uncertainty is fully described in [92]. Comparisons between the relative errors for the FGD1 and FGD2 samples are shown in Figs. A.25 and A.26. It can be seen that the relative error for CC0πNp is larger than that for CC0π0p. Since many protons are close to the reconstruction threshold, secondary interactions can determine whether a proton is reconstructed or not.

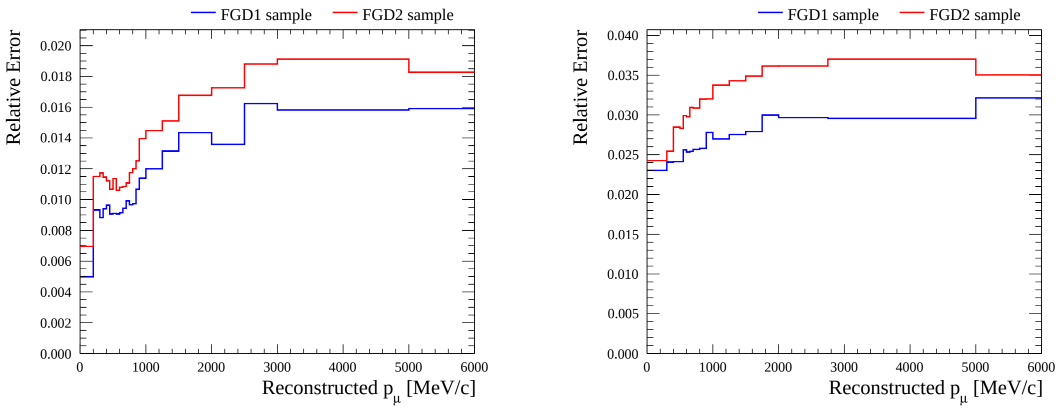

(a) CC0π0p (b) CC0πNp

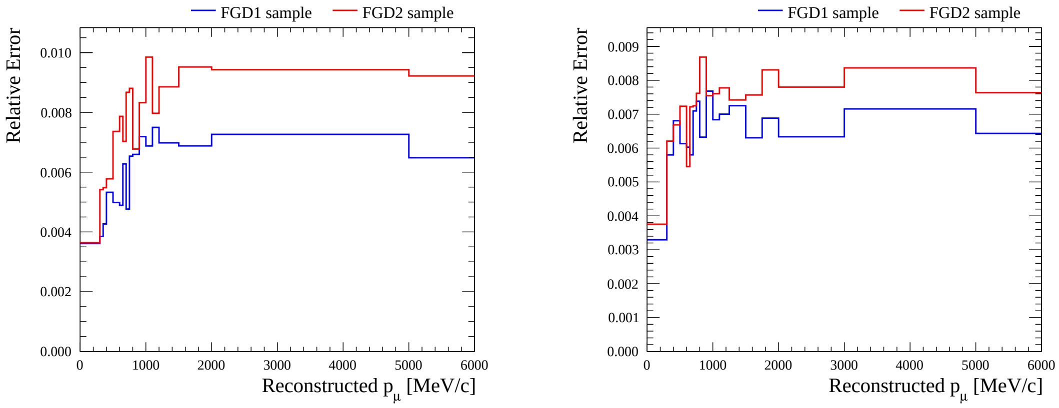

(c) CC1π^+ (d) CC-Photon

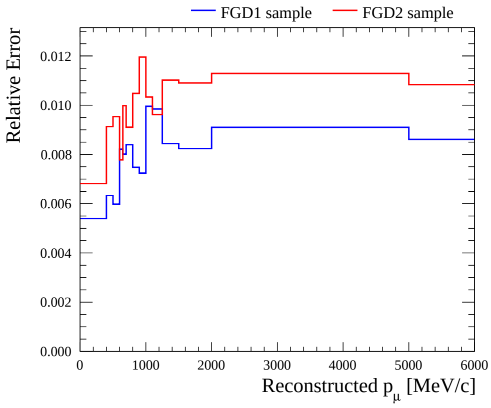

(e) CC-Other

Figure A.25: Relative error evaluated after the propagation of the uncertainty on the secondary proton interactions as function of the reconstructed muon momentum for ν_μ CC0π0p (a), CC0πNp (b), CC1π^+ (c), CC-Photon (d) and CC-Other (e) samples. The blue line shows the relative error for FGD1 while the red line for FGD2. The last bin in momentum includes all events with p_μ greater than 5000 MeV/c.

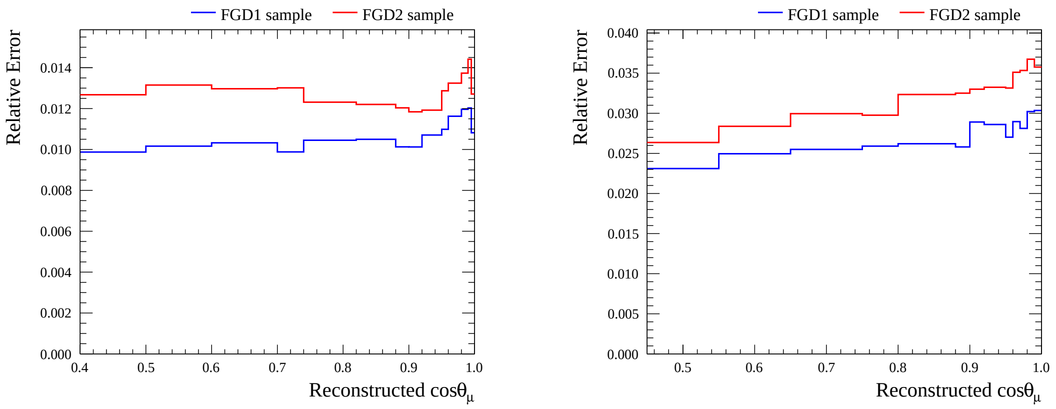

(a) CC0π0p (b) CC0πNp

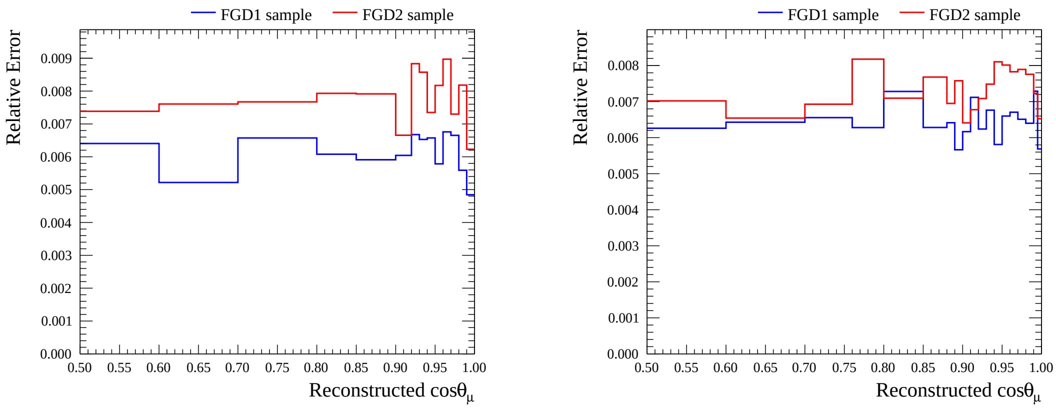

(c) CC1π^+ (d) CC-Photon

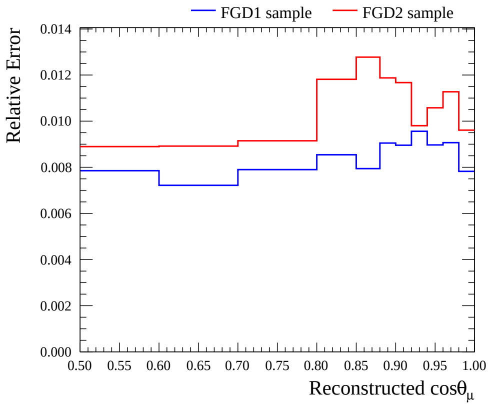

(e) CC-Other

Figure A.26: Relative error evaluated after the propagation of the uncertainty on the secondary proton interactions as function of the reconstructed muon $\cos\theta$ for ν_μ CC0π0p (a), CC0πNp (b), CC1π^+ (c), CC-Photon (d) and CC-Other (e) samples. The blue line shows the relative error for FGD1 while the red line for FGD2. The first bin in $\cos\theta_\mu$ includes all events with $\cos\theta_\mu$ below 0.6.

A.14 FGD Mass

The uncertainty for the FGD1 mass density inside the fiducial volume is approximately 0.6%, while for FGD2 it is approximately 0.4%. The difference between FGD1 and FGD2 comes from the fact that the water mass uncertainty is not correlated with the scintillator mass uncertainty. The relative errors for FGD1 and FGD2 are shown in Figs. A.27 and A.28. The reduced error at lower momentum is due to the contribution from out of fiducial volume events which are not affected by this systematic uncertainty.

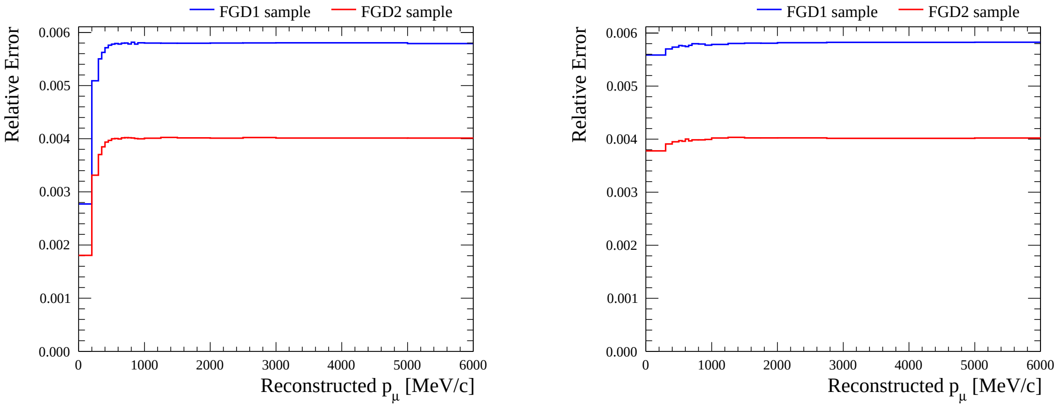

(a) CC0π0p (b) CC0πNp

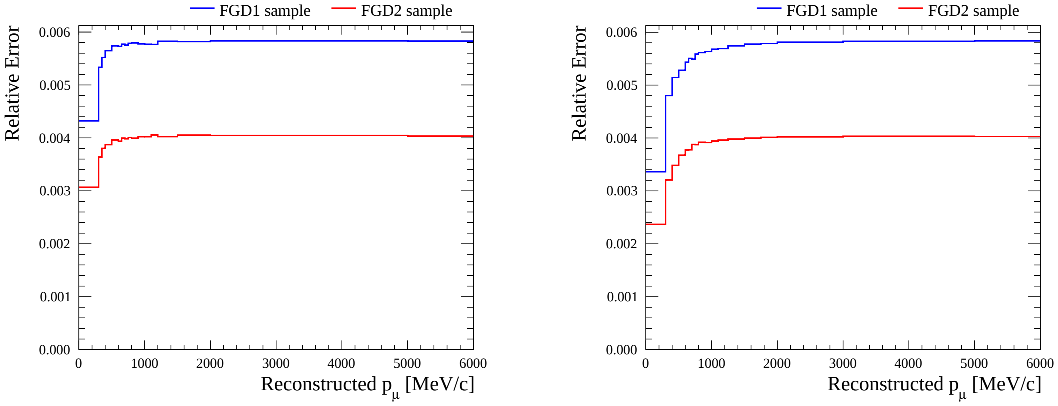

(c) CC1π^+ (d) CC-Photon

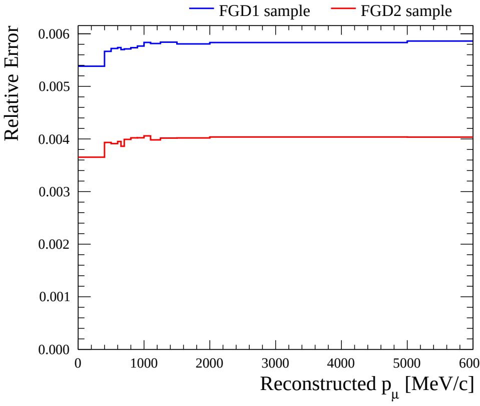

(e) CC-Other

Figure A.27: Relative error evaluated after the propagation of the uncertainty on the FGD mass as function of the reconstructed muon momentum for ν_μ CC0π0p (a), CC0πNp (b), CC1π^+ (c), CC-Photon (d) and CC-Other (e) samples. The blue line shows the relative error for FGD1 while the red line for FGD2. The last bin in momentum includes all events with p_μ greater than 5000 MeV/c.

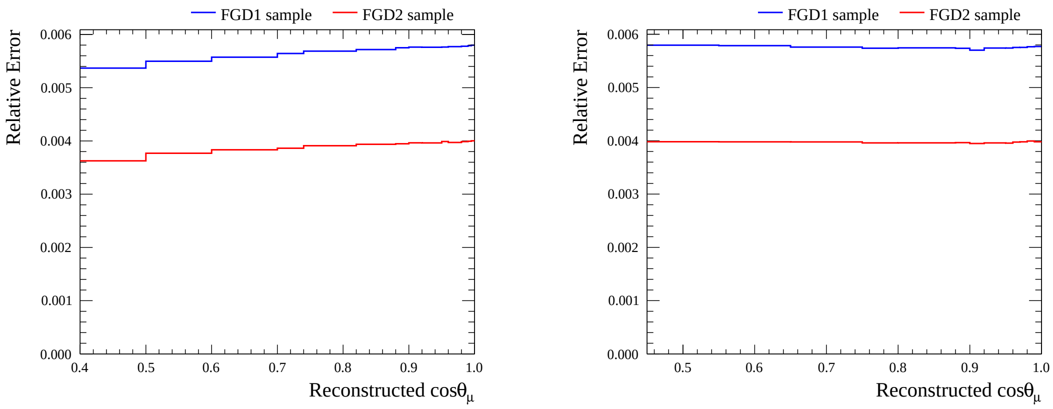

(a) CC0π0p (b) CC0πNp

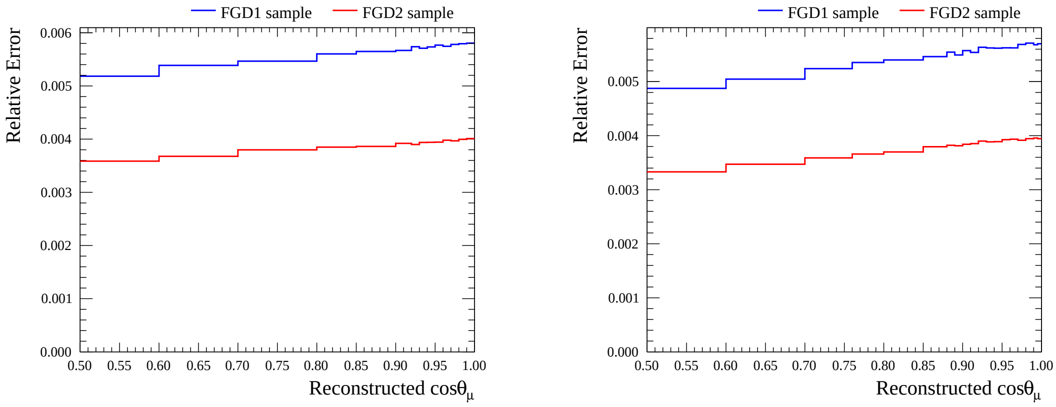

(c) CC1π^+ (d) CC-Photon

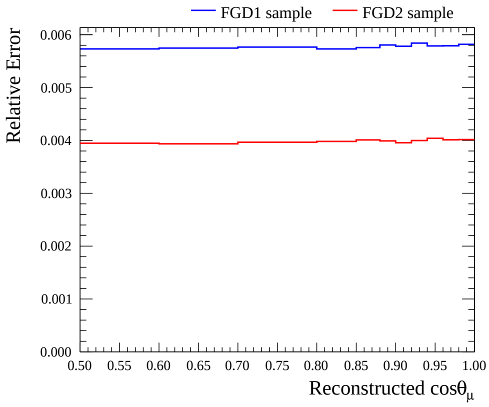

(e) CC-Other

Figure A.28: Relative error evaluated after the propagation of the uncertainty on the FGD mass as function of the reconstructed muon $\cos\theta$ for ν_μ CC0π0p (a), CC0πNp (b), CC1π^+ (c), CC-Photon (d) and CC-Other (e) samples. The blue line shows the relative error for FGD1 while the red line for FGD2. The first bin in $\cos\theta_\mu$ includes all events with $\cos\theta_\mu$ below 0.6.

A.15 Sand muon background

A dedicated Monte Carlo simulation is used to analyse particles originating from neutrino interactions outside of the ND280 detector, in rock surrounding the detector pit, that enter the detector and produce tracks which can mimic neutrino interactions in the FGD. The sand contamination is estimated in [95] for both antineutrino and neutrino components of the beam. The relative errors for FGD1 and FGD2 are shown in Figs. A.29 and A.30. The larger errors at low momentum are cue to this being the region where the sand muons populate the selection.

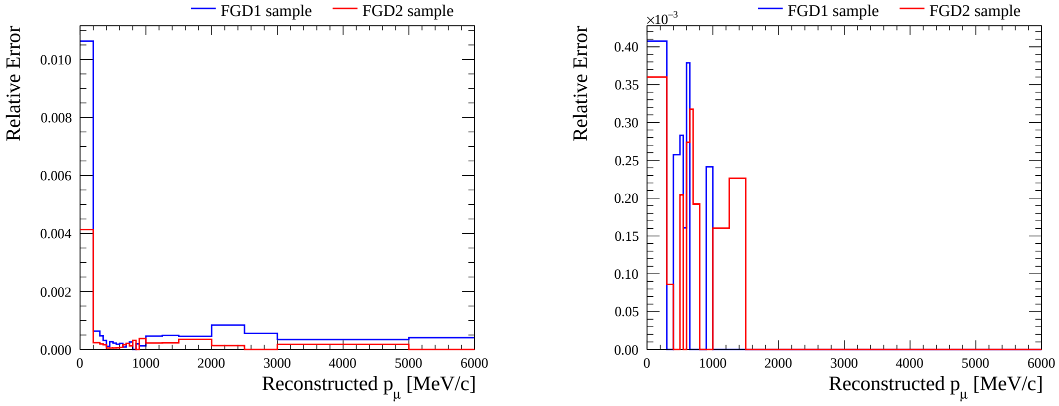

(a) CC0π0p (b) CC0πNp

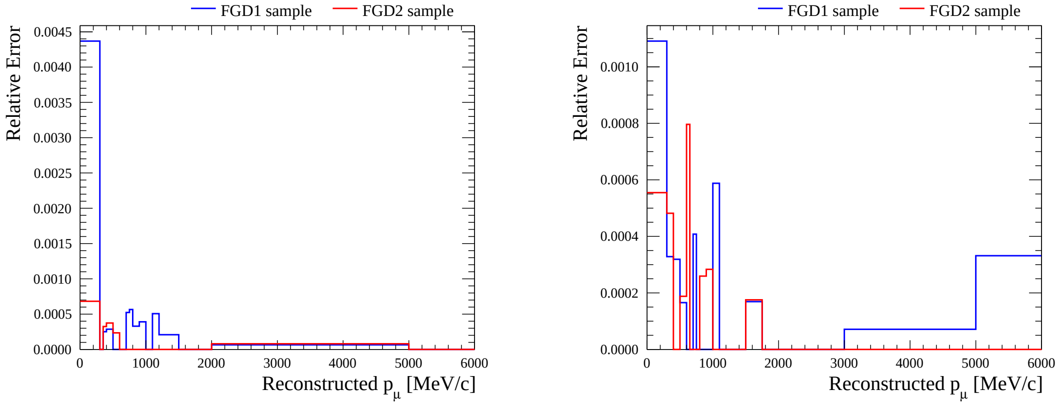

(c) CC1π^+ (d) CC-Photon

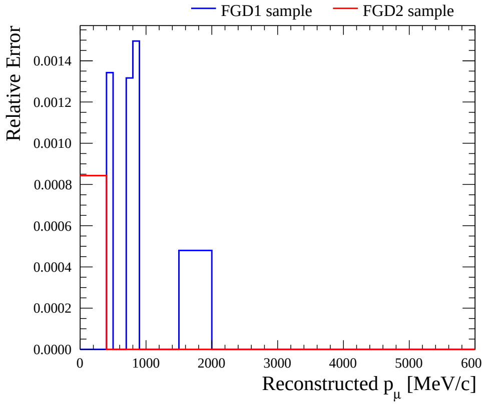

(e) CC-Other

Figure A.29: Relative error evaluated after the propagation of the uncertainty on the sand muon as function of the reconstructed muon momentum for ν_μ CC0π0p (a), CC0πNp (b), CC1π^+ (c), CC-Photon (d) and CC-Other (e) samples. The blue line shows the relative error for FGD1 while the red line for FGD2. The last bin in momentum includes all events with p_μ greater than 5000 MeV/c.

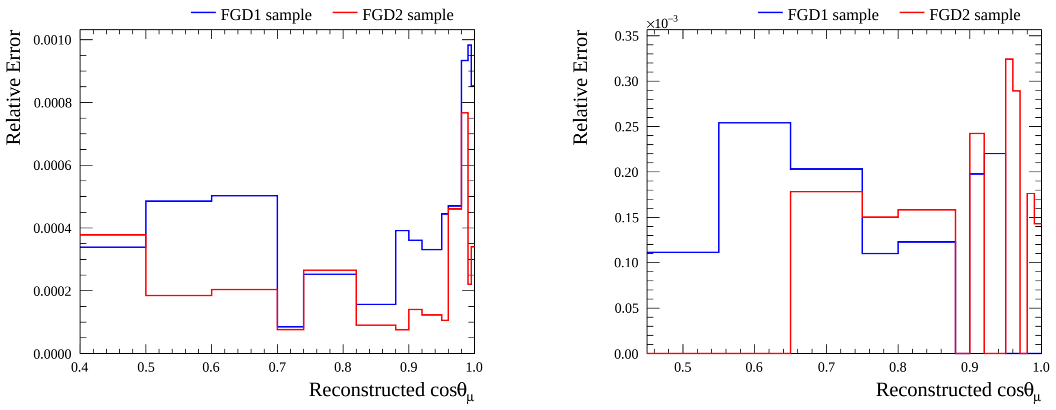

(a) CC0π0p (b) CC0πNp

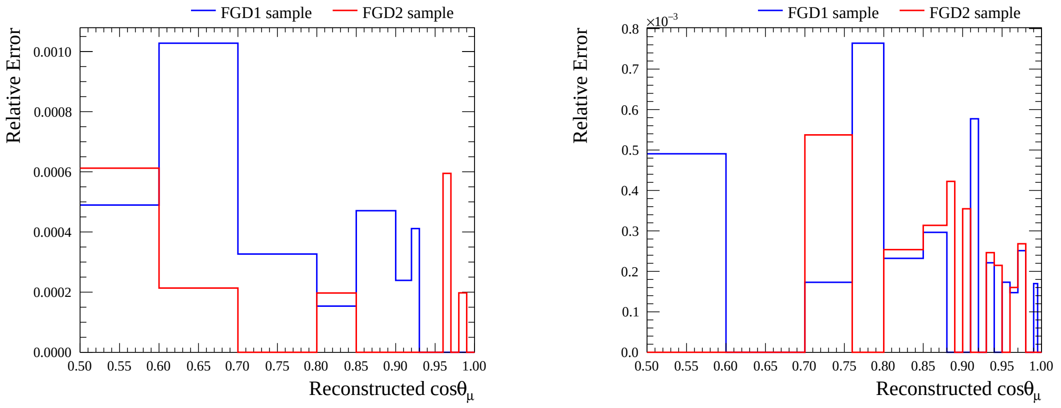

(c) CC1π^+ (d) CC-Photon

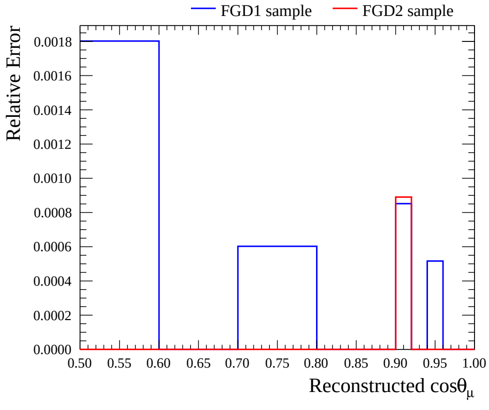

(e) CC-Other

Figure A.30: Relative error evaluated after the propagation of the uncertainty on the sand muon as function of the reconstructed muon $\cos\theta$ for ν_μ CC0π0p (a), CC0πNp (b), CC1π^+ (c), CC-Photon (d) and CC-Other (e) samples. The blue line shows the relative error for FGD1 while the red line for FGD2. The first bin in $\cos\theta_\mu$ includes all events with $\cos\theta_\mu$ below 0.6.

A.16 OOFV background

Out of FGD fiducial volume (OOFV) events are interactions reconstructed as originating in the FGD fiducial volume while the true vertex is outside. Comparisons between relative errors for the FGD1 and FGD2 samples are shown in Figs. A.31 and A.32. The larger error at low momentum occurs because this is the region OOFV events populate in the selections.

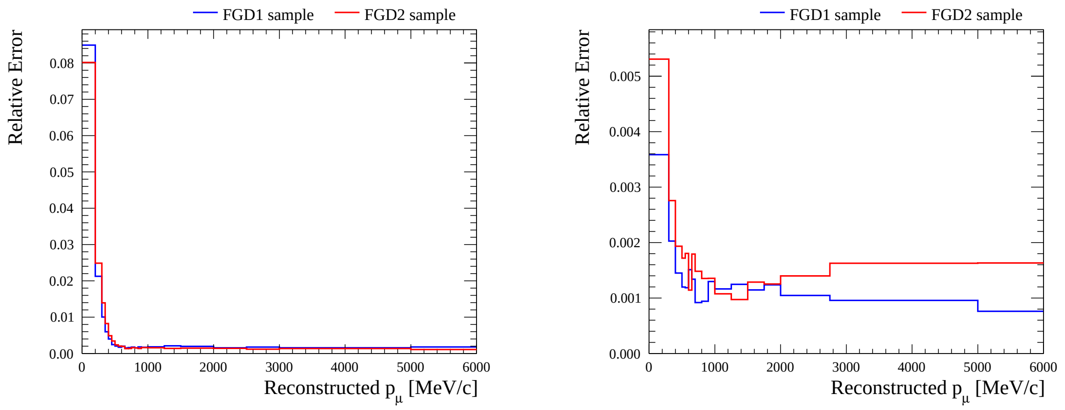

(a) CC0π0p (b) CC0πNp

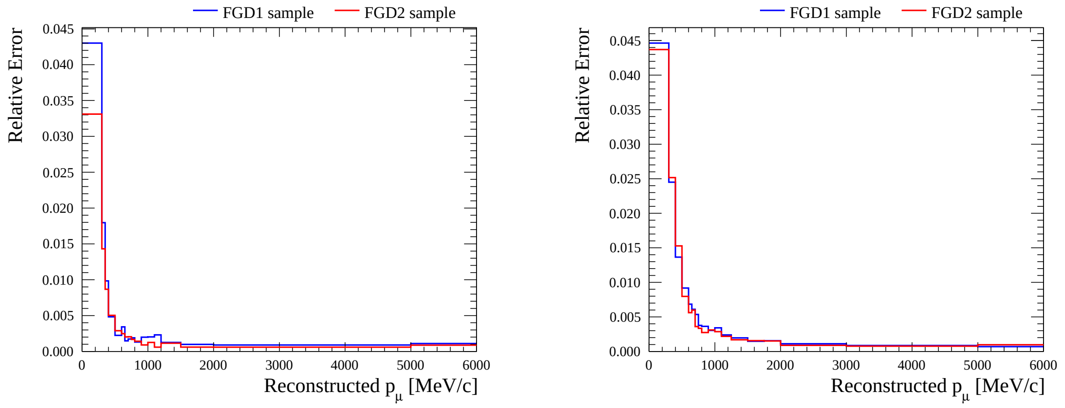

(c) CC1π^+ (d) CC-Photon

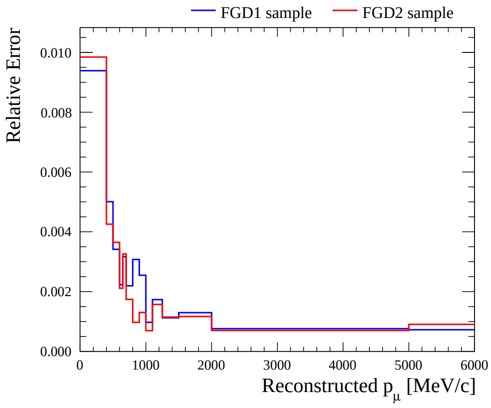

(e) CC-Other

Figure A.31: Relative error evaluated after the propagation of the uncertainty on the OOFV as function of the reconstructed muon momentum for ν_μ CC0π0p (a), CC0πNp (b), CC1π^+ (c), CC-Photon (d) and CC-Other (e) samples. The blue line shows the relative error for FGD1 while the red line for FGD2. The last bin in momentum includes all events with p_μ greater than 5000 MeV/c.

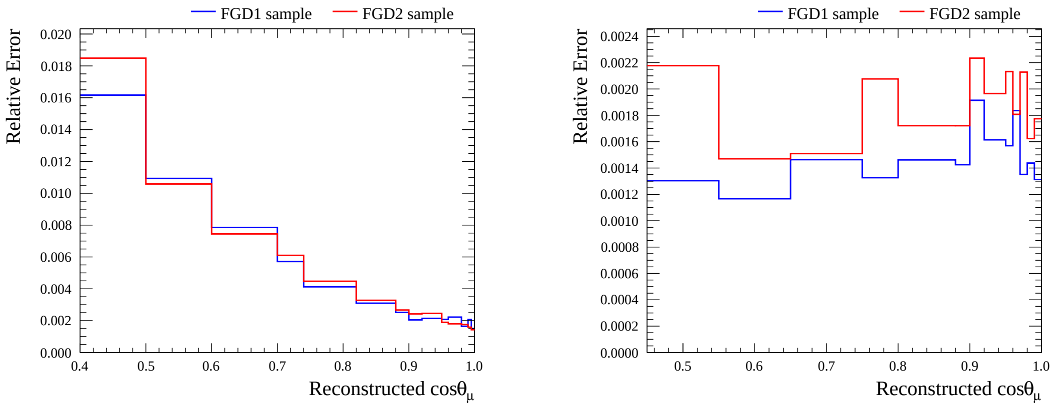

(a) CC0π0p (b) CC0πNp

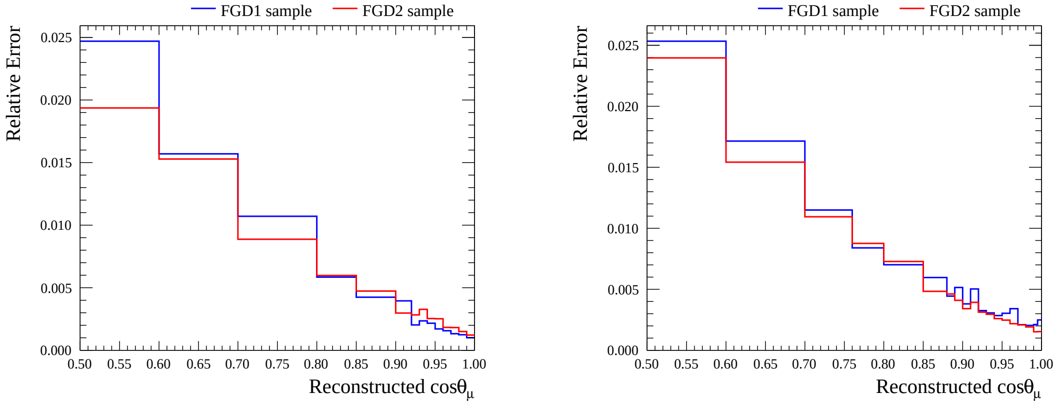

(c) CC1π^+ (d) CC-Photon

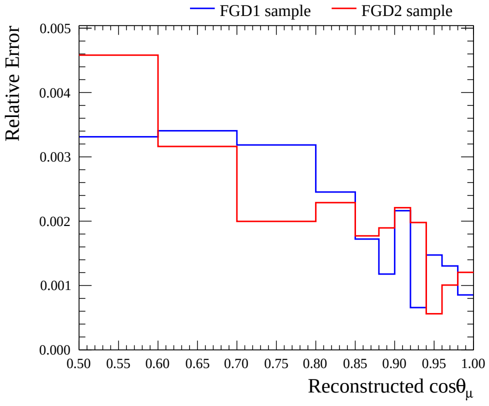

(e) CC-Other

Figure A.32: Relative error evaluated after the propagation of the uncertainty on the OOFV as function of the reconstructed muon $\cos\theta$ for ν_μ CC0π0p (a), CC0πNp (b), CC1π^+ (c), CC-Photon (d) and CC-Other (e) samples. The blue line shows the relative error for FGD1 while the red line for FGD2. The first bin in $\cos\theta_\mu$ includes all events with $\cos\theta_\mu$ below 0.6.

A.17 Pile-up

The main pile-up contribution comes from sand muons, which are not included in the standard Neut simulation, meaning a correction must be made. The evaluation of this systematic uncertainty is discussed in [95]. Comparisons between relative errors for the FGD1 and FGD2 selections are shown in Figs. A.33 and A.34. Since the the pile-up systematic is a normalisation weight applied to all events, the effect of this error is generally flat across the distributions.

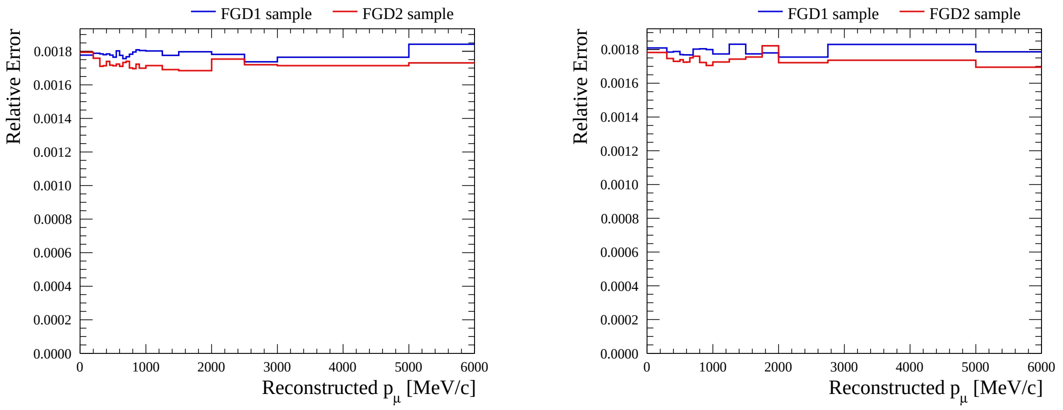

(a) CC0π0p (b) CC0πNp

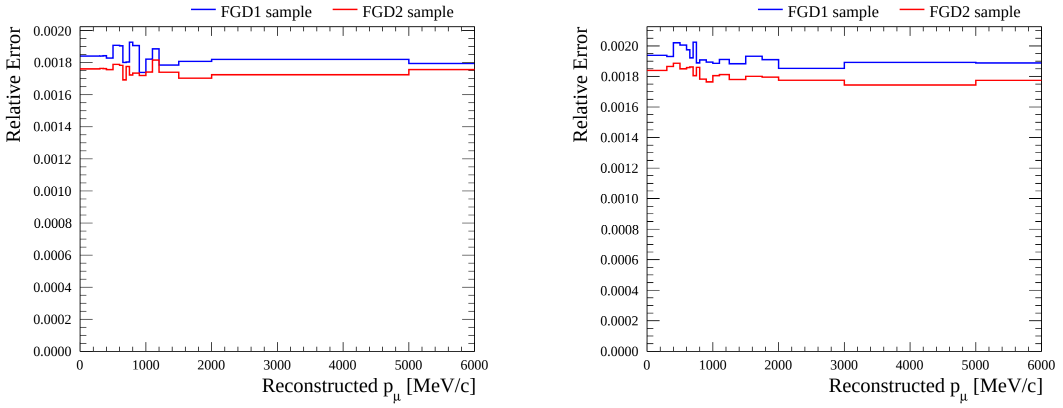

(c) CC1π^+ (d) CC-Photon

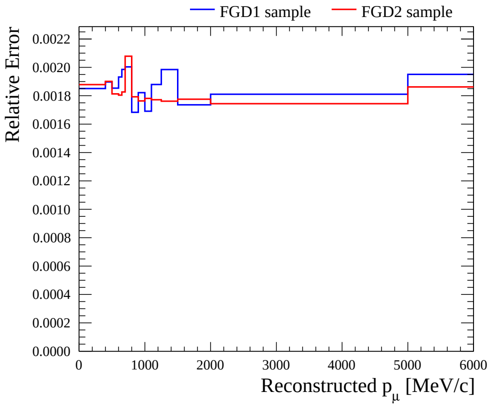

(e) CC-Other

Figure A.33: Relative error evaluated after the propagation of the uncertainty on the pile-up as function of the reconstructed muon momentum for ν_μ CC0π0p (a), CC0πNp (b), CC1π^+ (c), CC-Photon (d) and CC-Other (e) samples. The blue line shows the relative error for FGD1 while the red line for FGD2. The last bin in momentum includes all events with p_μ greater than 5000 MeV/c.

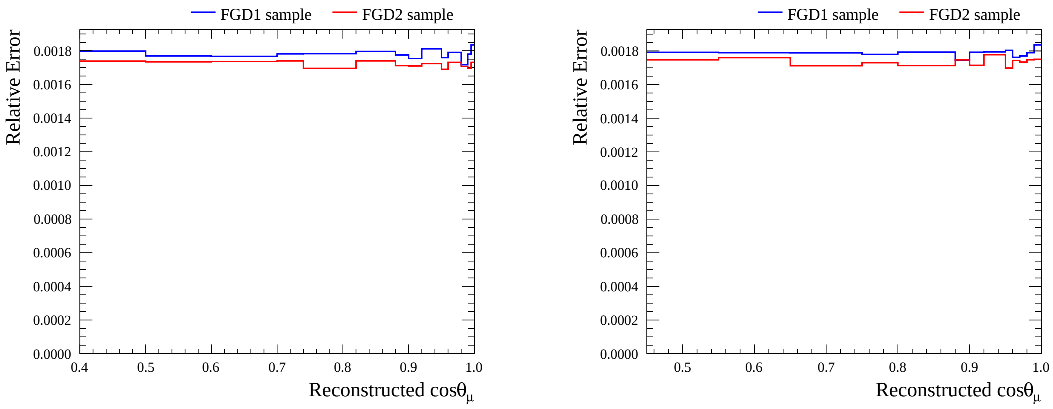

(a) CC0π0p (b) CC0πNp

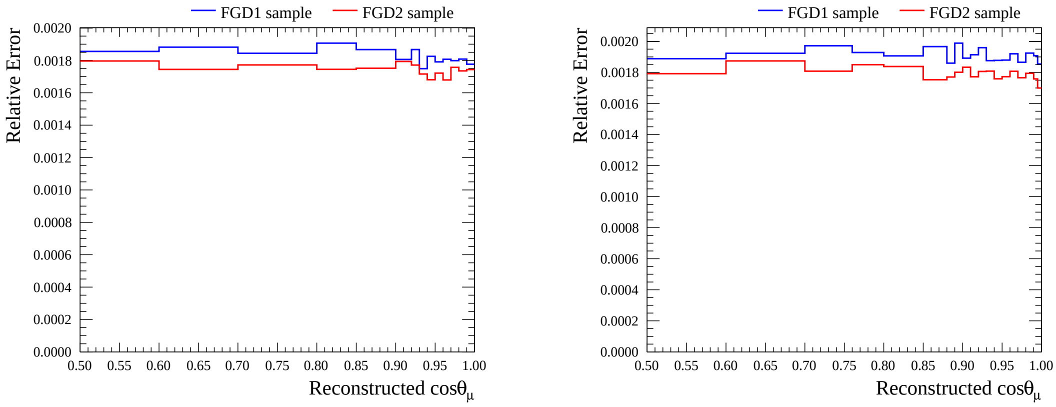

(c) CC1π^+ (d) CC-Photon

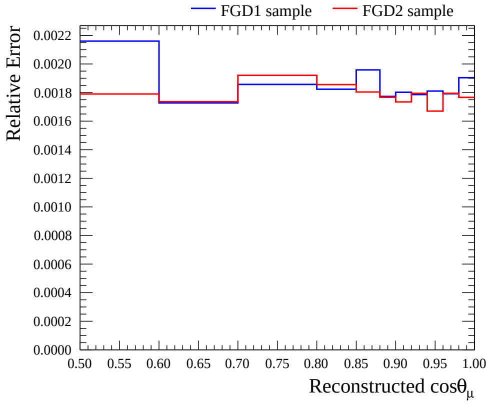

(e) CC-Other

Figure A.34: Relative error evaluated after the propagation of the uncertainty on the pile-up as function of the reconstructed muon $\cos\theta$ for ν_μ CC0π0p (a), CC0πNp (b), CC1π^+ (c), CC-Photon (d) and CC-Other (e) samples. The blue line shows the relative error for FGD1 while the red line for FGD2. The first bin in $\cos\theta_\mu$ includes all events with $\cos\theta_\mu$ below 0.6.